The Longitudinal and Transverse Response of the (e,e′p) Reaction in Helium-3 and Helium-4 in the Quasielastic Region

by

Richard E.J. Florizone

B.Eng., University of Saskatchewan (1990)
M.Sc., University of Saskatchewan (1992)

Submitted to the Department of Physics
in partial fulfillment of the requirements for the degree of

Doctor of Philosophy

at the

MASSACHUSETTS INSTITUTE OF TECHNOLOGY

February 1999
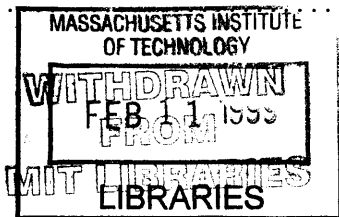
Signature of Author ....

Department of Physics
November 12, 1998

Certified by ....

William Bertozzi
Professor of Physics
Thesis Supervisor

Accepted by ....

Prof. Thomas J. Greytak
Associate Department Head for Education

The Longitudinal and Transverse Response of the (e,e′p) Reaction in Helium-3 and Helium-4 in the Quasielastic Region

by

Richard E.J. Florizone

Abstract

Measurements of the quasielastic (e,e′p) reaction have been made on ^{3}He and ^{4}He using the high-duty factor beam and high-precision 3-spectrometer system at the Insitut für Kernphysik in Mainz, Germany. Cross sections were measured at a central momentum transfer $|\vec{q}| = 685$ MeV/c, and at a central energy transfer corresponding to the center of the quasielastic peak ($\omega = 228$ MeV in ^{3}He and 242 MeV in ^{4}He). The measurements were performed in parallel kinematics and at three incident beam energies (corresponding to three values of the virtual photon polarization, ϵ) to study the longitudinal/transverse behavior of the cross sections. Coincident electrons and protons were detected in Spectrometers A and B respectively, while Spectrometer C monitored the luminosity by continuously measuring electrons scattered from the cold-gas Helium target. The momentum of Spectrometer B was varied in four steps to cover a range of proton momentum from 396 to 711 MeV/c, corresponding to a broad range of missing energy (0–150 MeV) and missing momentum (0–300 MeV/c). Calibration measurements of elastic and quasielastic electron scattering from ^{12}C were performed to study the solid angle acceptance of Spectrometers A and B. Additional measurements of Helium elastic scattering were used to determine the absolute density of the Helium gas target.

Absolute (e,e′p) cross sections for ^{3}He and ^{4}He were obtained as a function of missing energy (E_m) and missing momentum (p_m). Radiative corrections were performed with a two-dimensional unfolding technique, which revealed very large radiative contributions from the two-body breakup channel to the continuum region. At high E_m (> 20 MeV in ^{3}He, > 45 MeV in ^{4}He) and low p_m (< 100–150 MeV/c) the radiatively-unfolded measured cross sections were consistent with zero within our precision. This result was confirmed with a Monte Carlo simulation, which reproduced the shape of the measured cross section at one of the ^{3}He kinematics by applying radiative effects to a PWIA model. At higher p_m, the measured cross sections at high E_m were found to be increasingly dominated by background, which prohibited the extraction of detailed cross sections in the high (E_m, p_m) region.

At low missing energy ($E_m < 20$ MeV in ^{3}He, $E_m < 45$ MeV in ^{4}He) and low missing momentum ($p_m < 100$–150 MeV/c), radiative-corrected cross sections were determined with an estimated systematic uncertainty of 5–6%. Experimental spectral functions and momentum distributions were extracted from the data, employing de Forest's σ_{ep}^{CC1} prescription for the off-shell e-p cross section [18] and the free nucleon form factors of Simon et al. [46]. These data showed excellent shape agreement with several different theoretical spectral functions and momentum distributions, as predicted by PWIA. Accounting for an estimated 12% reduction due to final-state interaction (FSI) effects, the magnitude of the measured spectral functions

and momentum distributions was 3–22% below the PWIA+FSI prediction. The ^{4}He results indicated that the ratio (L/T) of the longitudinal (L) and transverse (T) response for both the two-body and continuum channels is consistent with σ_{ep}^{CC1}. The corresponding results in ^{3}He indicated that L/T is larger than that given by σ_{ep}^{CC1}, although the enhancement is comparable to the systematic uncertainty. Overall the (e,e'p) cross sections for ^{3}He and ^{4}He at these kinematics are relatively well-described by PWIA+FSI. More detailed theoretical predictions are required to further interpret the data.

Thesis Supervisor: William Bertozzi
Title: Professor of Physics

"...It seems probable to me, that God in the Beginning form'd Matter in solid, massy, hard, impenetrable, moveable Particles, of such Sizes and Figures, and with such other Properties, and in such Proportion to Space, as most conduced to the End for which he form'd them...their Truth appearing to us by Phaenomena, though their Causes be not yet discover'd."

Sir Isaac Newton, *Opticks*, 1730.

Contents

List of Figures

List of Tables

Chapter 1

Introduction

A powerful technique for studying the structure of the nucleus is electron scattering, in which the incident electron interacts with the nucleus via the electromagnetic (EM) interaction. The principal advantages of the EM interaction are that it is well-understood from quantum electrodynamics (QED), and it is relatively weak compared to the hadronic interaction between nucleons. The weakness of the interaction generally allows the use of the Born Approximation, which simplifies the form of the scattering cross section. It also means that the EM probe can fully sample the nuclear volume, in contrast to hadronic probes which interact mostly with the outer surface of the nucleus.

One disadvantage of electron scattering is that the highly-relativistic electrons used readily radiate real and virtual photons. The measured cross sections therefore need to be radiatively-corrected, or alternatively reaction models must include radiation processes. Although the mechanisms behind radiative corrections are described by QED and are hence well-understood, the kinematics of the radiation causes a re-distribution of the cross section that can be quite complicated. Depending on the circumstances, the radiative corrections can also be very large.

In electron scattering, the incident electron transfers energy (ω) and momentum (q) to the target through the emission of a virtual photon. At momentum transfers of several hundred MeV/c, the virtual photon has a wavelength of the order of 10^{-15} meters, so that it can resolve objects approximately the size of a nucleon. At this scale, theoretical models are typically based on a nucleus composed of strongly interacting individual nucleons. The effects of nucleon structure (that is, of the quarks and gluons comprising a nucleon) are accounted for by the

electromagnetic form factors that describe the charge and magnetization distributions of the nucleons.

To describe a typical nucleus (A>3) at these scales, most theories start from an independent particle model (IPM). In an IPM, the system of strongly interacting nucleons is replaced by nucleons moving independently, within the constraints of the Pauli exclusion principle, in a mean-field potential which represents the average effect on one nucleon of all the others. This single-particle potential can be derived with the Hartree-Fock technique [1] using a phenomenological 2-body nucleon-nucleon (NN) potential, which is determined from NN scattering data and the measured properties of ^{2}H. In addition, one needs to add short and long-range properties to describe the influence of three-body forces and density dependence. The single-particle wavefunctions can then be determined by solving the Schrödinger equation for the single-particle potential. For the two- and three-body systems, the single-particle wavefunctions can be obtained directly from the NN potential without resorting to the IPM approach.

From these wavefunctions, a variety of nuclear properties are calculated. Experimental measurements can then be performed to check the validity of the above picture, and to look for currents and new degrees of freedom that go beyond the traditional picture, such as meson exchange currents or isobar configurations.

In inclusive (e,e') electron scattering experiments, the measured cross section exhibits a broad peak known as the quasielastic peak, which largely corresponds to the knockout of a single nucleon by the incident electron. This description of the peak is supported by the fact that it is centered approximately at an electron energy transfer $\omega = q_\mu^2/2M$, where q_μ is the 4-momentum transfer of the scattered electron and M is the mass of the nucleon. This is the same relation as for the free electron-nucleon scattering process. In addition, the width of the quasielastic peak can be successfully interpreted as arising from the Fermi motion of a nucleon within the nucleus. Measurements of inclusive (e,e') cross sections on a range of nuclei in this region support the traditional mean-field view of the nucleus [2, 3, 4].

However, measurements of the separated longitudinal and transverse response functions which comprise the (e,e') cross section reveal a problem with our current understanding of the

reaction process in the quasielastic region. If the process is truly quasifree, the transverse and longitudinal scaling functions $f_T(y)$ and $f_L(y)$ should be equal (where y is the scaling variable defined in Ref. [2]). For ^{4}He [5] and ^{12}C [6] they differ substantially, even for $y \le 0$ where the effect of the delta (Δ) should be negligible. For ^{4}He, Carlson and Schiavilla [7] were able to reproduce the longitudinal and transverse responses in a calculation that included meson exchange currents (MEC) and final-state interactions (FSI). In contrast to the heavier nuclei, measurements of (e,e') on ^{3}He [5, 8] found $f_T(y)$ and $f_L(y)$ to be equal for $y \le 0$, as expected for a quasifree process.

A similar situation is seen in measurements of the (e,e'p) reaction in the quasielastic region. For the 2-body breakup of ^{3}He, the longitudinal and transverse components of the spectral function, S_L and S_T, were found to be equal, as expected [9, 10]. However, for ^{4}He the longitudinal strength was found to be suppressed with respect to the transverse strength by 20–40% [10], which is similar to what has been seen in inclusive scattering. In the continuum region (i.e. at missing energies above the 3-body breakup threshold), a suppression of S_L relative to S_T was also seen in ^{3}He [11]. However, it should be noted that this measurement was performed in the dip region, where meson-exchange currents and effects of the Δ (both transverse) are expected to be enhanced compared to the quasielastic region.

In ^{12}C at quasielastic kinematics, S_L and S_T were found to be equal for the 2-body breakup, but an enhancement of S_T over S_L was seen at higher missing energies, starting at about the 2-nucleon emission threshold [12]. This led to the speculation that the enhancement might come from some new transverse process involving at least two nucleons.

These and other pieces of experimental evidence seem to indicate some problems in the theoretical understanding of the quasielastic region. Whether the problem is with the dynamics of the reaction (for example, from radiative effects) or with our understanding of the nucleus (such as high momentum components, short-range NN correlations, or MEC) remains to be seen. This thesis reports on a systematic study of the longitudinal and transverse responses for the (e,e'p) reaction in ^{3}He and ^{4}He in the quasielastic region, which is of interest for the following reasons:

1. Exact 3-body calculations to the continuum are now becoming available, making ^{3}He an attractive testing ground for effects that are not included in conventional theory. Modern calculations are also forthcoming on the 4-body system.

2. The difference in the scaling functions $f_T(y)$ and $f_L(y)$ measured in inclusive ^{4}He(e,e′) is in striking contrast to the results in ^{3}He(e,e′), where no difference is seen.

3. Similarly, the difference in S_L and S_T measured in ^{4}He(e,e′p)^{3}H is in contrast to the measurement in ^{3}He(e,e′p)^{2}H, where no difference is seen.

4. The results on ^{12}C(e,e′p) at high missing energy suggest multi-nucleon processes. The difference in nuclear density between ^{3}He and ^{4}He may be important when investigating such processes.

5. The high-precision, high-duty factor setup at Mainz enables the measurement of these cross sections to a high statistical and systematic accuracy. This is particularly important in the high missing energy region, where previous measurements have shown that the (e,e′p) cross section is small in these two nuclei.

In Chapter 2, an overview of the (e,e′p) reaction formalism is given and all kinematic variables are defined. The experimental setup at Mainz, where the measurements were performed, is discussed in Chapter 3. The techniques and analysis of the various calibrations and normalizations are presented in Chapter 4, and the analysis of the (e,e′p) data is discussed in Chapter 5. The final results for the (e,e′p) cross sections are given in Chapter 6, and finally the conclusions and summary are presented in Chapter 7.

Chapter 2

The (e,e′p) Reaction

Overview

A brief review of the (e,e′p) reaction formalism is given. The kinematic variables are defined, and the the most general cross section is given in the Plane Wave Born Approximation (PWBA). The Plane Wave Impulse Approximation (PWIA), which is a simple model of the (e,e′p) reaction, is introduced.

2.1   Kinematics

We describe the kinematics of the (e,e′p) reaction using the following four-vectors:

particle	4-vector
incident electron	$k_i = (E_i, \vec{k}_i)$
scattered electron	$k_f = (E_f, \vec{k}_f)$
target nucleus	$p_A = (E_A, \vec{P}_A)$
detected proton	$p_p = (E, \vec{p}_p)$
residual nucleus	$p_B = (E_B, \vec{p}_B)$
virtual photon	$q = (\omega, \vec{q})$

Figure 2-1 contains a diagram illustrating the various vectors. Note that in the figure p_x is for the scattered proton and corresponds to our p_p.

In an (e,e′p) experiment, the momentum of the incident and scattered electrons and of the detected proton are measured, so that k_i, k_f, and p_p are known. Additionally, in the laboratory
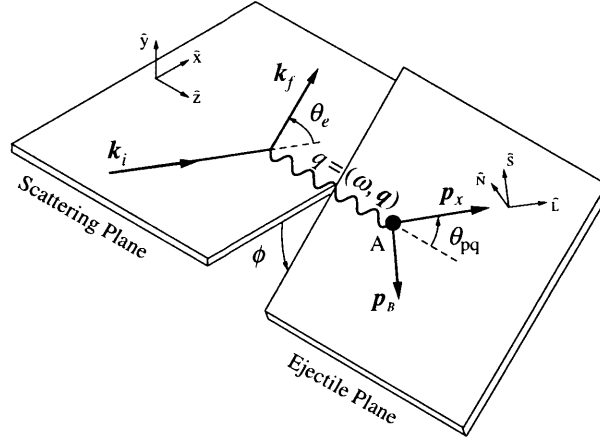
Figure 2-1: Kinematic definitions for the (e,e'p) reaction. Figure from ref. [13]

frame the target nucleus is at rest so that $p_A = (M_A, 0)$. The four-momentum of the virtual photon can be calculated from

$$q = k_i - k_f = (\omega, \vec{q}) \tag{2.1}$$

corresponding to an energy $\omega = E_i - E_f$ and 3-momentum transfer $\vec{q} = \vec{k}_i - \vec{k}_f$. Note that

$$q^2 = \omega^2 - |\vec{q}|^2 \leq 0 \tag{2.2}$$

and we define

$$Q^2 = -q^2 \geq 0. \tag{2.3}$$

The electrons that we consider are ultra-relativistic (i.e. $k \gg m_e$), so that $E_i \approx |\vec{k}_i|$ and $E_f \approx |\vec{k}_f|$ is a very good approximation.

The scattering plane is defined as the plane containing $\vec{k}_i$ and $\vec{k}_f$, and the reaction plane is similarly defined by $\vec{q}$ and $\vec{p}_p$. The angle between the scattering and reaction planes is given by ϕ. The two planes coincide when $\phi = 0$, which is referred to as "in-plane" kinematics. The angle of the detected proton with respect to $\vec{q}$ is labelled θ_{pq}, and the condition $\theta_{pq} = 0$ is

referred to as "parallel" kinematics (i.e. the detected proton emerges parallel to $\vec{q}$).

The three-momentum of the recoil nucleus, $\vec{p}_B$, can be calculated by applying conservation of 3-momentum at the reaction vertex:

$$\vec{p}_B = \vec{q} - \vec{p}_p \tag{2.4}$$

We define the missing momentum to be equal to p_B,

$$\vec{p}_m = \vec{p}_B = \vec{q} - \vec{p}_p \tag{2.5}$$

Note that some authors (for example, Ref. [13]) use the opposite sign convention ($\vec{p}_m = -\vec{p}_B$). However, we will generally be dealing with the magnitude of $\vec{p}_m$ so that this difference is inconsequential.

The excitation of the system is given by the missing energy, which we define as

$$E_m = \omega - (\sqrt{p_p{}^2 + M_p{}^2} - M_p) - (\sqrt{p_B{}^2 + M_{A-1}{}^2} - M_{A-1}) \tag{2.6}$$

where M_{A-1} is the mass of the nucleus which has a mass number $(A-1)$. Others (for example, Ref. [13]) use another expression for the missing energy which differs slightly from our definition in Eqn. (2.6). At our kinematics the two expressions yield approximately the same value, as discussed below.

In Ref. [13], the missing energy is defined as

$$\mathcal{E}_m = M_p + M_B - M_A \tag{2.7}$$

where we denote this missing energy as $\mathcal{E}_m$ to distinguish it from the E_m defined in Eqn. (2.6). In Eqn. (2.7) the recoil mass, M_B, includes the excitation energy of the recoiling nucleus and all relative kinetic energies associated with unobserved particles in the final state. In the laboratory frame, the target nucleus is at rest, so that $\vec{P}_A = 0$ and $E_A = M_A$. Conservation of

energy yields

$$\omega + M_A \;=\; E + E_B \tag{2.8}$$

$$=\; M_p + T_p + M_B + T_B \tag{2.9}$$

so that

$$M_p + M_B - M_A = \omega - T_p - T_B \tag{2.10}$$

where T_p and T_B are the kinetic energies of the detected proton and recoiling nucleus, and M_p and M_B are there masses. Substituting into Equation (2.7) gives

$$\mathcal{E}_m \;=\; \omega - T_p - T_B \tag{2.11}$$

$$=\; \omega - (\sqrt{p_p{}^2 + M_p{}^2} - M_p) - (\sqrt{p_B{}^2 + M_B{}^2} - M_B) \tag{2.12}$$

At our kinematics, $p_B \ll M_B$ so that the kinetic energy of the recoil system (T_B) is small. We can therefore make the substitution $M_B \approx M_{A-1}$ in T_B, so that $T_B \approx (\sqrt{p_B{}^2 + M_{A-1}{}^2} - M_{A-1})$. The missing energy is then

$$\mathcal{E}_m \approx \omega - (\sqrt{p_p{}^2 + M_p{}^2} - M_p) - (\sqrt{p_B{}^2 + M_{A-1}{}^2} - M_{A-1}) \tag{2.13}$$

where the RHS is equal to the definition of E_m given in Eqn. (2.6).

2.2   The (e,e′p) Cross Section in the Plane Wave Born Approximation

In calculating the (e,e′p) cross section for an arbitrary nucleus, the largest term is the one corresponding to the exchange of a single virtual photon, as shown diagrammatically in Figure 2-2. Higher order terms contain more than one photon, and are suppressed due to the weakness of the electromagnetic coupling constant. In calculating the cross section, these higher order
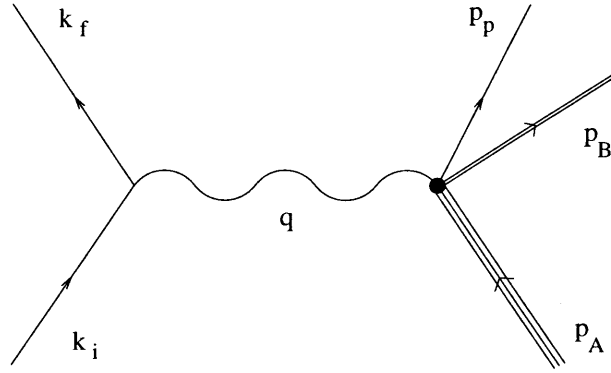
Figure 2-2: The (e,e′p) reaction in PWBA.

terms can therefore be discarded and only the single-photon exchange process considered. This is known as the Plane Wave Born Approximation (PWBA).

In PWBA, it can be shown that the most general (e,e′p) cross section consistent with Lorentz covariance and conservation of the electron current is a function of only four independent structure functions [14, 15]. This cross section can be written as (see Ref. [16]):

$$\frac{d\sigma}{d\omega dp_p d\Omega_e d\Omega_p} = p_p^2 \frac{e^2 \pi}{2|\vec{q}|} \Gamma \{\sigma_T + \epsilon \sigma_L + \sqrt{\epsilon(1+\epsilon)}\sigma_{TL}\cos\phi + \epsilon\sigma_{TT}\cos 2\phi\} \tag{2.14}$$

where ϵ is a measure of the transverse linear polarization of the virtual photon and Γ is the flux of virtual photons emitted by the electron:

$$\epsilon = \left[1 + 2\frac{|\vec{q}|^2}{Q^2}\tan^2\left(\frac{\theta}{2}\right)\right]^{-1} \tag{2.15}$$

$$\Gamma = \frac{\alpha}{2\pi^2}\frac{E'}{E}\frac{|\vec{q}|}{Q^2}\frac{1}{1-\epsilon} \tag{2.16}$$

The four independent response functions $(\sigma_T, \sigma_L, \sigma_{TL}, \sigma_{TT})$ are related to matrix elements of

various components of the nuclear current, $\vec{J}$ (see Ref. [16]):

$$
\begin{aligned}
\sigma_L &= 2\frac{Q^2}{|\vec{q}|^2}|J_0|^2 \\
\sigma_T &= |J_{+1}|^2 + |J_{-1}|^2 \\
\sigma_{TL}\cos\phi &= 2\left(\frac{Q^2}{|\vec{q}|^2}\right)^{1/2}\mathrm{Re}(J_0^*(J_{+1} - J_{-1})) \\
\sigma_{TT}\cos 2\phi &= -2\mathrm{Re}(J_{+1}^* J_{-1})
\end{aligned}
$$

where J_0 is the longitudinal component of the current (parallel to $\vec{q}$) and $J_{\pm 1}$ are the transverse components (both perpendicular to $\vec{q}$). The response functions σ_L and σ_T are therefore due only to longitudinal and transverse components of the current, respectively. The response function σ_{TL} is due to the interference of transverse and longitudinal components of the current and σ_{TT} is due to the interference of the two transverse components.

If the momentum vector of the detected proton is parallel to $\vec{q}$, then the angle θ_{pq} is zero. This is referred to as parallel kinematics. It can be shown [16] that the response functions σ_{TL} and σ_{TT} are proportional to $\sin(\theta_{pq})$ and $\sin^2(\theta_{pq})$, respectively, so that in parallel kinematics they are both zero. The cross section then contains only the longitudinal and transverse responses:

$$
\frac{d\sigma}{d\omega dp_p d\Omega_e d\Omega_p} = p_p^2\frac{e^2\pi}{2|\vec{q}|}\Gamma\{\sigma_T + \epsilon\sigma_L\} \tag{2.17}
$$

In general, all of the responses are functions of the four independent scalars $(Q^2, q \cdot p_A, q \cdot p_p, p_p \cdot p_A)$. An equivalent and usually more convenient set of variables is $(Q^2, \omega, p_p, \theta_{pq})$. By holding these four variables constant and measuring the experimental cross section in parallel kinematics at two or more values of ϵ, the response functions σ_T and σ_L can be determined from Equation (2.17). This technique is referred to as a Rosenbluth Separation [17].

2.3 The Plane Wave Impulse Approximation (PWIA)

In PWIA, the (e,e'p) cross section is derived using the PWBA and the following further assumptions:

1. The single virtual photon radiated by the scattered electron is fully absorbed by a single proton in the nucleus,

2. the proton exits the nucleus without undergoing any further interactions (i.e. no final state interactions (FSI)), and

3. it is this proton which is detected.

A diagram of the (e,e'p) process in PWIA is shown in Figure 2-3. Applying conservation of momentum to the photon-proton vertex, the initial proton momentum, $\vec{p}_i$, is given by

$$\vec{p}_i = \vec{p}_p - \vec{q} \tag{2.18}$$

Comparing to equation (2.5), we see that the initial proton momentum is related to the missing momentum, $\vec{p}_m$, by

$$\vec{p}_i = -\vec{p}_m \tag{2.19}$$

By measuring the missing momentum in an (e,e'p) experiment, one can therefore determine the initial momentum that the struck proton had inside the nucleus before the scattering occurred. Note that this interpretation is only valid within PWIA.

The (e,e'p) cross section in PWIA is given by (see Ref. [18]):

$$\frac{d^6\sigma}{d\Omega_e d\Omega_p dp_e dp_p} = p_p^2 \times \sigma_{ep} \times S(p_i, E_m) \tag{2.20}$$

where σ_{ep} is the off-shell electron-proton cross section. $S(p_i, E_m)$ is the spectral function, and represents the probability of finding a proton of momentum p_i and energy E_m inside the nucleus.
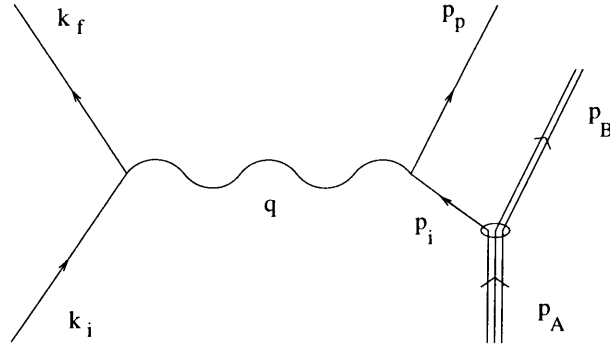
Figure 2-3: The (e,e'p) reaction in PWIA.

An experimental spectral function can be determined by dividing the measured (e,e'p) cross section by the appropriate factor,

$$S^{exp}(p_i, E_m) = \frac{1}{p_p^2 \sigma_{ep}} \times \frac{d^6\sigma}{d\Omega_e d\Omega_p dp_e dp_p} \qquad (2.21)$$

This requires a model of the off-shell electron-proton cross section, σ_{ep}. We chose to use the CC1 prescription of de Forest [18], which is discussed in detail in Appendix G.

If PWIA is valid, then the experimental spectral function determined from the measured (e,e'p) cross section should be equal to the theoretical spectral function, $S^{exp}(p_i, E_m) = S(p_i, E_m)$. Furthermore, in PWIA the spectral function is only a function of p_i and E_m, so that measurements of S^{exp} at different kinematics should yield the same result if p_i and E_m are fixed. This latter statement will be used to interpret the longitudinal and transverse response of the measured (e,e'p) cross sections.

Chapter 3

Experiment

Overview

In this chapter the main components of the experimental setup are discussed, including the electron beam, the targets, and the three magnetic spectrometers. The kinematic settings of the spectrometers for the Helium (e,e'p) measurements are given, and the technique for determining the density of the Helium target gas is presented.

3.1 Electron Beam

3.1.1 The electron accelerator

The Mainz accelerator (MAMI) consists of 3 microtron accelerators in series and is capable of delivering a 100% duty factor beam at a maximum current of 100 μamps and a maximum energy of 855 MeV. The third and final microtron (shown schematically in Figure 3-1) increases the energy from 180 to 855 MeV in 90 circulations of the microtron, increasing the beam energy by 7.5 MeV per turn. Extracted beam is available in 15 MeV steps. The energy width of the beam is approximately 30 keV FWHM at 855 MeV and the absolute centroid of the beam energy is known to $\pm$160 keV [19].

3.1.2 Beam Position and Rastering

The beam delivered to the spectrometer hall has a diameter of 0.5 mm (FWHM) and its absolute position is known to approximately 1 mm [21]. At the location of the experimental
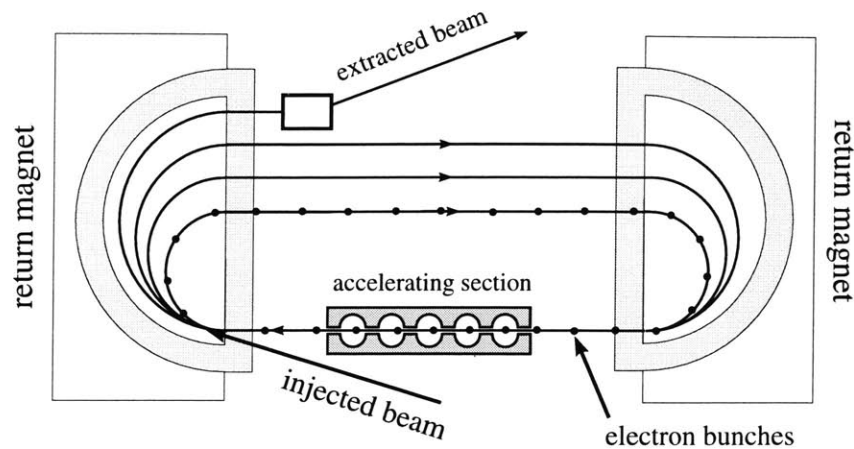
Figure 3-1: Schematic of the 3rd Mainz microtron. The electron beam passes through a series of 5 RF cavities on each turn, and acquires 7.5 MeV per turn. Figure is from Ref. [20].

target, a BeO target on the target ladder provides a visual beam spot which is viewed in the counting house on a video display. Whenever the electron beam was tuned, the BeO target was subsequently moved into the beam line and the beam position adjusted to fall in the center of the BeO. The beam spot could be visually centered on the BeO target with an accuracy of 0.5 mm.

When the Helium gas target was used, the incident electron beam was rastered at 3.6 kHz (2.5 kHz) by ±3.5 mm in the horizontal (vertical) direction to distribute the deposited heat and to prevent large local density fluctuations in the Helium target gas. The rastering is done by a series of coils placed in the beam line in the horizontal and vertical plane. A sinusoidal current passes through the coils, generating a magnetic field which deflects the incident electron beam. Calibration of the beam position is accomplished by the use of a special "SEM" target, which consists of a metal plate with a hole in the middle that is spanned by two thin havar strips. When the beam strikes the strips, a current is induced in the metal plate. By determining this current as a function of the current in the rastering coils, and using the known position of the havar strips, one can determine the absolute beam location as a function of the current in the coils. The calibration procedure is described in detail in Ref. [22]. The calibration parameters obtained in the raster calibration runs in this experiment are listed in Appendix E.

3.1.3   Current Monitoring

In this experiment, two techniques were used to measure the beam current:

1. Förster probe – The Förster probe [23] consists of two toroidal coils that surround the incoming beam and measure its absolute magnetic field. From the field the absolute beam current can be calculated to $\delta I = \pm\ 0.3$ μamps [23]. The Förster probe is therefore most accurate at high currents, where the relative uncertainty $(\delta I/I)$ in the current is smallest.

2. Photoeffect Monitor – Synchrotron light emitted in the last steering dipole of the beam line impinges on a stainless steel foil, producing electrons through the photoelectric effect. The photocurrent varies linearly with the beam current, providing a measure of the current accurate to $\pm$ 1% over a range from 1 nA to 60 μA [23]. After a few hours, changes in the surface of the foil result in a drift in the absolute calibration of the photoeffect monitor. The photoeffect monitor was therefore periodically re-calibrated against the Förster probe at high current. It can then be used reliably at low currents, where the Förster probe is less accurate.

3.2   Targets

3.2.1   Helium Target

The Helium target used in this experiment was a cold-gas ^{3,4}He cell operating at a nominal temperature of 21 K and pressures of 5–10 atm. The target cell was a stainless steel sphere 8 cm in diameter and approximately 82.5 μm thick. The complete target setup is shown in figure 3-2. A compressor, which uses ^{4}He as its working gas, produced liquid hydrogen at a temperature of approximately 20 K. The liquid hydrogen flows down a transfer line into the target loop, where it cools the Helium target gas. As the hydrogen warmed and evaporated, it flowed as gas back up the transfer line into the hydrogen reservoir. The hydrogen loop had a nominal pressure of 2.5 atm.

The target loop is show in Figure 3-3. The liquid hydrogen entered from the top as shown
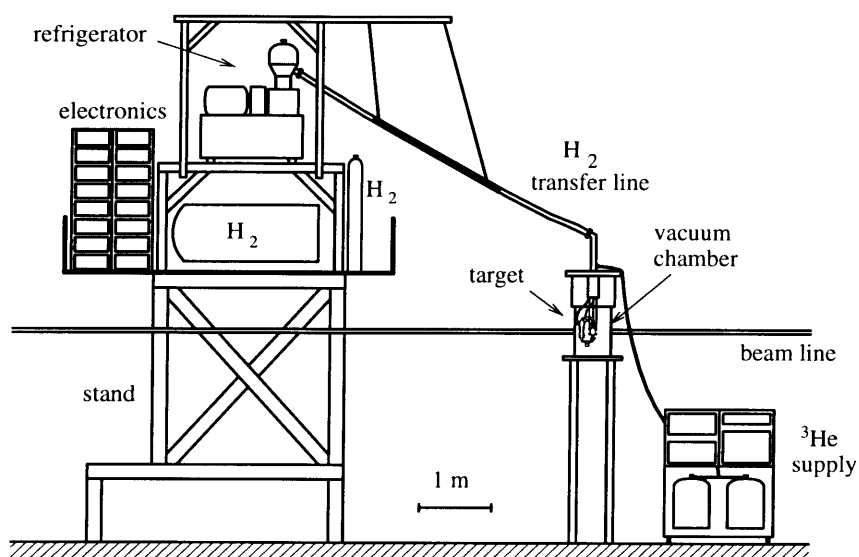
Figure 3-2: The Helium target system.

and flowed into the bath surrounding the Helium loop. The Helium loop contained a fan which circulated the gas in a counter-clockwise direction (for the view in Figure 3-3) down through the cooling bath and up through the target cell. A heater at the bottom of the loop was used for warming up the gas when the target was turned off and brought back to room temperature. A temperature sensor (labelled T_{Si} in the figure) monitored the temperature of the heater. The entire loop was enclosed in an evacuated scattering chamber with 120 μm thick kapton windows. The vacuum in the scattering chamber was monitored for leaks in the target cell.

The target loop contained temperature sensors (labelled T_A and T_B in Figure 3-3) above and below the cell, and a pressure sensor was located at the ^{3}He supply. These sensors provided an indication of the cell condition during the experiment but were not used to determine the absolute gas density, which fluctuates with the beam current. The density was instead obtained from measurements of elastic scattering cross sections as described in Section 4.2.

3.2.2 Other Targets

In addition to the Helium target, the scattering chamber contained several other targets mounted on a movable ladder. The ladder could be moved vertically in an out of the incident beam as
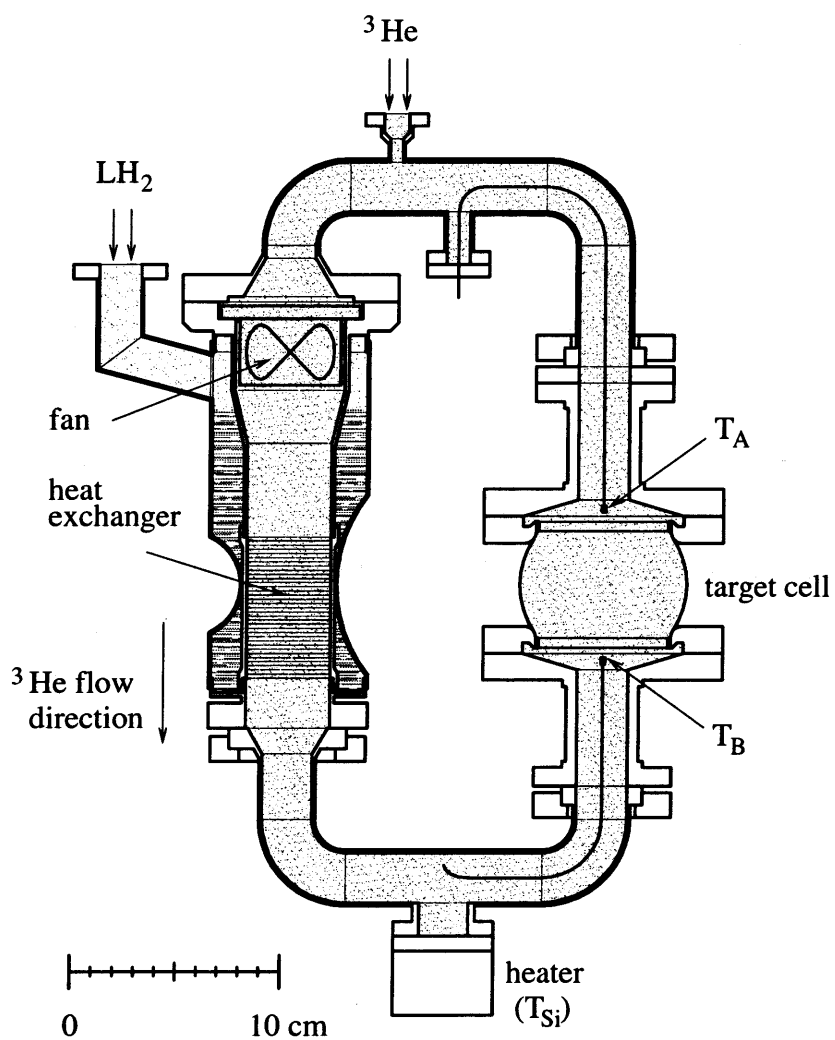
Figure 3-3: The Helium target loop. The symbols T_A, T_B and T_{Si} denote three temperature sensors located as indicated.

well as horizontally along the beam line. Targets mounted on the ladder included a 32.5 mg/cm^2 ^{12}C target, which was used for elastic and quasielastic measurements to study the solid angle of the spectrometers as discussed in Chapter 4. Measurements of elastic scattering from ^{12}C with a sieve slit were also performed to check the spectrometer reconstruction. An approx. 120 mg/cm^2 CH$_2$ target was used to measure ^{1}H(e, e'p), which provided a check of the angular reconstruction of the spectrometers. The ladder also contained the BeO and SEM targets, which were used for checking the beam position and calibrating the beam rastering as described in Section 3.1.2.

In the ^{12}C(e,e') measurements, the precise location of the target along the beam line was needed to calculate absolute cross sections. At each target position, the absolute location of the target along the beam line was obtained from

$$z = (1.008 \times V - 4.478 \pm 0.05) \text{ cm} \tag{3.1}$$

where V is the voltage across a variable resistor attached to the table and z is the target location in the beam coordinate system (see Figure 4-1 in Chapter 4). The linear coefficient (1.008) was obtained from a series of measurements of position and voltage performed before installing the table, and its estimated uncertainty is negligible (approx. 4×10^{-4}). The offset (-4.478) was obtained from the target position reconstructed in Spectrometers A and B during a ^{12}C elastic measurement with sieve slit collimators in both spectrometers. The position was determined from the values of y_{tgt} and ϕ_{tgt} measured for the central hole of the sieve slit, with an estimated uncertainty of 0.5 mm.

3.3   The 3-Spectrometer Setup

3.3.1   General Description

The A1 Spectrometer Hall at Mainz contains 3 magnetic spectrometers, labeled A, B, and C. Some basic properties of the spectrometers are summarized in Table 3.1 and a line drawing of the setup is shown in Figure 3-4. Spectrometers A and C have a similar design and each consist

spectrometer		A	B	C
magnet configuration		QSDD	D_{clam}	QSDD
maximum momentum	[MeV/c]	735	870	551
maximum induction	[T]	1.51	1.50	1.40
momentum acceptance	[%]	20	15	25
solid angle	[msr]	28	5.6	28
horizontal acceptance	[mrad]	±100	±20	±100
vertical acceptance	[mrad]	±70	±70	±70
angular range	[deg]	18–160	7–62	18-160
long-target acceptance	[mm]	50	50	50
momentum resolution		2×10^{-4}	1×10^{-4}	$1 \times 10^{-4\,a}$
angular res. at target (FWHM)	[mrad]	≤ 3	≤ 3	≤ 3
position res. at target (FWHM)	[mm]	6	1.5	6

Table 3.1: Properties of of the A1 spectrometers, from Ref. [20].

[a]design value

of a quadrupole, sextupole, and 2 dipole magnets. They have point-to-point focusing in the dispersive plane ($\langle x|\theta \rangle = 0$) for optimal momentum resolution, and parallel-to-point focusing in the non-dispersive plane ($\langle y|y \rangle = 0$) for optimal angle determination. Spectrometer B was designed to reach small scattering angles, and so has a very different design from Spectrometers A and C. It consists of a single dipole with a wedge-shaped gap, and has point-to-point focusing in both planes. It has a reduced angular and momentum acceptance compared to the other two spectrometers, but has improved target position resolution due to the point-to-point focusing in the non-dispersive plane. It is also narrower than Spectrometers A and C, allowing it to reach smaller scattering angles. A detailed description of the three spectrometers and their detector packages can be found in Ref. [19].

3.3.2 The Detector Package

Each spectrometer contains a detector package as shown in Figure 3-5. It consists of the following elements:

1. 2 vertical drift chambers (VDCs), each containing 2 wire planes, for precise determination
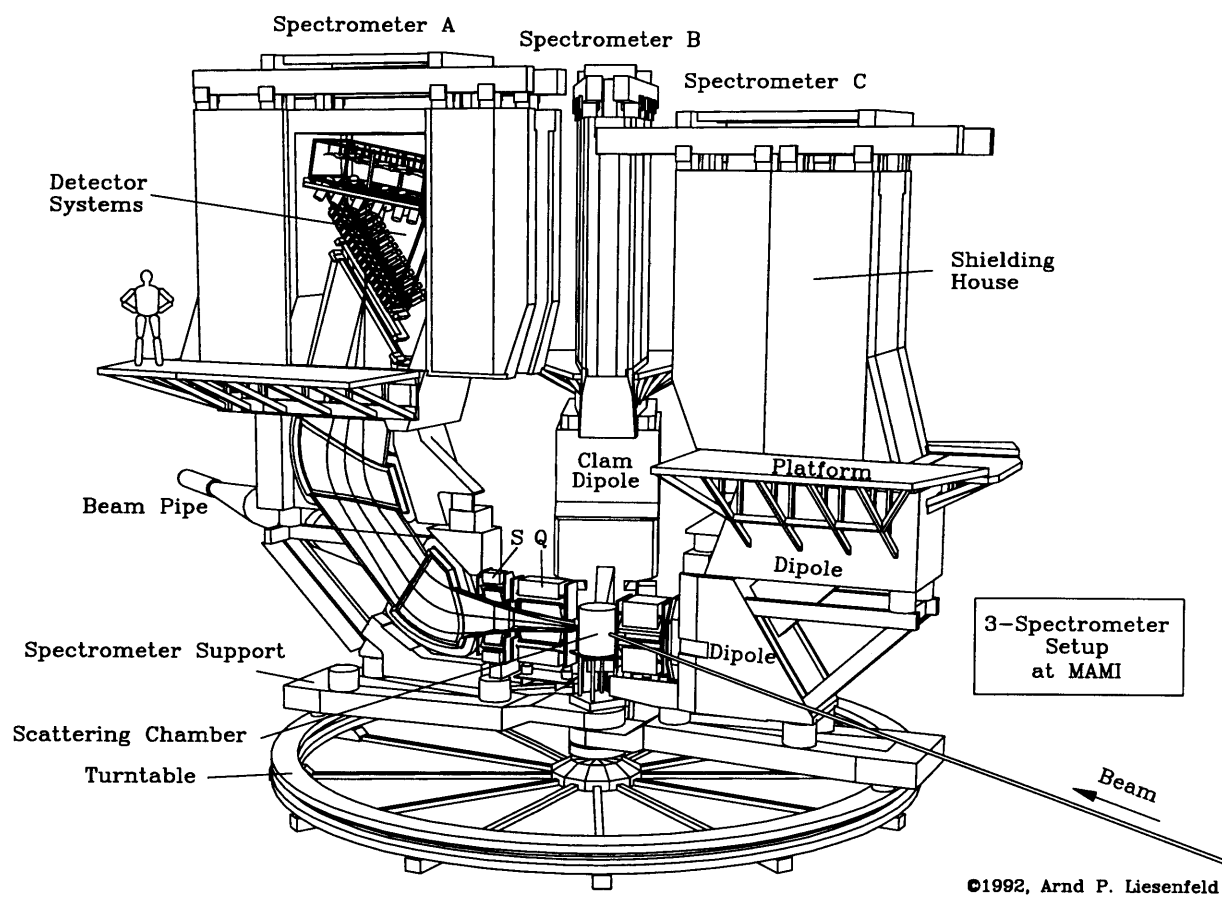
Figure 3-4: The 3-Spectrometer Setup at Mainz.

of the particle track within the spectrometer,

2. 2 planes of plastics scintillators in 15 (14 in Spec. B) segments for timing and particle identification, and

3. a freon-gas-filled Cerenkov counter for pion/electron discrimination.

A number of references cover the details of the various elements of the detector package [20, 24, 25], and an overview can be found in Ref. [19].

3.3.3 Determination of Spectrometer Central Angle

The central angle of each of the three spectrometers is adjusted with a hydraulic system which moves them along a round platform centered on the scattering vertex. A rail along the platform is marked with a series of grooves which indicate the angular position. An electronic readout device on each of the three spectrometers is used to calculate their position from the grooves to $\pm$ 0.6 mm at the rail, corresponding to an absolute angular uncertainty of $\pm$ 0.1 mrad with respect to the scattering vertex [23]. The conversion from readout value (R) to spectrometer angle (θ) in degrees is as follows:

$$\theta_A = \frac{13382.0 - R_A}{78.65} \tag{3.2}$$

$$\theta_B = \frac{13451.0 - R_B}{78.62} \tag{3.3}$$

$$\theta_C = \frac{13348.9 - R_C}{78.66} \tag{3.4}$$

where positive angles are on the left side of the beam line when looking downstream.

3.3.4 Momentum Calibration

The momentum p of a particle detected in one of the spectrometers is determined from

$$p = p_{ref} \times (1 + \delta) \tag{3.5}$$

Čerenkov Detector

VUV Mirror

Photomultiplier

Čerenkov
$(CF_2Cl)_2$ –
Radiator

1m

Scintillation
Trigger
Detectors

ΔE_2

ΔE_1

VDC3, VDC4

Focalplane
Track Detector

VDC1, VDC2
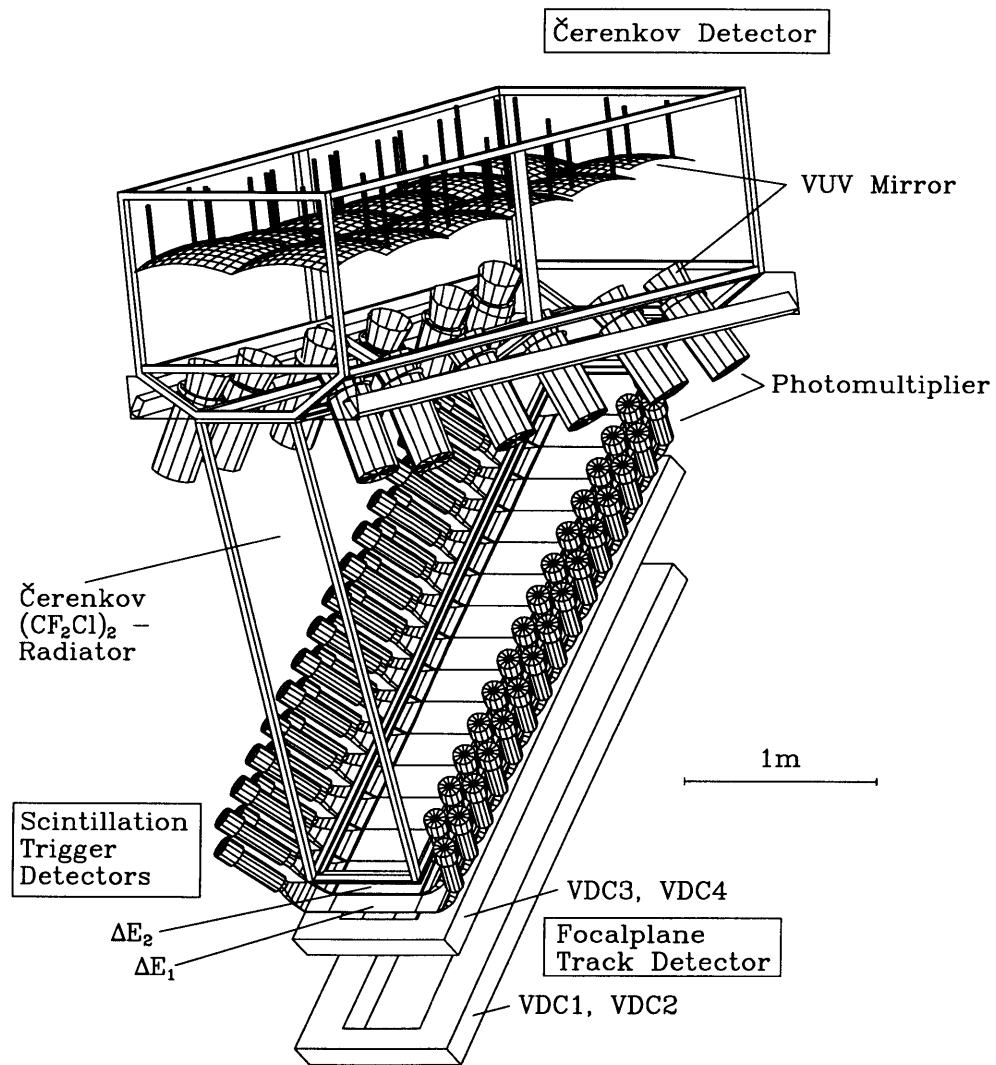
Figure 3-5: The Spectrometer Detector Package.

spectrometer	Γ_0 [MeV/c]	Γ_1 [(MeV/c)(kG)$^{-1}$]	Γ_2 [(MeV/c)(kG)$^{-2}$]	Γ_3 [(MeV/c)(kG)$^{-3}$]
A	1.0095E+00	4.1631E+01	5.1896E-02	-2.5145E-03
B	4.4459E+00	6.1211E+01	3.3219E-01	-1.6505E-02
C^a	0.0000E+00	3.2890E+01	0.0000E+00	0.0000E+00

Table 3.2: Reference Momentum Calibration Coefficients. The parameters for Spectrometers A and B are from Ref. [26].

^{a}preliminary values. This experiment did not require a precise calibration of Spec. C

where δ is the particles dispersive coordinate (obtained from the reconstruction matrix discussed in Section 5.4) and p_{ref} is the reference momentum (which depends on the field setting of the spectrometer). The reference momentum for a given spectrometer at a particular field setting was determined from either 1.) a standard calibration polynomial that relates the magnetic field inside the spectrometer (measured by one or more NMR probes) to the reference momentum, or 2.) an absolute calibration of p_{ref} obtained experimentally for that spectrometer at a particular field setting. This is described further below.

The standard calibration polynomial relating magnetic field to reference momentum was determined by Ref. [26] from elastic scattering measurements performed at a variety of field settings. In these measurements, the beam energy and scattering angle were well-known, so that the momentum p of the scattered electron detected in the spectrometer could be predicted. The reference momentum was then determined by solving for p_{ref} in equation (3.5). The process was repeated for a number of different settings of the spectrometer magnetic field, B, yielding a set of points (B, p_{ref}) that were fitted with a polynomial of the following form:

$$p_{\text{ref}} = \sum_{i=0}^{3} \Gamma_i B^i \tag{3.6}$$

with p_{ref} in MeV/c and B in kG. The coefficients Γ_i of the polynomial are listed in Table 3.2. Note that there is a different polynomial for each of the three spectrometers.

A check on these calibration polynomials for Spectrometers A and B was provided by ana-

lyzing the ^{12}C elastic scattering measurements done during our experiment (see Section 4.1.3). The measurements were performed with field values of 9.448 kG in Spectrometer A and 6.593 kG in Spectrometer B, corresponding to $p_{ref}^A = 396.85$ MeV/c and $p_{ref}^B = 418.13$ MeV/c, respectively (where p_{ref} has been calculated from the calibration polynomials, and the superscript indicates the spectrometer). As with the earlier measurements used to determine the calibration polynomials, the energy of the incident beam and the scattering angle were well-known, so that the momentum of the scattered electron could be predicted. The most-probable energy loss in the windows and target was then subtracted from this value to determine the momentum of the electron inside the spectrometer. This value is referred to as the **predicted momentum**. The momentum of the electrons was then measured directly from the data using equation (3.5), with p_{ref} calculated from the calibration polynomial and the measured field. This is referred to as the **measured momentum**. For these ^{12}C elastic measurements, the measured momentum was found to be larger than the predicted momentum by 0.2 MeV in Spectrometer A and 2.1 MeV in Spectrometer B. This indicated that the calibration polynomial for Spectrometer B is incorrect at this field setting, and raised the possibility that it might be incorrect at other field settings at well.

The uncertainty in the calibration polynomials at the field values used in the (e,e'p) measurements was resolved by absolutely calibrating the reference momentum of Spectrometers A and B for most of the kinematic settings with the following technique:

1. In the summer of 1996 (1 year after the experiment reported in this thesis was completed), elastic electron scattering from ^{12}C was measured with Spectrometer B at a field setting of 10.441 kG, corresponding to $p_{ref}^B = 661.63$ MeV/c (as calculated from the calibration polynomial). This field setting was chosen since it corresponds to the highest p_{ref}^B setting used in the (e,e'p) measurements (see Tables 3.3 and 3.4 for a full list of the (e,e'p) kinematics). With the analysis discussed in the last paragraph, the measured momentum was found to be smaller than the predicted momentum by 0.68 MeV. The Γ_0 coefficient for Spectrometer B was therefore increased by 0.68, defining a new calibration polynomial for Spectrometer B valid for fields around 10.4 kG.

2. The coincidence (e,e'p) data for $p_{ref}^B \approx 660$ MeV/c were analyzed and missing energy spectra acquired. For these measurements, electrons were detected in Spectrometer A and protons in Spectrometer B. The new value of Γ_0 for Spectrometer B determined in step 1.) was used in the analysis, so that the proton momentum was properly calibrated. The position of the two-body breakup missing-energy peak (which should appear at 5.49 MeV for ^{3}He(e,e'p)^{2}H and 19.81 MeV for ^{4}He(e,e'p)^{3}H after all energy loss is accounted for) was then used to absolutely calibrate the momentum in Spectrometer A. In all cases the missing energy peak appeared within 0.5 MeV of its expected value when using the standard calibration curve for p_{ref}^A. The missing energy peak was moved to its correct value by decreasing Γ_0 in Spectrometer A by 0.1–0.5 MeV/c, depending on the kinematic setting.

3. In the next (e,e'p) kinematics, the field of Spectrometer A was unchanged and the field of Spectrometer B was lowered to correspond to $p_{ref}^B \approx 585$ MeV/c. Since the field in Spectrometer A was unchanged, the calibration from step 2.) is still valid. The position of the two-body breakup missing energy peak was then used to calibrate Spectrometer B. The peak was brought to its correct location by adjusting the Γ_0 coefficient of Spectrometer B by -0.22–+0.08 MeV from its standard value.

4. At the (e,e'p) kinematics corresponding to the two lowest fields in Spectrometer B ($p_{ref}^B \approx$ 500 and 425 MeV/c) the field of Spectrometer A was left constant at the same value as in the $p_{ref}^B \approx 660$ and 585 MeV/c kinematics, so that it remained properly calibrated. Since the field in Spectrometer B was changed it required calibration. However, the two-body peak was not inside the acceptance at these kinematics, and so could not be used to calibrate the momentum of Spectrometer B. The calibration polynomial for the previous kinematics ($p_{ref}^B \approx 585$ MeV/c) was therefore used. An estimate of the maximum uncertainty in p_{ref}^B is 2 MeV/c, since this was the maximum error in the momentum that was seen using the standard calibration polynomial. (This is the error that was seen in the ^{12}C elastic measurements discussed earlier in this section.) This uncertainty was not important to the final results since these kinematic settings were dominated by background

and no detailed cross sections were extracted from them (see Section 5.10).

With p_{ref} calibrated with the above technique, the estimated uncertainty in the absolute momentum in the (e,e'p) measurements is 0.1 MeV/c for Spectrometer A at all kinematics, 0.1 MeV/c for Spectrometer B at the $p_{ref}^B \approx 660$ and 585 MeV/c kinematics, and 2 MeV/c for Spectrometer B at the $p_{ref}^B \approx 500$ and 425 MeV/c kinematics.

3.3.5   Collimators

Each of the spectrometers has a choice of collimators that can be remotely selected. The nominal values of the collimators used in this experiment were: 21 msr (Spectrometer A), 5.6 msr (Spectrometer B), and 22.5 msr (Spectrometer C). The detailed shape of the collimators in Spectrometers A and B was modelled as a series of horizontal and vertical slits as described in Appendix C.

3.4   Electronics and Data Acquisition

An overview and description of the electronics and data acquisition system for the three-spectrometer system at Mainz has been published in Ref. [19], and the reader is directed to that article for a complete description of the system. In the following two subsections we discuss details specific to our experiment.

3.4.1   Event Trigger Condition

The minimum trigger condition for an individual spectrometer in this experiment was a coincidence between one paddle in the ΔE scintillator layer and one paddle in the TOF scintillator layer. (Note that ΔE and TOF are also referred to as ΔE_1 and ΔE_2.) The trigger signals from individual spectrometers were fed into prescalers and a programmable lookup unit (PLU) to determine the overall event trigger, which was programmed to be a logical OR of the following two possibilities:

1. a "prescaled single", which was a valid trigger from a single spectrometer after some prescaling, and

2. a coincidence between Spectrometers A and B. These coincidences had no prescaling applied.

The singles prescale value was generally set to obtain 20-50 Hz of prescaled singles along with the coincidence data. In principle any other double or triple coincidence between the three spectrometers also triggered an event, but these were practically removed by using a very high prescale factor.

The maximum data rate used during this experiment was approximately 150 Hz per spectrometer. This rate was limited by the slave CPU of the front-end data-acquisition computers, which could read out and format data at a maximum rate of 250 Hz. The computer dead time increased as this rate was approached, so that at 150 Hz the individual CPUs were dead approximately 15–20% of the time.

3.4.2 Measurement of the Computer Dead Time

As part of the data acquisition system, each of the three spectrometers has a front-end computer that reads out and formats the data. The readout process takes approximately one millisecond, during which time the acquisition system for that spectrometer is inhibited and any arriving events are lost. This is referred to as the computer dead time.

The computer dead time of the front-end computer on each of the three spectrometers is measured by a dedicated dead-time module shown schematically in Figure 3-6. A valid trigger from an individual spectrometer sets a corresponding flip-flop, which is cleared only when that spectrometer's front-end computer is no longer busy (uB = False). The output of the flip-flops are then ANDed in various combinations with a clock signal, generating seven dead-time signals that correspond to various combinations of the spectrometers. For example, the signal 'A' corresponds to the time that the front-end computer on Spectrometer A was dead; 'A & B' corresponds to the time that both Spectrometers A and B were dead. Each of these timing signals is input to a scaler, and all of the scalers are read out for each event.
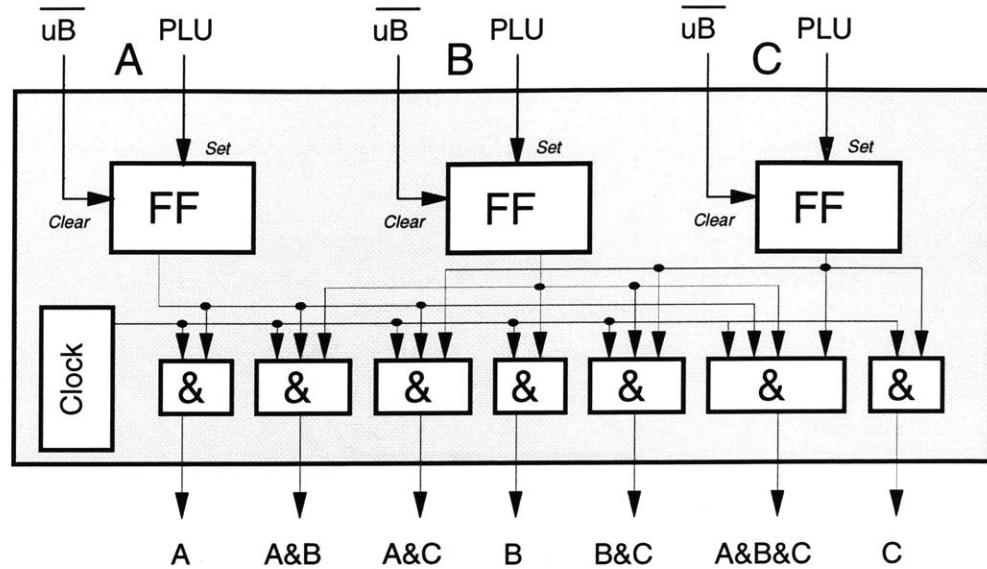
Figure 3-6: Schematic of the dead-time module, from ref. [25].

The values read out from the scalers are used to calculate dead-time corrections for singles and coincidence events as discussed in Appendix H.

3.5   Kinematics and Experimental Technique

3.5.1   Helium (e,e′p) Kinematics

The kinematics of the (e,e′p) measurements on ^{3}He and ^{4}He are given in Tables 3.3 and 3.4 respectively. For these measurements, Spectrometer A detected electrons and Spectrometer B detected protons. This choice was necessary because only Spectrometer B is capable of detecting the high momentum protons required. Throughout this thesis, the kinematics given in Tables 3.3 and 3.4 are referred to by specifying the **nominal** value of the beam energy (540, 675 or 855 MeV) and reference proton momentum (660, 585, 500 or 425 MeV), which form a unique combination at each kinematic setting. For example, the first line in Table 3.3 is labelled as

the "540/660" ^{3}He kinematics, corresponding to a beam energy of 540.11 MeV and a reference proton momentum of 661.59 MeV/c. These labels are given in the last column of Tables 3.3 and 3.4.

The angles given in the tables are the central angles of the spectrometers, with the electron spectrometer on the left side of the beam line (looking downstream) and the proton spectrometer on the right side. The spectrometers each spanned a range of momentum, p, given by $p = p_{ref} \times (1 + \delta)$ as discussed in Section 3.3.4, with $\delta = \pm 7.4\%$ in the proton spectrometer and $\delta = -5\%, +15\%$ in the electron spectrometer. A schematic of the experimental setup in Figure 3-7 illustrates the settings of each of the spectrometers for this experiment.

The measurements were performed at a fixed central 3-momentum transfer of $|\vec{q}| = 685$ MeV/c. The central energy transfer, ω, was chosen to correspond to the center of the quasielastic peak at this $|\vec{q}|$ using the following formula from Ref. [27]:

$$\omega = \sqrt{|\vec{q}|^2 + m_p^2} + M_{A-1} - M_A \tag{3.7}$$

At $q = 685$ MeV/c, this gave $\omega = 228.4$ MeV for ^{3}He and 242.7 MeV for ^{4}He.

With q and ω determined, the choice of the beam energy, E_i, then completely determined the electron kinematics. The beam energies were selected from the values available at Mainz to provide a broad range of values of the virtual photon polarization, ϵ, while resulting in values of the electron scattering angle, θ_e, that were compatible with the angular range of Spectrometer A. The measurements were performed at each of three beam energies, corresponding to three values of the virtual photon polarization.

The angle of the proton spectrometer was selected so that the central kinematics corresponded to "parallel kinematics", which is defined by $\vec{p}_p \parallel \vec{q}$ as discussed in Chapter 2. The central angle, θ_p, of the proton spectrometer was therefore determined from

$$\theta_p = \theta_q = \sin^{-1}\left(\frac{E_i - \omega}{|\vec{q}|} \sin(\theta_e)\right) \tag{3.8}$$

where all of the quantities are central values. The final remaining kinematic quantity is the
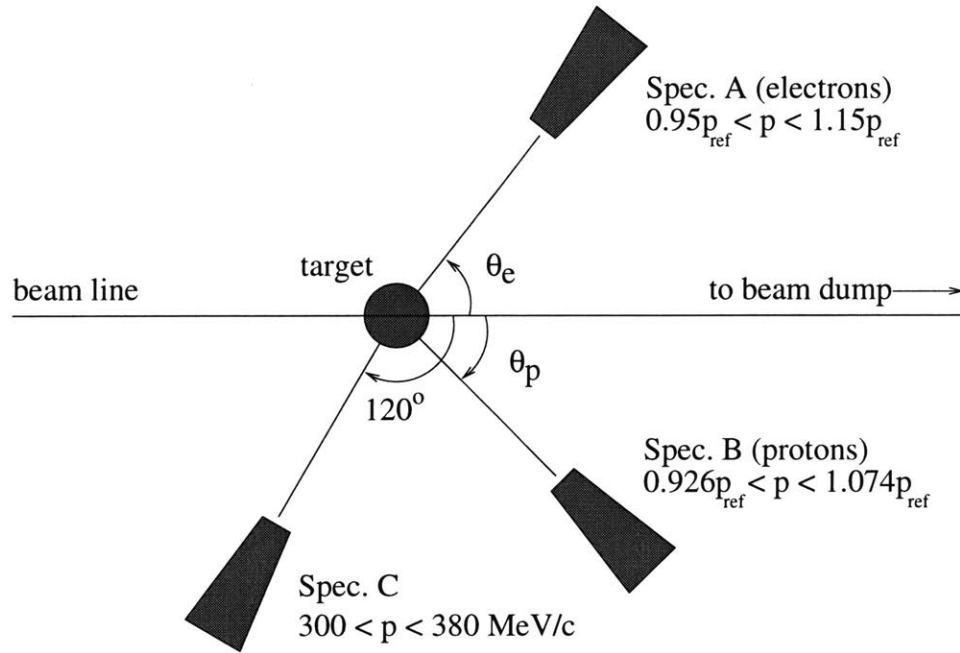
Figure 3-7: A schematic of the experimental setup, indicating the momentum acceptance and central scattering angle of each of the three spectrometers.

magnitude of the proton momentum, $|\vec{p}_p|$, which had four central settings corresponding to values of $|\vec{p}_p|$ ranging from 390 to 710 MeV/c. These values were chosen so that the experiment covered a nominal missing energy range of 0 to 150 MeV.

The range of missing energy and missing momentum spanned by each of the twelve ^{3}He(e,e'p) kinematics (3 beam energies × 4 proton momenta) is shown in Figure 3-8. The (E_m, p_m) range is similar for ^{4}He(e,e'p).

3.5.2   Helium Elastic Scattering

At each of the three beam energies ($E_i = 540, 675$ and 855 MeV) the elastic scattering cross section was measured for both ^{3}He and ^{4}He. The elastic scattering measurements at the two lower beam energies ($E_i = 540$ and 675 MeV) were performed with Spectrometer A. At the highest beam energy ($E_i = 855$ MeV), the elastically-scattered electrons have high momentum (up to ~ 840 MeV/c). Spectrometer B was therefore used for the $E_i = 855$ MeV measurements,

E_i (MeV)	ϵ_{cent}	electron arm		proton arm		label
		θ_e (deg)	p_{ref} (MeV/c)	θ_p (deg)	p_{ref} (MeV/c)	
540.11	0.214	103.85	297.67	26.23	661.59	540/660
					584.91	540/585
					502.74	540/500
					427.85	540/425
675.11	0.457	72.05	426.48	38.34	661.34	675/660
					584.75	675/585
					502.64	675/500
					427.75	675/425
855.11	0.648	52.36	597.16	46.41	661.34	855/660
					584.81	855/585
					502.58	855/500
					427.75	855/425

Table 3.3: ^{3}He kinematics. See text for details.

E_i (MeV)	ϵ_{cent}	electron arm		proton arm		label
		θ_e (deg)	p_{ref} (MeV/c)	θ_p (deg)	p_{ref} (MeV/c)	
540.11	0.198	106.15	284.49	24.64	661.41	540/660
					585.01	540/585
					503.44	540/500
			284.07		428.42	540/425
675.11	0.447	72.73	412.87	37.06	661.41	675/660
					584.91	675/585
					503.44	675/500
					428.55	675/425
855.11	0.642	52.55	583.75	45.20	661.34	855/660
					584.65	855/585
					503.44	855/500
					428.61	855/425

Table 3.4: ^{4}He kinematics. See text for details.
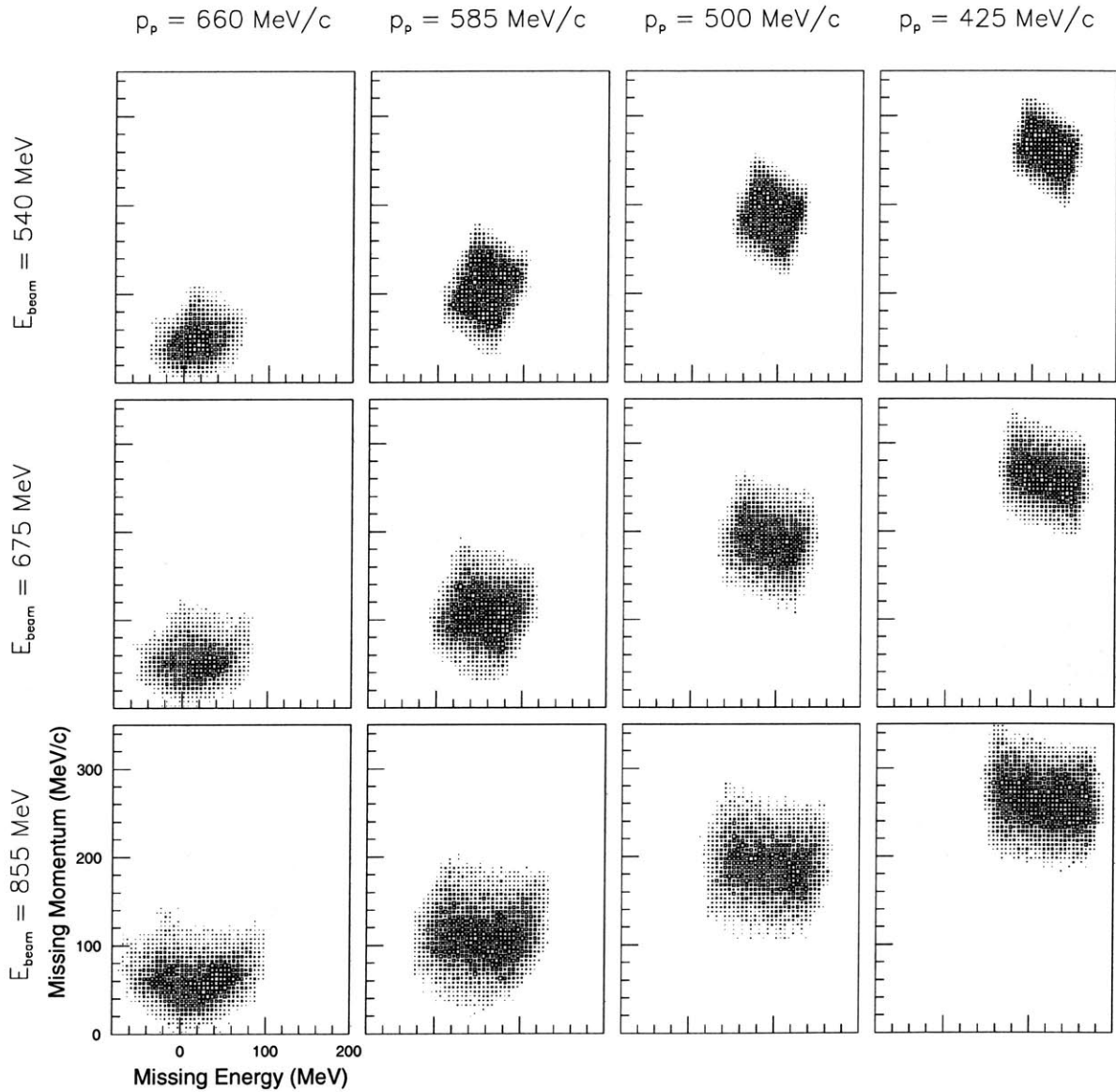
Figure 3-8: The range of missing energy and missing momentum spanned by the ^{3}He(e,e'p) measurements for each of the 12 kinematic settings. The beam energy and proton momentum at each setting are referred to by their nominal values (see text).

since it was the only spectrometer capable of detecting these high momenta.

The full kinematics and analysis of the elastic scattering data is presented in Chapter 4. By comparing the measured data to published cross sections, the absolute target density was obtained.

3.5.3   Target Density Measurement with Spectrometer C

The target density obtained from the Helium elastic scattering measurements is the average density of the target during the elastic scattering runs. In general, the density at other times differed from this value. Changes in the target density were mainly due to changes in the beam current (with a corresponding increase or decrease in the density of the target gas due to beam heating) and to changes in the total amount of gas in the cell (due to leaks in the cell, and to the addition of Helium gas to the cell to compensate for leaks).

Throughout the entire experiment (elastic and (e,e′p) measurements) Spectrometer C took data at a fixed momentum (340 ± 40 MeV/c), angle ($120°$, on the right side of the beam line when looking downstream) and polarity (negative) as illustrated in Figure 3-7. The number of counts detected in Spectrometer C therefore provided a continuous monitor of the relative target density. The absolute density in the (e,e′p) runs could then be obtained from the number of counts in Spectrometer C and the absolute density measured in the elastic scattering runs. This analysis is described in Chapter 4.

Chapter 4

Calibration and Normalization

Overview

This chapter describes two factors which are required for the determination of the absolute (e,e'p) cross sections: the solid angles of the spectrometers and the density of the Helium gas target.

The solid angle of Spectrometers A and B for an extended target was studied by measuring ^{12}C(e,e') elastic and quasielastic scattering with the carbon target placed at several positions along the beam line, corresponding to slices along the extended target. The spectrometers are designed so that the solid angle should be defined by the geometry of the collimators for $|y_{tgt}| <$ 2.5 cm, where y_{tgt} is the transport coordinate at the target, perpendicular to the central ray and in the horizontal plane. The measured solid angle in Spectrometer A was found to deviate from the geometric value for large values of $|\phi_{tgt}|$ that are geometrically allowed with increasing $|y_{tgt}|$. Deviations from the designed solid angle in Spectrometer A for large $|\phi_{tgt}|$ was accounted for by using a software cut $|\phi_{tgt}| < 75$ mrad which, when combined with the geometry of the collimator, defines the solid angle with a minimal loss of data.

The absolute density of the Helium gas target was determined from measurements of elastic scattering performed with Spectrometers A and B. The target density in those elastic runs (the "elastic density") was calculated by comparing the experimental radiative-corrected cross sections to cross sections predicted by a Monte Carlo employing the published elastic form factors for ^{3}He and ^{4}He. During the elastic runs the number of counts in Spectrometer C was measured at a fixed kinematics $\mathcal{K}$ ($\theta = 120°$, $p = 340 \pm 40$ MeV/c, negative polarity). In

the (e,e'p) runs, Spectrometer C continued to measure counts at kinematics $\mathcal{K}$, providing a measure of the relative target density. The absolute target density in the (e,e'p) runs was then determined from the "elastic density" by comparing the number of counts in Spectrometer C obtained in both the elastic and (e,e'p) runs.

4.1 Spectrometer Solid Angle

Ideally, the angular acceptance of a spectrometer is defined by its collimator. The solid angle for a particular experiment can then be exactly calculated from the combined geometry of the incident beam, target, and collimator positions. For a thin target (i.e. a target that has negligible length along the beam line) and a small ($\Delta\theta \ll 1$, $\Delta\phi \ll 1$) rectangular collimator the geometric solid angle is given by

$$\Delta\Omega_{geom} \approx \Delta\theta \times \Delta\phi = (\theta_{max} - \theta_{min}) \times (\phi_{max} - \phi_{min}) \qquad (4.1)$$

where (θ, ϕ) are the vertical and horizontal angles in the spectrometer transport notation as defined in Figure 4-1, and $(\theta_{min}, \theta_{max})$ and (ϕ_{min}, ϕ_{max}) are the limits of the angles determined by the edges of the collimator.

The 3 magnetic spectrometers at Mainz are designed to to have a flat acceptance over $y_{tgt} = \pm 2.5$cm, where y_{tgt} is the transport coordinate at the target in the horizontal plane and perpendicular to the central ray. By flat acceptance, we mean that the spectrometer solid angle is defined by the geometry of the collimator, as in equation (4.1). We performed measurements of elastic and quasielastic scattering from ^{12}C at a series of positions along the beam line to check this hypothesis. By comparing measured elastic cross sections to predictions, the effective solid angle of the spectrometer is compared to the geometric value.

4.1.1 Geometry

Figure 4-1 shows the geometry of the beam and spectrometer system with a target shifted a distance z_0 downstream along the beam line. From the figure it is apparent that a shift in the

target position results in a change in the range of angles that make it through the collimator. The exact range that is geometrically allowed is important for two reasons:

1. Changes in the range of scattering angles change the range of momentum transfers sampled in the measurement. Since we want to compare to an acceptance-averaged predicted cross section, we need to know the precise region over which to average the predictions.

2. Changes in the range of angles and in the distance from the target to the collimator result in a change in the geometric solid angle.

We wish to account for these effects so that comparisons of our measured cross sections to predictions will provide a measure of the acceptance variation which is not purely geometric.

The range of angles accepted by the collimator for a thin target shifted down the beam line a distance z_0 is given by

$$\phi_{max} = tan^{-1} \left(\frac{h + z_0 sin\theta_0}{d - z_0 cos\theta_0} \right) \qquad (4.2)$$

$$\phi_{min} = -tan^{-1} \left(\frac{h - z_0 sin\theta_0}{d - z_0 cos\theta_0} \right) \qquad (4.3)$$

in the horizontal plane, and

$$\theta_{max} = -\theta_{min} = tan^{-1} \left(\frac{v}{d - z_0 cos\theta_0} \right). \qquad (4.4)$$

in the vertical plane. The angle θ_0 is the central scattering angle of the spectrometer, and the other angles and distances are defined in Figure 4-1. The range of scattering angles (measured relative to the beam line) accepted by the collimator was calculated from

$$\theta_{scat} = \left| \theta_0 + \frac{1}{2}(\phi_{max} + \phi_{min}) \right| \pm \frac{1}{2}(\phi_{max} - \phi_{min}) \qquad (4.5)$$

where we have ignored the vertical extent of the collimator, which has a small contribution to the scattering angle.
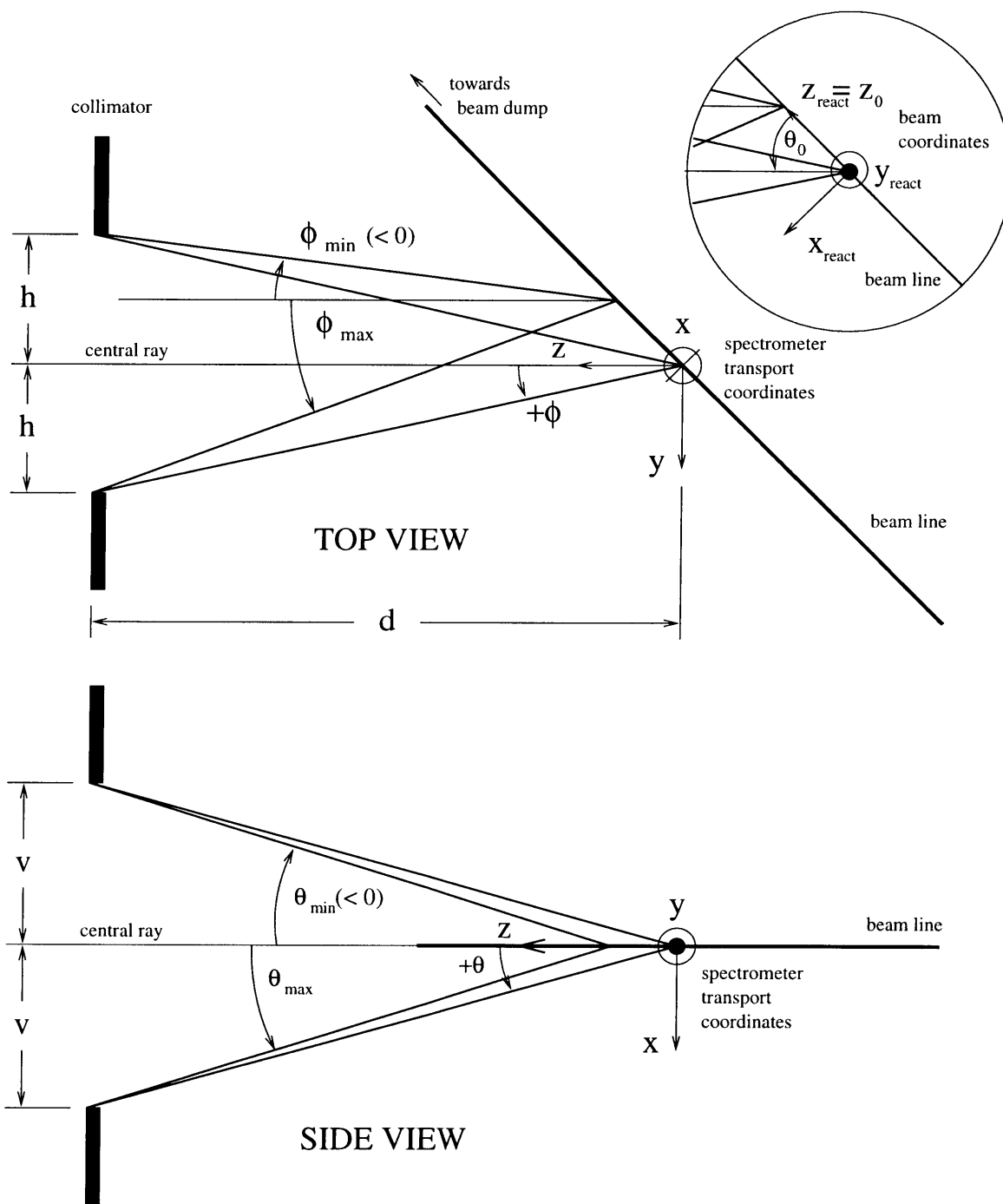
Figure 4-1: Top and side views of beam and spectrometer system with target displaced by $z_{react} = +z_0$ towards the beam dump. Note that the side view is in the x-z plane of the spectrometer transport coordinates.

z (cm)	y_{tgt} (cm)	ϕ_{min} (mrad)	ϕ_{max} (mrad)	θ_{max} (mrad)	$\Delta\Omega_{geom}$ (msr)	θ_{scat} (°)	$\frac{d\sigma}{d\Omega}^{pred}$ (fm^2/sr)
-3.877	+2.741	-113.345	27.288	66.606	18.734	42.535±4.029	22.957×10^{-6}
-2.670	+1.888	-101.851	41.890	67.576	19.427	43.282±4.118	16.891×10^{-6}
-0.161	+0.114	-76.439	72.756	69.685	20.793	44.894±4.274	8.3409×10^{-6}
2.361	-1.669	-48.386	104.194	71.672	21.871	46.599±4.371	3.6303×10^{-6}
3.557	-2.515	-33.945	119.262	72.646	22.260	47.444±4.389	2.3040×10^{-6}

Table 4.1: Calculated angles and predicted ^{12}C elastic cross sections as a function of target position for the (nominally) 21-msr collimator in Spectrometer A, for a central spectrometer angle $\theta_0 = 45.00°$.

An added complication is that the collimators in Spectrometers A and B are not a simple pair of slits as shown in Figure 4-1, but have edges with complicated shapes. The shape of each collimator was modeled as a series of slits as given in Appendix C, and the slit edges that define the solid angle for each target location were calculated. From the slit location, the range of angles that are accepted was then determined, and the solid angle calculated from (4.1).

The calculated angles and resulting geometric solid angles are given as a function of target position in Tables 4.1 and 4.2 for Spectrometer A and B respectively. A complication in the measurements with Spectrometer B was that the sieve slit was not completely removed and obstructed the acceptance in θ_{tgt}. The result was a 3–4 mrad reduction in the θ_{tgt} acceptance at the negative-θ_{tgt} limit (i.e. from about -70 to -66 mrad at the central target location). A software cut of $\theta_{tgt} = \pm60$ mrad was therefore applied to the data to eliminate the effect of the sieve slit and to keep the θ_{tgt} acceptance symmetric for simplicity. The θ_{tgt}-acceptance in Spectrometer B was therefore defined by this software cut and not by the collimator in these measurements. This is accounted for in all the geometric calculations.

4.1.2 Predicted ^{12}C(e,e′) Elastic Scattering Cross Sections

For each location of the carbon target along the beam line, the predicted ^{12}C elastic cross section was obtained from the phase-shift program MEFIT [28] (see also Ref. [29, 30]), which determines the charge density through a fit to a large collection of the world's measurements

z (cm)	y_{tgt} (cm)	ϕ_{min} (mrad)	ϕ_{max} (mrad)	θ_{max} (mrad)	$\Delta\Omega_{geom}$ (msr)	θ_{scat} (°)	$\frac{d\sigma}{d\Omega}^{pred}$ (fm^2/sr)
-3.877	-2.741	-11.276	28.291	60.000	4.748	44.513±1.134	6.1099×10^{-6}
-2.670	-1.888	-13.976	25.725	60.000	4.764	44.663±1.137	5.6510×10^{-6}
-0.161	-0.114	-19.635	20.347	60.000	4.798	44.980±1.145	4.7772×10^{-6}
2.361	+1.669	-25.328	14.824	60.000	4.818	45.301±1.150	4.0101×10^{-6}
3.557	+2.515	-28.048	12.182	60.000	4.828	45.455±1.152	3.6803×10^{-6}

Table 4.2: Calculated angles and predicted ^{12}C elastic cross sections as a function of target position for the 5.6-msr collimator in Spectrometer B, for a central spectrometer angle $\theta_0 =$ 45.00°. Note that a software cut has been applied to θ_{tgt} (see text).

of elastic scattering from ^{12}C. The program input includes the angular ranges θ_{scat} and θ_{max} from Tables 4.1 and 4.2, and the experimental beam energy and target thickness. The output is the predicted cross section averaged over the experimental angular acceptance and corrected for Coulomb distortion and energy loss in the target. The values of the predicted cross section as a function of target position are given in Tables 4.1 and 4.2.

This predicted cross section assumes that the acceptance of the spectrometer is ideal (i.e. that the actual solid angle is equal to the geometric solid angle). Comparison of the experimental cross section to this value then provides a comparison of the actual solid angle to the ideal one.

4.1.3   Measured ^{12}C(e,e′) Elastic Scattering Cross Sections

The ^{12}C elastic scattering measurements were performed using Spectrometers A and B. The measurements were done at an incident beam energy of 420.11 MeV and a central spectrometer angle of 45.00°. The nominal collimator sizes were 21 msr in Spectrometer A and 5.6 msr in Spectrometer B. The central momentum of the spectrometers was set to correspond to the momentum of the elastically scattered electrons, so that the elastic peak appeared at the center of the momentum acceptance. This point is emphasized to indicate that these elastic measurements can be used to study the spectrometer solid angle for only the central region of

the momentum acceptance ($\delta = \frac{p - p_{ref}}{p_{ref}} \approx 0.05$ for Spectrometer A* and $\delta = \frac{p - p_{ref}}{p_{ref}} \approx 0$ for Spectrometer B). To examine the dependence of the solid angle on δ we performed quasielastic measurements, which are reported in the next section.

The measurements were performed with a solid 32.5 mg/cm^2 carbon target with isotopic abundancy 98.9% ^{12}C and 1.1% ^{13}C. The target was mounted on a movable table, which could be remotely positioned and read out. The read-out and calibration of the table are described in Chapter 3. The elastic measurements were performed for 5 different locations of the target table. The positions and calculated angles are given in Tables 4.1 and 4.2 for Spectrometers A and B respectively.

Sample spectra of the reconstructed coordinates ($\theta_{tgt}, \phi_{tgt}, y_{tgt}$) are given in Figure 4-2. These data are for Spectrometer A (the spectra for Spectrometer B are similar) and were measured with the target located at $z = -0.117$ m. Software cuts (given in Table 4.3) were placed on these coordinates at each target position to remove events that reconstructed far outside the collimator or far from the location of the target. In Figure 4-2 these cuts are shown as the solid vertical lines. At each position, the (θ_{tgt}, ϕ_{tgt}) cuts were chosen to discard reconstructed angles that were more than 15 mrad outside of the collimator edges. For comparison, the angular resolution of both spectrometers is 3 mrad FWHM, so that the cuts were effectively far from the collimator edges. An exception to this is the ± 60 mrad cut on θ_{tgt} in Spectrometer B, which was inside the limits of the collimator for the reasons discussed in Section 4.1.1. The software cuts to y_{tgt} was chosen to discard events that reconstructed more than ± 30 mm (Spectrometer A) or ± 20 mm (Spectrometer B) away from the target location. For comparison, the y_{tgt} resolution is approximately 1.5 mm FWHM in Spectrometer B and 6 mm in Spectrometer A.

In both Spectrometers A and B and at all target locations, some of the data discarded by the ϕ_{tgt} and y_{tgt} cuts have a detected momentum corresponding to elastic scattering from ^{12}C. That is, even though these events reconstruct with ϕ_{tgt} far outside the collimator and/or y_{tgt} far from the target location, they appear to be electrons elastically scattered from the target.

---

*The full momentum acceptance of Spectrometer A is $\delta = -5 \to +15\%$, so that the center of the momentum acceptance is approximately $\delta = +5\%$.
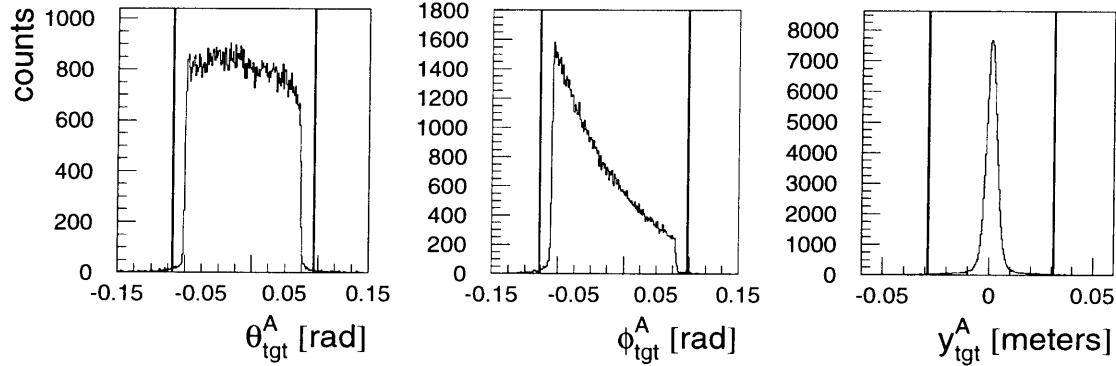
Figure 4-2: Sample spectra of the coordinates $(\theta_{tgt}, \phi_{tgt}, y_{tgt})$ reconstructed in Spectrometer A. The target was positioned at $z = -0.161$ cm. The solid lines show the position of the software cuts.

z (cm)	Spectrometer A cuts			Spectrometer B cuts		
	θ_{tgt} (rad)	ϕ_{tgt} (rad)	y_{tgt} (m)	θ_{tgt} (rad)	ϕ_{tgt} (rad)	y_{tgt} (m)
-3.877	±0.082	-0.129,0.043	-0.0026,0.0574	±0.060	-0.027,0.044	-0.0474,-0.0074
-2.670	±0.083	-0.117,0.057	-0.0111,0.0489	±0.060	-0.029,0.041	-0.0389,0.0011
-0.161	±0.085	-0.092,0.088	-0.0289,0.0311	±0.060	-0.035,0.035	-0.0211,0.0189
2.361	±0.087	-0.064,0.120	-0.0467,0.0133	±0.060	-0.041,0.030	-0.0033,0.0367
3.557	±0.088	-0.059,0.135	-0.0552,0.0048	±0.060	-0.043,0.027	0.0052,0.0452

Table 4.3: Cuts to reconstructed coordinates used in the analysis of the ^{12}C elastic scattering data. The cuts are given for each location, z, of the target along the beam line.

At the central target location ($z = -0.161$ cm), the number of these events relative to "good" events (where "good" indicates events that satisfy all of the software cuts) is approximately 3%. In calculating final cross sections, one must decide whether or not to include these events. One possibility is that they are good events that were somehow mis-reconstructed in angle and position by the spectrometers, and should therefore be included in the final cross section. However, the information from the vdc's doesn't indicate any problem with these tracks, indicating that the reconstruction is likely valid. A second possibility is that these events are due to electrons which rescatter into the spectrometer from the collimator edges, the scattering chamber, or some other piece of the setup. The rescattering changes the angle and position of the electrons, so that the vdc's (correctly) reconstruct the new, rescattered value of the coordinates. In this case the electrons are not valid events since they would not normally enter the acceptance, and so should be discarded. This second explanation is more consistent with the measured data, since it explains why the reconstructed coordinates are distorted from their nominal values while the vdc information indicates that the tracks are valid. Note that similar types of rescattering have been observed in the (e,e′p) measurements (as discussed in Chapter 5). The events discarded in the software cuts are therefore not included in the final cross sections.

Sample spectra of the detected momentum and kinematically-corrected momentum (defined in Appendix A) are shown in Figure 4-3. The peak at 415.5 MeV/c corresponds to elastic scattering from ^{12}C, and several excited states are observed as peaks at lower momentum. The spectra were corrected for radiation using the program ALLFIT [31]. A sample of the output from ALLFIT is shown in Figure 4-4 illustrating the fit of the elastic peak and radiative tail. Relatively few counts appear at excitation energies below the ^{13}C elastic peak, indicating that background contributions to the ^{12}C elastic cross sections are negligible.

Experimental cross sections were determined from the data as follows:

$$\frac{d\sigma}{d\Omega}^{exp} = \frac{N^c}{\Delta\Omega_{geom}} \times \frac{eA}{QN_A\rho_A} \times \eta_{dt-pre} \qquad (4.6)$$
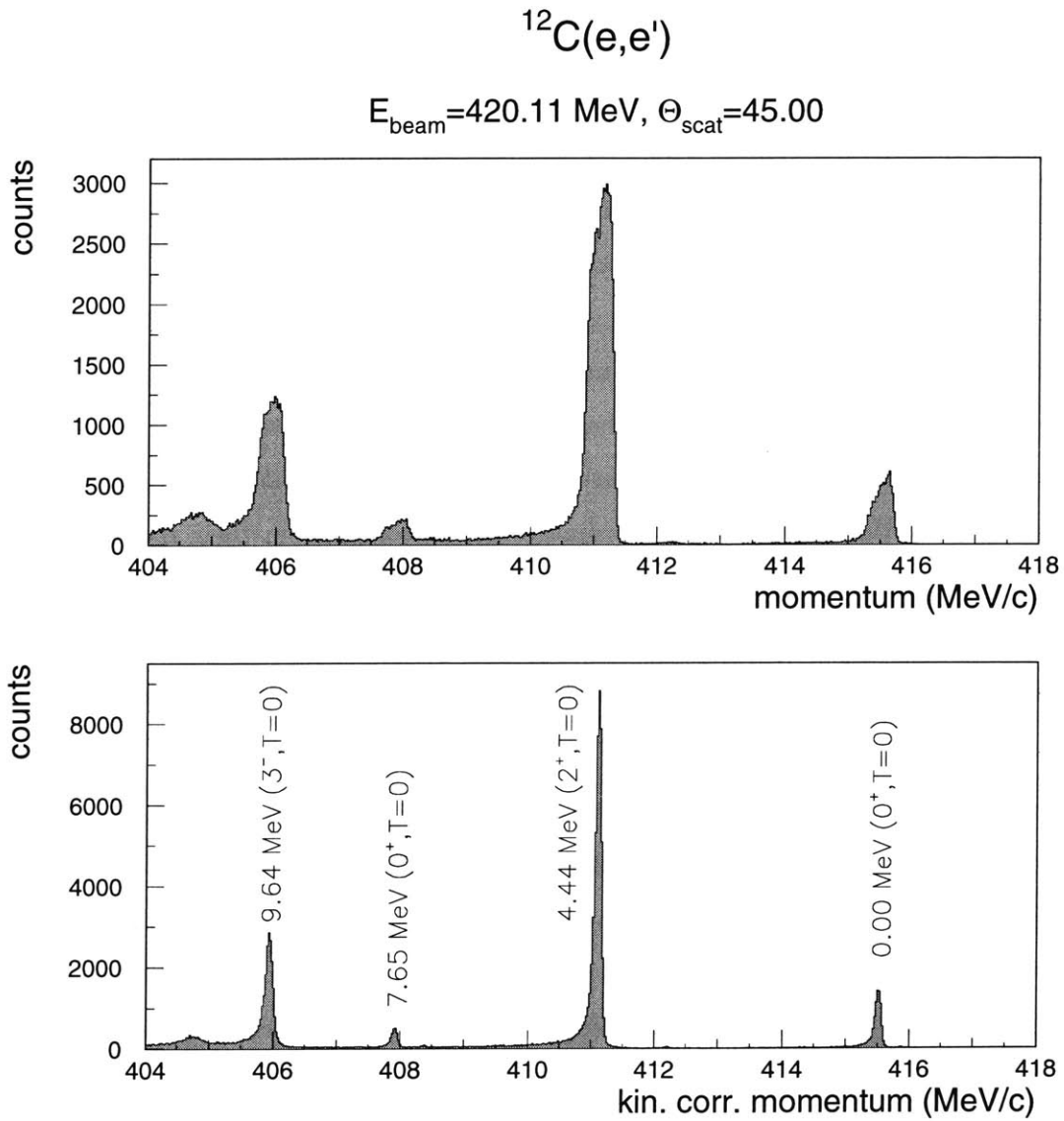
Figure 4-3: Momentum spectra of electrons scattered from ^{12}C and detected in Spectrometer B, before and after kinematic correction.
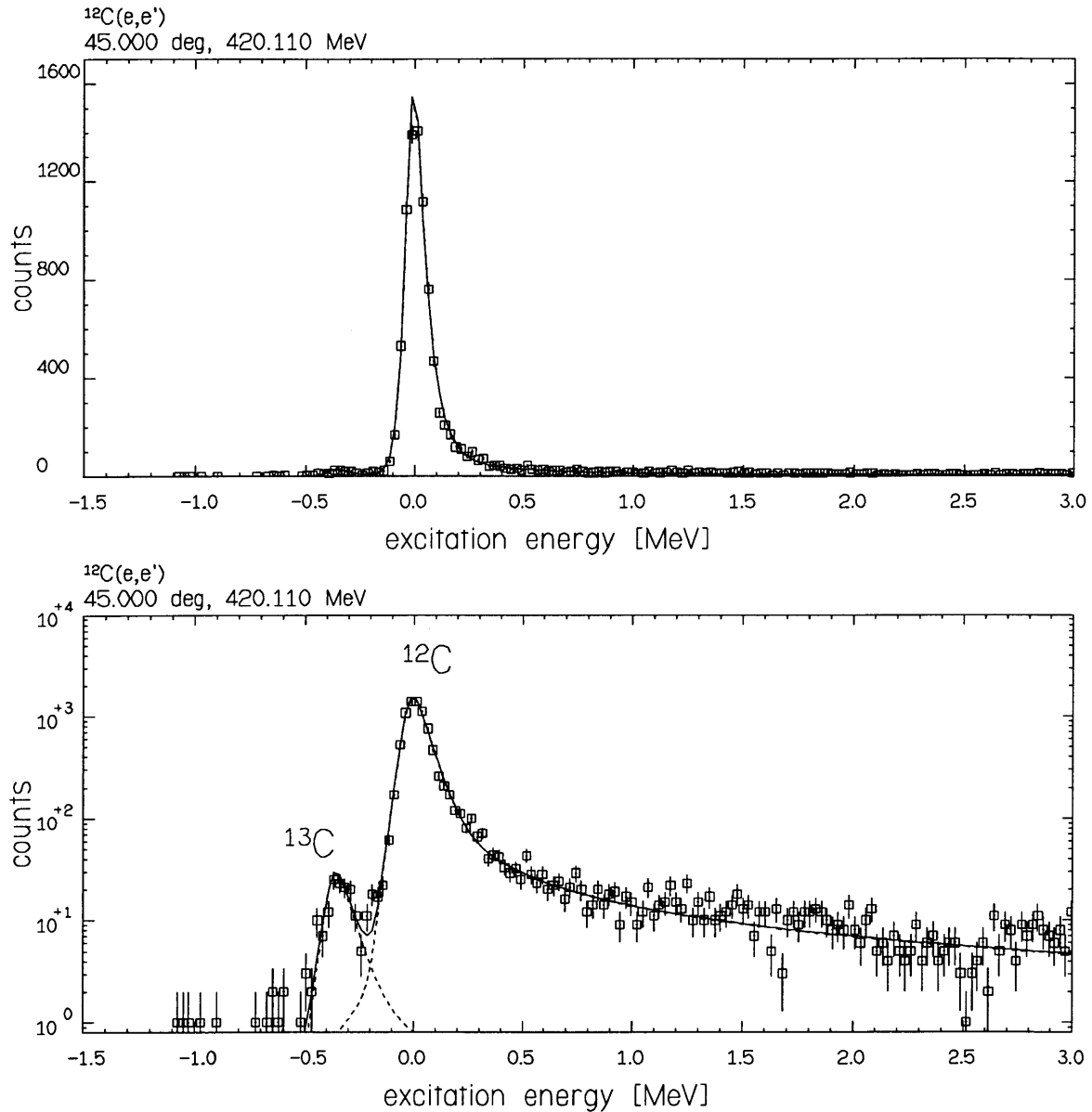
Figure 4-4: Counts vs. Excitation Energy in ^{12}C on a linear (top plot) and log (lower plot) scale, measured in Spectrometer B. The two peaks are from elastic scattering from ^{13}C and ^{12}C, and the solid line is the fit from ALLFIT.

z	run analyzed	charge	Spec. A	Spec. B
(cm)		(mC)	η_{dt-pre}	η_{dt-pre}
-3.877	950629103621	9.977	6.078	1.242
-2.670	950629092119	9.938	6.070	1.233
-0.161	950629082037	7.038	6.078	1.283
2.361	950629084632	10.25	6.035	1.223
3.557	950629095557	10.37	6.025	1.208

Table 4.4: Factors used in calculation of the measured carbon elastic cross section at each target position.

where

$$N^c \quad = \quad \text{number of counts, corrected for radiation by ALLFIT}$$

$$\Delta\Omega_{geom} \quad = \quad \text{geometric solid angle, tabulated in Tables 4.1 and 4.2}$$

$$e \quad = \quad 1.602 \times 10^{-19}\text{C}$$

$$A \quad = \quad 12.00 \times 10^3\text{mg/mol}$$

$$Q \quad = \quad \text{accumulated charge (C)}$$

$$N_A \quad = \quad 6.022 \times 10^{23}$$

$$\rho_A \quad = \quad \text{density of } ^{12}\text{C in target} = 32.113 \text{ mg/cm}^2$$

$$\eta_{dt-pre} \quad = \quad \text{dead-time and prescaling correction factor (see Appendix H)}$$

The values of η_{dt-pre} and Q for each run are listed in Table 4.4. The prescaling values for Spectrometers A and B were 6 and 1, respectively. The reduced effect of dead time for Spectrometer A vs. Spectrometer B is a result of its higher prescale factor, as explained in Appendix H.

4.1.4   Systematic Uncertainty

Table 4.5 shows the total statistical and systematic uncertainties for the measured cross sections. The first two columns are the absolute uncertainties in the cross sections measured in

		Spec. A	Spec. B	A ÷ A	B ÷ B	A ÷ B
ALLFIT (stat.+fit)	[%]	0.5–1.2	0.8–1.1	0.7–1.7	1.3–1.6	0.9–1.6
dead time	[%]	1	1	1.4	1.4	1.4
target position (±0.5 mm)	[%]	±1.5	±0.4	-	-	±1.1
central scatt. angle (±0.1 mrad)	[%]	0.3	0.3	-	-	0.4
horiz. beam position (±1 mm)	[%]	±3.0	∓0.8	-	-	±3.8
total charge	[%]	1.8	1.8	1.4	1.4	-
average target thickness	[%]	4	4	-	-	-
beam energy (±160 keV)	[%]	∓0.7	∓0.7	-	-	-
total	[%]	5.7–5.8	4.7–4.8	2.1–2.6	2.4–2.5	4.3–4.5

Table 4.5: Statistical and estimated systematic uncertainties in the measured ^{12}C elastic cross sections.

Spectrometers A and B. When a given uncertainty is correlated or anti-correlated in the two spectrometers, a sign is given to indicate the correlation. For example, a +1 mm change in the horizontal beam position would give a +3% change in the cross section in Spectrometer A and a -0.8% change in the cross section in Spectrometer B. Some of the uncertainties cancel when considering ratios of the results, and the column labelled 'A ÷ A' gives the systematic uncertainty in the ratio of cross sections measured at different target locations with Spectrometer A. Similarly, 'B ÷ B' denotes the uncertainty for the ratio of measurements with Spectrometer B. The column 'A ÷ B' corresponds to the uncertainty in the ratio of cross sections measured in the two spectrometers at the same target location. The total in the final row of each column corresponds to the sum of the individual uncertainties, added in quadrature.

The error from ALLFIT includes the statistical error and a small systematic contribution from the fitting procedure and varies over the range given depending on the run analyzed (each target position corresponds to a different run). The systematic uncertainty in the total charge is the 1% uncertainty in the value read out from the photoeffect monitor and the uncertainty in its calibration against the Förster probe at high current, added together in quadrature. The uncertainty due to the absolute target position was determined from the change in the acceptance-averaged cross section calculated by MEFIT for a target displaced ±0.5 mm relative to the central target location ($z = -0.161$ cm). The sign of the uncertainty is the same for

both spectrometers, but the magnitude is larger in Spectrometer A because of the shorter drift distance to its collimator. The relatively small error in the target position (0.5 mm) reflects the fact that the absolute position of the target table was determined with sieve slit measurements in Spectrometers A and B, as described in Chapter 3. The uncertainty in the cross section due to the estimated uncertainty in the central scattering angles and the beam energy was calculated with MEFIT by the same technique used for the uncertainty in the target position. The uncertainty in the horizontal beam position (± 1 mm) was estimated from the drift in the beam position on the BeO target observed at different times during the experiment. Since the central spectrometer angle is $45°$, a horizontal shift in the beam position is equivalent to a shift of equal magnitude in the target position. The systematic uncertainty in the cross section due to the beam position was therefore estimated from the uncertainty due to the target position. Note that the effect of a horizontal drift in the beam position in one of the spectrometers has an opposite sign of that in the other spectrometer since they are on opposite sides of the beam line.

Other possible sources of systematic uncertainty include the thickness of the target at the beam spot. Only the average target thickness has been measured (by measuring the target dimensions and weight) so that the thickness at the beam is unknown. However, the exact normalization of the cross sections is not critical to our analysis, since we are primarily interested in studying the change in the solid angle as a function of y_{tgt}. The cross sections measured at the central target location could therefore be viewed as a calibration of the target thickness. Another source of uncertainty is the uncertainty in the ^{12}C elastic cross section calculated by MEFIT, which is assumed to be small compared to the other uncertainties and is therefore ignored.

4.1.5 ^{12}C Elastic Scattering Results

The results of the ^{12}C elastic scattering measurements are given in Table 4.6 and Figure 4-5. The ratio of measured and predicted cross sections at the central target location ($z = -0.161$ cm) is 0.98 ± 0.06 for Spectrometer A and 0.96 ± 0.05 for Spectrometer B, where the absolute

	Spectrometer A			Spectrometer B		
z [cm]	y_{tgt} [cm]	$\left(\frac{d\sigma}{d\Omega}\right)^{exp}$ $[10^{-6}\ \mathrm{fm}^2/\mathrm{sr}]$	$\left(\frac{d\sigma}{d\Omega}\right)^{exp} / \left(\frac{d\sigma}{d\Omega}\right)^{pred}$	y_{tgt} [cm]	$\left(\frac{d\sigma}{d\Omega}\right)^{exp}$ $[10^{-6}\ \mathrm{fm}^2/\mathrm{sr}]$	$\left(\frac{d\sigma}{d\Omega}\right)^{exp} / \left(\frac{d\sigma}{d\Omega}\right)^{pred}$
-3.877	+2.741	12.34	0.538	-2.741	5.467	0.895
-2.670	+1.888	15.10	0.894	-1.888	5.261	0.931
-0.161	+0.114	8.154	0.978	-0.114	4.583	0.959
2.361	-1.669	3.524	0.971	+1.669	3.825	0.954
3.557	-2.515	2.181	0.947	+2.515	3.375	0.917

Table 4.6: Results of the ^{12}C elastic scattering measurements (see text). Uncertainties are given in Table 4.5.

errors are those listed in Table 4.5. The ratios are consistent with unity and with each other, indicating that the experimental solid angle is defined by the collimator within the systematic uncertainty of the measurement.

As the target is moved from the central location, the experimental cross section in Spectrometer A falls significantly below the prediction, indicating that for $y_{tgt} \neq 0$ the solid angle of Spectrometer A is not defined by its collimator. The true solid angle is significantly less than the geometric value. The effect appears to be asymmetric about $y_{tgt} = 0$, but this is likely to be an artifact of the strong ϕ_{tgt} dependence of the cross section, as discussed in the next section.

A similar although reduced effect is apparent in Spectrometer B. However, inside the design region $|y_{tgt}| < 2.5$ cm, the ratios of measurement and prediction are consistent with each other within the quoted relative uncertainty (2.4–2.5%, from Table 4.5), and nearly consistent with unity within the absolute uncertainty (4.7–4.8%). This indicates that there is little acceptance loss in Spectrometer B in the design region, and that the solid angle is defined by the collimator for $|y_{tgt}| < 2.5$ cm.

From these data it is clear that the solid angle of Spectrometer A is not defined by the collimator for target locations away from the central position ($y_{tgt} = 0.114$ cm). The solid angle of Spectrometer A is needed to measure an absolute cross section, and if it is not defined by the geometry of the collimator alone, there is no straightforward way of determining it. Two

Spectrometer A
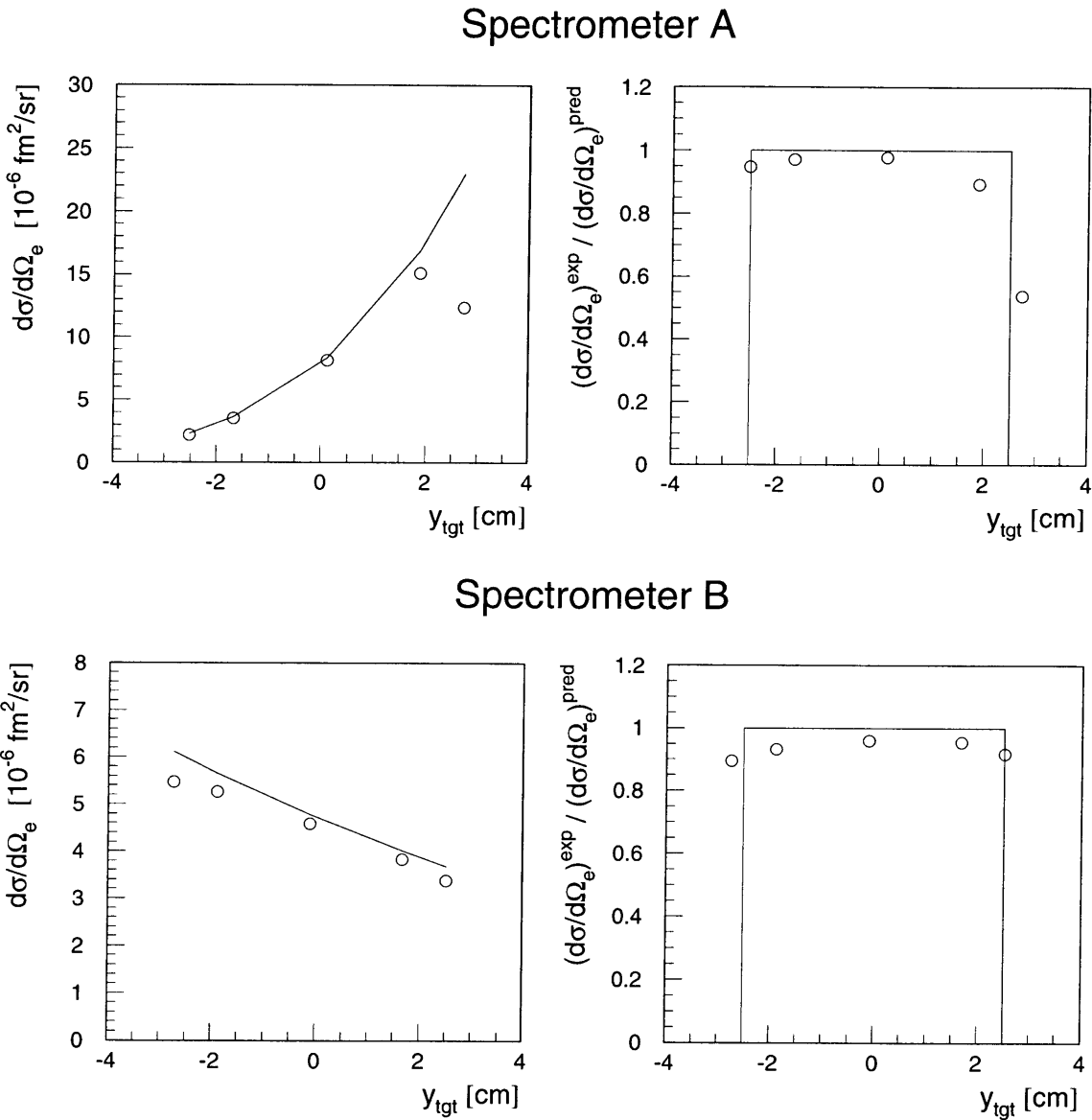
Spectrometer B

Figure 4-5: Predicted and measured ^{12}C elastic cross sections for Spectrometer A (upper plots) and Spectrometer B (lower plots) as a function of y_{tgt}. On the left figure, the measured cross sections are drawn as circles and the predicted cross sections are joined by lines to guide the eye. On the right, the points are the ratio of the measured and predicted cross sections and the lines represent the design acceptance (100% over $y_{tgt} = \pm 2.5$ cm).

possible solutions to this problem are:

1. Do a complete study of the variation of the solid angle so that it can be parameterized. This could be quite complicated and time-consuming, since the solid angle depends on a nuber of variables. It is dependent on y_{tgt} (as shown in Figure 4-5), δ (as will be seen in the quasielastic data), and ϕ_{tgt} (as outlined in the next section).

2. Try to determine what region of the spectrometer acceptance the losses come from. If the region is small, software cuts could then be placed on the data to restrict to a region where the solid angle is determined by the combined geometry of the cuts and the collimator.

We have chosen the second option. Closer analysis of the ^{12}C elastic data revealed that the acceptance losses come from events with large $|\phi_{tgt}|$ values, which are geometrically allowed with increasing y_{tgt}. In the analysis of data taken with the extended Helium target, deviations from the designed solid angle in Spectrometer A for large $|\phi_{tgt}|$ were accounted for by using a software cut $|\phi_{tgt}| < 75$ mrad. This software cut, when combined with the geometry of the collimator, defines the solid angle of Spectrometer A with a minimal loss of data. The identification of these acceptance losses at large $|\phi_{tgt}|$ is discussed in the next section.

4.1.6 Identification of Acceptance Losses

The following analysis of the ^{12}C elastic data revealed that the acceptance loss in Spectrometer A come from events with large $|\phi_{tgt}|$ values, which are geometrically allowed when the target is shifted away from $y_{tgt} = 0$. The effective solid angle for these events appears to be a complicated function, but the region of $|\phi_{tgt}|$ where it deviates from the geometric value is quite well-defined.

The ϕ_{tgt}-dependence of the acceptance in Spectrometer A is illustrated in Figure 4-6. The quantity plotted in the figure is

$$N'(\phi_{tgt}) = \frac{N(\phi_{tgt}) \cdot \eta_{dt-pre}}{Q} \tag{4.7}$$

where $N(\phi_{tgt})$ is the number of counts measured in a particular ϕ_{tgt} bin. In determining $N(\phi_{tgt})$, a cut of $\theta_{tgt} = \pm 64$ mrad was placed on the data, so that the range of θ_{tgt} averaged over was

the same for every value of y_{tgt}. The cuts on y_{tgt} were the same as those given in Table 4.3, and no cuts were made on ϕ_{tgt}. Also, $N(\phi_{tgt})$ is accumulated over a finite range of the momentum acceptance ($0.018 \leq \delta \leq 0.05$ for Spectrometer A) so that it includes some of the excited states as well as the carbon elastic peak. With this definition, $N'(\phi_{tgt})$ is proportional to the cross section, and its value at a particular ϕ_{tgt} should be a constant independent of y_{tgt} (with the limitation that all values of ϕ_{tgt} are not geometrically allowed by the collimator at a given target position). By comparing $N'(\phi_{tgt})$ spectra measured at different y_{tgt}, we can therefore study losses in the solid angle acceptance as a function of ϕ_{tgt}.

In each of the four plots in Figure 4-6, the shaded region is identical and corresponds to N' measured at the central target location ($y_{tgt} = +0.114$ cm), and the thick solid line corresponds to N' measured at the indicated value of y_{tgt}. The ϕ_{tgt} limits of each of the N' distributions is defined by the edges of the collimator, so that the limits shift when the target is moved along the beam line (as discussed in Section 4.1.1). These ϕ_{tgt} limits defined by the collimator were given in Table 4.1 for each target position. To illustrate these limits, consider the first plot in the upper left-hand corner of Figure 4-6. The shaded region is for the central target location, so that the limits of N' are approximately 76 mrad and +73 mrad. For the thick line, the target position is $y^A_{tgt} = +2.74$ cm (corresponding to $z = -3.877$ cm) so that the limits are approximately -113 mrad and +27 mrad. The two arrows in the figure mark these limits for $y^A_{tgt} = +2.74$ cm.

For small values of $|\phi_{tgt}|$ (< 70 mrad), the plots in figure 4-6 show excellent overlap with the data taken at the central target position. Note that the normalization of each of these curves has been independently determined. The good overlap indicates that in the region of small $|\phi_{tgt}|$, the acceptance at shifted y_{tgt} is consistent with the value at the central y_{tgt}. In other words, for a shifted target we observe no acceptance loss for small $|\phi_{tgt}|$.

However, one can see a clear drop in the acceptance for larger $|\phi_{tgt}|$. The effect is very large for $|y_{tgt}| > 2.5$ cm, which is outside of the design region of the spectrometer. Consider the value of N' at $y_{tgt} = +2.74$ cm (upper left-hand plot of Figure 4-6). As ϕ_{tgt} decreases below 70 mrad, N' drops relative to the shaded region, indicating a loss in the acceptance.
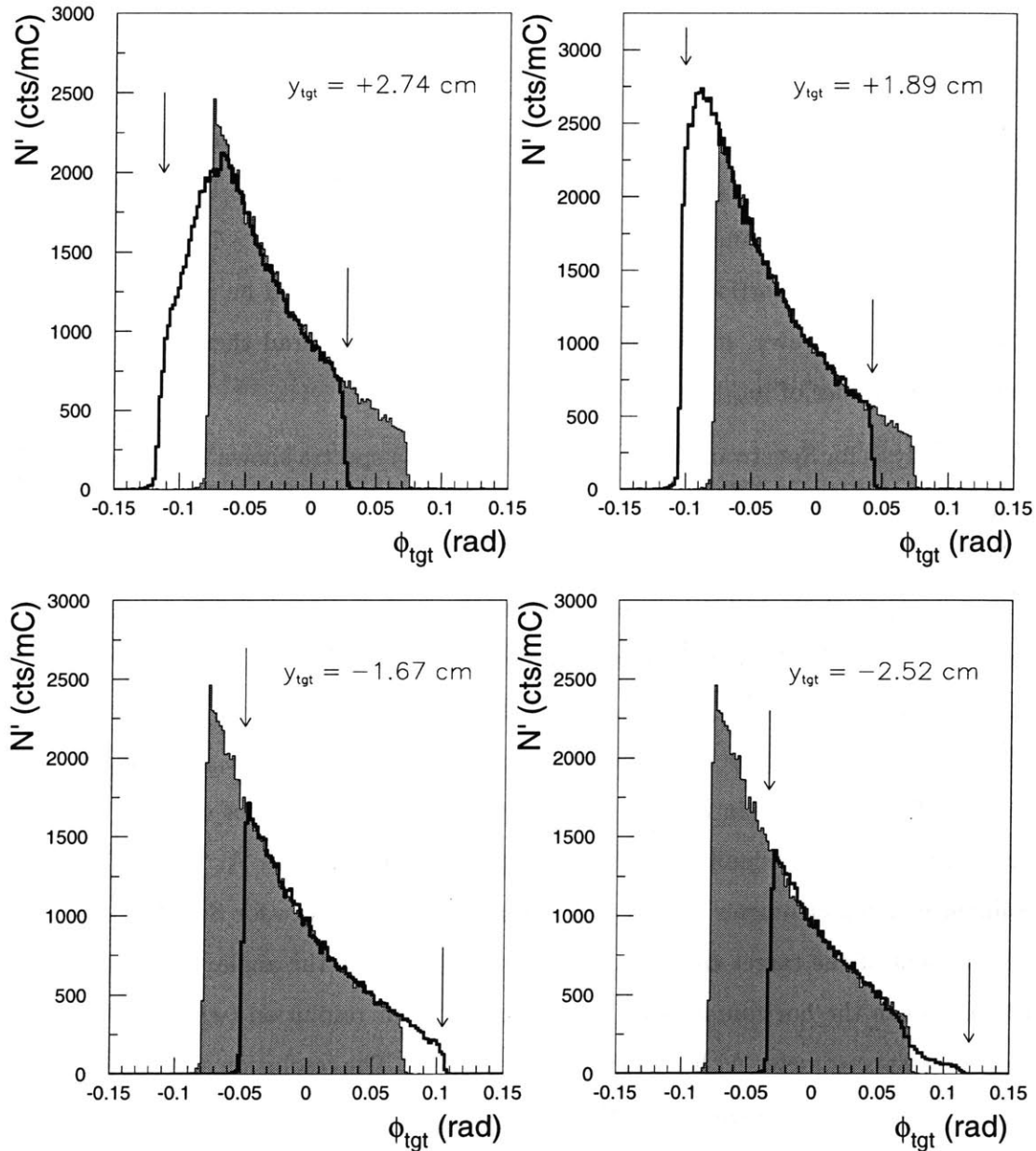
Figure 4-6: $N'(\phi_{tgt})$ (see text for definition) for $^{12}C(e,e')$ measured at various values of y_{tgt} for Spectrometer A. The shaded plot is identical in all four figures and is the data for the "central" target location ($y_{tgt} = +0.11$ cm). The heavy line is the data for the y_{tgt} value indicated and the arrows mark the calculated geometric limits of the collimator at that y_{tgt}.

As ϕ_{tgt} decreases further there is no overlapping shaded region to compare directly to, but a worsening acceptance loss is nevertheless apparent from the sharp decrease in N'. A similar effect is observed for $+\phi_{tgt}$ in the data for $y_{tgt} = -2.52$ cm (lower right hand plot in Figure 4-6).

For the two smaller values of $|y_{tgt}|$, the values of N' show excellent agreement with the shaded region over the entire region of overlap, indicating no acceptance loss in that region. There is probably some acceptance loss outside the overlap region ($|\phi_{tgt}| > 75$ mrad) where the shape of N' shows some distortion at large $|\phi_{tgt}|$, but more data would be required to make a definitive statement. However, it is clear that within $|\phi_{tgt}| < 75$ mrad there is no significant acceptance loss for values of $|y_{tgt}| < 2$ cm.

A similar analysis for Spectrometer B yielded the $N'(\phi_{tgt})$ spectra shown in Figure 4-7. The cuts on θ_{tgt} and y_{tgt} are the same as given in Table 4.3, no cut was made on ϕ_{tgt}, and the cut on δ ($-0.024 \leq \delta \leq 0.01$) was made to include both the elastic peak and a few of the excited states as in the Spectrometer A analysis. As expected from the analysis of the absolute cross sections in the previous section, no significant acceptance loss is seen in Spectrometer B for $|y_{tgt}| < 2$ cm. At the two largest values of y_{tgt} ($+2.52$ and -2.74 cm) there is also no significant loss for $|\phi_{tgt}| < 20$ mrad, although there might be some loss at larger values of $|\phi_{tgt}|$. A quantitative conclusion is difficult to make in these regions where the data sets do not overlap. Also, the angular resolution is a more significant effect here then in Spectrometer A. The drift distance to the collimator in Spectrometer B is several times the drift distance for Spectrometer A, so that the movement of the target causes a much smaller change in the angle. The collimator is also much smaller in the horizontal plane, so that the angular resolution (which has the same absolute value as Spectrometer A) has a larger relative effect. The resolution also appears to get worse with increasing $|y_{tgt}|$, judging from the reconstruction of the collimator edges. However, from these data we can conclude that for $|y_{tgt}| < 2$ cm the solid angle of Spectrometer B is defined by the collimator.

To summarize, Spectrometers A and B are designed so that their solid angles should be defined by the geometry of the collimators for $|y_{tgt}| < 2.5$ cm, where y_{tgt} is the transport
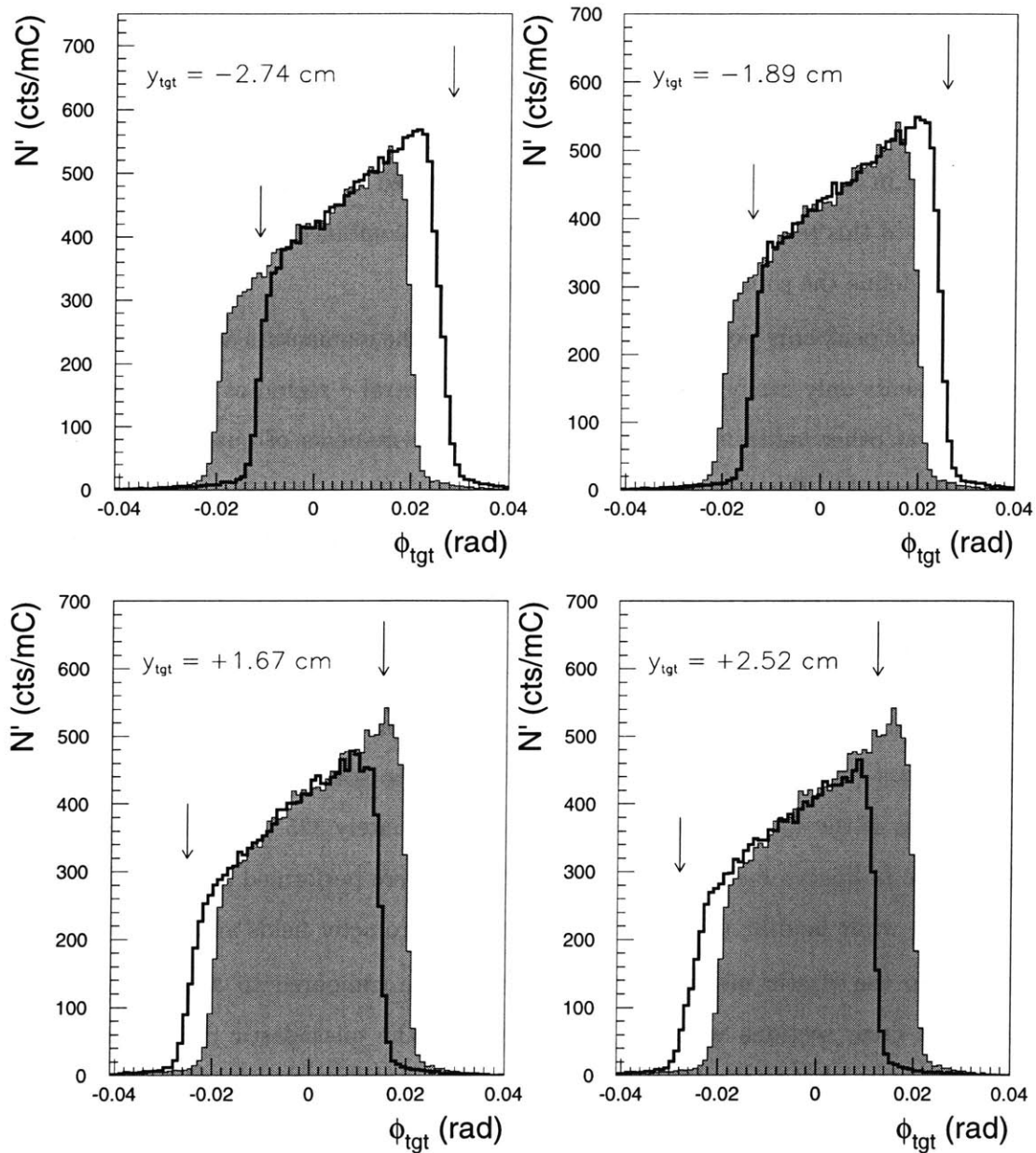
Figure 4-7: $N'(\phi_{tgt})$ for ^{12}C(e,e') measured at various values of y_{tgt} for Spectrometer B

coordinate at the target, perpendicular to the central ray and in the horizontal plane. This statement was checked by measuring ^{12}C(e,e') elastic scattering with a thin carbon target placed at several positions along the beam line. The measured solid angle in Spectrometer B was found to be consistent with the collimator for $|y_{tgt}| < 2$ cm. The measured solid angle in Spectrometer A was found to deviate from the geometric value for large values of $|\phi_{tgt}|$ that are geometrically allowed with increasing $|y_{tgt}|$. For $|y_{tgt}| < 2$ cm, no acceptance loss is visible for $|\phi_{tgt}| < 75$ mrad. Therefore in analyzing data taken with an extended target software cuts should be placed to restrict to this region. These software cuts, when combined with the geometry of the collimator, then define the solid angle of Spectrometer A.

Since the elastic peak only populates a central region of the momentum acceptance (δ), these elastic measurements only verify the solid angle for the central δ region of each spectrometer. The solid angle at other values of δ is studied using measurements of quasielastic scattering from ^{12}C, as discussed in the next section.

4.1.7   Measured ^{12}C(e,e') Quasielastic Cross Sections

Measurements of quasielastic scattering from ^{12}C were performed with Spectrometers A and B and with the same beam energy (420.11 MeV), collimators (5.6 and 21 msr), and central spectrometer angles (45.00 degrees) used in the ^{12}C elastic scattering measurements. The reference momenta of the spectrometers was set to approximately 325 MeV/c in Spectrometer A and 342 MeV/c in Spectrometer B. The measurements were performed at three positions of the carbon target while holding the beam energy and spectrometer fields and angles constant.

In contrast to the elastic measurements, which can be compared to a well-known cross section, absolute cross sections were not extracted from the quasielastic data. Instead, we proceed directly to the analysis of N'(ϕ_{tgt}), which was defined in the previous section. The software cuts placed on the data are given as a function of target position in Table 4.7. As with the elastic analysis, cuts on the vertical angle θ_{tgt} are the same at each target location to hold the solid angle constant. The criteria for the y_{tgt} cuts is the same as in the elastic analysis: ± 30 mm and ± 20 mm about the target position in Spectrometers A and B, respectively.

		Spectrometer A cuts		Spectrometer B cuts	
z (cm)	run number	θ_{tgt} (rad)	y_{tgt} (m)	θ_{tgt} (rad)	y_{tgt} (m)
-0.143	950629153731	±0.064	-0.029,0.031	±0.060	-0.021,0.019
+2.886	950629160407	±0.064	-0.0504,0.0096	±0.060	0.0004,0.0404
-3.173	950629163824	±0.064	-0.0076,0.0524	±0.060	-0.0424,-0.0024

Table 4.7: Cuts to reconstructed coordinates used in the analysis of the ^{12}C quasielastic scattering data. The cuts are given for each location, z, of the target along the beam line.

As with the elastic analysis, $N'(\phi_{tgt})$ is proportional to the cross section and should be independent of the target location, y_{tgt}. By comparing $N'(\phi_{tgt})$ spectra measured at different y_{tgt}, we can therefore study losses in the solid angle acceptance as a function of ϕ_{tgt}. Furthermore, by making cuts on different sections of the momentum acceptance (δ) we can study the acceptance loss as a function of δ.

The spectra of N' versus ϕ_{tgt} for Spectrometer A are shown in Figure 4-8. Each plot shows the data for all three target locations, with the shaded region corresponding to the central target location ($y_{tgt} = +0.10$ cm). The first plot in the upper left is for all of the data, spanning the full momentum acceptance ($-5\% \le \delta \le +15\%$) of Spectrometer A. The arrows indicate the geometric limits of ϕ_{tgt} defined by the collimator for the two displaced target locations, $y_{tgt} = -2.04$ and $+2.24$ cm. For an explanation of these geometric limits, see the previous discussion of the carbon elastic data. Two main features are visible in this first plot. First, the overlap in the central ϕ_{tgt} region (corresponding to the lesser of $|\phi_{tgt}| = \pm 75$ mrad or the geometric limit of the collimator) is quite good. $N'(\phi_{tgt})$ is independent of y_{tgt} in this region, indicating that the acceptance here is 100%. Second, the change in shape of $N'(\phi_{tgt})$ for $|\phi_{tgt}| > 75$ mrad indicates that there is a substantial drop in the acceptance in this region for the two displaced values of y_{tgt}. This indicates that the collimator is not defining the solid angle in these regions, which is consistent with the observations in the elastic scattering measurements. Events with large values of $|\phi_{tgt}|$ that are geometrically allowed into the collimator are being reduced.

The next four plots in the figure study the dependence of this effect on $\delta = (p - p_{ref})/p_{ref}$. The momentum acceptance is broken up into four sections, each spanning one-quarter of the full acceptance. Each plot corresponds to one of these sections. From these plots it is clear that the acceptance reduction is clearly a function of δ, and is most enhanced at the high momentum side $(+10\% \leq \delta \leq +15\%)$ of the focal plane. At the low momentum side, the distribution of $N'(\phi_{tgt})$ is smooth for all three values of y_{tgt} and extends up to the geometric limits of the collimator. As δ is increased, the distributions contract significantly in the range of ϕ_{tgt}, indicating an increasing reduction in events with large ϕ_{tgt}. These data show that the acceptance loss in Spectrometer A increases with δ.

A similar plot of the data in Spectrometer B is shown in Figure 4-9. The first plot is for the full momentum acceptance and the following three plots are for the acceptance broken into three equal sections. The arrows indicate the geometric limits of ϕ_{tgt} defined by the collimator for the two displaced target locations, $y_{tgt}^B = +2.04$ and -2.24 cm. For an explanation of these geometric limits, see the previous discussion of the carbon elastic data. In contrast to Spectrometer A, there does not appear to be a significant drop in the acceptance for Spectrometer B. The N' distributions are smooth as a function of ϕ_{tgt} and the collimator edges reconstruct in approximately the correct locations. From these data we conclude that the collimator defines the solid angle of Spectrometer B at all δ for $y_{tgt} \leq 2$ cm.
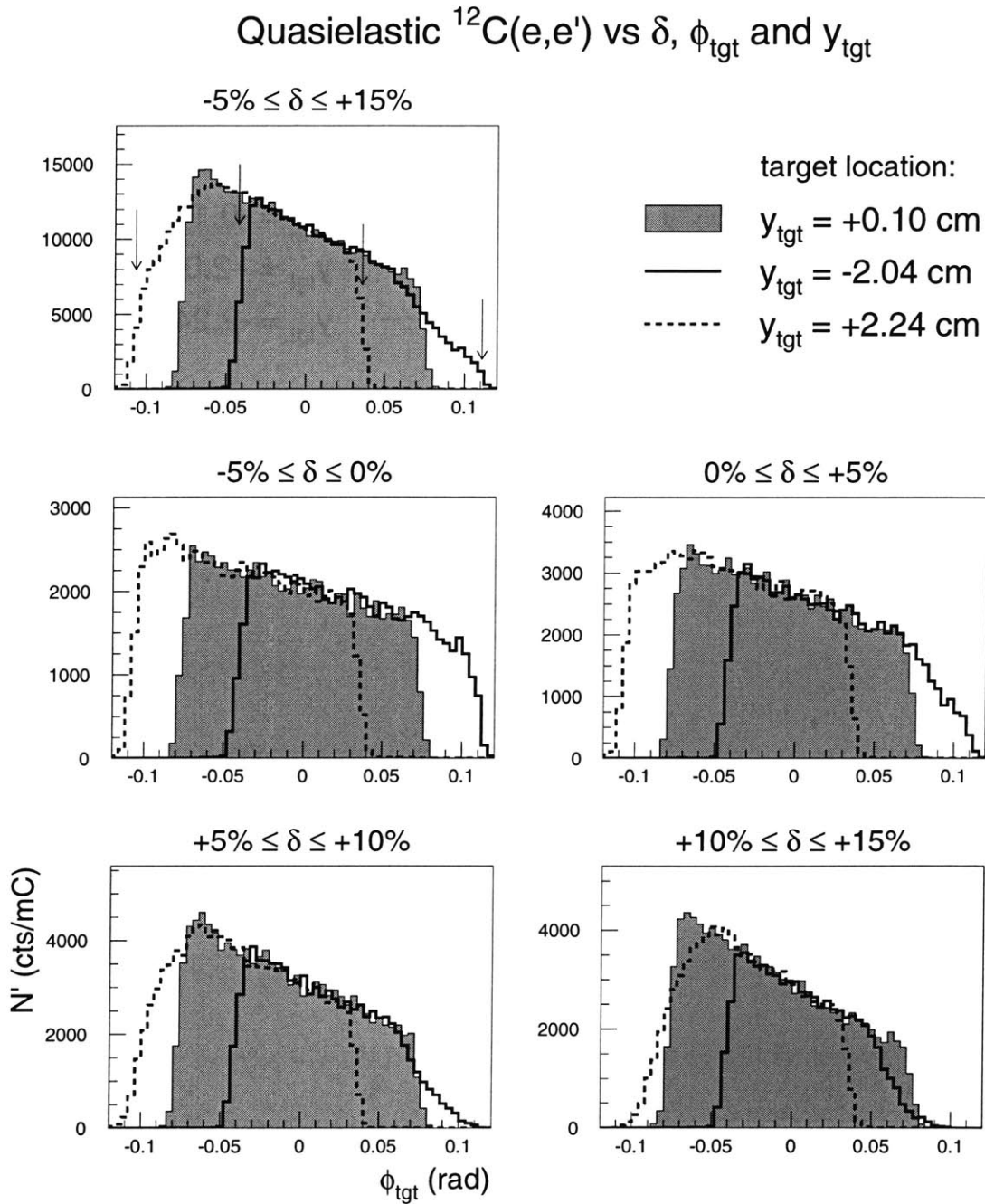
Figure 4-8: $N'(\phi_{tgt})$ for $^{12}C(e,e')$ at quasielastic kinematics measured at three values of y_{tgt} in Spectrometer A. See text for details.
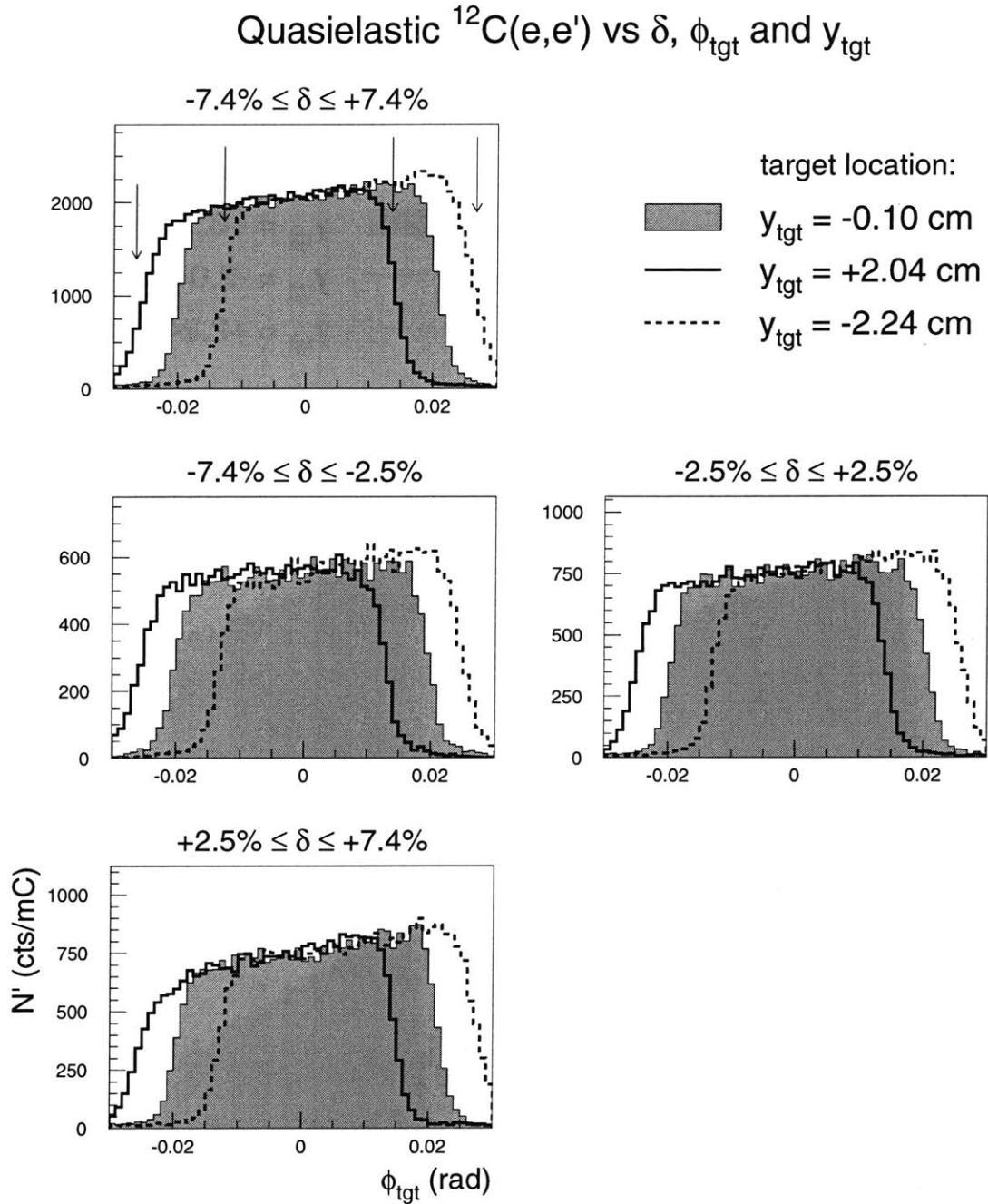
Figure 4-9: $N'(\phi_{tgt})$ for $^{12}C(e,e')$ at quasielastic kinematics measured at three values of y_{tgt} in Spectrometer B. See text for details.

4.1.8 Conclusions of Acceptance Studies

Analysis of the elastic and quasielastic scattering data from ^{12}C indicated that the solid angle of Spectrometer B is defined by the collimator for $|y_{tgt}^B| < 2$ cm. In contrast, the solid angle in Spectrometer A is not defined by the collimator for $|y_{tgt}^A| < 2$ cm. A reduction in the solid angle of Spectrometer A was observed as the target was moved from its central location ($y_{tgt}^A = +0.114$ cm). This reduction was observed to occur only for events with large values of $|\phi_{tgt}|$ that are geometrically allowed by the collimator for increasing $|y_{tgt}|$. For $|y_{tgt}^A| < 2$ cm, no acceptance reduction is observed in the elastic measurements for $|\phi_{tgt}| < 75$ mrad. The quasielastic data indicated that this acceptance reduction increases with δ and is reduced for small values of δ.

Since the acceptance reduction is complicated and multi-dimensional (it was shown to depend on y_{tgt}, ϕ_{tgt}, and δ) it would be difficult to accurately parameterize the effective solid angle of Spectrometer A. A simpler solution is to apply software cuts to the data to restrict the data to a region of ϕ_{tgt} and y_{tgt} where there is no observed acceptance loss. We have chosen this solution to analyze the cross sections measured with the extended Helium target. These cuts are applied in the same way in both the data analyzer and the Monte Carlo calculation of the detection volume. The software cuts combined with the geometry of the collimator then define the solid angle of Spectrometer A.

The cuts used for this purpose in the coincidence Helium (e,e'p) measurements were $z = \pm 2.0$ cm and $|\phi_{tgt}^A| < 75$ mrad, where z is the location of the event vertex along the beam line (determined with Spectrometer B) and ϕ_{tgt}^A is the horizontal transport angle at the target reconstructed in Spectrometer A. This cut on z restricts the nominal[†] range of y_{tgt} to $|y_{tgt}| \leq 2\sin(\theta_0)$ cm, where θ_0 is the central spectrometer angle (given in Tables 3.3 and 3.4 in Chapter 3). Based on the results of carbon measurements, restricting y_{tgt} to small values in this way effectively limits any acceptance reduction in either spectrometer. The cut on ϕ_{tgt}^A then eliminates the acceptance reduction in Spectrometer A by removing the large values of ϕ_{tgt}^A where the acceptance reduction is generated. The ability of these software cuts to define

---

[†]The magnitude of $|y_{tgt}|$ is only approximately $|z\sin(\theta_0)|$. There is also a small contribution from the rastering of the incident beam.

the acceptance and the systematic uncertainty introduced by them is studied and discussed in section 6.4 of Chapter 6.

In analyzing the Helium elastic measurements performed with Spectrometer A (discussed in Section 4.2), a cut of $\phi_{tgt}^A = \pm 75$ mrad was also used. However, only a broad y_{tgt}^A cut (± 4.0 or ± 4.5 cm) was applied, so that it removed data that reconstructed far outside the target while not defining the detection volume. The range of y_{tgt} was therefore determined by the target extent, corresponding to a maximum (nominal) range of $y_{tgt} = \pm 4 \sin(40°) = \pm 2.57$ cm. The data were analyzed for several different cuts on ϕ_{tgt}^A, all of which yielded a target density constant to $< 1\%$. This result shows that a cut of $\phi_{tgt}^A = \pm 75$ mrad is sufficient to define the solid angle of Spectrometer A at this kinematic setting. This analysis is presented in Section 4.2.3.

4.2 Elastic Scattering from Helium

Overview

The density of the Helium target was needed to calculate absolute ^{3,4}He(e,e$'$p) cross sections. The density was measured in the experiment using the following technique:

1. For each beam energy, an elastic scattering measurement was performed using either Spectrometer A or B. The absolute average target density during that run was then determined by comparing the measured result to published ^{3,4}He elastic cross sections.

2. During the entire experiment (i.e. in both the elastic scattering and the (e,e$'$p) measurements) Spectrometer C took data at a constant field, angle and polarity. The absolute target density in the (e,e$'$p) runs was then determined from the density in the elastic runs using the number of counts in Spectrometer C.

The analysis of the Helium elastic scattering data is discussed in the following sections, and the analysis of the Spectrometer C data is discussed in Section 4.3.

4.2.1 Measured Helium (e,e$'$) elastic cross sections

An elastic scattering measurement was performed for ^{3}He and ^{4}He at each of the 3 beam energies (540, 675, and 855 MeV). As with ^{12}C, the radiative-corrected experimental elastic cross sections were calculated using ALLFIT [31]. A sample excitation spectrum is shown in figure 4-10, with the fit results superimposed. Three distinct features are visible:

1. background from quasielastic scattering on the stainless steel target walls, fit with a function of the form $A_1 + A_2 \cdot \omega + A_3 \cdot \omega^2$ over the entire E_x range,

2. the ^{3}He elastic peak at $E_x = 0$, followed by a radiative tail, and

3. starting at about 5.5 MeV, a contribution from quasielastic scattering from ^{3}He, fit with a function of the form $f(E_x) = A_6 \cdot (E_x - A_5) + A_7 \cdot (E_x - A_5)^2$ for $E_x \geq A_5$. The fitted value of A_5 was approximately 5.5 MeV (= the binding energy of the first proton in ^{3}He).
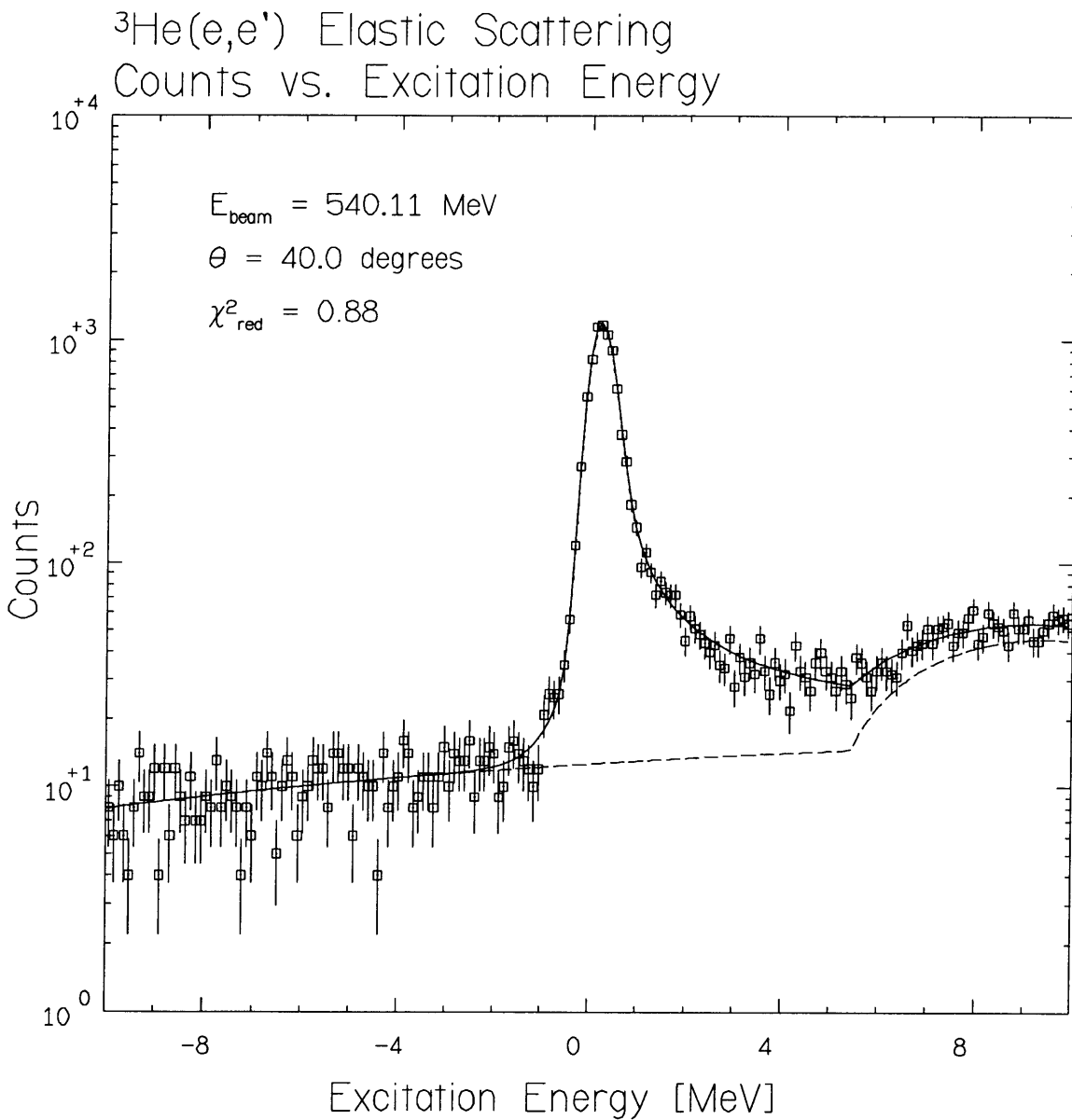
Figure 4-10: Counts vs. Excitation Energy for ^{3}He(e,e$'$) at E_{beam} = 540.11 MeV.

A similar elastic spectrum for ^{4}He is shown in the upper plot of Figure 4-11. Note that the contribution from quasielastic scattering from ^{4}He is not visible in this figure since it appears at higher excitation energy ($E_x = 19.8$ MeV). The data in the lower plot of Figure 4-11 are with a $\pm$ 1.0 cm cut on the reconstructed variable y_{tgt}, which removes the target walls. The counts at negative excitation energy are clearly removed, demonstrating that they are all due to scattering from the walls. We chose not to make a cut on y_{tgt} in the analysis since it would introduce an uncertainty in the target extent, and the contribution from the target walls is easily subtracted by fitting the full spectrum obtained without a cut on y_{tgt}.

For both ^{3}He and ^{4}He, ALLFIT fits the central elastic peak with an asymmetric hyper-gaussian convoluted with a theoretical radiative tail. The radiative-corrected cross section is then calculated from the sum of the counts in the de-convoluted peak times the integral of the theoretical radiative tail. The fit included additional empirical tails to the left and right of the main peak, which improved the appearance and χ^2 of the fit, and typically resulted in an increase in the extracted cross section of 0.5–3 %.

To account for external bremsstrahlung in both the target gas and the cell walls, ALLFIT treats the total target as a composite iron/helium target. This requires the total target thickness of the composite gas-wall system seen by the incident and scattered electron beam, as well as the isotopic abundance of each material. The density of the gas target is not known a priori, so an estimate of the gas density was first used to determine an experimental cross section. The cross section was then compared to the predicted cross section and a new gas density calculated. ALLFIT was then run again to generate a new experimental cross section. The procedure was iterated until the experimental and predicted cross sections differed by only a few percent, and the final value of the target density then determined by correcting the previous value for this small difference.

The total target thickness and isotopic abundance were calculated as follows:

$$d_{tot} = d_1 + d_2 \tag{4.8}$$
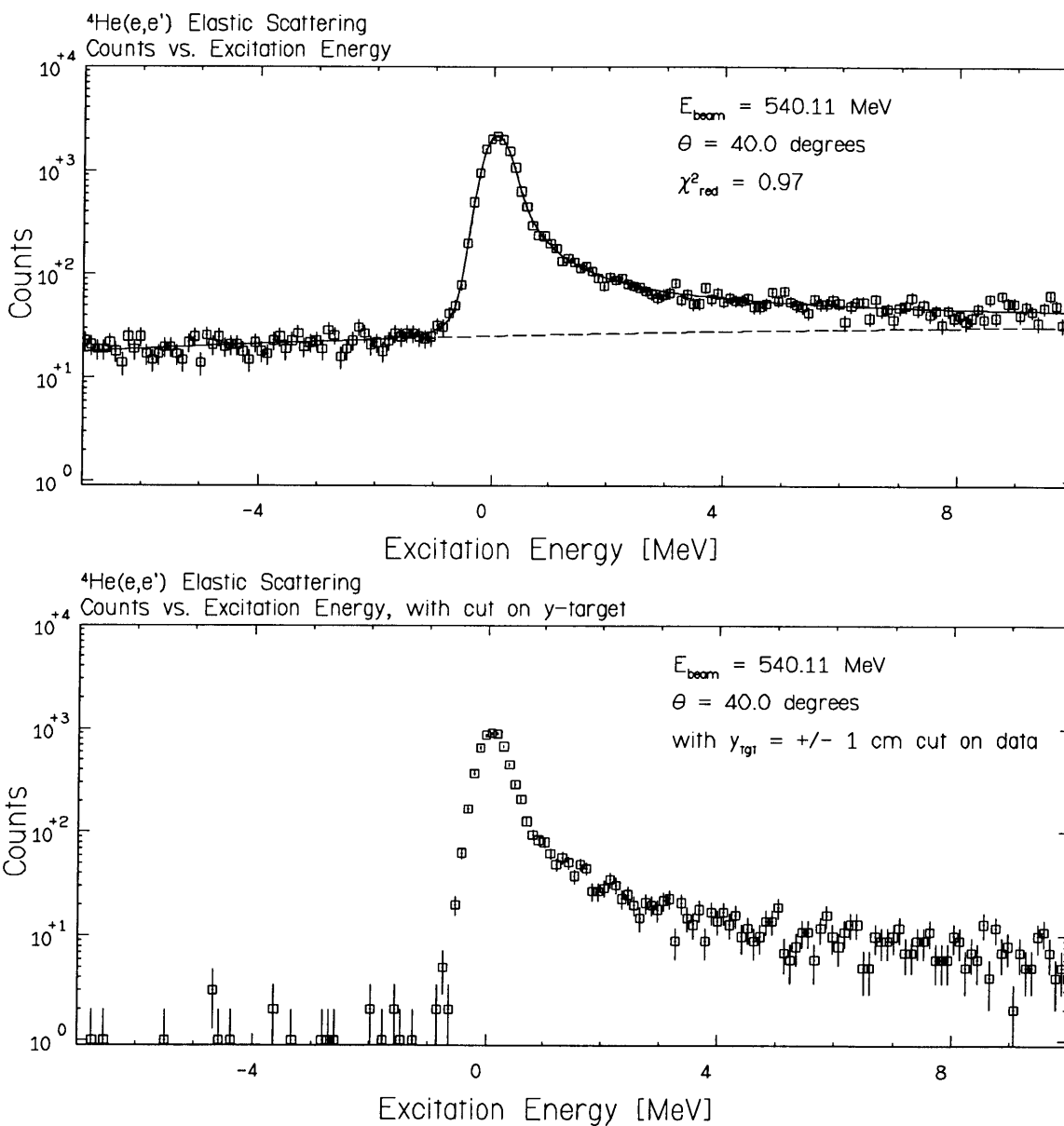
Figure 4-11: Counts vs. Excitation Energy for ^{4}He(e,e$'$) at E_{beam} = 540.11 MeV. The upper plot is the data and fit used to determine the elastic cross section. The data in the lower plot are with a cut applied on the reconstructed variable y_{tgt}, which removes the target walls.

$$w_i = \frac{d_i/A_i}{d_1/A_1 + d_2/A_2} \tag{4.9}$$

where w_i is the isotopic abundance (i.e. the number of atoms of a particular isotope as a fraction of the total atoms) of the ith isotope, and d_i and A_i are the thickness (gm/cm^2) and atomic mass (gm/mole) of the ith isotope, respectively. For each material, the thickness is the sum of that seen by the incident and scattered electron beam. For the target gas ($i = 1$), $d_1 = \rho_1 \cdot 8$ cm where ρ_1 is the gas density obtained as discussed in the above paragraph and 8 cm is the diameter of the spherical cell. For the target walls ($i = 2$), $d_2 = \rho_2 \cdot 165\mu$m, where 165μm is twice the estimated thickness of the target cell walls as described in Appendix D. The density and atomic mass of ^{56}Fe ($\rho_2 = 7.86$ gm/cm^3, A_2=55.847) were used for the stainless steel walls, since iron is the largest component in stainless steel. The external radiative correction also requires the atomic number (Z) of the target materials; for the stainless steel walls, the value for iron was used (Z=26).

Experimental cross sections were determined from the data as follows:

$$\frac{d\sigma}{d\Omega}^{exp} = \frac{N^c}{t \cdot d\Omega} \times \frac{eA}{QN_A\rho} \times \eta_{dt-pre} \tag{4.10}$$

where

N^c = number of counts in elastic peak, corrected for radiation by ALLFIT

e = 1.602×10^{-19}C

A = atomic mass of ^{3}He (^{4}He) = 3.016 (4.003) gm/mol

Q = accumulated charge [C]

N_A = 6.022×10^{23} mol^{-1}

ρ = target density [gm/cm^3]

η_{dt-pre} = dead-time and prescaling correction factor (see Appendix ?)

The product of the target thickness and solid angle, t·$d\Omega$ (in units of msr·cm), was calculated using the Monte Carlo AEEXB [32]:

$$t \cdot d\Omega = \frac{N_{\text{thru}}}{N_{\text{trials}}} \cdot \Delta z \cdot \Delta\Omega \qquad (4.11)$$

where

$$
\begin{aligned}
N_{\text{thru}} &= \text{ number of trials making it through the cuts} \\
N_{\text{trials}} &= \text{ total number of trials} \\
\Delta z &= \text{ target length} = 8 \text{ cm} \\
\Delta\Omega &= \text{ solid angle sampled over [msr]}
\end{aligned}
$$

The sampling solid angle $\Delta\Omega$ is chosen to be significantly larger than the real acceptance so that when the geometric constraints of the collimator (and any other software cuts) are applied the true solid angle is determined. The Monte Carlo approach is necessary because of the complicated geometry that arises from the combination of the extended target, the collimator and the software data cuts.

A summary of the various factors used in the calculation of the experimental cross sections is given in Table 4.8. The run numbers analyzed and the cuts placed on the data are given in Table 4.9. The software cuts on the date were generally defined to eliminate background that reconstructed well outside of the spectrometer acceptance, with the exception of two cuts:

1. the cut on ϕ_{tgt} in the 540 and 675 MeV kinematics, which was made smaller than the angular range defined by the collimator to restrict the solid angle of Spectrometer A to regions where it is well-understood (see Section 4.1), and

2. the cut on θ_{tgt} in the 855 MeV kinematics, which was made smaller than the angular range defined by Spectrometer B. This cut was necessary because the edge of the sieve slit in Spectrometer B obstructed the solid angle during most of the experiment, as discussed in Section 4.1.1.

		^{3}He			^{4}He		
E_{beam}	[MeV]	540.11	675.11	855.11	540.11	675.11	855.11
Spectrometer		A	A	B	A	A	B
θ^{scat}_{cent}	[deg]	40.00	35.00	-24.99	40.00	35.00	-24.99
$|\vec{q}_{cent}|$	[fm^{-1}]	1.836	2.020	1.853	1.836	2.020	1.853
software collimation^a		ϕ_{tgt}	ϕ_{tgt}	θ_{tgt}	ϕ_{tgt}	ϕ_{tgt}	θ_{tgt}
$t \cdot d\Omega$ (AEEXB)	[msr·cm]	142.67	144.99	38.260	142.78	145.93	38.271
σ_{AVG} (AEEXB)	[10^{-5} fm^2/sr]	1.558	0.9892^b	3.521	2.282	1.449	5.190
η_{dt-pre}		197.70	25.16	49.60	69.25	142.34	23.186
Q_{tot}	[mC]	5.715	10.061	25.772	3.277	6.373	11.229

Table 4.8: Parameters used in calculating the Helium target density from the elastic scattering measurements.

^{a}Indicates that the software cut on the specified angle was less than the value defined by the collimator, so that the solid angle is determined by the combined geometry of the software cut and the collimator.

^{b}Original aeexb result reduced by 1.5%. See section 4.2.2 for details.

The systematic error due to these cuts was investigated by analyzing the data with a series of ϕ_{tgt} and θ_{tgt} cuts of different sizes and is discussed in Section 4.2.3.

4.2.2 Predicted Helium (e,e$'$) elastic cross sections

Ottermann et al. [33] have measured and parameterized the elastic scattering cross sections for ^{3}He and ^{4}He over a momentum transfer range of 0.45–2.0 fm^{-1}. They write the total elastic cross section as

$$\frac{d\sigma}{d\Omega} \bigg/ \left(\frac{d\sigma}{d\Omega}\right)_{Mott} = \frac{F_c^2(q^2)}{\tau} + \left[\frac{1}{2\tau} + \tan^2\left(\tfrac{1}{2}\theta\right)\right] \frac{2\mu^2 F_m^2(q^2)q^2}{4m_p^2 Z^2} \tag{4.12}$$

$$\left(\frac{d\sigma}{d\Omega}\right)_{Mott} = \left(\frac{Z\alpha}{2E_1}\right)^2 \frac{\cos^2\left(\tfrac{1}{2}\theta\right)}{\sin^4\left(\tfrac{1}{2}\theta\right)} \frac{1}{1 + \dfrac{2E_1}{M}\sin^2\left(\tfrac{1}{2}\theta\right)} \tag{4.13}$$

where ($\mu = -2.12755, M = 2808.42$ MeV) for ^{3}He, ($\mu = 0, M = 3727.41$ MeV) for ^{4}He, $m_p = 938.28$ MeV (the mass of the proton), Z=2, and $\tau = 1 + q^2/(4M^2)$. E_1 is the beam energy, and

	E_{beam} [MeV]	Run Number(s)	θ_{tgt} [mrad]	ϕ_{tgt} [mrad]	y_{tgt} [cm]	z_{beam} [cm]	Density [mg/cm^3]
^{3}He	540.11	950622162640	±90	±75	±4.5	none	14.807
	675.11	950625015506	±90	±75	±4	none	11.511
	855.11	950703050505	±60	±40	none	±6	7.186
^{4}He	540.11	950629234552	±90	±75	±4.5	none	14.356
	675.11	950707143036	±90	±75	±4	none	20.889
	855.11	950703025106–31817[a]	±60	±40	none	±6	11.286

Table 4.9: Run numbers and software cuts used in the analysis of the Helium elastic scattering data, and the resulting measured gas densities.

[a]includes 3 consecutive runs combined: 950703025106, 950703030615, and 950703031817.

q^2 is the 4-momentum transfer squared[‡]. For ^{4}He, the magnetic form factor is zero (since it is a spin 0 nucleus) and the charge form factor parameterization is

$$F(q) = (1 - (a^2 q^2)^6)e^{-b^2 q^2}$$
(4.14)

with a=0.316 rm and b=0.675 fm. For ^{3}He, the charge and magnetic form factor are parameterized by

$$F(q) = e^{-Aq^2} - Bq^2 e^{-Cq^2}$$
(4.15)

with (A=0.462 fm^2, B=0.176 fm^2, C=0.812 fm^2) for the charge form factor and (A=0.48 fm^2, B=0.18 fm^2, and C=0.85 fm^2) for the magnetic form factor.

These formulae for the elastic scattering form factors and total cross section were put into the Monte Carlo code AEEXB [32]. The code was then used to average the cross sections over the experimental acceptance, including the geometry of the extended target, beam rastering, collimator, and software cuts. The mean energy loss of the incident beam in the target gas

---

[‡]An ambiguity in the Ottermann paper was whether q^2 referred to the 3- or 4-momentum transfer squared. We assumed the latter, since it yields cross sections that are more consistent with the Amroun [34] parameterization. If we assume that q^2 instead corresponds to the 3-momentum transfer squared, the predicted ^{3}He elastic cross sections decrease by 1.3–1.8% at the central kinematics.

and target walls was also accounted for. The q_{eff} formalism[35] was used in AEEXB to modify the sampled momentum transfer to account for Coulomb distortion, which resulted in an approximately 2.7% (1.7%) reduction in the predicted cross section at the lowest (highest) beam energy. This average cross section obtained from AEEXB was then directly compared to the experimental cross section to determine the experimental target density.

For ^{3}He, a more recent and complete parameterization to higher q^2 has been published by Amroun *et al.* [34][§]. We compared this to the Ottermann result by calculating the cross section at the central scattering angle (i.e. no acceptance averaging was done) with both the Ottermann and Amroun parameterizations. For the 540 and 855 MeV beam energies, the difference in the cross section was 0.5% or less. For 675 MeV, the Amroun parameterization yields a cross section 1.5% less than that calculated from the Ottermann parameterization. Since the 675 MeV measurement has a central 4-momentum transfer of $q^2 = 4.06$ fm^{-2}, which is just beyond the q^2 range of the Ottermann data, the Amroun result is more reliable. We incorporated the Amroun result by decreasing the cross section calculated by AEEXB (which uses the Ottermann parameterization) by 1.5% for the 675 MeV setting.

[§]Tripp [36] points out an error in the formula for the sum-of-gaussians form-factor parametrization given by Amroun - the factor $\frac{1}{2}$ in the exponent should be $\frac{1}{4}$.

E_{beam}		^{3}He			^{4}He		
	[MeV]	540.11	675.11	855.11	540.11	675.11	855.11
total charge	[%]	2.4	1.7	2.0	1.7	1.6	2.4
ALLFIT (stat.+fit)	[%]	1.2	0.5	0.6	0.9	1.0	0.5
beam energy ($\pm$160 keV)	[%]	0.2	0.2	0.2	0.2	0.2	0.2
central spect. angle ($\pm$0.1 mrad)	[%]	0.1	0.2	0.2	0.1	0.2	0.2
target position ($\pm$1 mm)	[%]	1.4	1.6	0.3	1.4	1.7	0.3
horiz. beam position ($\pm$1 mm)	[%]	1.7	2.3	0.6	1.7	2.3	0.6
solid angle	[%]	0.6	0.6	0.4	0.6	0.6	0.4
dead time	[%]	1	1	1	1	1	1
knowledge of F_C, F_M	[%]	2.4	3.3	2.4	2.4	3.3	2.4
total	[%]	4.4	4.8	3.4	4.0	4.9	3.7

Table 4.10: Estimated uncertainty in the target density measured from the Helium elastic scattering runs.

4.2.3   Total Error in the Measurement of the Helium Target Density

The total estimated uncertainty for the Helium elastic scattering measurements is summarized in Table 4.10. Each of the individual uncertainties is discussed in detail below. The total uncertainty is the sum of the individual uncertainties, added in quadrature, and is given for each kinematics in the final row of the table.

The systematic uncertainty in the total charge is the uncertainty in the value read out from the photoeffect monitor and the uncertainty in its calibration against the Förster probe at high current, added together in quadrature. The error from ALLFIT includes the statistical error and a small systematic contribution from the fitting procedure. The effect of uncertainty due to systematic shifts in beam energy was estimated by taking the difference in the cross section calculated (based on the Ottermann form factors discussed below) at (E_{beam}, θ_e) and at $(E_{beam} \pm \delta E, \theta_e)$. The uncertainties due to shifts in the central spectrometer angle, and target and beam location were calculated in a similar manner. The effect of the shifts is very similar in ^{3}He and ^{4}He. The sensitivity to beam and target position is reduced in the 855 MeV kinematics since they were measured with Spectrometer B, compared to the 540 and 675 kinematics which were measured with Spectrometer A. Compared to Spectrometer A, Spectrometer B has a

longer drift distance from target to collimator so that changes in target and beam position have a reduced effect on the scattering angle.

The experimental solid angle was determined by the combined geometry of the beam, the collimator and the software cuts. Its uncertainty was determined by analyzing the data with several different values of the software cuts, as shown in Tables 4.11 and 4.12 for Spectrometers A and B, respectively. Ideally the measured density of the target gas is independent of the cuts, so that the variation in the measured density provided an estimate of the uncertainty in the solid angle. As shown in Tables 4.11 and 4.12, the maximum change observed in the measured density was 0.6% in Spectrometer A and 0.4% in Spectrometer B.

The uncertainty in the form factors F_C and F_M is not as straightforward. For the form factor parameterizations used in this experiment, Ottermann *et al.* quote an overall normalization uncertainty of 0.65% and a systematic uncertainty of 0.7%. They also quote total errors on their individual measurements of F_C and F_M at particular values of q^2, but do not give an uncertainty in their form-factor parameterizations, which were obtained by fitting to all the data. It is therefore difficult to estimate the uncertainty in using their parameterization to calculate F_C and F_M at our values of q^2. For ^{3}He, Amroun *et al.* give a graph of the total systematic and statistical uncertainty in their form factor parameterization as a function of q^2, which gives $\delta F_C = \delta F_M \approx 2 \times 10^{-3}$ at $q^2 = 4$ fm^{-2}. Since the Amroun and Ottermann parametrizations gave similar results for the cross section at our kinematics (except for the small difference at $E_{beam} = 675$ MeV, where we rescaled the results to be consistent with Amroun) and the the Amroun parametrization includes the data from Ottermann, we have used this uncertainty. At our kinematics, this yields uncertainties of $\delta F_C/F_C = 1.1$ %, $\delta F_M/F_M = 1.2$ % at $q^2 = 3.42$ fm^{-2} and $\delta F_C/F_C = 1.6$ %, $\delta F_M/F_M = 1.5$ % at $q^2 = 4.05$ fm^{-2}. The uncertainty $\delta F_M/F_M$ has a negligible effect and can be discarded since the the charge term $\frac{F_C^2(q^2)}{\tau}$ accounts for > 90% of the cross section at all three of our kinematics. The uncertainty in the elastic cross section is therefore $\delta\sigma/\sigma \approx 2 \times \delta F_C/F_C$.

For ^{4}He, the magnetic form factor is zero so that only the charge form factor F_C contributes to the cross section. The fractional uncertainty in the charge form factor, $\delta F_C/F_C$, was as-

ϕ_{tgt} cut [mrad]	σ_{AVG} (AEEXB) [10^{-6} fm^2/sr]	$t \cdot d\Omega$ (AEEXB) [msr·cm]	density [mg/cm^3]	change [%]
±75	22.82	142.78	14.36	-
±70	22.46	136.91	14.32	-0.3
±65	22.09	130.35	14.37	+0.1
±60	21.73	123.15	14.28	-0.6
±55	21.37	115.26	14.29	-0.5

Table 4.11: Density of the ^{4}He target gas measured in the $E_{beam} = 540$ MeV elastic scattering run with Spectrometer A, for various cuts on ϕ_{tgt}.

θ_{tgt} cut [mrad]	σ_{AVG} (AEEXB) [10^{-6} fm^2/sr]	$t \cdot d\Omega$ (AEEXB) [msr·cm]	density [mg/cm^3]	change [%]
±60	51.90	38.27	11.29	-
±55	52.14	35.07	11.30	+0.1
±50	52.37	31.87	11.33	+0.4
±45	52.58	28.68	11.30	+0.1

Table 4.12: Density of the ^{4}He target gas measured in the $E_{beam} = 855$ MeV elastic scattering run with Spectrometer B, for various cuts on θ_{tgt}.

sumed to be the same as determined above for ^{3}He. The reasoning is that the ^{4}He form-factor parameterization that we used is from the same experiment (Ottermann et $al.$) as the ^{3}He parameterization, so that the overall systematic errors are similar. Also, the statistical errors in their measurements of F_C are similar in ^{3}He and ^{4}He in our region of q^2. One possible discrepancy is that our $E_{beam} = 675$ MeV kinematics is just outside their q^2 range. In the case of ^{3}He, the Amroun parameterization (which extends to higher q^2) was used to correct the cross section by 1.5%. A similar procedure is not possible for ^{4}He since the Amroun parameterization is for ^{3}He only. However, since the ^{4}He form factor has a simpler functional dependence (the fit has only two parameters compared to three for ^{3}He), the error in the cross section due to the extrapolation should be less than 1.5%.

4.3   Target Density Measurement with Spectrometer C

4.3.1   Overview

The density of the Helium target gas is needed to determine absolute cross sections. In the previous section, it was shown how the target density in the elastic scattering runs was determined by comparing the measured results to published cross sections. That density corresponds to the average density of the target gas over the time that the elastic scattering measurements were performed. The density at other times was determined from the counts measured in Spectrometer C, as explained below.

4.3.2   Technique

Throughout the experiment (i.e. in both the elastic scattering and (e,e'p) measurements), Spectrometer C took data at a fixed momentum ($p = 340 \pm 40$ MeV/c), angle (120°, on the right side of the beam line when looking downstream) and polarity (negative). It therefore constantly measured negatively charged particles with a fixed angle and momentum. The number of particles, N_1^t, that scattered from the Helium target gas and entered the spectrometer in a particular run period can be written as

$$N_1^t = \frac{Q_1}{e} \frac{\rho_1 N_A}{A} \cdot \int \frac{d^3\sigma}{d\Omega dp}(E_i, p, \theta) d\Omega dp dz \qquad (4.16)$$

where $\frac{d^3\sigma}{d\Omega dp}$ is the scattering cross section, which in general can be written as a function of the incident beam energy (E_i), scattered momentum (p) and the scattering angle (θ). The variable z is the coordinate along the beam line, and the limits of the integral are the experimental acceptance. The subscript '1' indicates run period 1, and the superscript 't' indicates that the

particles are scattered from the target gas. The constants in the above equation are

$$
\begin{aligned}
Q_1 &= \text{accumulated charge [C]} \\
e &= 1.602 \times 10^{-19} \text{C} \\
N_A &= 6.022 \times 10^{23} \text{ mol}^{-1} \\
\rho_1 &= \text{target density [gm/cm}^3]
\end{aligned}
$$

The number of particles in a second run period can similarly be written as

$$
N_2^t = \frac{Q_2}{e} \frac{\rho_2 N_A}{A} \cdot \int \frac{d^3\sigma}{d\Omega dp}(E_i, p, \theta) d\Omega dp dz \tag{4.17}
$$

If the beam energy in run period 2 is the same as in period 1, then the integral is equal for the two periods, since both the cross section and the limits of the integral are constant. The integral therefore cancels out in the ratio of N_1^t and N_2^t:

$$
\frac{N_1^t}{N_2^t} = (Q_1 \rho_1)/(Q_2 \rho_2) \tag{4.18}
$$

Solving for ρ_2 yields

$$
\rho_2 = \rho_1 \left(\frac{Q_1}{Q_2} \cdot \frac{N_2^t}{N_1^t} \right) \tag{4.19}
$$

Therefore if run period 1 is the elastic run, where the target density (ρ_1) has been measured, the target density (ρ_2) for a second run at the same beam energy can be determined using N_1^t, N_2^t, and the total charge (Q_1 and Q_2) collected in each run.

4.3.3   Determination of N_i^t

To determine the density of the Helium target as outlined above, we require the number of particles N_i^t that scatter from the Helium gas and enter Spectrometer C in run period i. We

define N_i as the number of events measured in Spectrometer C in run period i. N_i^t was obtained from N_i by applying corrections for dead time, prescaling, and cosmic-ray and empty-target background as described below.

First, a run was performed with the beam off, acquiring N_{cos} cosmic ray events in Spectrometer C in time t_{cos}. The number of counts measured in run period i corrected for dead time, prescaling and cosmic-ray background was then calculated from

$$N_i' = N_i \eta_i - N_{cos} \eta_{cos} \cdot \frac{t_i}{t_{cos}} \tag{4.20}$$

where N_i is the number of counts measured in run period i, t_i is the length of the run period in seconds, and the η's are the dead-time/prescaling correction factors.

Next, a run was performed with the target empty, with the beam on, and at at the same beam energy used in run period 1. The number of counts in this empty target run was corrected for prescaling, dead time, and cosmic-ray background, yielding

$$N_{emp}' = N_{emp} \eta_{emp} - N_{cos} \eta_{cos} \cdot \frac{t_{emp}}{t_{cos}} \tag{4.21}$$

which reflects the number of counts due to the target walls and to any other background proportional to the beam current.

Finally, the number of counts in run period 1 due to just the target gas was calculated by correcting N_i' for the empty target contribution:

$$N_i^t = N_i' - N_{emp}' \cdot \frac{Q_i}{Q_{emp}} \tag{4.22}$$

where Q_i and Q_{emp} are the total charge collected in run period 1 and in the empty target run, respectively.

An analogous set of equations determined the background-corrected number of counts, N_2^t, in run period 2.

quantity		lower value	upper value
Cerenkov	[ADC channels]	200	2000
momentum	[MeV/c]	300	380
ϕ_{tg}	[rad]	-0.120	0.120
θ_{tg}	[rad]	-0.080	0.080
y_{tg}	[m]	-0.050	0.050

Table 4.13: Software cuts on Spectrometer C.

4.3.4   Background Suppression

In the above analysis, the data taken with the empty target runs and the cosmic ray run provide an estimate of the background contributions to the counts at all other times. This assumes that the backgrounds are constant over all time. In Spectrometer C, the raw trigger rate was seen to vary depending on the beam tune, indicating that some of the background was not constant. It is therefore necessary to apply cuts to the data to suppress the background and to ensure that the vast majority of the measured counts correspond to particles that scatter from the Helium target gas. With the cuts applied, the empty-target and cosmic-ray contributions are kept small, so that any fluctuation in the background should introduce a small systematic uncertainty in the final result.

The final cuts used for Spectrometer C are given in Table 4.13. The Cerenkov ADC is the sum of the individual ADCs corresponding to a single phototube in the Cerenkov counter, and the cut on the ADC ensures that the measured particles are all electrons. Cuts are also placed on the coordinates $(\phi_{tg}, \theta_{tg}, y_{tg})$, which are the reconstructed coordinates of the particle at the target as defined in Figure 4-1. High-precision reconstruction of the particle coordinates for Spectrometer C was not necessary for these measurements, and the reconstruction matrix (obtained from Ref. [37]) used was very preliminary.

The cuts were chosen such that the cosmic-ray and empty-target backgrounds were small. A sample of the results is shown in Table 4.14, which shows (for three different run periods) the number of counts in Spectrometer C before and after the various corrections. The correction

run number	I_{avg} $[\mu A]$	N_i	$\eta_i N_i$	N'_i	N^t_i
950703042231	5	2410	7410	7395	7326
950703044032	10	3443	21182	21166	20953
950703050505	15	4648	42483	42453	42029

Table 4.14: The number of counts in Spectrometer C before and after the various corrections (see text for details).

for cosmic ray background is 0.2% or less in all cases, so that $N'_i \approx \eta_i N_i$. Additionally, the correction for empty-target background is approximately 1% in all cases, so that $N^t_i \approx N'_i$. With these small background corrections, we therefore have $N^t_i \approx \eta_i N_i$. The value of N^t_i determined from the data is therefore insensitive to small changes in the cosmic-ray and empty-target background.

4.3.5 Statistical Uncertainty

Since the empty-target and cosmic-ray background corrections are small, their contribution to the statistical uncertainty can be discarded. Since $N^t_i \approx N_i \eta_i$, the statistical uncertainty in N^t_i can be estimated from

$$\left(\frac{\delta N^t_i}{N^t_i}\right) \approx \left(\frac{\delta N_i}{N_i}\right) = \frac{1}{\sqrt{N_i}} \qquad (4.23)$$

Chapter 5

The (e,e′p) Analysis

Overview

In this chapter the major elements of the (e,e′p) analysis are presented and discussed. An overview of the (e,e′p) analysis is given in Figure 5-1. The data analysis code ESPACE [38] was used to analyze the raw data, producing histograms of the measured counts after various cuts for background suppression and subtraction. The Monte Carlo code AEEXB [32] was used to calculate the corresponding detection volume histograms, which were then combined with the ESPACE output to produce cross sections. Radiative corrections were applied by radiatively-unfolding the cross sections with RADCOR [39]. In a second technique (not shown in Figure 5-1), radiative effects were applied to a theoretical model of the (e,e′p) cross section in a Monte Carlo simulation of the experiment. The output of the simulation was then compared to the measured spectrum to study the radiative effects in regions where radiative unfolding could not be accurately performed.

The main steps in this analysis are discussed in detail in the following sections.

5.1 Coincidence Timing

The coincidence timing is the relative time between the arrival of particles in each of the two spectrometers. The time was measured by two TDCs (time-to-digital converters) that had a relative delay of 54.65 nsec (1093 channels) between them. Two TDCs were used to provide a larger timing range, which was required by the range in proton momenta used in the experiment.

```
┌─────────────────────────────────────┐          ┌─────────────────────────────────────┐
│              AEEXB                   │          │              ESPACE                 │
│                                     │          │                                     │
│  - random sampling of particle coords.│          │  - timing cut, particle i.d.        │
│  - cuts and geometric constraints    │          │  - vertex reconstruction            │
│  - histogramming (weight options)    │          │  - cuts to reconstructed coordinates │
│                                     │          │  - histogramming                    │
└─────────────────────────────────────┘          └─────────────────────────────────────┘
```

foreground yield

detection volume   background yield

```
                    ┌─────────────────────────┐
                    │        HISTMAN          │
                    │  (subtraction, division)│
                    └─────────────────────────┘
```

accidental-corrected cross section

```
                    ┌─────────────────────────┐
                    │        RADCOR           │
                    │  (radiative corrections)│
                    └─────────────────────────┘
```

radiative-corrected cross section

```
                    ┌─────────────────────────┐
                    │        HISTMAN          │
                    │        +others          │
                    │ (normalization, projection, slicing)│
                    └─────────────────────────┘
```

normalized cross section

```
                    ┌─────────────────────────┐
                    │      MPLOT, PAW         │
                    │       (plotting)        │
                    └─────────────────────────┘
```

Figure 5-1: An overview of the (e,e'p) data analysis.

Both TDCs were combined into a single spectrum by accounting for the delay between them.

The TDC start was provided by the electron arm (Spectrometer A) and the stop provided by the proton arm (Spectrometer B). The raw timing signal was corrected in ESPACE for several factors which broaden it: 1.) a hardware offset in the TDC start or stop depending on which scintillator paddle triggered it, 2.) the time required for the light created in the scintillator to reach the phototube, which depends on where the particle struck along the paddle, and 3.) variations in the time-of-flight of the detected particle for different momenta and different paths through the spectrometer. The paddle offsets and time-of-flight corrections were individually optimized at each kinematics using ESPACE. A sample spectrum (taken at the 540/585 kinematics) of the coincidence timing before and after these corrections is shown in Figure 5-2. For the $p_p = 660$ and 585 MeV/c kinematics, the signal-to-noise ratio was very large before and after the corrections, and the FWHM of the peak after corrections was approximately 1 ns (20 channels).

The timing also varies with the pulse height (which varies with the energy deposited) in the scintillator, which is accounted for in the paddle offsets: the scintillators are segmented along x_{fp}, so that at a fixed central momentum each paddle corresponds to a narrow range of momenta and therefore an (approximately) constant pulse height. An exception to this is when a particle crosses near a gap and strikes two scintillator paddles, so that the pulse height in either paddle is reduced and a shift in the coincidence timing is observed. The result is an asymmetric broadening at the base of the corrected coincidence timing peak. These events are allowed for by using a wide coincidence timing cut in the analysis, which ensures the inclusion of the events.

In the data analysis, a timing cut of width t_1 centered on the coincidence peak defined the "foreground" yield, N_1. Two cuts, each in the flat region on either side of the peak and of total width t_2, defined the "background" yield, N_2. The accidental-corrected yield was then determined from

$$N = N_1 - \frac{t_1}{t_2} N_2 \qquad (5.1)$$

Coincidence Time Spectrum (uncorrected)
^{3}He(e,e'p) : 540/585 kinematics

Coincidence Time Spectrum (corrected)
^{3}He(e,e'p) : 540/585 kinematics
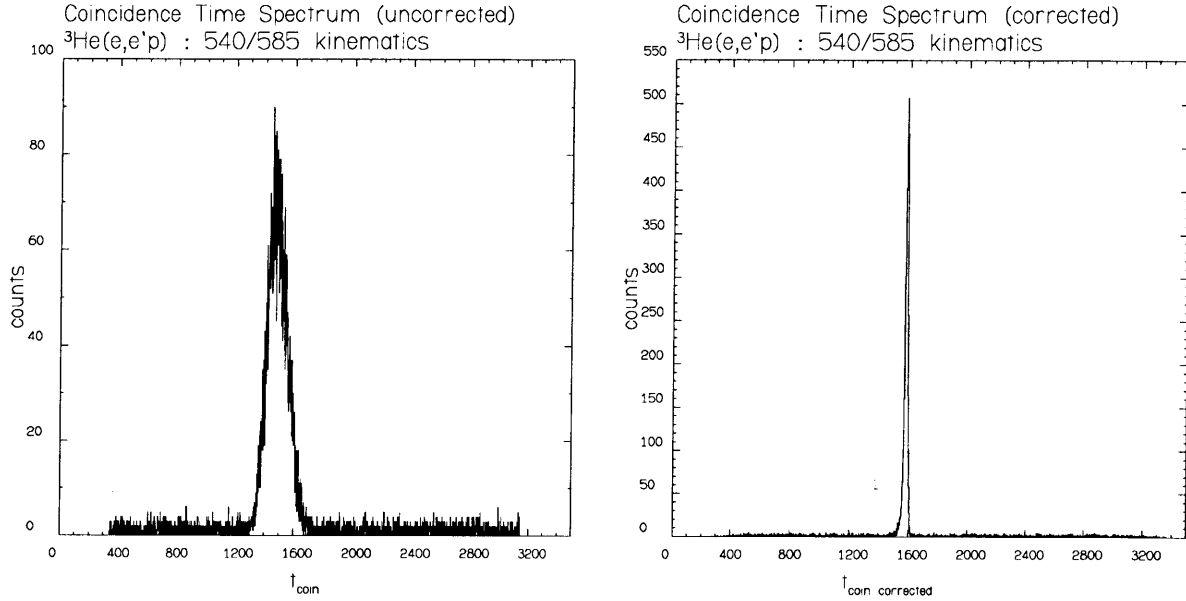
Figure 5-2: Coincidence timing before and after corrections. Data are for ^{3}He(e,e′p) at the 540/585 kinematics. The horizontal scale is in TDC channels, with 1 channel = 50 picoseconds $(10^{-9}$ s). The cuts placed on the data are those given in section 5.4. The FWHM of the corrected peak is 1.0 nsec.

where the second term corrects for the random coincidences that fall inside the foreground timing cut. In the remainder of the thesis, the phrase "corrected for accidentals" refers to spectra that have been corrected according to Equation 5.1.

5.2   Particle Identification

To ensure that the events we histogram were indeed (e,e′p) events, the particle identification was checked in each of the spectrometers.

In the electron spectrometer (Spectrometer A), pions were distinguished from electrons by the Cherenkov detector, which uses Freon as a radiator gas. The threshold for production of Cherenkov light in the Freon gas is 10 MeV for electrons and 2.7 GeV for pions [19]. Any signal in the Cherenkov ADCs was therefore taken as a valid electron.

For the proton spectrometer (Spectrometer B), the vast majority of the particles detected in coincidence were protons. This was deduced from the observation that the energy deposited in

the scintillators is the same for the vast majority of the particles, and that they also reconstruct to the expected missing energy spectrum. Nevertheless, some pion and deuterons are detected in the proton spectrometer in coincidence with the electron arm, and can be identified in the scintillator ADC spectra.

An ADC on each phototube provided a measure of the energy deposited in the scintillator. The ADC value was corrected for light attenuation depending on where the particle struck on a particular paddle, and a further empirical amplitude correction was applied to compensate for any gain mismatch between phototubes, so that a given particle passing through the scintillator results in approximately the same corrected ADC value regardless of which scintillator paddle it passed through. A plot of the ADC values in the two scintillator layers is shown in Figure 5-3 for ^{4}He(e,e'p) at the 855/585 kinematics. The x-axis is the energy deposited in the bottom scintillator layer (dE) and the y-axis is the energy deposited in the top layer (TOF). From the 1-dimensional projections it is apparent that the majority of the data fall in the central proton peak.

In addition to the central proton peak, a number of other distinct regions are visible in the scatter plot:

1. A horizontal and a vertical band extending from the central proton peak. These are due to the particle passing near the gap between two scintillator segments, so that the energy deposited in a single segment is reduced (we only consider the segment that fired first). These are valid (e,e'p) events and should not be discarded.

2. A deuteron region, appearing at high dE and high TOF values. A few of the deuterons are true coincidences, and appear as a small peak in the coincidence timing spectrum approximately 65 nsec later than the proton peak, consistent with their longer time-of-flight through the spectrometer. The remainder of the deuterons are random coincidences. The coincidence timing cuts for the (e,e'p) analysis were made such that they avoid the deuteron peak, so that after correction for accidental coincidences we have excluded the real coincident deuterons and corrected for the random ones as demonstrated in Figure 5-4.
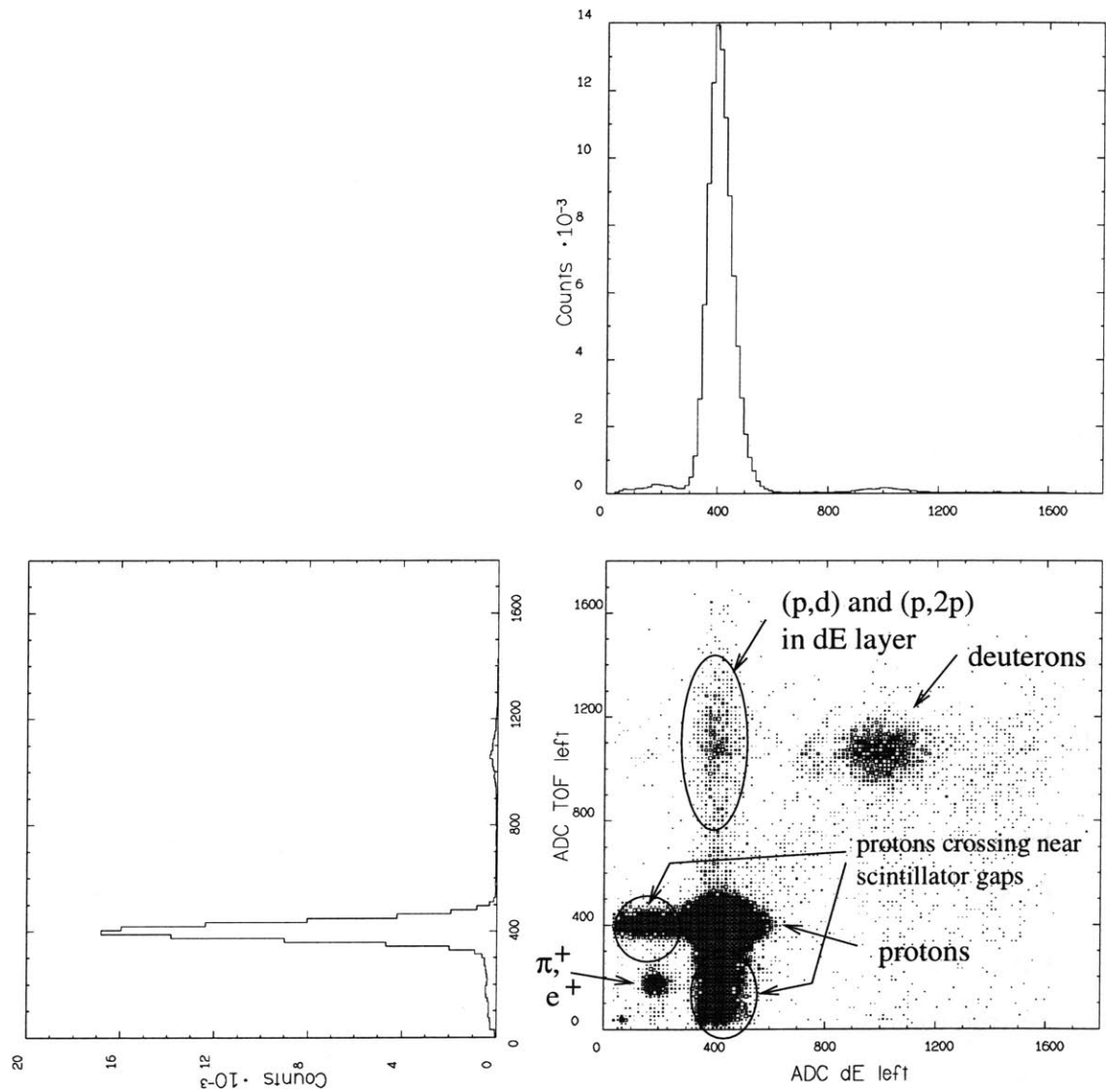
Figure 5-3: A scatter plot and 1-dimensional projections of the energy deposited in the TOF and dE scintillators in the proton spectrometer, for ^{4}He(e,e'p) events at the 855/585 kinematics with acceptance cuts (see section 5.4) applied. See text for discussion.

3. A region that appears as protons in dE but as deuterons in TOF. We assume that these events are due to (p,d) and (p,2p) reactions in the dE scintillator, and are therefore valid (e,e′p) events that should not be discarded.

4. A region at low dE and low TOF, due to pions and/or positrons. These are predominantly random coincidences, and are removed by the accidental subtraction as demonstrated in Figure 5-5.

All backgrounds were either excluded by the TDC cut or corrected for in the coincidence timing background subtraction, as demonstrated in the 1-dimensional projections of the scintillator ADC spectra in Figures 5-4 and 5-5. After correction for accidental coincidences, only the proton peak remained in the spectra. Therefore no cuts to the scintillator ADCs were required in the analysis.

Energy deposited in dE Scintillator
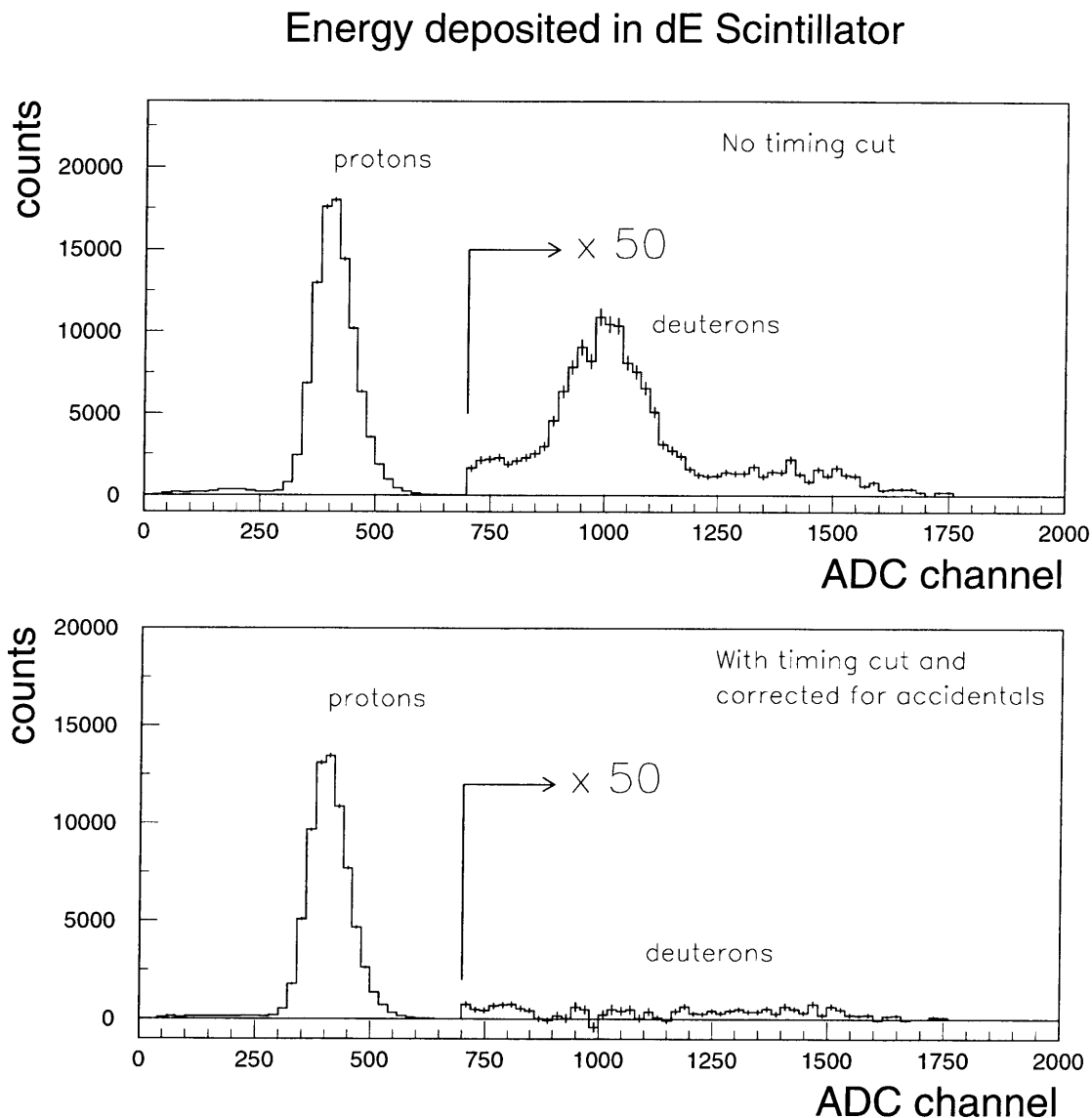
Figure 5-4: ADC spectra for the dE scintillator for coincidence ^{4}He(e,e′p) events at E_{beam} = 855 MeV and p_p = 585 MeV/c with acceptance cuts (see section 5.4) applied. The top plot is before the coincidence timing cut and accidental subtraction, and the bottom plot is after. The deuteron events visible in the top plot are clearly removed after the coincidence timing cut and correction for accidental coincidences.
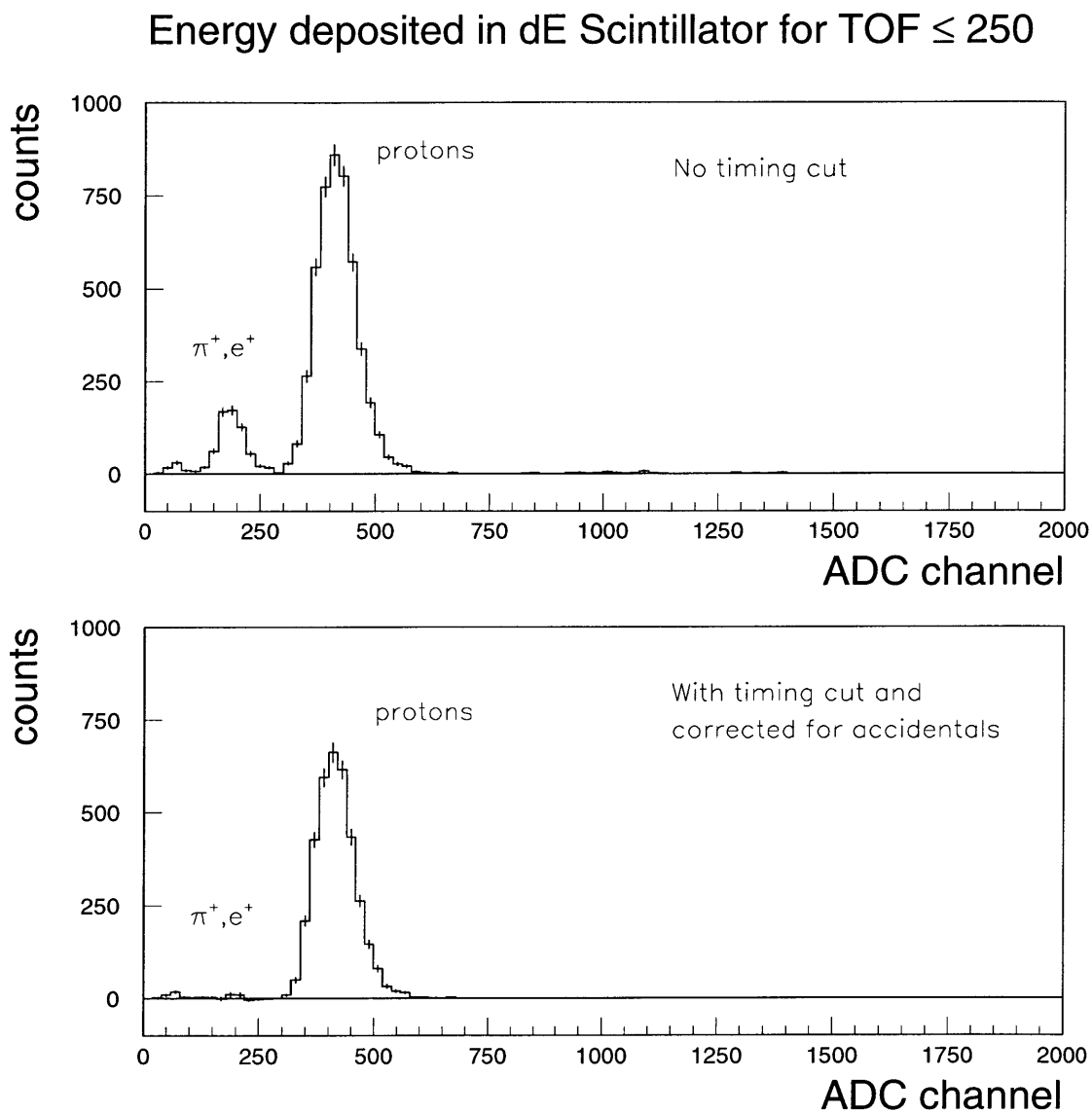
Figure 5-5: ADC spectra for the dE scintillator for coincidence events as in figure 5-4, but with an additional cut on the TOF ADC to study the minimum ionizing region. The pion/positron peak visible in the top plot is cleanly removed after the coincidence timing cut and correction for accidental coincidences.

5.3 Missing Energy Spectra

An example of the accidental-corrected ^{3}He(e,e'p) missing energy spectrum is shown in Figure 5-6 for data measured in the 855/660 kinematics. The 2-body ^{3}He(e,e'p)^{2}H (E_m = 5.49 MeV) and 3-body ^{3}He(e,e'p)np ($E_m \geq$ 7.72 MeV) breakup reaction channels are cleanly resolved, and there is very little background at missing energies below the 2-body breakup peak. Similar spectra for ^{4}He are shown in Figure 5-7, where the onset of the 3-body breakup channel ^{4}He(e,e'p)^{2}Hp at E_m = 26.07 MeV is only barely visible on top of the large radiative tail. The features of the ^{3}He and ^{4}He missing energy spectra are discussed in more detail in Chapter 6.

To improve the experimental missing energy resolution, small changes were made to the standard values of the matrix elements $\langle\theta|\delta\rangle$ (Spectrometers A and B) and $\langle\theta^2|\delta\rangle$ (Spectrometer A only). At each of the (e,e'p) kinematic settings, the values of the matrix elements were chosen to minimize the width of the 2-body breakup peak. A sample spectrum in Figure 5-8 shows the effect of these small corrections in Spectrometer A, where the corrections were largest.

In the missing energy spectra shown in Figures 5-6 and 5-7, several software cuts were placed on the momenta and reconstructed coordinates of the detected particles. These software cuts were a standard set used in the (e,e'p) analysis, and are discussed in the following section.
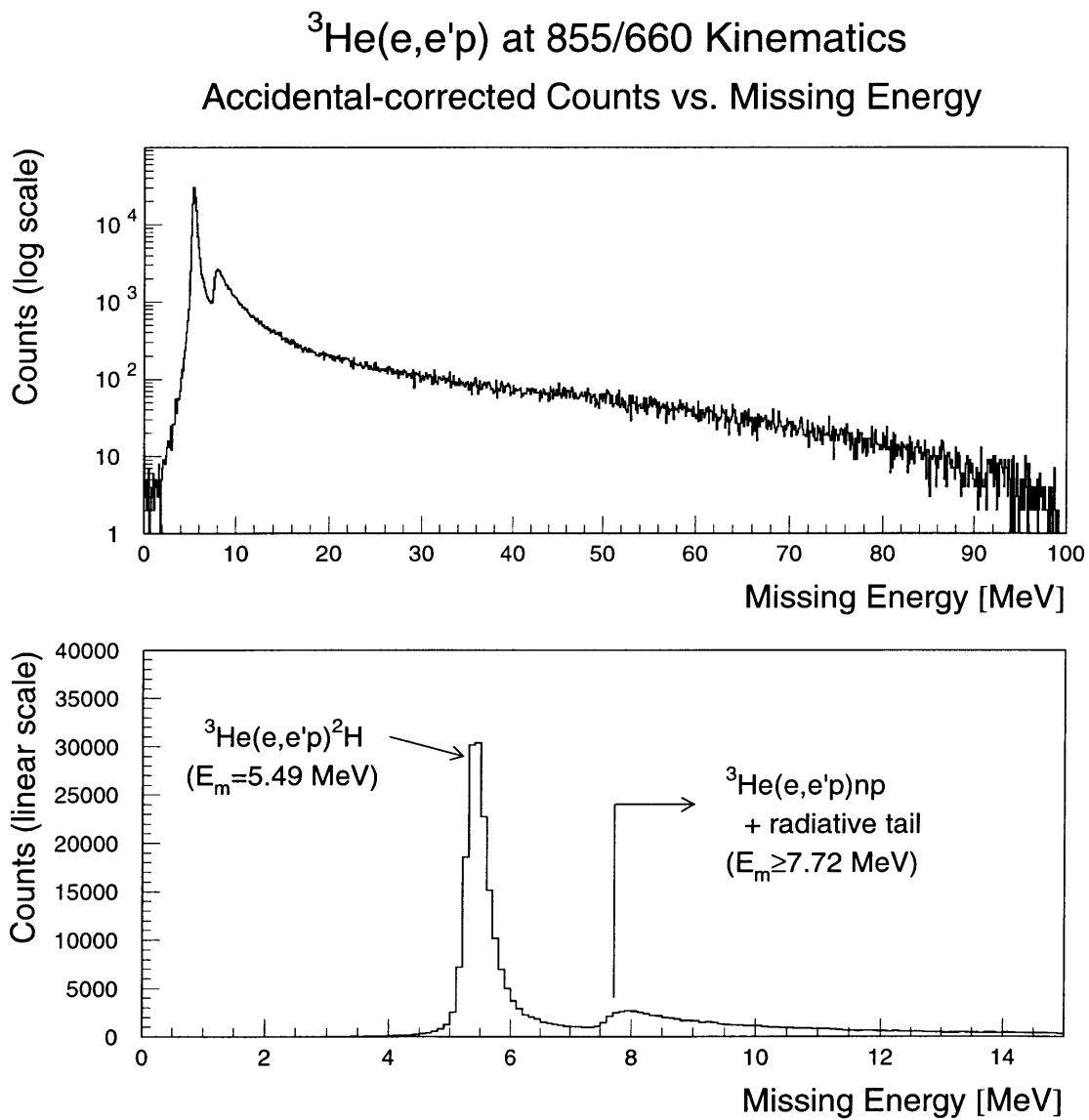
Figure 5-6: Sample missing energy spectrum for ^{3}He(e,e$'$p) after all software cuts and accidental subtraction.
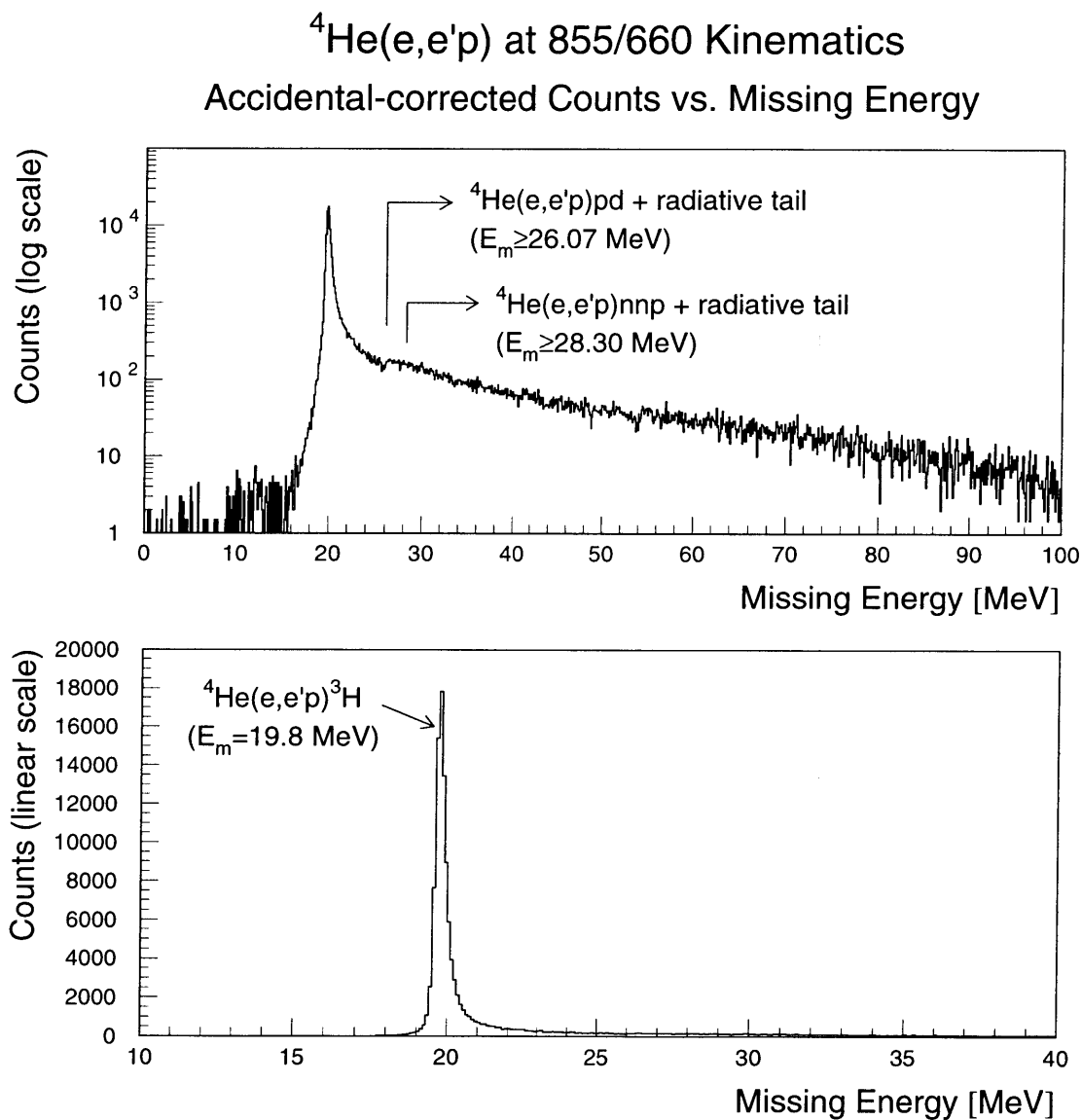
Figure 5-7: Sample missing energy spectrum for ^{4}He(e,e'p) after all software cuts and accidental subtraction.
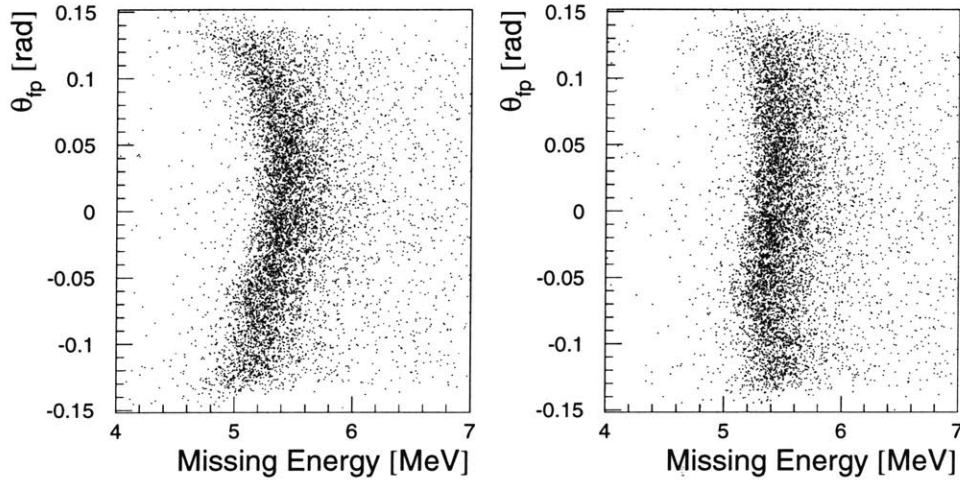
Figure 5-8: The dispersive angle (θ_{fp}) in the focal plane of Spectrometer A vs. missing energy, for ^{3}He(e,e′p) measured in the 855/660 kinematics. The left plot is using the standard matrix elements and the right is after small corrections to $\langle\theta|\delta\rangle$ and $\langle\theta^2|\delta\rangle$.

5.4 Spectrometer Reconstruction and Software Cuts

The coordinates of each particle were reconstructed in ESPACE, which used a standard set of matrix elements for Spectrometers A and B (the '495 MeV long-target' set, determined by Ref. [26]) to transform the position and angles of the particle measured in the wire chambers to the momentum of the detected particle and to its coordinates $(\theta_{tgt}, \phi_{tgt}, y_{tgt})$ at the target. The coordinates $(\theta_{tgt}, \phi_{tgt}, y_{tgt})$ of the particle at the target are in the spectrometer transport system, as defined in Figure 4-1 in Chapter 4. By combining the reconstructed value of y_{tgt} with the beam rastering information, ESPACE also reconstructs the position z_{react} of the particle along the beam line in the beam coordinate system (also defined in Figure 4-1).

The reconstruction of the angles θ_{tgt} and ϕ_{tgt} was verified at a single field setting (corresponding to a central momentum of approximately 415 MeV/c) for Spectrometers A and B with measurements of elastic scattering from ^{12}C using a sieve slit collimator in each spectrometer. A sample spectrum for Spectrometer A is shown in Figure 5-9. The intersections of the solid lines in the figure mark the locations of the hole in the sieve slit, and the scattered points are
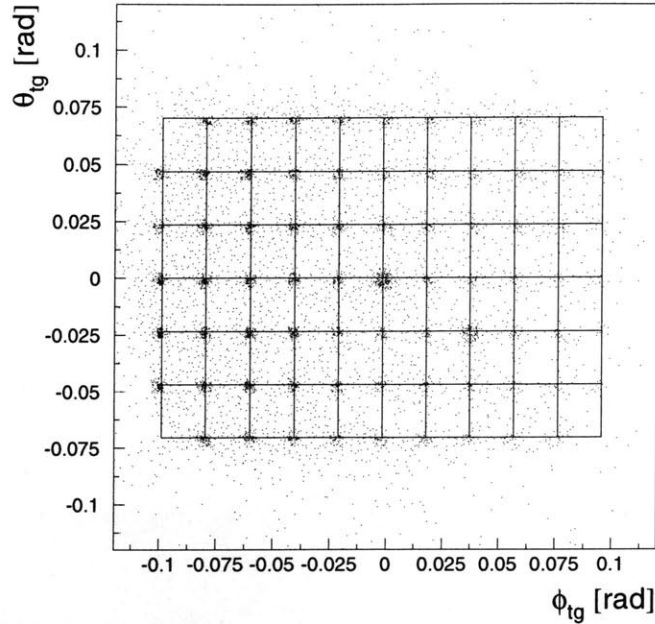
Figure 5-9: Reconstructed θ_{tgt} vs. ϕ_{tgt} for electrons elastically scattered from ^{12}C and detected in Spectrometer A, which had a sieve slit collimator (see text).

the measured data. (Note that the decrease in counts at increasing ϕ_{tg} is due to the increase in the scattering angle and corresponding decrease in the cross section.) The spectra for B show similar good agreement.

The software cuts to the momenta and reconstructed coordinates used in the (e,e′p) analysis are listed in Table 5.1. The cuts were the same for the ^{3}He and ^{4}He analysis, with the exception of the cut on θ_{tgt} as noted in the table. The dispersive coordinate δ is related to the detected momentum of the particle via $\delta = (p - p_{ref})/p_{ref}$, as discussed in Section 3.3.4, and the cuts on δ were chosen to be the same as those used in Ref. [20]. The δ-cut in Spectrometer A was for the design region of that spectrometer, and in Spectrometer B the cut excluded a small region ($7.4 < |\delta| < 7.5\%$) of the design acceptance.

The ϕ_{tgt} cut in Spectrometer A was made significantly smaller then the limits defined by the target/collimator geometry, so that the data were constrained to a region where the solid angle

Spectrometer	δ (%)	θ_{tg} (mrad)	ϕ_{tg} (mrad)	y_{tg} (cm)	z_{react} (cm)
A (electrons)	-5.0→+15.0	±90	±75	±8	-
B (protons)	±7.4	±60[a], ±45[b]	±50	-	±2

Table 5.1: Cuts to momenta and reconstructed coordinates used in the (e,e′p) analysis.

[a]Used in ^{3}He(e,e′p) analysis.
[b]Used in ^{4}He(e,e′p) analysis.

of Spectrometer A is well-understood as described in Chapter 4. The ϕ_{tgt} cut in Spectrometer B was made significantly larger than the limits defined by the target/collimator geometry, so that it excluded background that reconstructed at values of ϕ_{tgt} far outside the collimator while allowing the collimator to define the ϕ_{tgt} acceptance.

In both spectrometers, the nominal limit of θ_{tgt} defined by the collimators is ±70 mrad. In Spectrometer A, the cut to θ_{tgt} was chosen to be larger than this to exclude background while allowing the collimator to define the θ_{tgt} acceptance. In Spectrometer B, the θ_{tgt} cut was chosen to be smaller then this limit for two reasons:

1. In many of the runs, the sieve slit in Spectrometer B was not completely removed and so obstructed the acceptance in θ_{tgt}. This resulted in a 3–4 mrad reduction in the θ_{tgt} acceptance at the negative-θ_{tgt} limit (i.e. from about -70 to -66 mrad at the central target location). This was discussed in the analysis of the Carbon and Helium elastic scattering data in Chapter 4, where it was accounted for by applying a software cut of $\theta_{tgt} = \pm 60$ to eliminate the effect of the sieve slit.

2. In the (e,e′p) measurements, some of the coincident protons rescattered from the upper edge of the scattering chamber exit window. The energy lost by the protons shifted the events to higher missing energy, so that an enhancement in the number of counts at missing energies approximately 15 MeV above the 2-body breakup peak was observed. This enhancement is indicated as a shaded region in the missing energy spectra shown in Figures 5-10 and 5-11. These missing energy spectra have no cut on the proton angle θ_{tgt}^p, but

have the standard software cuts on all the other coordinates. Applying a missing energy cut on this shaded region yields the θ_{tgt}^p spectra shown in the lower right-hand corner of Figures 5-10 and 5-11, where the enhancement near $\theta_{tgt}^p = -70$ mrad is clearly visible, consistent with particles scattering from the upper edge of the scattering chamber exit window (positive θ_{tgt} points downward in the spectrometer transport coordinate system). The rescattering was probably due to a misalignment in the position of the scattering chamber. This interpretation was verified in a subsequent Helium (e,e'p) experiment in 1998 (not reported in this thesis) where the enhancement was seen to vanish when the vertical position of the scattering chamber was changed.

To eliminate both these effects, a cut on θ_{tgt} in Spectrometer B was employed. The value of the cut was ± 60 mrad in the ^{3}He data and ± 45 mrad in the ^{4}He data. In the ^{3}He data, radiative effects were found to dominate the spectrum above $E_m > 20$ MeV (as will be discussed later in this chapter), so that no cross sections were extracted above that missing energy. The contamination from the exit window rescattering was therefore not critical, and a cut of ± 60 mrad removed most of the rescattered events and defined the θ_{tgt} acceptance while not discarding more data than necessary. In ^{4}He the radiative corrections were also very large, but the region where we extracted cross section extended past $E_m = 40$ MeV, which includes the region where the enhancement from exit window scattering is observed. It was determined that a software cut of $\theta_{tgt} = \pm 45$ mrad effectively suppressed the enhancement, and this cut was therefore used throughout the ^{4}He(e,e'p) analysis. The systematic uncertainty due to these cuts was examined by varying their size, and is discussed in Chapter 6.

Two other cuts listed in Table 5.1 and used in the (e,e'p) analysis are on y_{tgt} measured in Spectrometer A and z_{react}, which was reconstructed be combining the value y_{tgt} measured in Spectrometer B and the beam rastering information. The y_{tgt} cut in Spectrometer A was made much larger than the size of the target, so that it discards small background contributions while not defining the acceptance. The cut on z_{react} in Spectrometer B. satisfied a number of criteria and is discussed further in the next section.
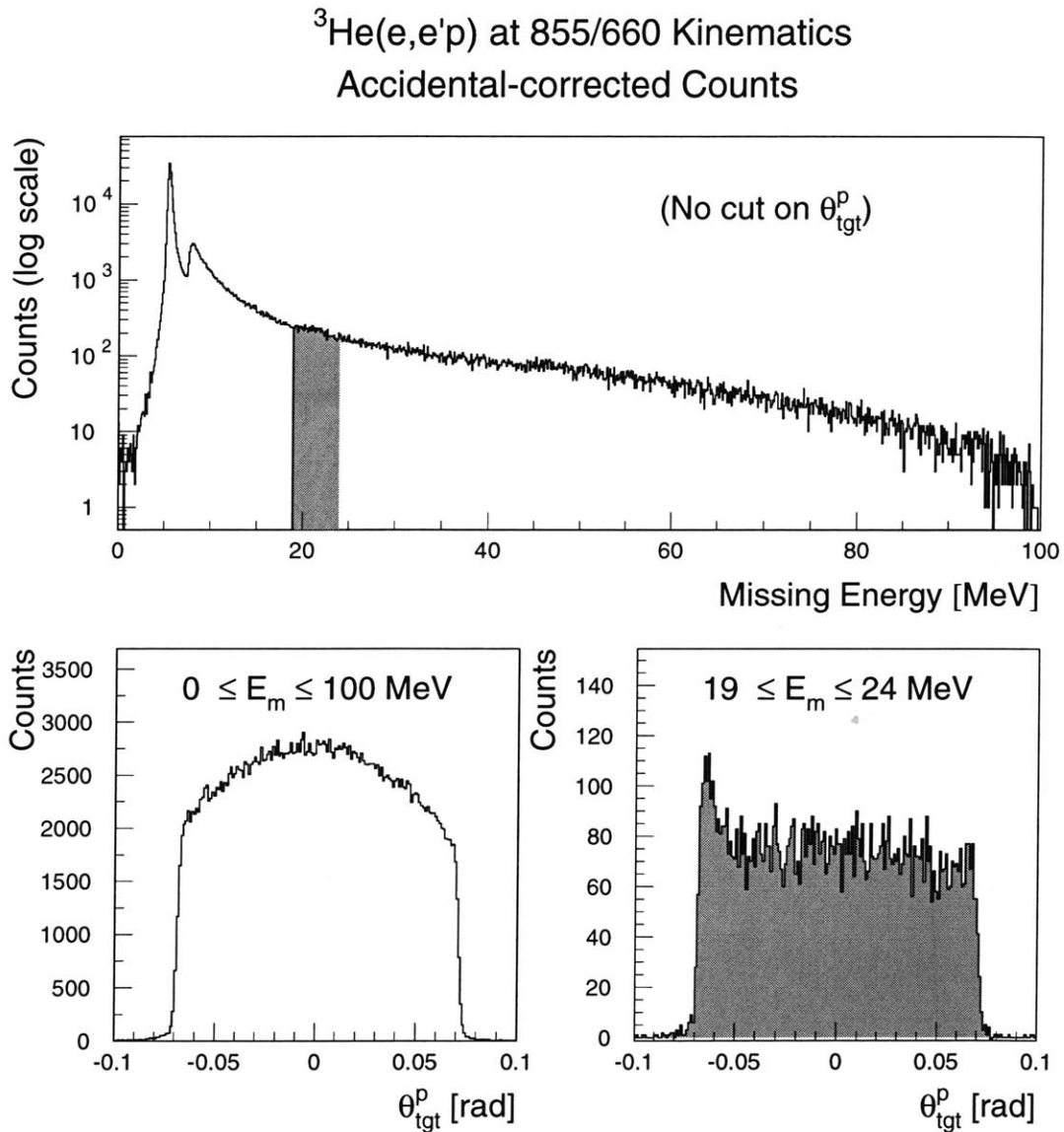
Figure 5-10: Accidental-corrected E_m and θ^p_{tgt} spectra for ^{3}He(e,e′p), illustrating the effect of rescattering from the scattering chamber exit window. The two θ^p_{tgt} spectra are for different regions of missing energy as indicated. See text for details.

^{4}He(e,e'p) at 855/660 Kinematics
Accidental-corrected Counts
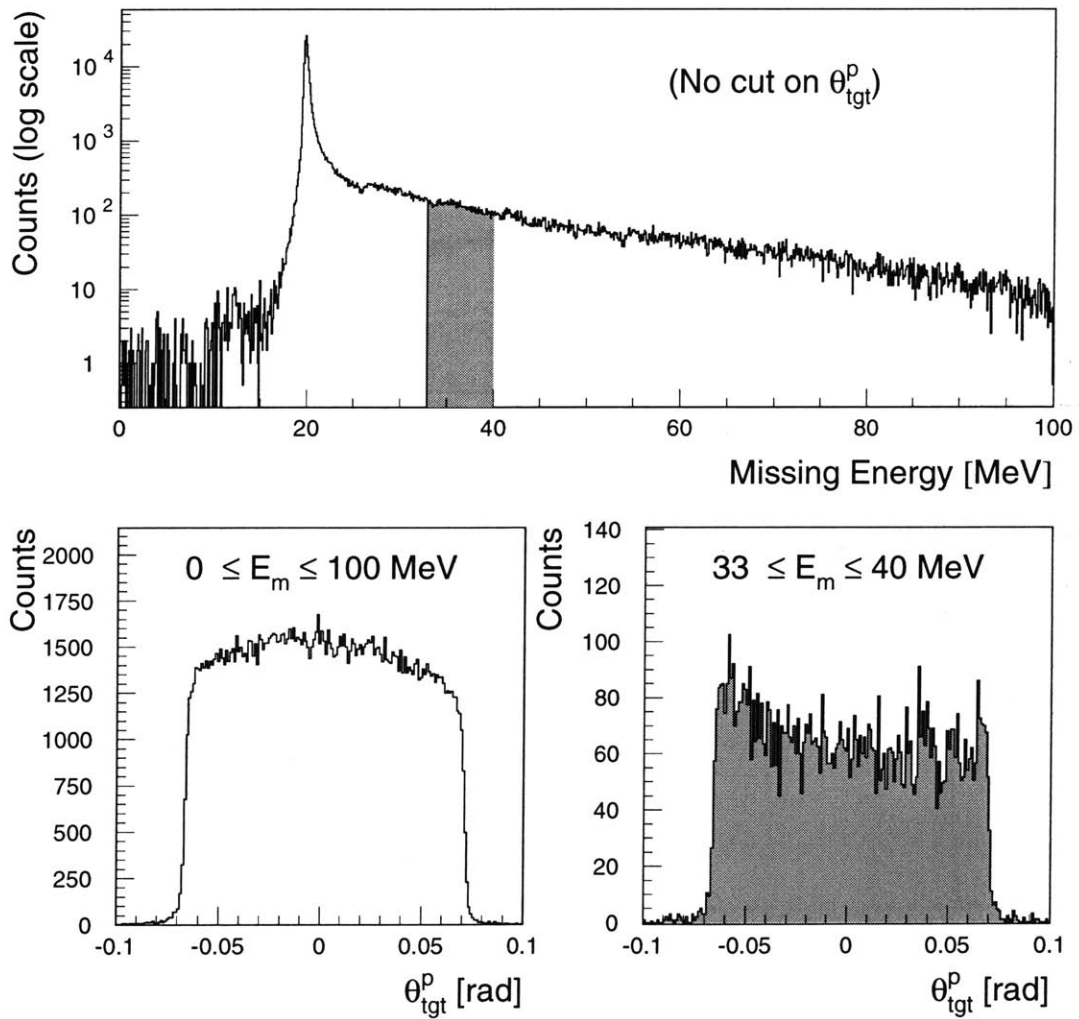
Figure 5-11: E_m and θ_{tgt}^p spectra as shown in Figure 5-10, but for ^{4}He(e,e′p) instead of ^{3}He(e,e′p). See text for details.

5.5 Cut on z_{react}

The variable z_{react} is the reconstructed position of the particle along the beam line. It was calculated from y_{tgt} as measured in Spectrometer B and the instantaneous beam position as determined from the beam rastering calibration. The purpose of the z_{react} cut was to

1. eliminate the contribution of the target walls to the (e,e'p) cross section,

2. eliminate snout-scattering contributions to the (e,e'p) cross section,

3. restrict the range of $|y_{tgt}|$ to where the acceptance of the spectrometers is well-understood, and

4. define the target thickness.

The z_{react} cut used throughout the (e,e'p) analysis was ± 2.0 cm. A wider cut would increase the amount of data that could be analyzed and hence decrease the statistical error, but would result in a greater systematic uncertainty due to background and acceptance effects. Since the uncertainty in our final result is mainly driven by systematic uncertainty, the choice to increase statistical error to decrease systematic error is justified.

The background contributions from the target walls and snout scattering are discussed in detail in the following two sections.

5.5.1 Contribution from Target Walls

To study how well the z_{react} cut suppresses the contributions of the target cell walls, we studied the shape of the missing energy histogram for z_{react} cuts of different dimensions. The shape of the histogram should be approximately independent* of the z_{react} cut. In Figure 5-12 are missing energy spectra for various z_{react} cuts for $^3\mathrm{He}(e,e'p)$ at $E_{beam} = 855$ MeV and $\mathrm{p}_p = 660$

---

*To first order, cutting on z_{react} reduces the amount of target material seen in the experiment so that the number of counts should be reduced accordingly. In reality, the number of counts in a particular missing energy bin is given by the integral in equation (5.5). The limits of (Ω_e, Ω_p) in $\mathcal{B}_{ij}$ depend on z, so that a cut in z changes the range of angles that the cross section is integrated over. The shape of the missing energy spectrum is therefore somewhat dependent on the z_{react} cut.

and 585 MeV/c. The number of counts is scaled so that each spectrum has the same number of counts in the region around the 2-body breakup ^{3}He(e,e'p)^{2}H (4.0 < E_m < 7.0 MeV), since this region is least sensitive to wall contributions. At both kinematics, we see that the shape of the spectrum in the continuum differs substantially from the shape when no z_{react} cut is made. In the p_p = 660 MeV/c spectrum without a z_{react} cut, a further wall contribution is visible around E_m = 0, which we attribute to ^{1}H(e,e'p) from ice forming on the outer surface of the target cell. When z_{react} cuts are applied the ^{1}H(e,e'p) contribution is reduced by a factor of 20 relative to the Helium 2-body peak, and the overall shape of the spectrum is independent of which z_{react} cut is used. We can therefore conclude that the z_{react} cut successfully suppresses the target-cell wall contributions to the (e,e'p) cross section.

5.5.2   Contributions from Snout Scattering

Figure 5-13 shows the accidental-subtracted counts as a function of z_{react} at two different beam energies (E_{beam} = 540 and 855 MeV) for ^{3}He(e,e'p) at p_p = 585 MeV/c. The data have no cuts on z_{react}, but otherwise have the usual acceptance cuts as given in Table 5.1. The spectra show a significant number of events reconstructing outside of the target walls, which were situated at z_{react} = −0.042 m and +0.038 m (the 8 cm -diameter target was shifted 2 mm upstream for the entire experiment). Most of these spurious events appear downstream from the target, at z_{react} > 0.04. However, their distribution peaks at a different value of z_{react} for the two different kinematics, indicating that the source of these events is not localized at a particular value of z_{react}. A detailed analysis indicated that the events are the result of coincident protons rescattering from the front of the snout on Spectrometer B. The identification of this background and the technique for excluding it are discussed below.

The front of Spectrometer B has a snout approximately 2.4 meters long that extends from the collimator position towards the target chamber. On the front of the snout is a kapton entrance window mounted in a 60 mm -thick aluminum flange. The distance from the back of the flange (i.e. the side closest to the collimator) to the center of the target is 0.448 m [40]. A test performed on the events was to track the protons to the flange position on the front of the

Scaled Missing Energy Spectra for
^{3}He(e,e'p) at 855/660 kinematics

Scaled Missing Energy Spectra for
^{3}He(e,e'p) at 855/585 kinematics
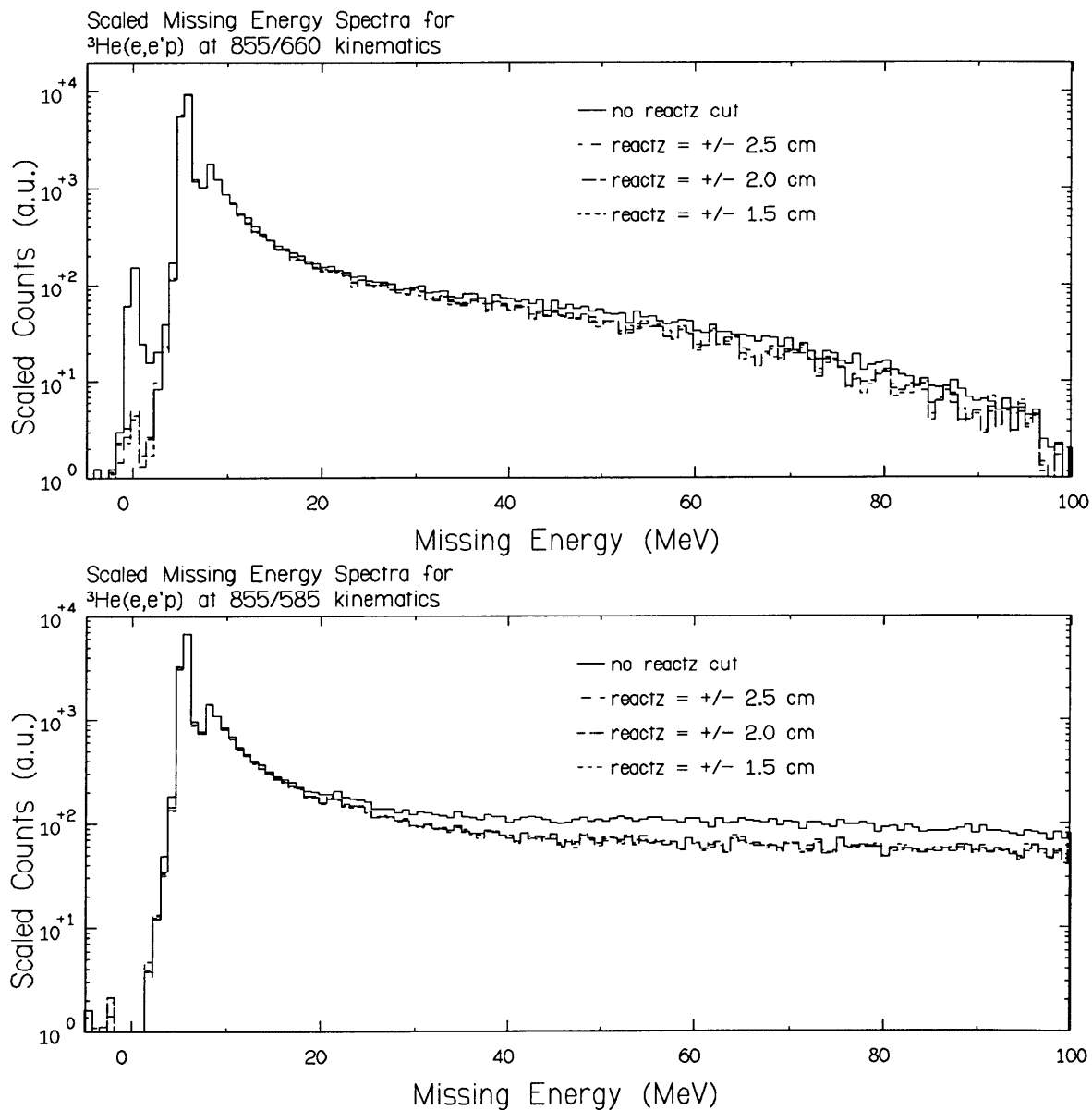
Figure 5-12: ^{3}He(e,e'p) missing energy spectra with various z_{react} cuts (see text for details).
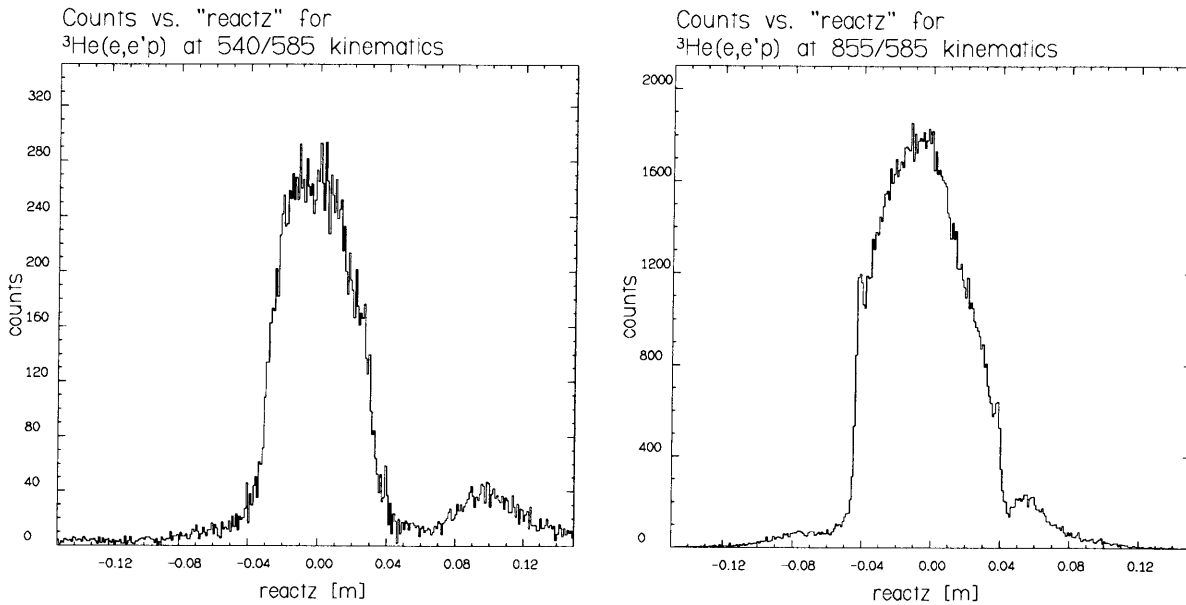
Figure 5-13: Accidental-corrected counts vs. z_{react} for ^{3}He(e,e'p) at the 540/585 (left plot) and 855/585 kinematics (right plot). A significant number of counts reconstruct outside the target walls, at a value of z_{react} that varies with the kinematics.

snout. Two new coordinates were calculated along the flange,

$$y_{flang} = y_{tgt} + \phi_{tgt} \times 0.448 \tag{5.2}$$

in the horizontal direction, and

$$x_{flang} = \theta_{tgt} \times 0.448 \tag{5.3}$$

in the vertical direction (note that positive x points downward in the transport notation). A plot of the accidental-subtracted counts vs. y_{flang} is shown in Figure 5-14, for the same data and cuts as shown in Figure 5-13. In this new variable, the background peak now has a similar position and shape for the two kinematics: it peaks sharply around $y_{flang} = 4$ cm and then falls off as y_{flang} increases. Analysis of the third kinematics (675/585) at this proton momentum gave the same result, indicating that the source of the events is localized in the flange system instead of the beam system. This explains why the events reconstructed at different values of
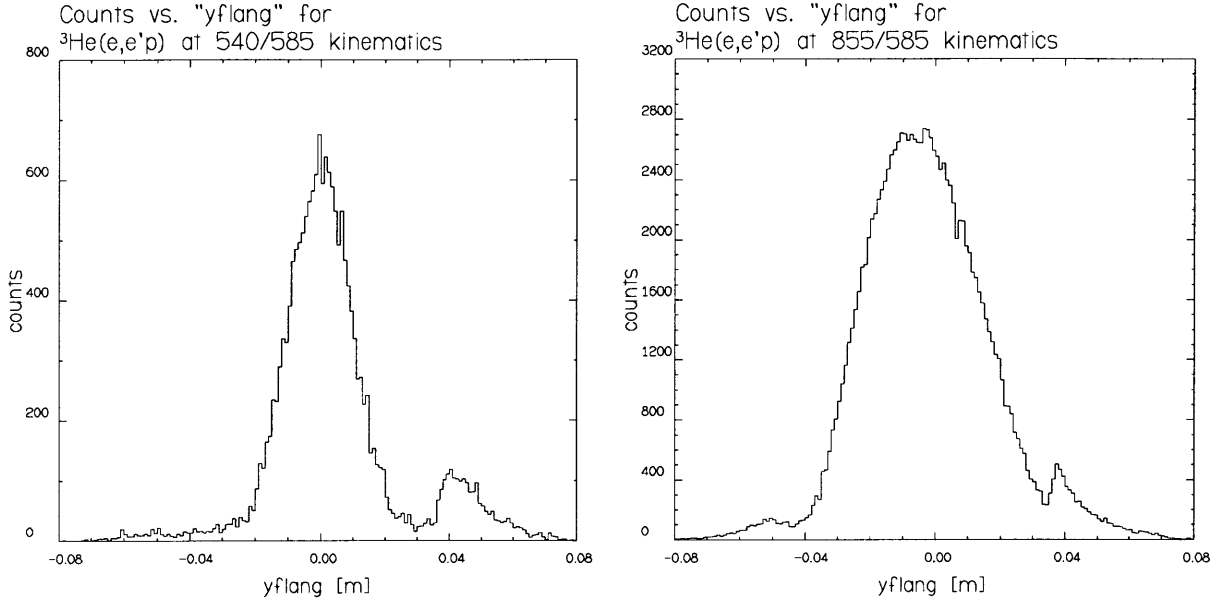
Figure 5-14: Accidental-corrected counts vs. y_{flang} for ^{3}He(e,e'p) at the 540/585 (left plot) and 855/585 kinematics (right plot). In contrast to z_{react}, the background peak is now localized, and appears at a constant value at the two kinematics.

z_{react} for the three kinematics: as the central spectrometer angle is changed, a fixed position on the flange corresponds to a different value of z_{react}.

To compare the data to the position of the flange and entrance window on Spectrometer B, a 2-dimensional plot of x_{flang} vs. y_{flang} for the ^{3}H(e,e'p) 540/585 kinematics is shown in Figure 5-15, with the flange position superimposed. The entrance window is mounted in the flange opening, which is ± 42.5 mm wide. The background around $y_{flang} = 4$ cm reconstructs near the edge of the flange, indicating that the particles are probably either passing through the flange or being rescattered by it. The effect is greatly reduced on the opposite side of the flange (around $y_{flang} < -4$ cm), although it is still somewhat visible, especially in the 1-dimensional plots in Figure 5-14. One possible explanation is that the end of the snout on Spectrometer B is displaced approximately 5 mm upstream. This would account for the asymmetry in the reconstructed y_{flang} spectrum. However, we also note that the accuracy of the coordinate reconstruction might be reduced for events with large y_{flang}, since these events have large values of y_{tgt} (the reconstruction matrix we used was determined in Ref. [26] from

measurements that had a maximum $|y_{tgt}|$ value of 1.84 cm).

To completely understand this apparent rescattering from the flange, four further characteristics of the background events were noted:

1. The events appear to be (e,e′p) events, as determined in both particle identification in the two spectrometers and by the coincidence timing. In the raw coincidence timing spectrum they appear in the same region of time as the (e,e′p) events from the interior region.

2. The y-reconstruction in Spectrometer A generally places the events in the interior of the target, in conflict with the z_{react} reconstruction (which is based on the y-reconstruction in Spectrometer B because of its higher resolution) which generally places them outside (Figure 5-13).

3. The events do not reconstruct to any particular missing energy.

4. At other kinematic settings (we have only discussed the background $p_p = 585$ MeV/c), the size of the background relative to the central target region increases at lower proton momentum settings and is not visible at the highest proton momentum setting.

An explanation consistent with all of these observations is that the events are ^{3}He(e,e′p) events from the target where the coincident electron is detected as usual, but the proton hits the aluminum flange, loses energy, and rescatters into the spectrometer. To show that the kinematics of this mechanism are feasible, consider that at our kinematics the ^{3}He(e,e′p)^{2}H reaction will generate protons with a distribution of momenta that peaks around q= 685 MeV/c. A 685 MeV/c proton has a kinetic energy of about 223 MeV, and will lose approximately 59 MeV in 6 cm of aluminum. If the proton passes through the entire flange, it will therefore have a final kinetic energy of 164 MeV and a momentum of 578 MeV/c. This is well inside the acceptance of the kinematic setting we have been discussing ($p_p = 585$).

Since these events rescattered from the flange into the spectrometer acceptance, they are indeed background and should be removed. The flange region is cut away by the ±2.0 cm cut on z_{react}, as shown in Figure 5-16. The ability of the cut to suppress the flange scattering was checked by the analysis of Figure 5-12, where the shape of the missing energy spectrum
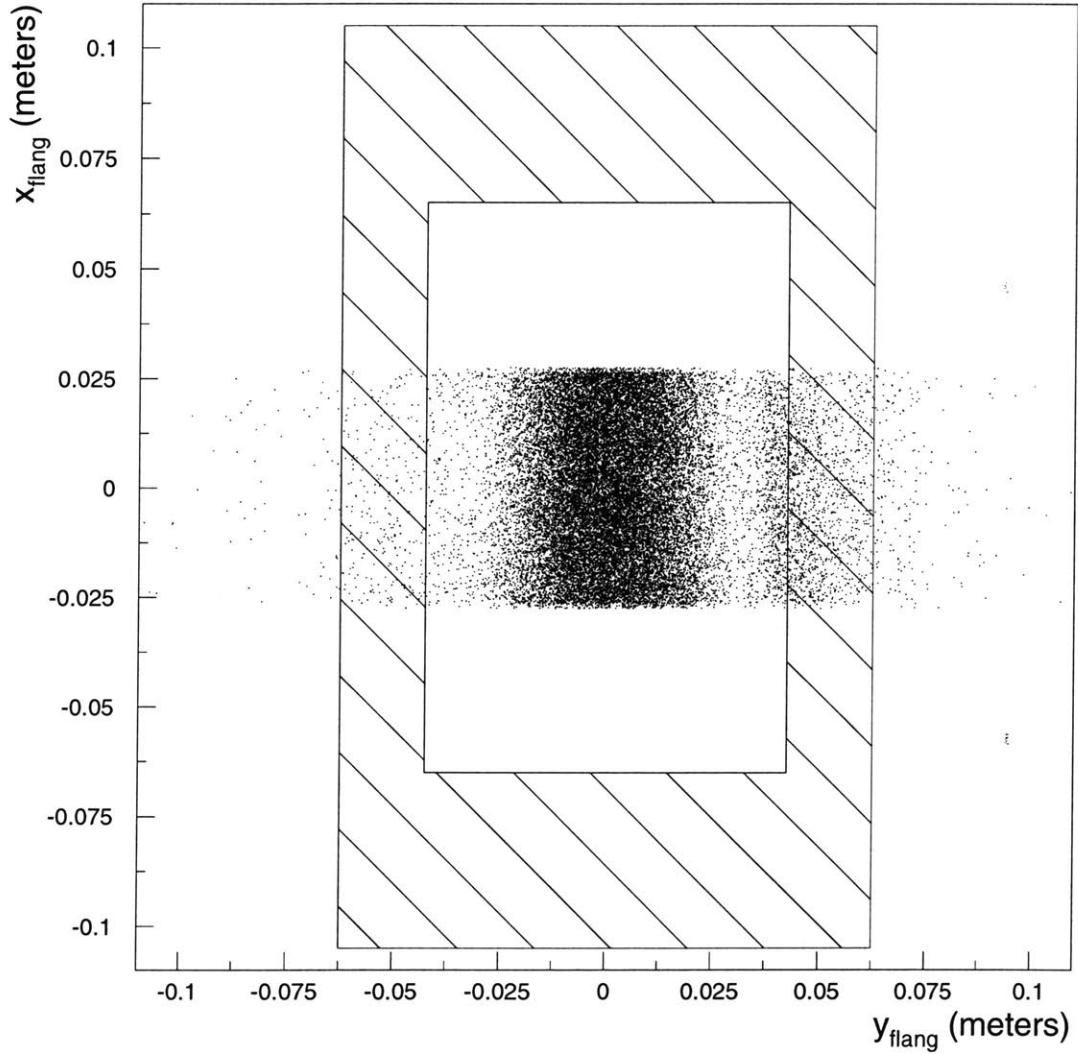
Figure 5-15: A scatter plot of x_{flang} vs. y_{flang} for ^{3}He(e,e'p) at the 540/585 kinematics. Acceptance cuts on $(\theta_{tgt}, \phi_{tgt}, \delta)$ only have been made – there is no z_{react} cut or accidental subtraction. Superimposed on the plot is the aluminum flange on the front of the snout of Spectrometer B. Many of the suspect events reconstruct inside the flange or near its inner edge.

Counts vs. "yflang" after reactz=+/−2 cm cut
³He(e,e'p) at 540/585 kinematics

Counts vs. "yflang" after reactz=+/−2 cm cut
³He(e,e'p) at 855/585 kinematics
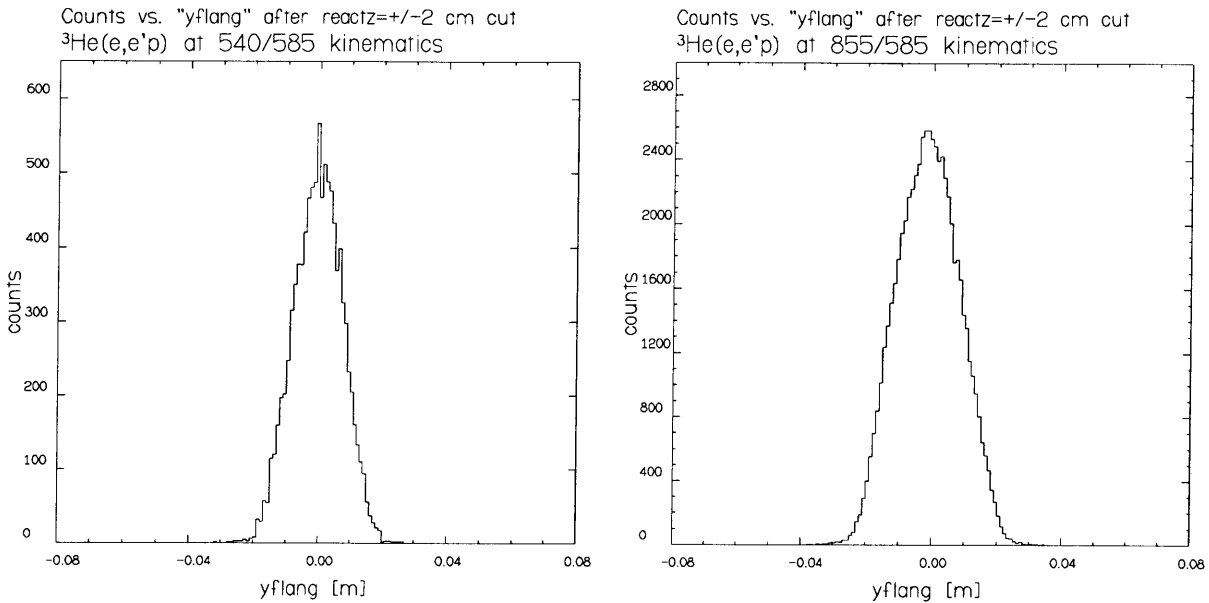
Figure 5-16: Accidental-corrected counts vs. y_{flang} as in Figure 5-14, but after the $z_{react} = \pm 2$ cm cut is applied. The background region near the flange edge has been eliminated by the z_{react} cut.

was found to be independent of the z_{react} cut. The $E_{beam} = 855$ MeV kinematics shown in that figure are the worst case since they have the largest proton angle, which means that the accepted range of y_{flang} is largest for a fixed z_{react}.

We have not discussed in detail the two lowest proton momentum settings ($p_p = 500$ and 425 MeV/c). The flange scattering is very visible at those kinematics also, but the counts from even the central target region are dominated by another type of background and so are unusable. The background there is due to collimator scattering, which is a mechanism similar to that seen in flange scattering, and will be discussed in Section 5.10.

5.6   The Experimental (e,e'p) Cross Section

The (e,e'p) cross sections extracted in the experiment are an average of the theoretical cross section over the experimental acceptance, and are either six-fold (in the continuum) or five-fold (in the case of two-body breakup) differential. The method of extracting the cross sections and

their relation to the theoretical cross section is discussed below.

5.6.1 Six-Fold Differential Cross Section

In an (e,e'p) experiment, we measure the number of events $N(E_m^i, p_m^j)$ that fall into the missing energy and missing momentum bin (E_m^i, p_m^j). The bin spans a range of missing energy and missing momentum given by

$$E_{\text{miss}} = E_m^i \pm \frac{\Delta E_m}{2} \ , \qquad p_{\text{miss}} = p_m^j \pm \frac{\Delta p_m}{2} \tag{5.4}$$

In terms of the theoretical cross section, the number of events $N(E_m^i, p_m^j)$ measured from scattering from an extended target is given by

$$N(E_m^i, p_m^j) = \frac{1}{\eta_{dt}} \frac{Q}{e} \rho_v \cdot \int_{\mathcal{B}_{ij}} \frac{d^6\sigma}{d\Omega_e d\Omega_p dp_e dp_p} d\Omega_e d\Omega_p dp_e dp_p dz \tag{5.5}$$

where z is the coordinate along the beam line and originating at the center of the target. The constants in the above equation are

$$\begin{aligned}
\eta_{dt} &= \text{dead-time correction factor } (> 1) \\
Q &= \text{accumulated charge (C)} \\
e &= 1.602 \times 10^{-19} \text{C} \\
\rho_v &= \text{number density of target atoms, per unit volume}
\end{aligned}$$

The symbol $\mathcal{B}_{ij}$ indicates the limits of the integration, which is constrained such that

1. $(p_e', p_p, \Omega_e, \Omega_p, z)$ lie within the physical limits of the experimental setup (i.e. they "fall within the acceptance"),

2. the missing energy and missing momentum fall within the values given in (5.4), and

3. any other limitations used in the determination of $N(E_m^i, p_m^j)$ (i.e. cuts placed on the

data) are satisfied.

Although the cross section has no explicit z-dependence, the limits of the angular integrations depend on z in a complicated fashion. This was demonstrated in Chapter 4, where the z-dependence of the angular acceptance was calculated for a point target.

We now define two quantities: the *acceptance-averaged* cross section,

$$\left\langle \frac{d^6\sigma}{d\Omega_e d\Omega_p dp_e dp_p} \right\rangle_{\mathcal{B}_{ij}} \equiv \frac{\int_{\mathcal{B}_{ij}} \frac{d^6\sigma}{d\Omega_e d\Omega_p dp_e dp_p} d\Omega_e d\Omega_p dp_e dp_p dz}{\int_{\mathcal{B}_{ij}} d\Omega_e d\Omega_p dp_e dp_p dz} \tag{5.6}$$

and the *detection volume*,

$$\Delta V(E_m^i, p_m^j) \equiv \int_{\mathcal{B}_{ij}} d\Omega_e d\Omega_p dp_e dp_p dz \tag{5.7}$$

Substituting these expressions into the right hand side of equation (5.5) gives

$$N(E_m^i, p_m^j) = \left\langle \frac{d^6\sigma}{d\Omega_e d\Omega_p dp_e dp_p} \right\rangle_{\mathcal{B}_{ij}} \frac{1}{\eta_{dt}} \frac{Q}{e} \rho_v \cdot \Delta V(E_m^i, p_m^j) \tag{5.8}$$

Solving this equation for the acceptance-averaged cross section gives

$$\left\langle \frac{d^6\sigma}{d\Omega_e d\Omega_p dp_e dp_p} \right\rangle_{\mathcal{B}_{ij}} = \frac{\eta_{dt}}{\rho_v} \frac{e}{Q} \cdot \frac{N(E_m^i, p_m^j)}{\Delta V(E_m^i, p_m^j)} \tag{5.9}$$

This is the cross section that is extracted from the experimental data. It is an average of the theoretical cross section over the experimental acceptance as defined in equation (5.6). The detection volume $\Delta V(E_m^i, p_m^j)$ is calculated with a standard Monte Carlo technique [41] using the program AEEXB [32]:

$$\Delta V(E_m^i, p_m^j) = \frac{N_{thru}(E_m^i, p_m^j)}{N_{trials}} \times \Delta p_e \Delta p_p \Delta\Omega_e \Delta\Omega_p \Delta z \tag{5.10}$$

where $\Delta p_e \Delta p_p \Delta\Omega_e \Delta\Omega_p \Delta z$ is the total volume sampled over in the Monte Carlo. The total volume was set to exceed the experimental acceptance in all dimensions except for Δz, which was set to the physical target length. N_{trials} is the total number of trials, and $N_{thru}(E_m^i, p_m^j)$

is the number of successful trials landing in the bin (E_m^i, p_m^j). The kinematic variables of the outgoing electron and proton for a particular trial were randomly sampled from the volume $\Delta p_e \Delta p_p \Delta \Omega_e \Delta \Omega_p \Delta z$, and the position of the incident electron beam on the target was rastered as in the experiment. Particle vectors generated at the event vertex were modified for energy loss in the target and target walls, and then cuts applied to determine if the events land inside the collimators[†]. Further cuts in angle, momentum, and vertex position as used on the experimental data (given in Table 5.1) were then applied, and successful events were histogrammed according to their values of E_m and p_m at the reaction vertex. The vertex values are appropriate since these are the values used in histogramming the experimental data (ESPACE corrects the detected momenta for energy loss in the target and target walls.)

5.6.2   Five-Fold Differential Cross Section

The two-body breakup reactions channels $^4\text{He}(e,e'p)^3\text{H}$ and $^3\text{He}(e,e'p)^2\text{H}$ appear as peaks in missing energy, with a width determined by the overall energy resolution of the experiment. The cross section for these reactions is obtained by integrating the six-fold differential cross section over missing energy with the appropriate Jacobian, yielding a five-fold differential cross section:

$$\frac{d^5\sigma}{d\Omega_e d\Omega_p dp_e} = \int_{E_1}^{E_2} \frac{d^6\sigma}{d\Omega_e d\Omega_p dp_e dp_p} \frac{1}{\left| \frac{\partial E_m}{\partial p_p} \right|} dE_m \tag{5.11}$$

where the limits of integration (E_1, E_2) are the experimental range of missing energy spanned by the two-body peak. The partial derivative is taken at constant p_e, Ω_e and Ω_p, and for our definition of missing energy it has the following value:

$$\left. \frac{\partial E_m}{\partial p_p} \right|_{p_e, \Omega_e, \Omega_p} = -\frac{p_p}{E_p} + \frac{\vec{p_p} \cdot \vec{p_b}}{p_p E_b'} \tag{5.12}$$

where $E_b' \equiv \sqrt{p_b^2 + m_{A-1}^2}$, and m_{A-1} is the mass of the (A-1) recoil nucleus.

[†]The collimators in Spectrometer A and B were modelled as a series of slits as discussed in Appendix C

In the data analysis, this procedure is done in two steps. First, the Jacobian is used to calculate a histogram of the six-fold cross section differential in missing energy. Then that histogram is integrated over the 2-body peak to obtain a histogram of the five-fold differential cross section. The six-fold differential cross section is calculated from

$$\left\langle \frac{d^6\sigma}{d\Omega_e d\Omega_p dp_e dE_m} \right\rangle_{\mathcal{B}_{ij}} = \frac{\eta_{dt}}{\rho_v} \frac{e}{Q} \cdot \frac{N(E_m^i, p_m^j)}{\Delta V_{wt}^{jac}(E_m^i, p_m^j)} \tag{5.13}$$

Note that this is identical to the equation (5.9) for the measured cross section, except for the substitution $V \rightarrow V_{wt}^{jac}$, where V_{wt}^{jac} is the detection volume weighted by $\left| \frac{\partial E_m}{\partial p_p} \right|$,

$$\Delta V_{wt}^{jac}(E_m^i, p_m^j) = \int_{\mathcal{B}_{ij}} \left| \frac{\partial E_m}{\partial p_p} \right| \cdot d\Omega_e d\Omega_p dp_e dp_p dz \tag{5.14}$$

As with the unweighted detection volume in equation (5.7), the weighted detection volume is calculated with the Mone Carlo technique. Each trial is weighted by the factor $\left| \frac{\partial E_m}{\partial p_p} \right|$, so that

$$\Delta V_{wt}^{jac}(E_m^i, p_m^j) = \frac{N_{thru}^{wtjac}(E_m^i, p_m^j)}{N_{trials}} \times \Delta p_e \Delta p_p \Delta\Omega_e \Delta\Omega_p \Delta z \tag{5.15}$$

A one-dimensional histogram of the five-fold differential cross section is then calculated by integrating over missing energy:

$$\left\langle \frac{d^5\sigma}{d\Omega_e d\Omega_p dp_e} \right\rangle_{\mathcal{B}_j} = \sum_{i=n}^{m} \left\langle \frac{d^6\sigma}{d\Omega_e d\Omega_p dp_e dE_m} \right\rangle_{\mathcal{B}_{ij}} \Delta E_m \tag{5.16}$$

where n and m are the bins corresponding to the limits (E_1, E_2) of the integration.

5.7   The Experimental Spectral Function

In PWIA, the (e,e'p) cross section can be written as [18]

$$\frac{d^6\sigma}{d\Omega_e d\Omega_p dp_e dp_p} = p_p^2 \cdot \sigma_{ep} \cdot S(E_m, p_m) \tag{5.17}$$

where S is the spectral function. Substituting this into equation (5.5)

$$N(E_m^i, p_m^j) = \frac{1}{\eta_{dt}} \frac{Q}{e} \rho_v \cdot \int_{\mathcal{B}_{ij}} {p_p}^2 \sigma_{ep} S(E_m, p_m) \cdot d\Omega_e d\Omega_p dp_e dp_p dz \qquad (5.18)$$

This can be written as

$$N(E_m^i, p_m^j) = \frac{1}{\eta_{dt}} \frac{Q}{e} \rho_v \cdot \left\langle S(E_m^i, p_m^j) \right\rangle_{\mathcal{B}_{ij}} \int_{\mathcal{B}_{ij}} {p_p}^2 \sigma_{ep} \cdot d\Omega_e d\Omega_p dp_e dp_p dz \qquad (5.19)$$

where

$$\left\langle S(E_m^i, p_m^j) \right\rangle_{\mathcal{B}_{ij}} \equiv \frac{\int_{\mathcal{B}_{ij}} {p_p}^2 \sigma_{ep} S(E_m, p_m) \cdot d\Omega_e d\Omega_p dp_e dp_p dz}{\int_{\mathcal{B}_{ij}} {p_p}^2 \sigma_{ep} \cdot d\Omega_e d\Omega_p dp_e dp_p dz} \qquad (5.20)$$

Solving (5.19) for $\langle S \rangle$,

$$\left\langle S(E_m^i, p_m^j) \right\rangle_{\mathcal{B}_{ij}} = \frac{\eta_{dt}}{\rho_v} \frac{e}{Q} \cdot \frac{N(E_m^i, p_m^j)}{\Delta V_{wt}^{kCC1}(E_m^i, p_m^j)} \qquad (5.21)$$

This is the "experimental spectral function" that we extract in the experiment. Note that the right hand side is identical to that in equation (5.9) for the measured cross section, except for the substitution $V \to V_{wt}^{k\sigma_{ep}}$, where $V_{wt}^{k\sigma_{ep}}$ is the detection volume weighted by ${p_p}^2 \sigma_{ep}$,

$$\Delta V_{wt}^{k\sigma_{ep}}(E_m^i, p_m^j) = \int_{\mathcal{B}_{ij}} {p_p}^2 \sigma_{ep} \cdot d\Omega_e d\Omega_p dp_e dp_p dz \qquad (5.22)$$

The weighted detection volume is calculated with the Monte Carlo technique by weighting each trial by the factor ${p_p}^2 \sigma_{ep}$, so that

$$\Delta V_{wt}^{k\sigma_{ep}}(E_m^i, p_m^j) = \frac{N_{thru}^{wtk\sigma_{ep}}(E_m^i, p_m^j)}{N_{trials}} \times \Delta p_e \Delta p_p \Delta \Omega_e \Delta \Omega_p \Delta z \qquad (5.23)$$

The version of σ_{ep} used in the analysis was the CC1 prescription of de Forest [18], which is described in Appendix G.

5.8   Manipulation of (E_m, p_m) Histograms

In the analysis of the (e,e′p) data, a number of operations were performed on the 2-d (and in some cases 4-d) histograms. These operations included combining the data from different kinematics, masking the histograms to remove the regions at the edge of the acceptance, and rebinning and projecting of the final cross sections. Each of these is discussed below in more detail.

5.8.1   Combining Data

At each beam energy, data were taken at four different central proton momenta (Tables 3.3 and 3.4). The data taken at $p_p = 660$ and 585 MeV/c were combined into a single spectrum by separately adding the accidental-corrected counts and normalized detection volume histograms and dividing them to calculate a cross section:

$$\left\langle \frac{d^6\sigma}{d\Omega_e d\Omega_p dp_e dp_p} \right\rangle_{\mathcal{B}_{ij}} = \frac{N_1(E_m^i, p_m^j) + N_2(E_m^i, p_m^j)}{\nu_1 \Delta V_1(E_m^i, p_m^j) + \nu_2 \Delta V_2(E_m^i, p_m^j)} \tag{5.24}$$

where the subscripts 1 and 2 indicate the two different kinematics, N is the accidental corrected counts, and ΔV is the detection volume. The factor ν_1 (ν_2) is a normalization factor for the first (second) kinematics:

$$\nu_1 = \frac{\rho_v^{(1)}}{\eta_{dt}^{(1)}} \frac{Q^{(1)}}{e}, \nu_2 = \frac{\rho_v^{(2)}}{\eta_{dt}^{(2)}} \frac{Q^{(2)}}{e} \tag{5.25}$$

The two lowest proton momentum settings ($p_p = 500$ and 425 MeV/c) were not combined with the other data, but were analyzed separately. These settings correspond to the highest missing energy and missing momentum in the experiment (see Figure 3-8) and were found to be dominated by collimator scattering. This is discussed in detail in Section 5.10.

5.8.2 Histogram Masking

The number of counts in a particular bin of the N or ΔV histograms varied strongly with the missing energy and missing momentum. Since the two histograms were divided to form a cross section, some limit needed to be placed on the range of (E_m, p_m) used to avoid large fluctuations at the edges of the acceptance where both histograms drop off sharply. The limit used in the analysis was to require that the value of $\Delta V(E_m^i, p_m^j)$ in a particular bin exceed 10% of the maximum value in the ΔV histogram. A 2-d (E_m, p_m) histogram was created, with a 1 in the bins that meet this criteria and a 0 in the bins that do not. The N and ΔV histograms were then multiplied by this "mask" histogram to exclude the unwanted regions.

5.8.3 Projection and Rebinning of the Data

To radiative unfold the data (discussed in the next section) it is sometimes necessary to have a smaller bin size or more dimensions then is desired in the final result. For this reason, it is necessary to rebin or project the cross sections after radiative corrections.

The rebinning or projection was done by first multiplying the radiative-corrected cross section by the normalized detection volume, effectively calculating a radiative-corrected counts histogram. The rebinning (or projecting) was then done separately on this radiative-corrected counts histogram and on the normalized detection volume histogram. The two were then divided to calculate the rebinned (or projected) cross section.

The advantage of this technique is that it is conceptually similar to analyzing the data with a larger bin size or (in the case of projection) in fewer dimensions. A disadvantage is that the error propagation is unclear. The division, multiplication and rebinning of histograms is done by the program HISTMAN, which properly propagates the errors for each of those operations according to the standard formulae [42]. However, the radiative-corrected cross section before re-binning already has the full statistical errors from the division of N and ΔV, as well as an additional error from the radiative unfolding procedure. When doing the rebinning, it would therefore be incorrect to again propagate the errors in ΔV in the multiplication and subsequent division done in the rebinning procedure. The solution taken was to zero the errors in the

ΔV histogram before the multiplication. The relative error in the radiative-corrected cross section then gets completely associated with the radiative-corrected counts and is propagated accordingly when the counts are rebinned. Any error caused by this assumption should be small, since the error in ΔV is generally much smaller then the error in N.

5.9   Radiative Corrections

The radiative corrections to the (e,e'p) cross sections were performed by radiatively-unfolding the data with the code RADCOR [39]. The techniques used by the code are described in Ref. [39, 62, 63], and the correction factors it used for each type of radiative process are given in Appendix B. For our kinematics, the unfolding technique seems to fail at high missing energy, for reasons discussed below. A Monte Carlo simulation was therefore done using theoretical models of both the ^{3}He(e,e'p) cross section and the radiative processes, and the result then directly compared to the (un- radiative-corrected) experimental cross section.

5.9.1   Radiative Unfolding

The radiative correction of a particular cross section bin is done in two distinct steps. First, the contribution from radiative tails originating in all other bins is subtracted. Second, the contents of the bin (after the preceding subtraction) is increased to account for the strength lost from that bin by radiation. This technique is referred to as *radiative unfolding*.

In (e,e'p), radiative tails always propagate strength from lower to higher missing energy. Radiative unfolding is therefore done by starting with the bin at lowest missing energy, into which no strength can radiate. That bin is first corrected for radiative effects, resulting in an increase in the contents of the bin. The trajectories of the radiative tails from that bin through the (multi-dimensional) kinematic space are then calculated, and the contributions from the tails are subtracted from the corresponding bins.

The radiative corrections were first done in a 2-dimensional (E_m, p_m) space. Yield and phase space histograms were accumulated in 2-dimensions, and then divided and normalized to form a 2-d cross section histogram. The radiative unfolding of the cross sections was done by

RADCOR [39]. Some details of the code are given in Appendix B.

To exactly calculate the trajectory of the radiative tails, the full kinematics (6 independent variables) of each (e,e'p) event would be required. Since the data have been binned in 2+1 dimensions ((E_m, p_m) + the fixed beam energy) this information is no longer available, so that the following assumptions are made by RADCOR to fix the kinematics. First, the angles of $\vec{p}_m$ with respect to $\vec{q}$ are fixed at zero (which is true for the center of the acceptance). Secondly, the value of $|\vec{q}|$ is fixed at its central value. A final constraint, required for the calculation of the tail from the incident electron, is that the angle of the detected proton is held constant.

With these assumptions, the 2-d cross sections were radiatively-unfolded. An example of the direction of the radiative tails in the (E_m, p_m) plane is shown in Figure 5-17. A 1-dimensional projection of the resulting ^{3}He spectral function for a narrow, fixed p_m slice is shown in Figure 5-18. The radiative unfolding improves the separation between the 2- and 3-body breakup regions, removing most of the measured strength in the unphysical region between them. At low missing energy (< 25 MeV), the shape and magnitude of the corrected spectral function is brought closer to the theory by the radiative correction procedure. This is especially noticeable above about 20 MeV, where the radiative correction to the data are very large, indicating that the vast majority of the measured strength in that region is due to radiation.

For $E_m > 25$ MeV, this 2D radiative-corrected spectrum shows erratic behaviour, first going negative and then positive as the missing energy increases. This behaviour can be attributed to limitations of the unfolding technique. Under the kinematic assumptions used in the 2D unfolding, the radiative tails tend to concentrate around the contour where numerically $E_m \approx c \cdot p_m$, so that the results tend to go negative around that contour and positive above and below it. When the results are averaged over a larger p_m range as shown in Figure 5-19, the cross section (or spectral function) no longer fluctuates from negative to positive with increasing missing energy. However, the cross section at high missing energy ($E_m > 25$ MeV) is then consistently negative, which is an unphysical result.

A limitation of the 2-d unfolding is the assumption that $\vec{p}_m$ is parallel to $\vec{q}$. In this experiment, the magnitude of $\vec{p}_m$ is small compared to $|\vec{q}|$ and $|\vec{p}_p|$, so that $\vec{p}_m$ can actually
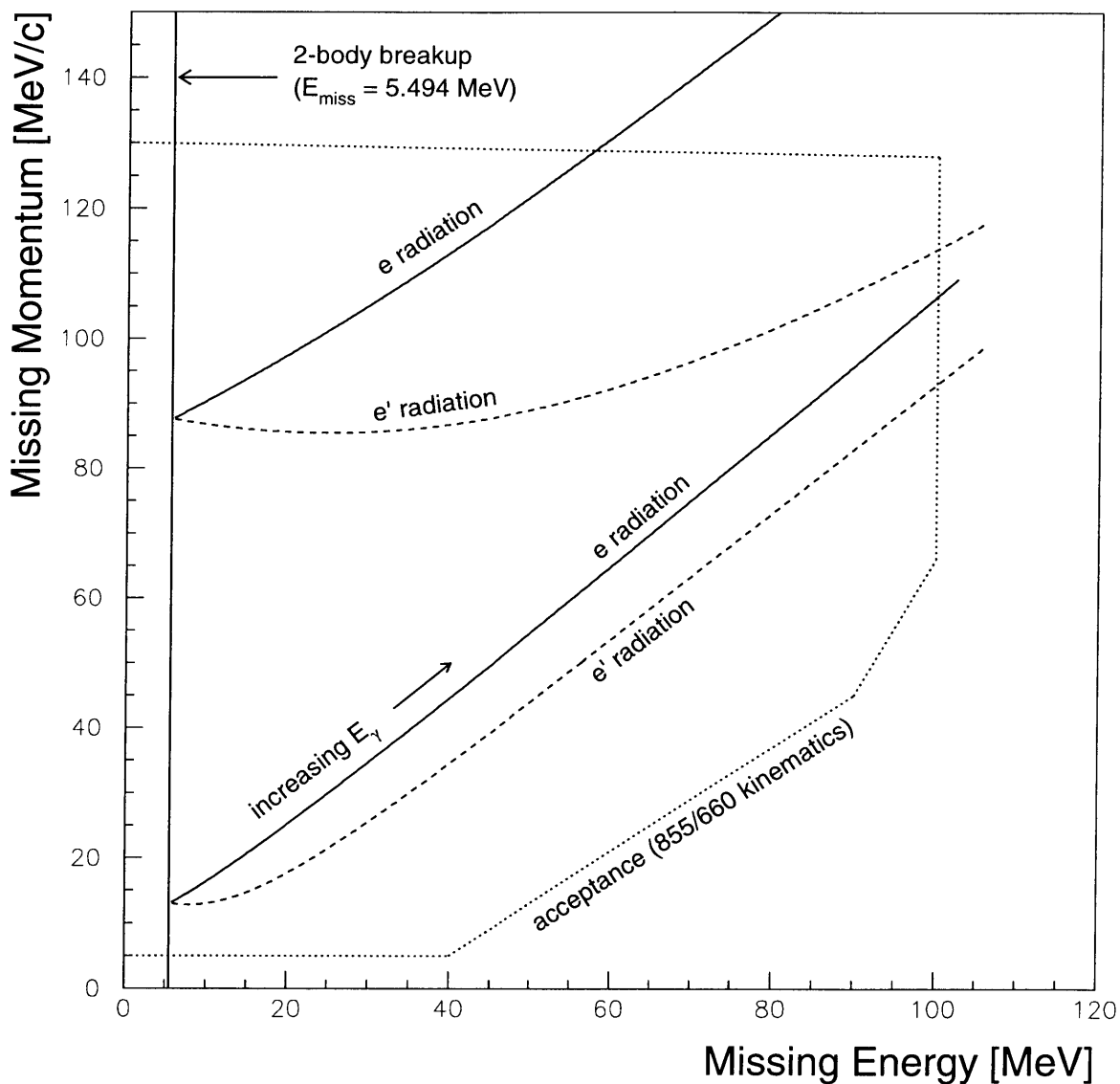
Figure 5-17: Two examples of the radiative tails propagating into the continuum from a single (E_m, p_m) bin in the 2-body breakup region for ^{3}He(e,e'p). The tails were determined with the program RADCOR [39]. The trajectory of the tails is different depending on whether the incident (e) or final (e') electron radiated. Larger missing energy along the trajectories corresponds to a larger energy of the radiated photon.

$$40 \leq p_{miss} \leq 50 \text{ MeV/c}$$
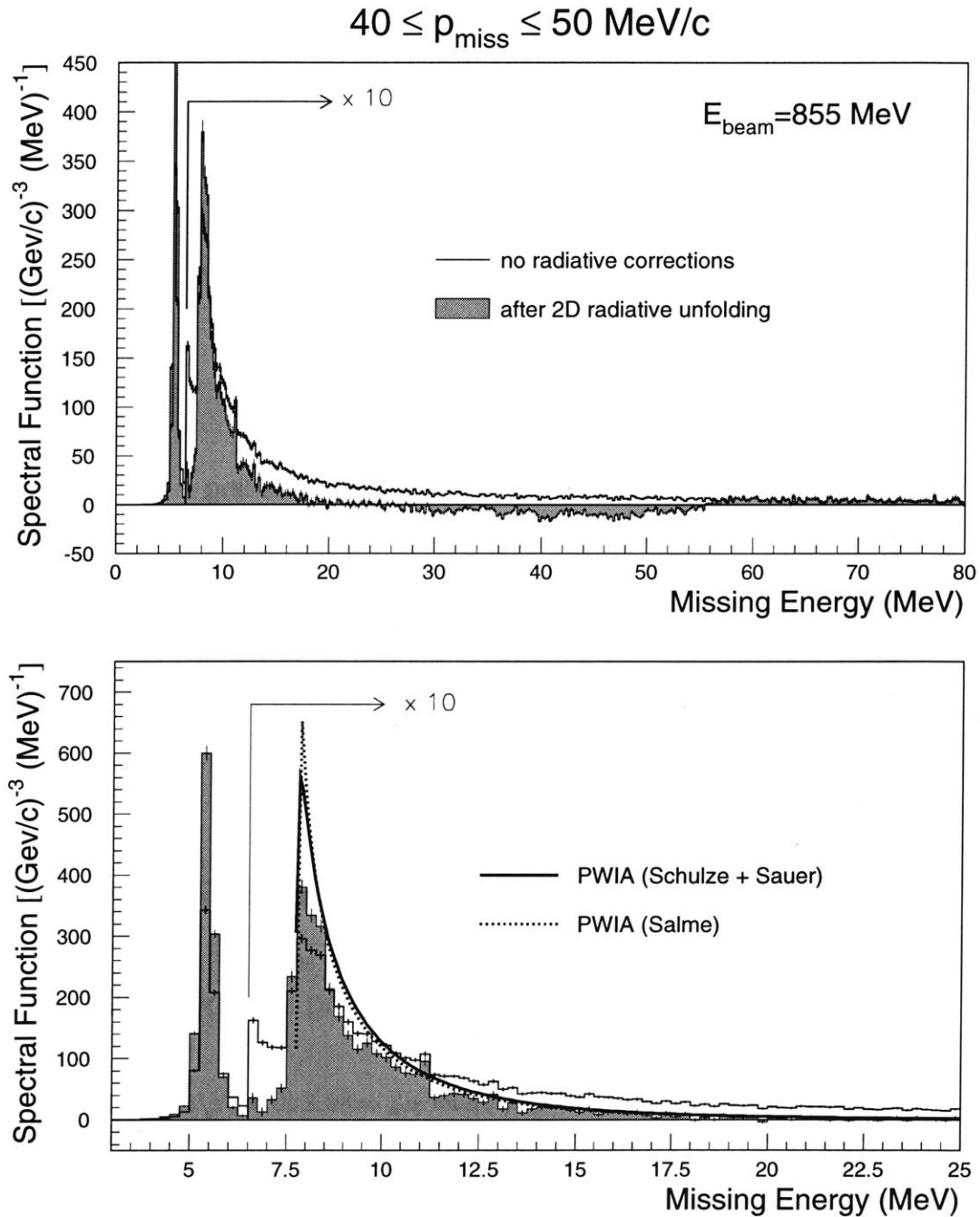
Figure 5-18: The experimental ^{3}He spectral function for $p_m = 45 \pm 5$ MeV/c after 2D radiative unfolding. Kinematics are 855/660 and 855/585 combined.
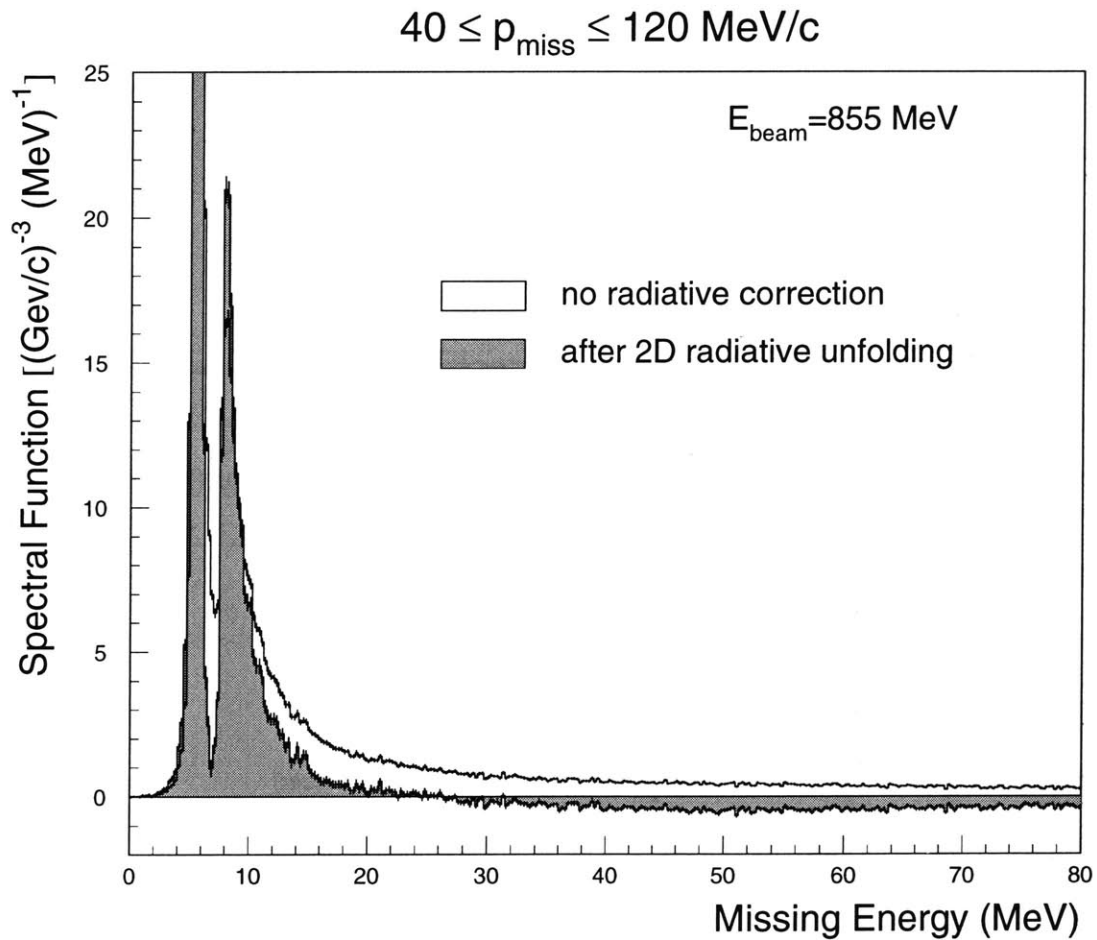
Figure 5-19: The experimental ^{3}He spectral function for $p_m = 80 \pm 40$ MeV/c after 2D radiative unfolding. The radiative-corrected result in the $E_m > 20$ MeV region is now smoother, although it is consistently negative.

have many orientations with respect to $\vec{q}$ while approximately maintaining parallel kinematics $(\vec{p}_p \parallel \vec{q})$. Since the angle of $\vec{p}_m$ with respect to $\vec{q}$ changes the trajectory of the radiative tails in the (E_m, p_m) plane (Figure 5-20), an attempt was made to account for these different orientations by binning the data and doing the radiative unfolding in 4 dimensions. The angular range was broken up into 3 bins in both θ_{qpm} and ϕ_{qpm}, and 4-dimensional cross sections were calculated by binning both counts and detection volume in the 4-d $(E_m, p_m, \theta_{qpm}, \phi_{qpm})$ space. The $3 \times 3 = 9$ two-dimensional (E_m, p_m) spectra corresponding to each $(\theta_{qpm}, \phi_{qpm})$ combination were then independently unfolded in RADCOR.

The radiative-corrected results were then rebinned and projected on to the 1-dimensional E_m axis. A sample spectrum is shown in Figure 5-21. Compared to the 2-d results, the high missing energy region ($E_m > 25$ MeV) is less negative. At low E_m, the results are basically unchanged: the integral of the experimental spectral function over $7 < E_m < 20$ MeV in the 4-d analysis is only 2% less than the corresponding integral in the 2-d analysis.

However, in four dimensions the concept and technique of radiative unfolding become very complicated, and there were some inconsistencies which were not resolved in this analysis. One of these inconsistencies is the contribution from radiative tails that originate outside the experimental acceptance. Estimating the contribution from these tails requires either a model of the cross section, or else an extrapolation of the measured data into regions outside of the acceptance. In the 2D analysis, an extrapolation of the data showed that the tails that originate outside the acceptance only contribute to the edges of the measured (E_m, p_m) spectrum. Their contributions could therefore be avoided by discarding the outer edges of the spectrum. In contrast, in the 4D analysis the (E_m, p_m) region spanned by each $(\theta_{qpm}, \phi_{qpm})$ bin is not necessarily the same. It is therefore difficult to define a large region of (E_m, p_m) space that is both common to all $(\theta_{qpm}, \phi_{qpm})$ and is insensitive to radiative contributions from outside the acceptance. A model or extrapolation of the data in 4 dimensions could eliminate the need to discard data, but would be difficult to implement accurately.

Since both the 4D and 2D radiative unfolding techniques both yield a negative cross section at high missing energy ($E_m > 20$ MeV in ^{3}He), another unfolding technique was investigated.
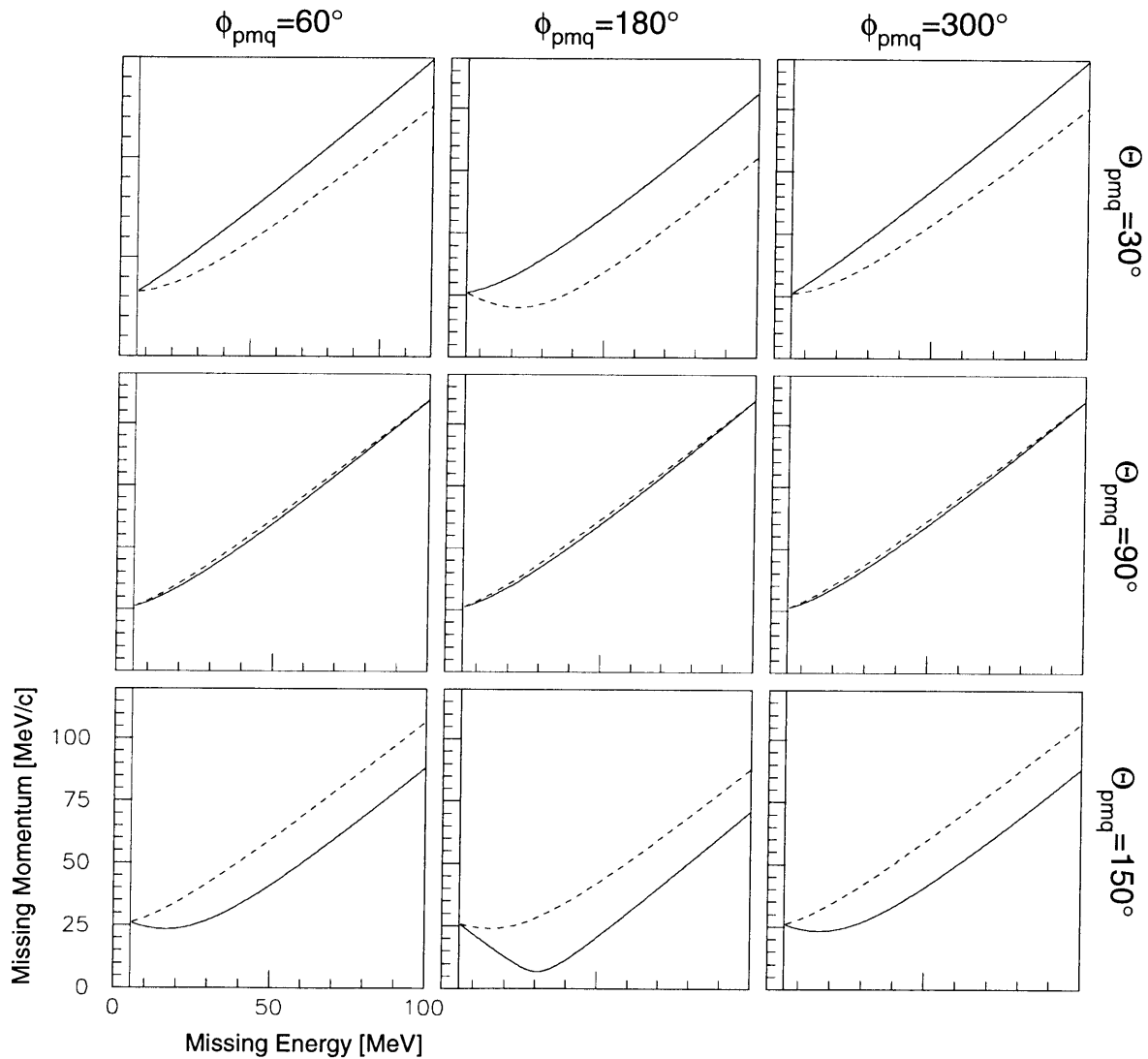
Figure 5-20: Propagation of the radiative tails in the (E_m, p_m) plane for the 4D analysis. The angles $(\theta_{pmq}, \phi_{pmq})$ are of $\vec{p}_m$ with respect to $\vec{q}$ for the single (E_m, p_m) bin where the tails originate. The tails were calculated with the program RADCOR [39].
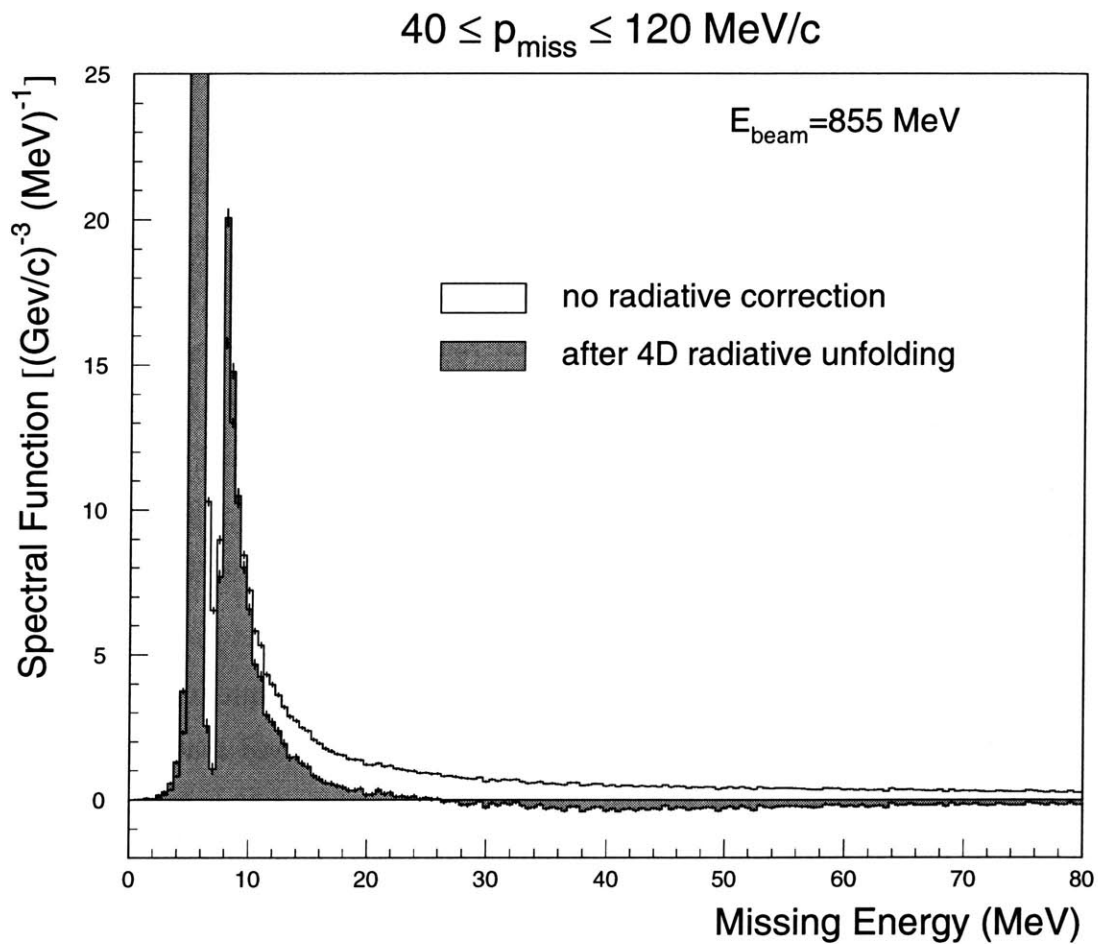
Figure 5-21: The experimental ^{3}He spectral function for $p_m = 80 \pm 40$ MeV/c after 4D radiative unfolding. The radiative-corrected result in the $E_m > 20$ MeV region is less negative compared to the 2D analysis.

We refer to this third technique as '2DFPM', for '2-dimensional at fixed missing momentum'. In this technique the radiative unfolding was done in two dimensions, but the missing momentum was held constant for both the incident (e) and final (e') electron tails. The trajectory of the radiative tails (for example, those shown as the solid and dashed lines in Figure 5-17) are then horizontal lines in the (E_m, p_m) plane. By ignoring the change in p_m, this technique provided an estimate of the error in the cross section introduced by the uncertainty in the (E_m, p_m) trajectories in the 2D unfolding technique.

A sample spectrum of the ^{3}He(e,e'p) results with the 2DFPM unfolding technique is shown in Figure 5-22. The kinematics are the same as in Figures 5-19 and 5-21. In contrast to the 2D and 4D unfolding results, the 2DFPM radiative-corrected cross section is positive at high missing energy ($E_m > 20$ MeV). This illustrates that the radiative-corrected cross section in the high E_m region is very sensitive to the trajectory of the radiative tails in the (E_m, p_m) plane. At lower missing energy, the shape of the spectrum is similar to the 2D and 4D techniques. The integral of 2DFPM radiative-corrected spectral function over $7 \leq E_m \leq 20$ MeV is 4.6% greater than the corresponding 2D result. The final results in Chapter 6 are presented with both the 2D and 2DFPM unfolding techniques.

All of the unfolding techniques discussed above yielded an uncertain result at higher missing energy ($E_m > 20$ MeV in ^{3}He). All of the techniques consistently showed that the radiative corrections to the continuum are large, but the corrected cross section at high E_m varied from positive to negative depending on the unfolding technique employed. A possible explanation for the failure of radiative unfolding at high missing energy is that, as a result of binning the data in less than five dimensions, all of the kinematic variables are not known for each event. The exact trajectories of the radiative tails in the (E_m, p_m) plane can therefore not be calculated. The sensitivity of the high E_m region to the exact trajectories was demonstrated in the 2DFPM technique, and is further illustrated by considering the radiative tails propagating from the two-body breakup peak, as shown in Figure 5-17. For small photon energies, the change in both E_m and p_m is quite small, so that any uncertainty in the trajectory of the tail will generate only a small change in p_m. At high missing energy, any uncertainty in the slope of the tail
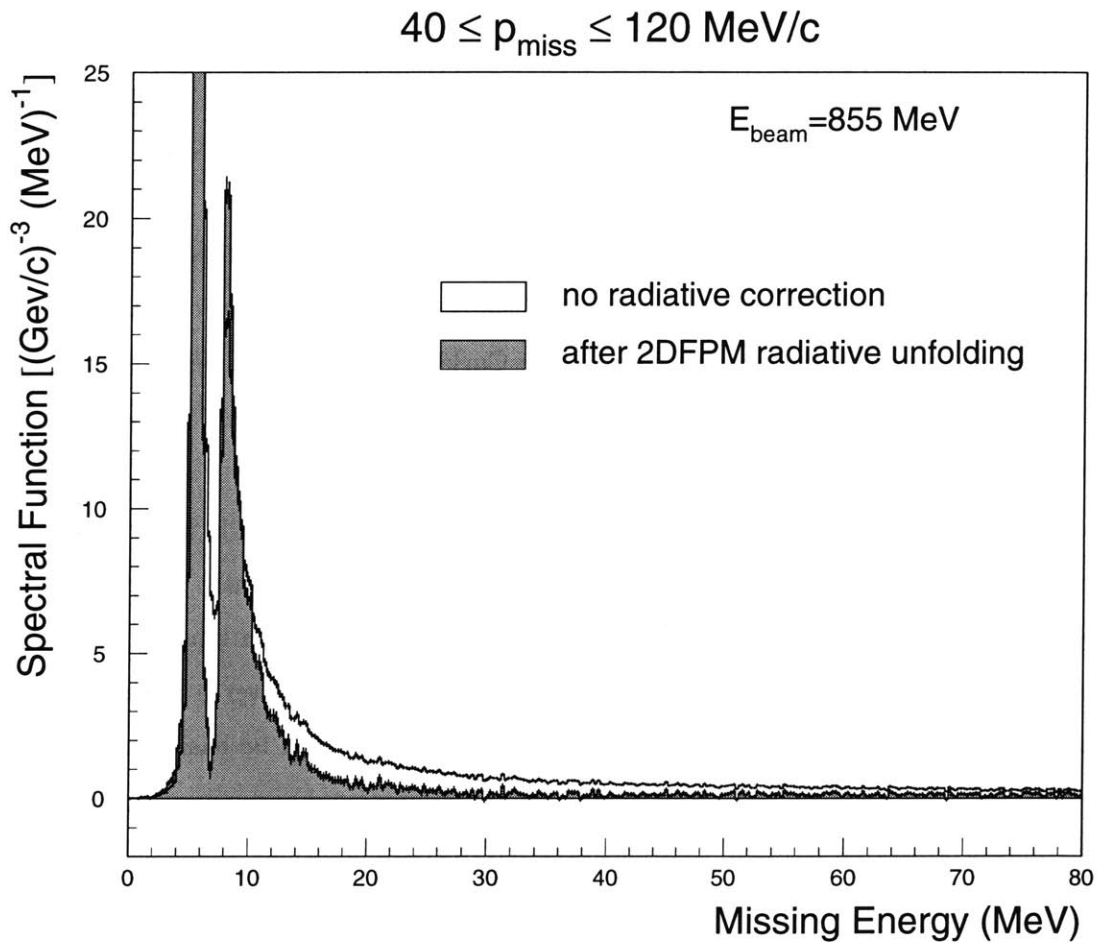
Figure 5-22: The experimental ^{3}He spectral function for $p_m = 80 \pm 40$ MeV/c after 2DFPM radiative unfolding (see text). In contrast to the results obtained with 2D and 4D radiative unfolding, the radiative-corrected result in the $E_m > 20$ MeV region is now positive.

generates a larger change in p_m and hence a larger uncertainty in the radiative correction. The uncertainty in the trajectory of the radiative tails is then compounded by the fact that the radiative corrections at high E_m are very large relative to the measured cross sections.

Since radiative unfolding yielded an uncertain result at high missing energy, another technique was used to study the effect of radiation on the measured continuum cross section. This second technique employed a Monte Carlo simulation and is discussed below.

5.9.2   Monte Carlo Simulation of Radiative Effects

A second approach to radiative corrections is to fold radiative effects into a theoretical description of the (e,e'p) cross section, and then compare the result to the measured (unradiative-corrected) cross section. The technique uses a Monte Carlo to sample the (e,e'p) cross section over the experimental acceptance while allowing for the radiation of real and virtual photons by the incident and scattered electrons.

An advantage of the technique is that the full kinematic information is known for each Monte Carlo trial, so that the trajectory of a radiated event in the kinematic hyperspace can be precisely calculated. Stated more simply, the effect of radiation on each kinematic variable is completely known. Another advantage is that the model used can cover a large region of phase space, so that radiation from regions outside the acceptance can be easily handled. A possible disadvantage to the technique is in the case that the simulated and measured spectrum disagree significantly. In that case an iterative approach to the simulations might be necessary, where the input model is modified to improve the agreement to experiment.

For the analysis of our data, a simulation was run for the 855/660 ^{3}He kinematics to study the high E_m region and to compare to the result obtained by radiative unfolding. This simulation is described in detail in Ref. [43]. The Monte Carlo code used was titled AEEXB although it is heavily modified and is a distinct code from the version of AEEXB used to calculate the detection volume histograms. An unpublished manual (Ref. [44]) details the technique used by the code to simulate the radiative effects. The input model for the ^{3}He(e,e'p) cross section was PWIA employing the spectral function of Salme *et al.* [45], the CC1 prescription of the

off-shell e-p cross section [18], and the free-nucleon form factors of Ref. [46].

For the results presented here, the final cross sections from the simulation were scaled by a factor of 0.84, to account for the difference between our measured (radiative-unfolded) ^{3}He(e,e'p)^{2}H momentum distribution at 45 MeV/c and the corresponding value given by the Salme spectral function. The rescaling is intended to account for the gross differences between the model and the measured data. The value of the rescaling factor will be apparent in the following chapter where the final results are given.

The results of the simulation are shown in Figure 5-23. The plots are of the six-fold differential cross section $\frac{d^6\sigma}{d\Omega_e d\Omega_p dp_e dp_p}$ as a function of missing energy for $p_m = 45 \pm 5$ MeV/c. The experimental cross sections are not radiative-corrected, and are shown as the shaded region in both plots. The results of the simulation are shown as the solid line. In the top plot, the simulation includes only the 2-body breakup part of the spectral function. Everything in the simulated curve that appears a few MeV above the 2-body peak at 5.5 MeV is therefore purely radiative tail from the 2-body breakup channel. For $E_m > 25$ MeV, we see that this radiative tail from the 2-body accounts for the majority of the measured data. In the bottom plot, the simulation includes the continuum part of the theoretical spectral function as well as the 2-body breakup. The theoretical continuum cross section without radiation is shown as the dashed line, and the full simulation of both 2-body and continuum cross sections with radiation is the solid line.

The overall shape of the simulation and the data agree very well, and the simulation indicates that the measured cross section above $E_m > 25$ MeV is entirely radiative tail. We note that the simulation does not reproduce the detailed shape of the two-body breakup peak centered at 5.49 MeV. The measured peak shape is a result of the experimental resolution, which is not well-modelled by the simulation. Refinements to the Monte Carlo could probably improve the agreement, but the motivation to do so would be mostly cosmetic.

In the continuum region, the simulation overestimates the data by about 20%. A second simulation was performed for a larger region of the acceptance ($p_m = 65 \pm 35$ MeV/c) and is shown in Figure 5-24. The use of a a larger fraction of the acceptance reduces the statistical

uncertainty. The results of this second simulation in the continuum overestimate the data by approximately 15%. Part of these discrepancies in magnitude may be due to the fact that the overall scaling factor was obtained from a single point, namely the two-body breakup at 45 MeV/c. The radiative contributions to this spectrum come from a broader region of phase space (for example, two-body breakup reactions at other p_m), so that the use of a single scaling factor introduces an error if the data and the model differ by more that a single constant. Secondly, the full simulation of the radiative effects is complicated, and the techniques used by the Monte Carlo are still in development.

This discrepancy in the absolute magnitude of the simulated cross sections does not alter the central conclusion, which is that the measured spectrum is completely dominated by radiative tail above $E_m > 20$ MeV. This conclusion is consistent with the result obtained from radiative unfolding. The 15-20% difference between the simulated and measured cross sections requires further work to resolve, and may be related to the detailed shape of the input model and/or the simulation techniques, which are still under development.

5.10   Collimator Scattering at Higher (E_m, p_m)

The two lowest proton momentum settings ($p_p = 500$ and 425 MeV/c) probe the cross section at higher missing energy and missing momentum, as shown in the acceptance plots of Figure 3-8. Since most of the kinematic range covered by these settings is far from the 2-body breakup peak, radiative correction of the cross sections with radiative unfolding is even more difficult then at the higher p_p kinematics. In many cases the source of the radiative tails comes from kinematic regions that were not measured in this experiment, namely the 2-body breakup channel at high p_m. Radiative unfolding would require either an extrapolation of the experimental data into these regions or the inclusion of a model of the cross section.

In this instance it makes more sense to proceed directly to the Monte Carlo simulation of the radiative tail, which includes a theoretical model of the cross section in all regions, as well as having the other advantages outlined in the previous section. This was done for the ^{3}He 855/500 kinematics, and the results are given in Figure 5-25. The shaded region is the un- radiative-
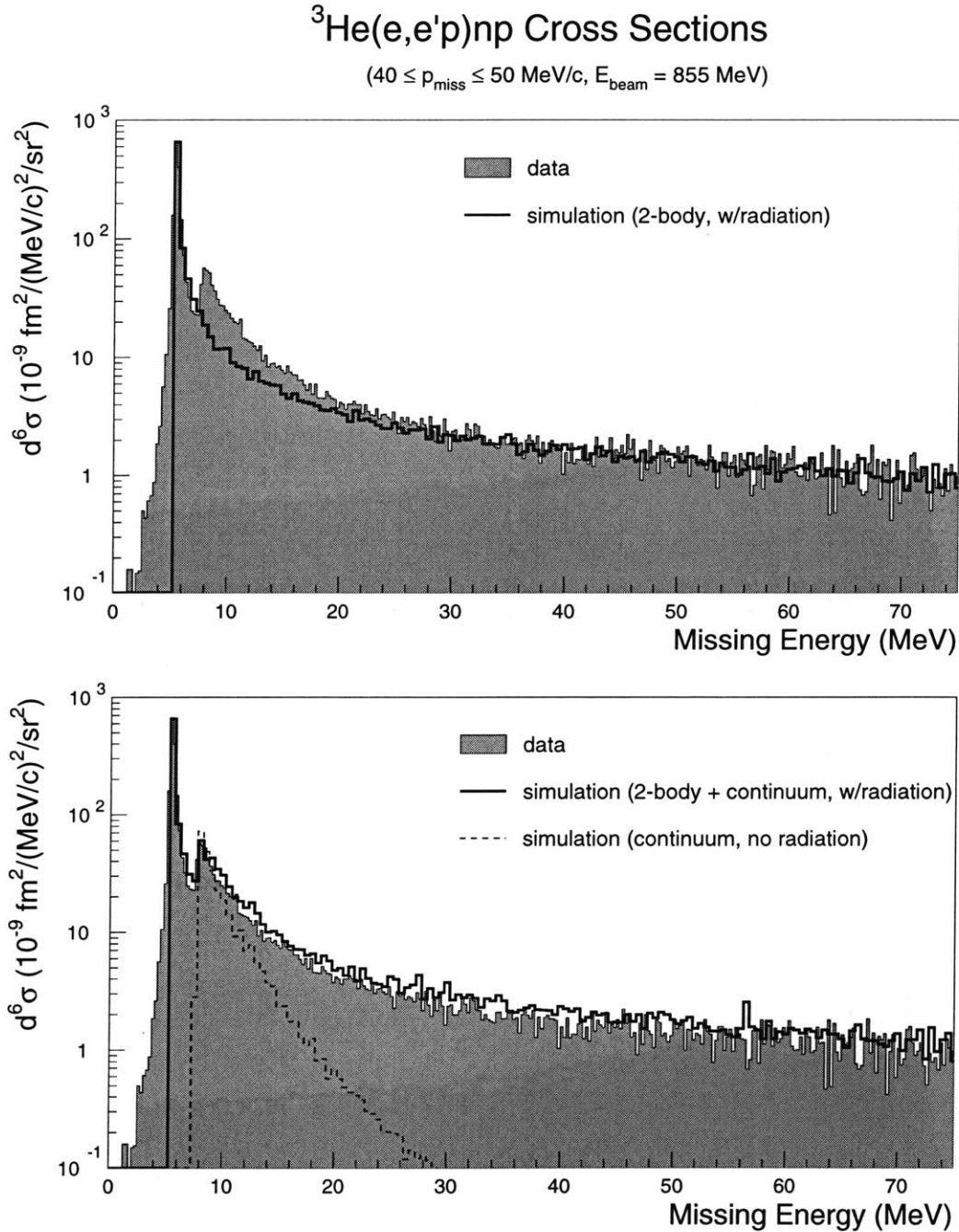
Figure 5-23: Experimental cross sections without radiative correction vs. simulation. The input for the simulation is the spectral function of Salme [45] scaled by 0.84. The scaling factor was chosen to normalize the theory to the measured 2-body breakup momentum distribution at 45 MeV/c.
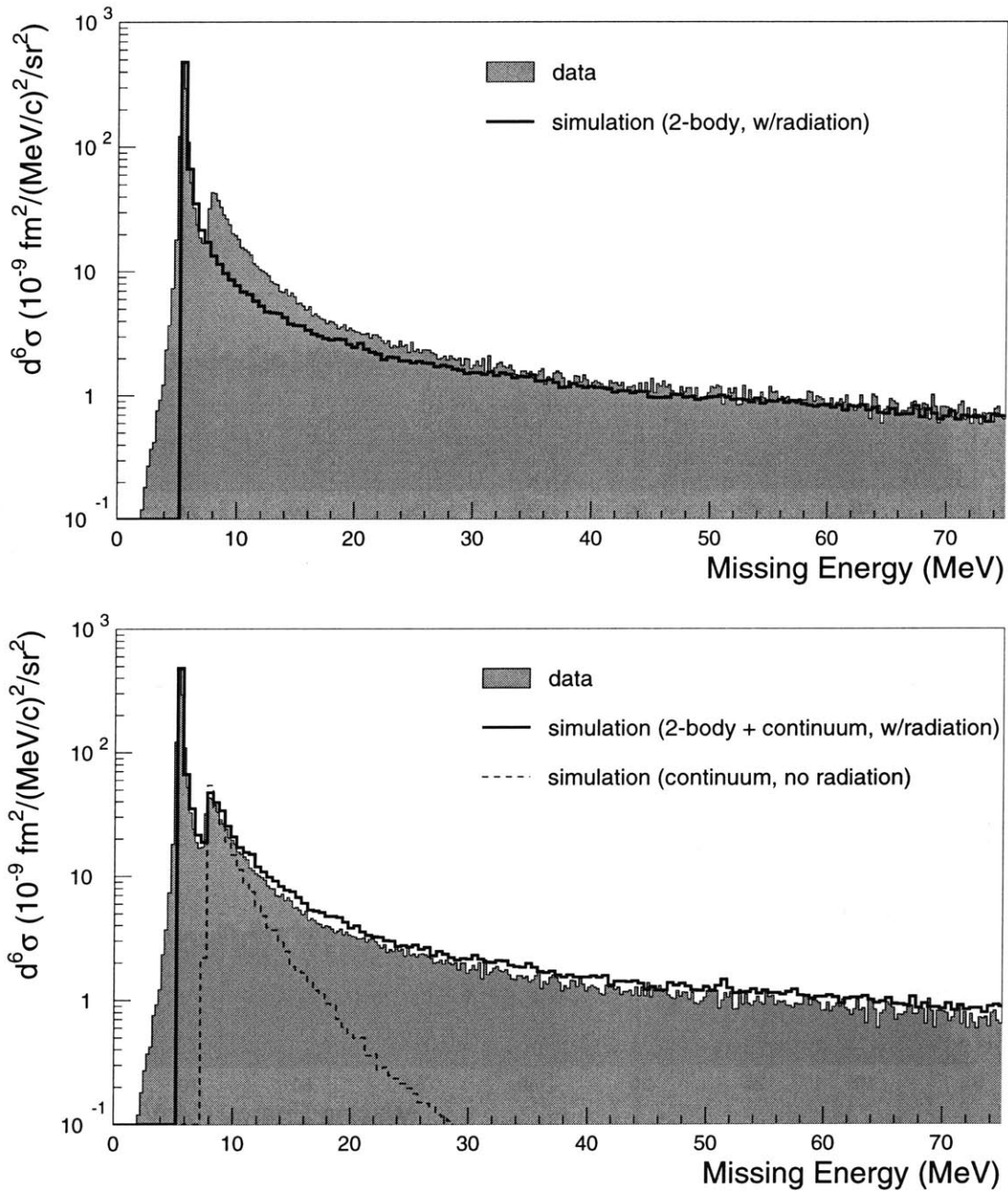
Figure 5-24: Experimental cross sections without radiative correction vs. simulation as in Figure 5-23, but for the expanded acceptance region corresponding to $p_m = 65 \pm 35$ MeV/c.

corrected data, and the solid line is the full simulation of the radiated spectral function. As with the previous kinematics, the simulation yields a cross section that is dominated by the radiative tail at high missing energy ($E_m > 30$ MeV). The measured cross section and the full simulation show reasonable agreement at the limits of the spectrum, but there is a striking disagreement in shape and magnitude over most of the missing energy range. The measured cross section is approximately four times larger than the simulation at the central missing energy. A second important feature is that the simulated and measured cross sections are relatively small compared to those measured at lower p_m (higher p_p), as seen by comparing Figure 5-25 to Figure 5-23. Even without radiative corrections, the measured cross section at the 855/500 kinematics is approximately 10^{-10} fm^2 (1 picobarn), which is about a factor of ten smaller than the cross section measured at lower p_m. With this reduction in the magnitude of the cross section one might expect an increased sensitivity to background.

A closer look at other aspects of this data set revealed that there is a large (coincident) background contribution to the measured cross sections at these kinematics. Figure 5-26 shows a histogram of the proton angle in the vertical plane, which is strongly peaked near the edges of the collimator for the real coincidences, in contrast to the accidental coincidences, which have a relatively flat distribution spanning the width of the collimator (± 70 mrad). This peaking of θ_{tgt} suggests that many of the coincident protons were rescattered from the collimator edges.

From our measurements at higher proton momentum, we know that there are many coincident high-momentum protons from the 2-body breakup and low missing-energy region. From the coincidence timing spectrum (for example, Figure 5-2) of these measurements we know that most of these protons are real coincidences and very few are accidentals. When the proton spectrometer is set at a lower momentum, these high-momentum protons are coincident with the detected electron, but would normally not be detected since they have momenta above the acceptance. However, if the protons lose energy by passing through the collimator material they can then fall into the momentum acceptance and appear as good coincidences. The fact that most of the high-momentum protons are real coincidences explains why the θ_{tgt} peaking is seen only in the real coincidence spectrum, and not in the accidental coincidences: if the
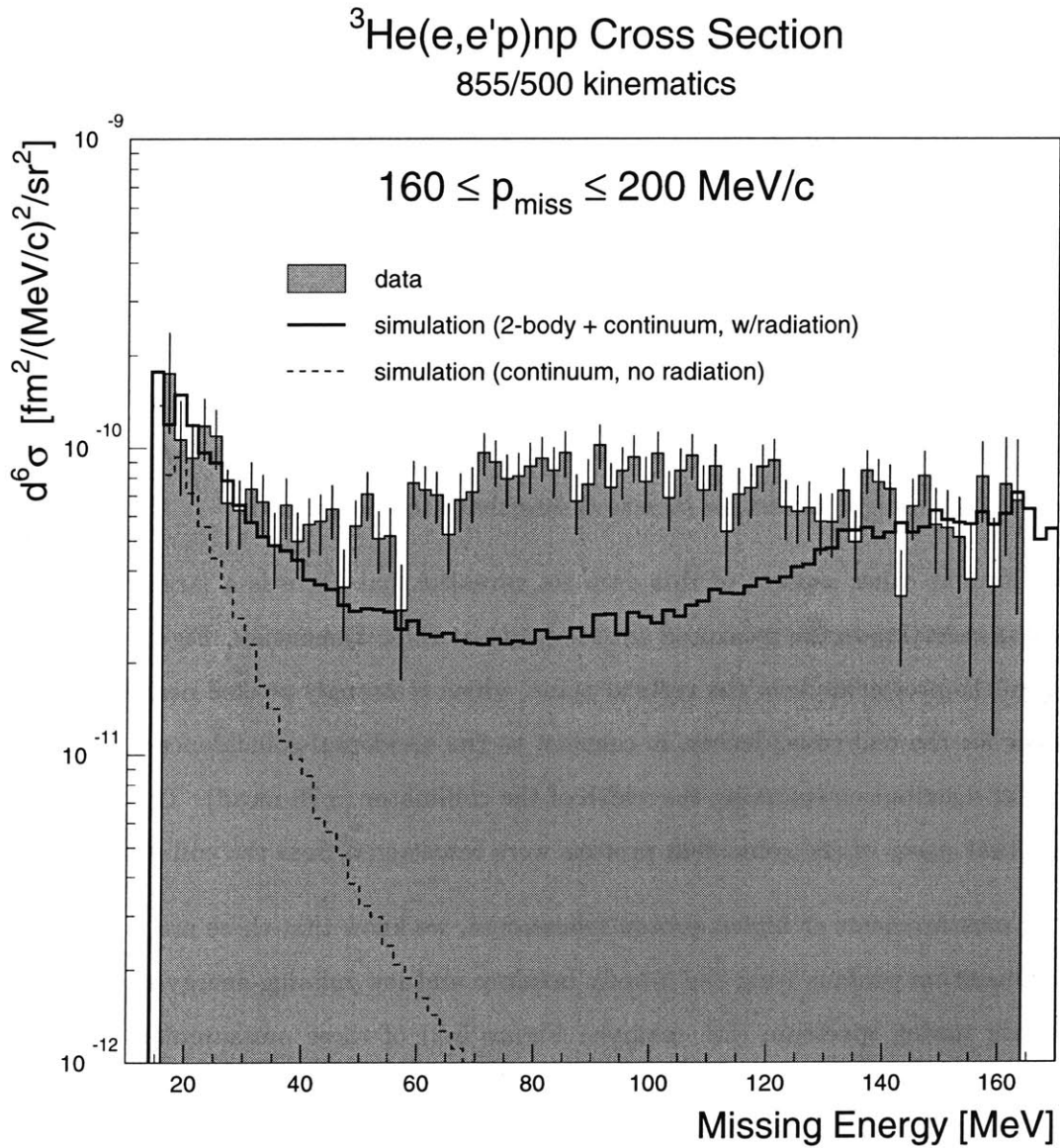
Figure 5-25: Experimental ^{3}He(e,e'p) cross section (measured in 855/500 kinematics) without radiative corrections vs. simulation. Data and simulation are for $p_m = 180 \pm 20$ MeV/c. The input for the simulation is the spectral function of Salme [45] scaled by 0.84.
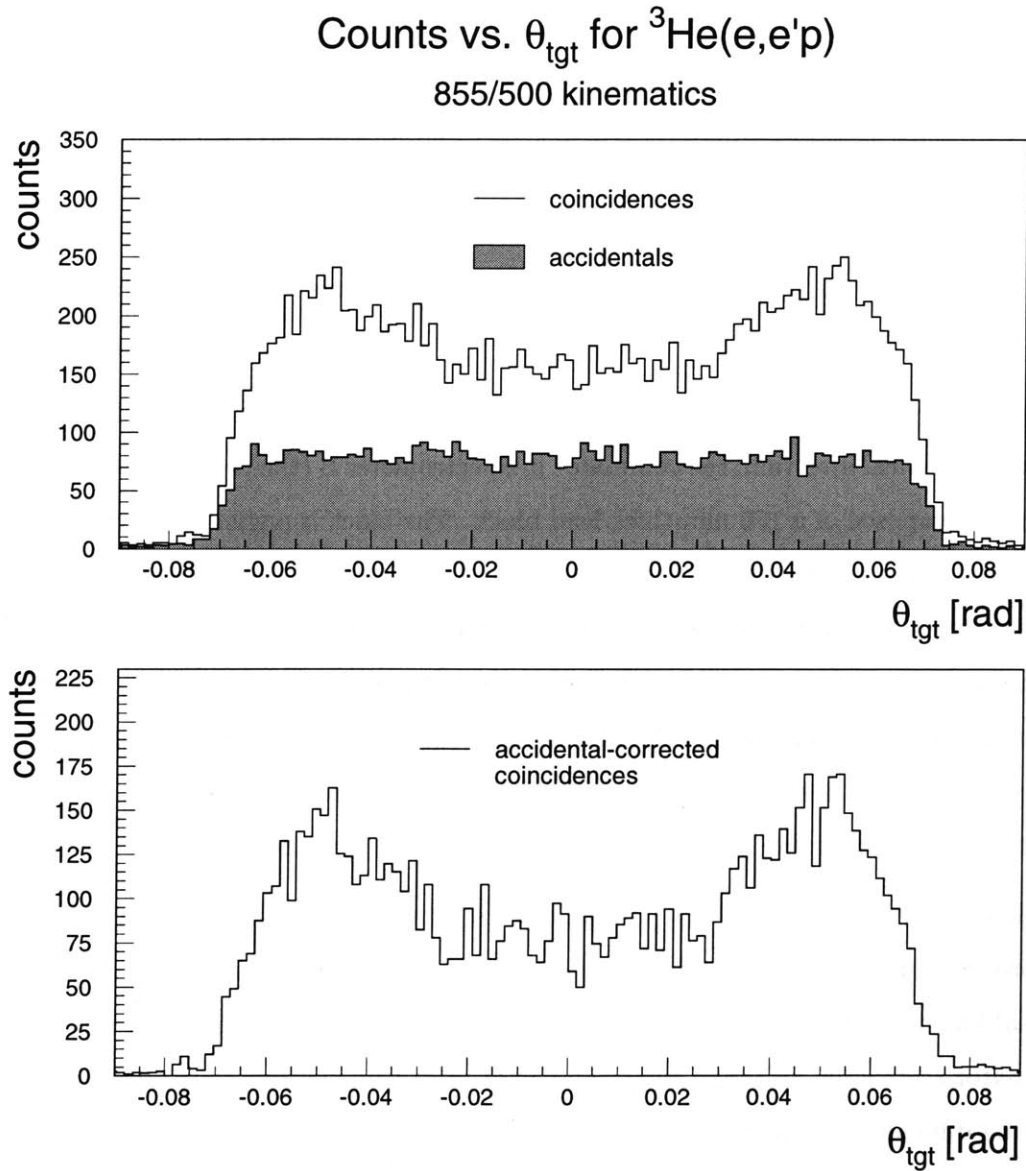
Figure 5-26: The vertical angle of the detected proton (θ_{tgt} in the transport notation) for ^{3}He(e,e'p) at the 855/500 kinematics. The upper plot is for coincidence events with a foreground (solid line, labelled "coincidences") and a background (shaded region, labelled "accidentals") tdc cut. The background region has been scaled for the foreground/background tdc gate width. The lower plot is the coincidences after accidental subtraction.

high-momentum protons that rescatter from the collimator are real coincidences then they will still be real coincidences after the rescattering from the collimator.

To show that this hypothesis is reasonable, consider that the accidental-corrected ^{3}He(e,e′p) count rate (with the usual cuts in Table 5.1 applied) at the 855/660 kinematics is 2.8×10^6 counts/Coulomb. In comparison, the corresponding rate at the 855/500 kinematics is 3.0×10^4 cts/C, which is a factor of 93 smaller. So there are very many high-momentum coincident protons, and if even $\sim 1\%$ lose energy and fall into the low-momentum acceptance, they will dominate the signal.

A restriction on the number of protons that can rescatter is the energy lost in the collimator material. In the vertical direction, the collimator in Spectrometer B (the proton spectrometer) is predominantly composed of a 156 mm-thick lead block. The block is angled at 70 mrad relative to the horizontal plane, so that its face is parallel to the direction of motion of particles generated at the center of the target and impinging on the collimator edge as shown schematically in Figure 5-27. The momentum of the incident coincident protons is peaked around 685 MeV/c (the value of $|\vec{q}|$). Protons of this momentum cannot pass through the entire collimator, and would have to rescatter and exit the collimator after passing through approximately one-fourth of its thickness to exit with enough momentum to appear in the $p_p = 500$ MeV/c bite.

A full simulation of the energy loss and multiple scattering is required to fully understand the above process, where a small fraction of a large number of high-momentum protons contaminates the real low-momentum events. A detailed simulation might reveal the exact contribution of the collimator scattering, although the large size of the effect suggests that correction of the data would be difficult. As this thesis went to press, there was speculation [47] that the value of the collimator rotation angle shown in Figure 5-27 was significantly less that 70 mrad. This would increase the exposed surface area of the collimator and therefore enhance the collimator scattering effect that we have observed. Without a simulation, strong evidence of the hypothesis is provided by the θ_{tgt} spectra themselves, which show a distinct peaking around the collimator edges at all the $p_p = 500$ and 425 MeV/c kinematics, for both ^{3}He (Figure 5-28) and ^{4}He (Figure 5-29). It is hard to imagine that this peaking could be due to valid (un- re-scattered)
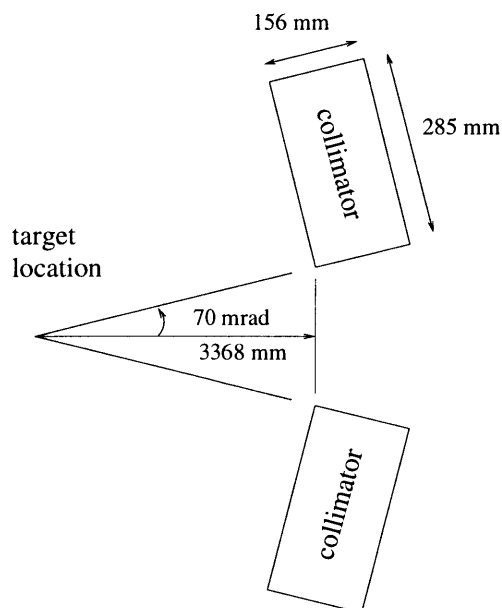
Figure 5-27: A schematic of the Spectrometer B collimator (not drawn to scale) in the vertical plane.

(e,e′p) events. Even if the hypothesis of collimator rescattering is not the complete picture, it seems very likely that the peaking in θ_{tgt} comes from some background process and so should be excluded.

In all cases the peaking is a large contribution to the spectrum, and in some cases the central θ_{tgt} region has very few counts, indicating that the collimator rescattering completely dominates the spectrum. For this reason these data were not analyzed any further and are not included in the final data set. A rough upper limit on the ^{3}He(e,e′p) cross section at the 855/500 kinematics is provided by Figure 5-25, where the cross section is less than 10^{-10} fm^2/(MeV/c)^2/sr^2 over the given missing energy and missing momentum interval.
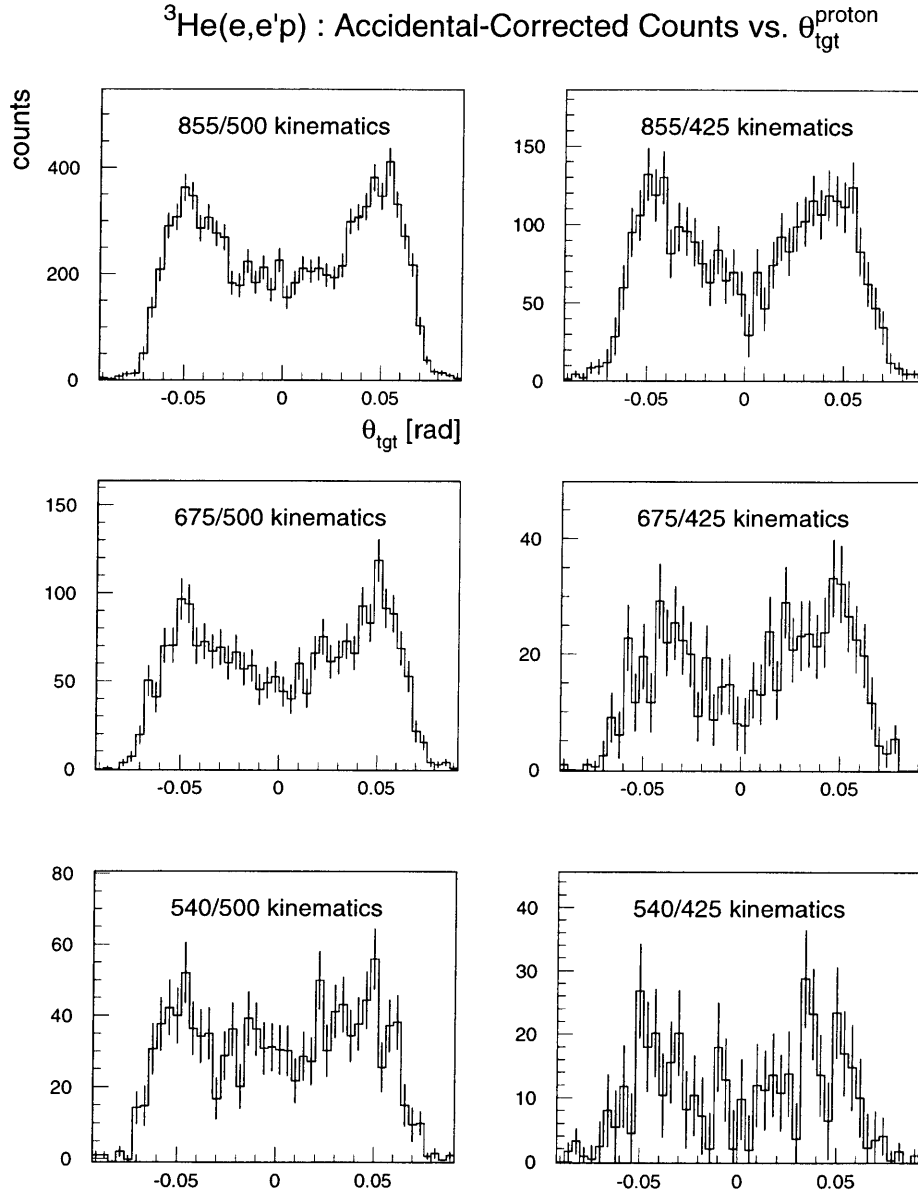
Figure 5-28: The vertical angle of the detected proton (θ_{tgt} in the transport notation) for ^{3}He(e,e′p) for all $p_p = 500$ (left plots) and $p_p = 425$ (right plots) MeV/c kinematics. The software data cuts for the 855/500, 855/425, 675/500 and 540/500 kinematics are the standard ones given in Table 5.1, with the exception of a ±90 mrad cut on θ_{tgt} of the proton. The cuts in the 540/425 and 675/425 kinematics were similarly defined, but loosened in two variables (no ϕ^e_{tgt} cut, and $|z_{react}| \leq 2.5$ cm) to improve the statistical uncertainty.

^{4}He(e,e'p) : Accidental-Corrected Counts vs. θ_{tgt}^{proton}
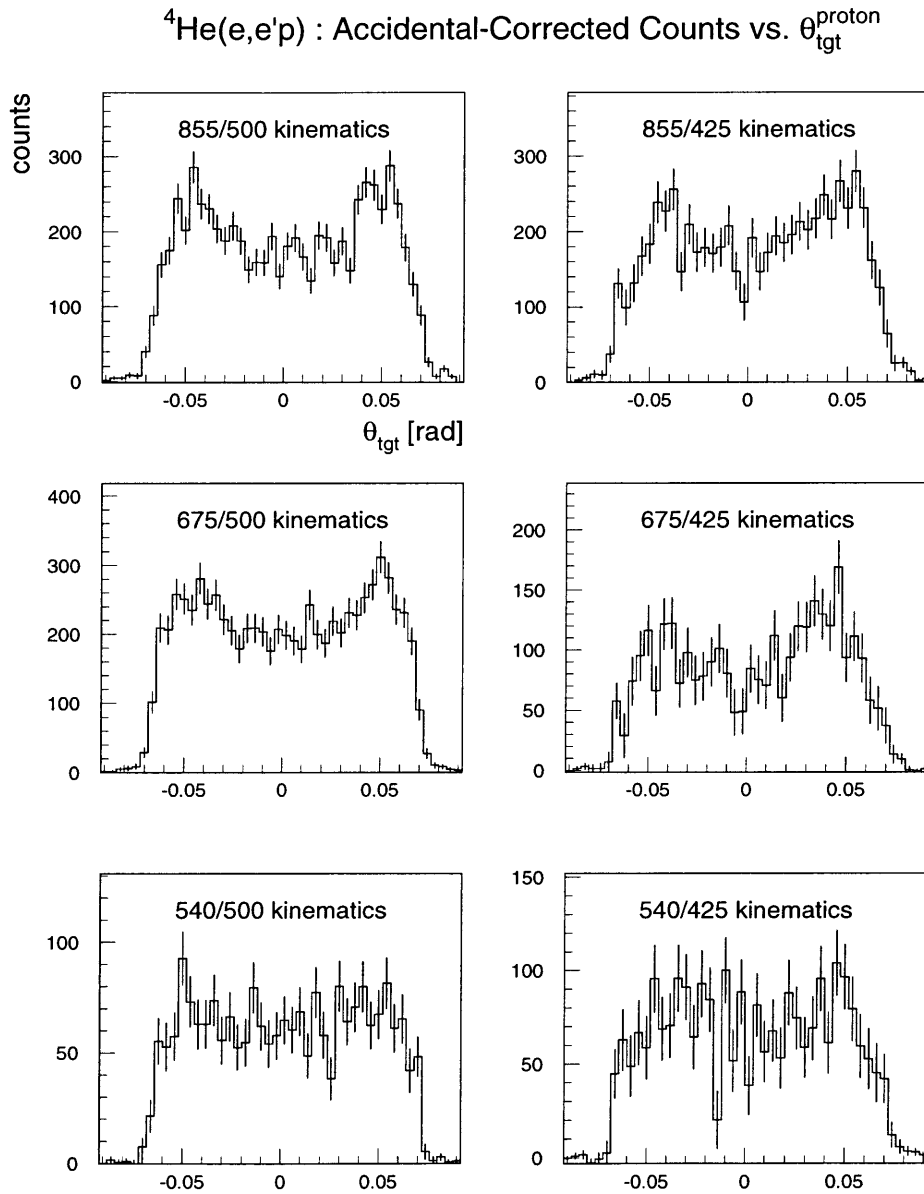
Figure 5-29: The vertical angle of the detected proton as in Figure 5-28, but for ^{4}He instead of ^{3}He.

Chapter 6

Results

Overview

The analysis techniques presented in the previous chapters were used to extract absolute ^{3}He(e,e'p) and ^{4}He(e,e'p) cross sections and spectral functions from the experimental data. Results obtained for the two-body breakup and continuum channels are presented here.

The full kinematics of the measurements were given in Tables 3.3 and 3.4 in Chapter 3. The complete data set included (e,e'p) measurements on ^{3}He and ^{4}He at three nominal values of the beam energy (540, 675, and 855 MeV), corresponding to three different values of the virtual photon polarization, ϵ. At each of these beam energies, measurements were performed at 4 nominal values of the proton momentum: 660, 585, 500, and 425 MeV/c. The measurements taken at the two lowest proton momentum settings (500 and 425 MeV/c) were found to be dominated by protons rescattering from the collimator edges (as discussed in Chapter 5) and so are not included in the final results. The final results therefore consist of only the other two proton momentum settings ($p_p = 660$ and 585 MeV/c), which were combined into a single (E_m, p_m) spectrum at each beam energy as described in Chapter 5. The final results are therefore referred to by their beam energy, so that, for example, "855 MeV" kinematics corresponds to the combined results of the measurements taken at $p_p = 660$ and $p_p = 585$ MeV/c at a beam energy of 855 MeV (in the nomenclature of Tables 3.3 and 3.4, this is the "855/660" and "855/585" kinematics combined).

This chapter is broken up as follows. Examples of the missing energy spectra are presented and their general features discussed in section 1. In section 2, 5-fold differential cross sections

and momentum distributions for the 2-body breakup channels are presented. The momentum distributions obtained are compared to previous measurements and to PWIA calculations. In section 3, six-fold differential cross sections and spectral functions are presented for the continuum channel and compared to various PWIA calculations.

6.1 Missing Energy Spectra

6.1.1 ^{3}He(e,e′p) Missing Energy Spectrum

The theoretical missing energy spectrum for the ^{3}He(e,e′p) reaction has two main features: a delta function at $E_m = 5.49$ MeV, corresponding to the two-body breakup ^{3}He(e,e′p)^{2}H, and a continuum starting at $E_m = 7.72$ MeV, corresponding to the 3-body breakup ^{3}He(e,e′p)np and containing the excitation of the unbound singlet S-state of the deuteron. Higher missing energies correspond to higher relative kinetic energies of the undetected neutron and proton.

A sample of the measured spectrum is shown in Figure 6-1, which shows the cross section before and after radiative unfolding is applied. The two-body and three-body regions are clearly visible, and the high missing-energy region ($E_m > 20$ MeV) has zero strength after radiative unfolding. The data are for a fixed missing momentum slice of $p_m = 100 \pm 60$ MeV/c and were measured in the $E_{beam} = 855$ MeV kinematics, and the spectra measured at the other two beam energies ($E_{beam} = 540$ and 675 MeV) have a similar shape. The data at low missing energy ($E_m < 6.75$ MeV) have been scaled by one-tenth as indicated to make the entire missing energy range visible on one graph. The 2-body breakup peak is centered at 5.49 MeV and has a finite width (approximately 0.5 MeV FWHM) due to the overall energy resolution of the experiment. At missing energies above the 2-body peak but below the threshold of the continuum channel ($5.5 < E_m < 7.7$ MeV), the measured strength is due to the radiative tail from the 2-body breakup and is largely removed in the radiative unfolding procedure (this region is shown in more detail in Figure 6-2). Above this region, the ^{3}He(e,e′p)np continuum channel starts at 7.7 MeV, where the cross section rises sharply. This peaking just above the 3-body threshold is identified with the singlet $^1S_0$ state of the unbound np system. The measured cross section

then falls rapidly with increasing missing energy and is finally dominated by the radiative tail at high missing energy.

Above 25 MeV the radiative-corrected cross section is less than zero when the 2D radiative-unfolding procedure is applied (upper plot, Figure 6-1). This is due to uncertainty in the trajectory of the radiative tails in the (E_m, p_m) plane, as discussed in Chapter 5. A Monte Carlo simulation of the radiative effects in this region (presented in Chapter 5) using a normalized theoretical spectral function confirmed that the measured strength is entirely due to radiative tail, so that the radiative-corrected ^{3}He(e,e'p)np cross section is consistent with zero within our precision for $E_m > 20$ MeV.

The uncertainty in radiative unfolding that generates this negative result at high missing energy also introduces some uncertainty in the radiative-unfolded results at lower missing energy ($E_m < 20$ MeV). However, this uncertainty at low E_m is much less than at high E_m. To estimate this uncertainty, the radiative unfolding was done a second time with a simplified "2DFPM" ("2-Dimensional at Fixed p_m") technique as discussed in Chapter 5. In this technique, p_m was held constant for each radiative tail. The trajectories shown in Figure 5-17 were then simply horizontal lines in the (E_m, p_m) plane. By ignoring the change in p_m, this technique provides an estimate of the error introduced by uncertainty in the (E_m, p_m) trajectories in the 2D unfolding technique. A sample spectrum with this 2DFPM unfolding is shown in the lower plot of Figure 6-1. The measured continuum cross sections and spectral functions presented in this chapter are given for both the 2D and 2DFPM unfolding techniques. The difference between the two results is an estimate of the uncertainty in the radiative unfolding procedure.

6.1.2 ^{4}He(e,e'p) Missing Energy Spectrum

The theoretical ^{4}He(e,e'p) missing energy spectrum also features a two-body breakup peak and a continuum region, with the two-body breakup channel ^{4}He(e,e'p)^{3}H appearing at $E_m =$ 19.81 MeV. The continuum contains two reaction channels: the three-body breakup ^{4}He(e,e'p)^{2}Hn starting at $E_m = 26.07$ MeV and the four-body breakup ^{4}He(e,e'p)nnp starting at $E_m =$ 28.30 MeV.
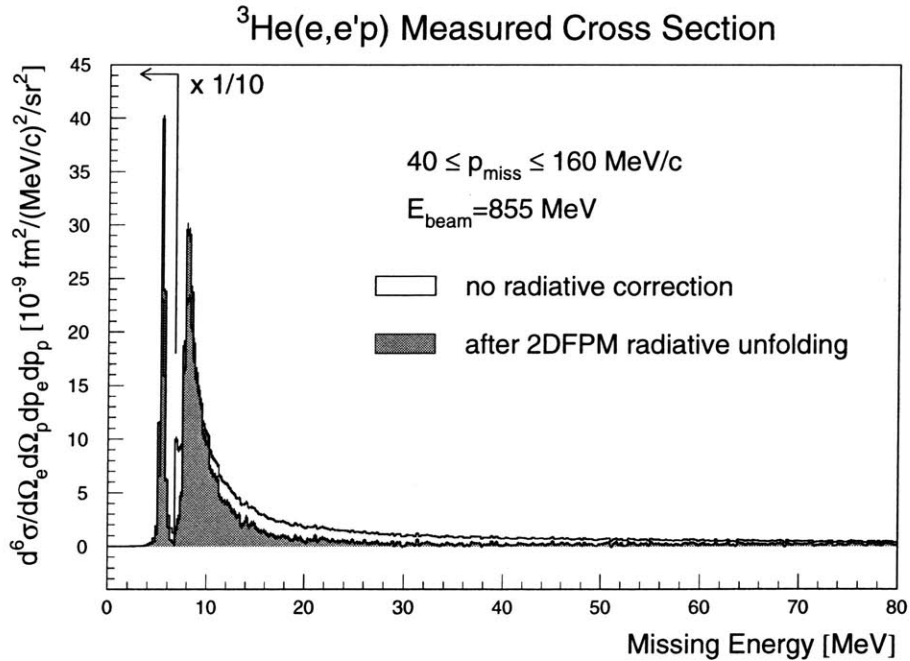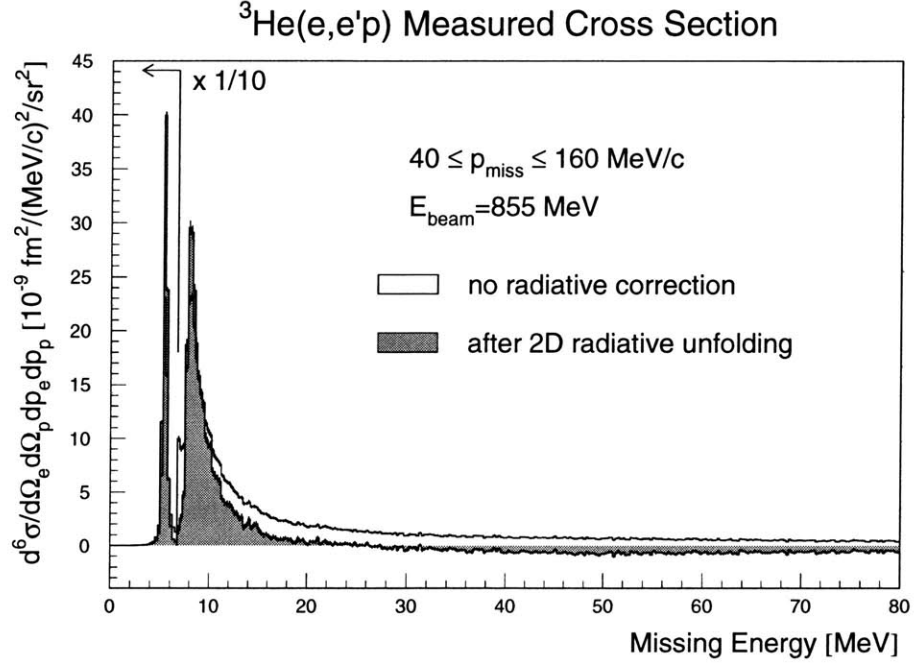
Figure 6-1: Measured ^{3}He(e,e$'$p) cross section as a function of missing energy for $E_{beam} = 855$ MeV and $p_m = 100 \pm 60$ MeV/c, with 2D (upper plot) and 2DFPM (lower plot) radiative unfolding (see text).
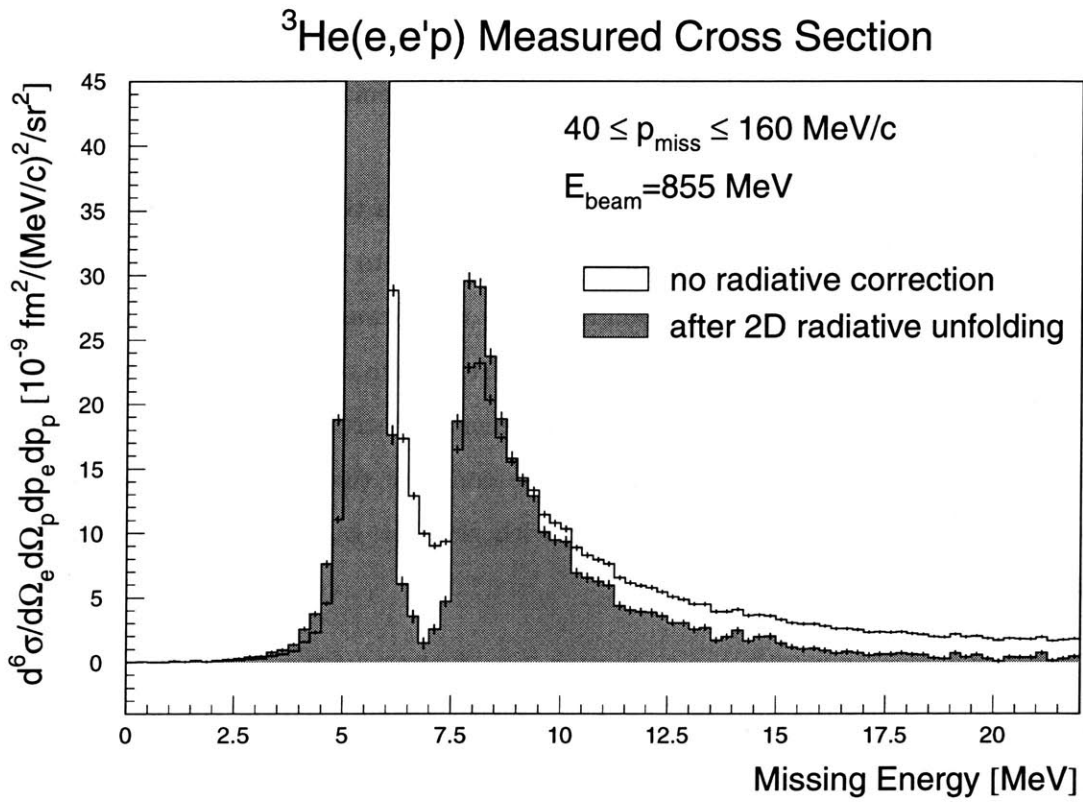
Figure 6-2: Measured ^{3}He(e,e'p) cross section with 2D radiative unfolding as in Figure 6-1, but showing only the low missing energy region.

A sample of the measured missing energy spectrum is shown in Figure 6-3 for kinematics similar* to the ^{3}He data in Figure 6-1. The data at low missing energy ($E_m < 21.5$ MeV) have been re-scaled by a factor of one-fiftieth as indicated to fit the data on one plot. The measured strength in the unphysical region between the two-body peak (19.8 MeV) and the continuum threshold (26.1 MeV) is largely removed by the radiative corrections, so that the two regions are cleanly resolved. The size of the two-body peak is very large relative to the continuum, so that the contribution of the radiative tail from the two-body peak to the continuum is also very large. This large radiative correction introduces a larger systematic uncertainty in the final continuum cross sections.

The radiative-unfolded cross section tends to go negative (in the 2D unfolding) or positive (in the 2DFPM unfolding) at higher missing energy, similar to the ^{3}He results. In ^{3}He a simulation confirmed that the measured strength in this region was indeed all due to radiative tail, so that the radiative-corrected cross section is consistent with zero. Based on the similarity of the ^{3}He and ^{4}He unfolding results at high missing energy (fluctuating between positive and negative depending on the unfolding technique), we conclude that at these kinematics the continuum ^{4}He(e,e'p) cross section is consistent with zero for $E_m > 45$ MeV without any additional simulation.

6.2   Two-Body Breakup Reaction Channels

Five-fold differential cross sections for the two-body breakup reactions considered, ^{3}He(e,e'p)^{2}H and ^{4}He(e,e'p)^{3}H, were determined by integrating the six-fold differential experimental cross section over the two-body missing energy peak as described in section 5.6.2. Similarly, measured momentum distributions were obtained by integrating the experimental spectral function over the peak. The limits of the missing energy integration were $4.0 < E_m < 7.0$ MeV for ^{3}He and $16.7 < E_m < 23.0$ MeV for ^{4}He.

---

*Note that for the same beam energy, the ^{3}He kinematics and ^{4}He kinematics differ slightly. See Tables 3.3 and 3.4 for the full kinematics.
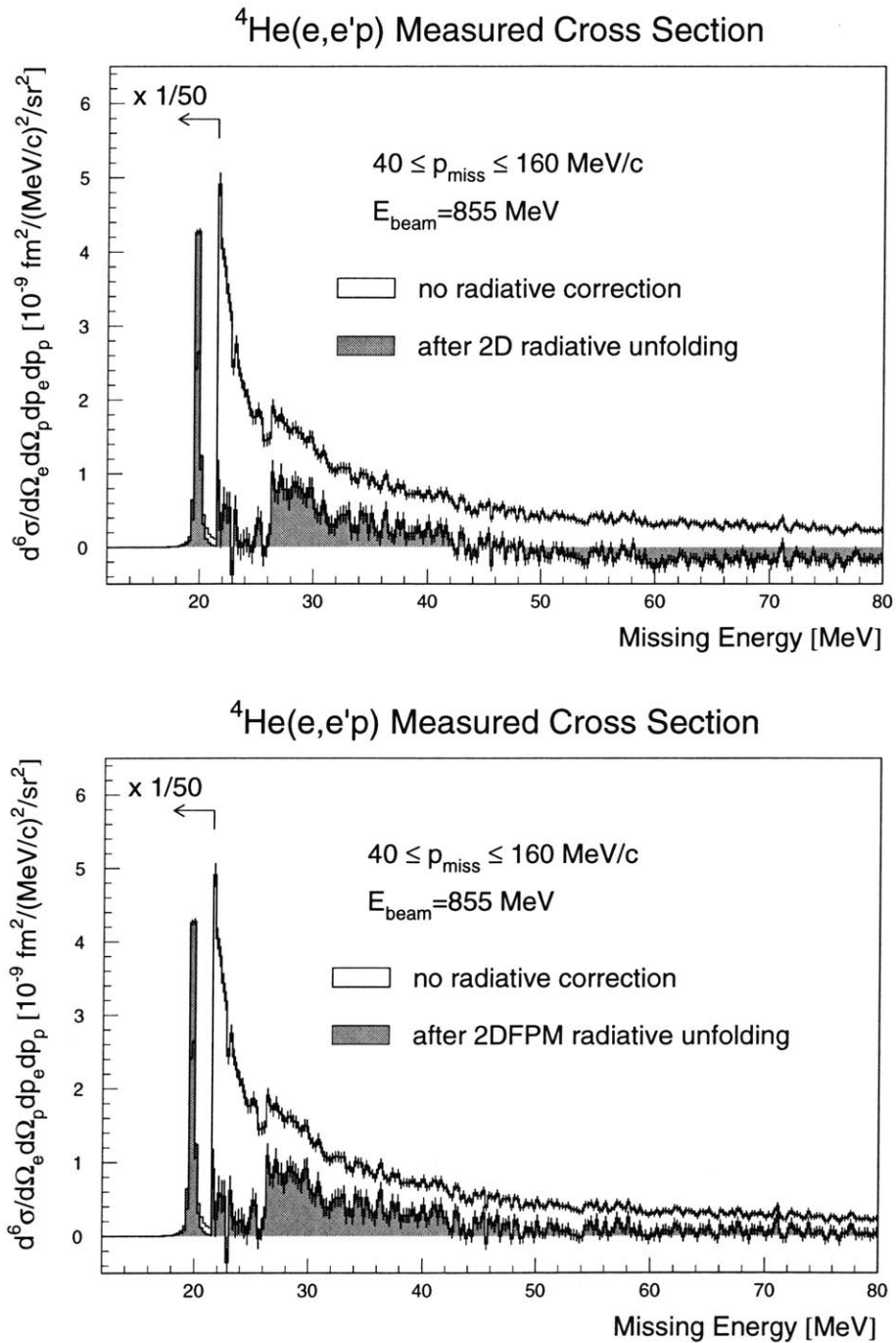
Figure 6-3: Measured ^{4}He(e,e$'$p) cross section as a function of missing energy for E$_{beam}$ = 855 MeV and p_m = 100 ± 60 MeV/c, with 2D (upper plot) and 2DFPM (lower plot) radiative unfolding (see text).
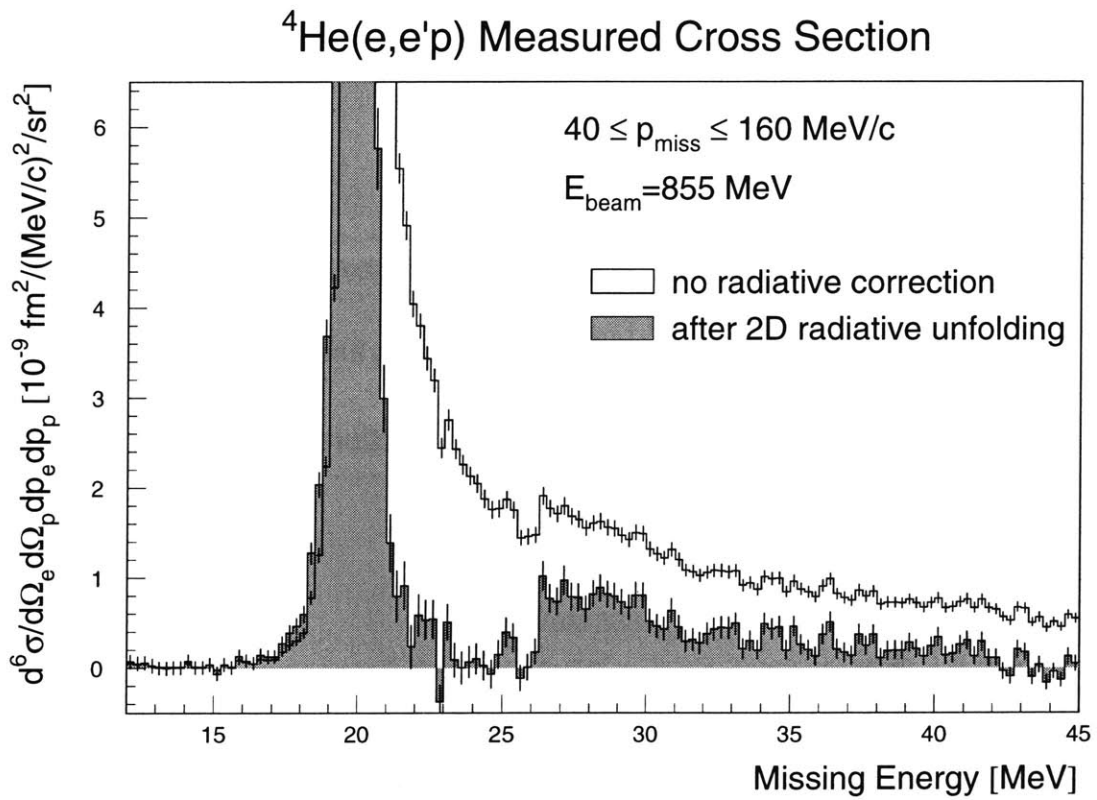
Figure 6-4: Measured ^{4}He(e,e$'$p) cross section with 2D radiative unfolding as in Figure 6-3, but showing only the low missing energy region.

p_{miss}	Cross Section $[10^{-9} \text{ fm}^2(\text{MeV/c})^{-1}\text{sr}^{-2}]$		
[MeV/c]	540	675	855
15.0	352.13 ± 5.93	740.39 ± 13.24	1534.35 ± 32.11
25.0	308.57 ± 3.65	666.62 ± 8.24	1444.84 ± 21.13
35.0	271.77 ± 2.92	558.31 ± 6.14	1215.00 ± 15.62
45.0	216.52 ± 2.50	476.97 ± 5.66	998.45 ± 12.20
55.0	162.07 ± 2.35	370.06 ± 4.89	775.83 ± 9.38
65.0	120.15 ± 2.29	257.56 ± 3.73	571.27 ± 7.26
75.0	87.08 ± 2.10	179.58 ± 2.88	398.48 ± 5.64
85.0	61.71 ± 1.95	136.39 ± 2.46	283.52 ± 4.70
95.0	46.98 ± 2.58	95.00 ± 2.03	203.70 ± 3.96
105.0		71.27 ± 2.04	147.84 ± 3.38
115.0		53.90 ± 2.23	102.11 ± 2.95
125.0		37.26 ± 2.53	87.08 ± 3.22
135.0			54.78 ± 2.74
145.0			38.34 ± 2.54
155.0			29.25 ± 2.64
165.0			16.87 ± 2.53

Table 6.1: Measured ^{3}He(e,e'p)^{2}H cross sections.

6.2.1 ^{3}He(e,e'p)^{2}H

The measured cross sections for ^{3}He(e,e'p)^{2}H as a function of missing momentum are presented in Table 6.1 and Figure 6-5 for each of the 3 beam energies. The errors given in the table and shown in the figure are statistical only, and the absolute systematic uncertainties are 5–6% as discussed at the end of this chapter. The statistical error bars are too small to be visible in the figure, except for the first few points at 855 MeV. The shape of the measured cross section vs. missing momentum is similar in all three kinematics, although the magnitude varies by a factor > 4 from the lowest to the highest beam energy.

The measured momentum distributions for the same data are presented in Figure 6-6 and Table 6.2. As with the cross section data, the errors given are statistical only, and the systematic uncertainty is 5–6%. If PWIA is valid, the measured momentum distributions should be a function of p_m only and should therefore be independent of the kinematics. The measured momentum distributions at the three kinematics are indeed very similar, indicating that most
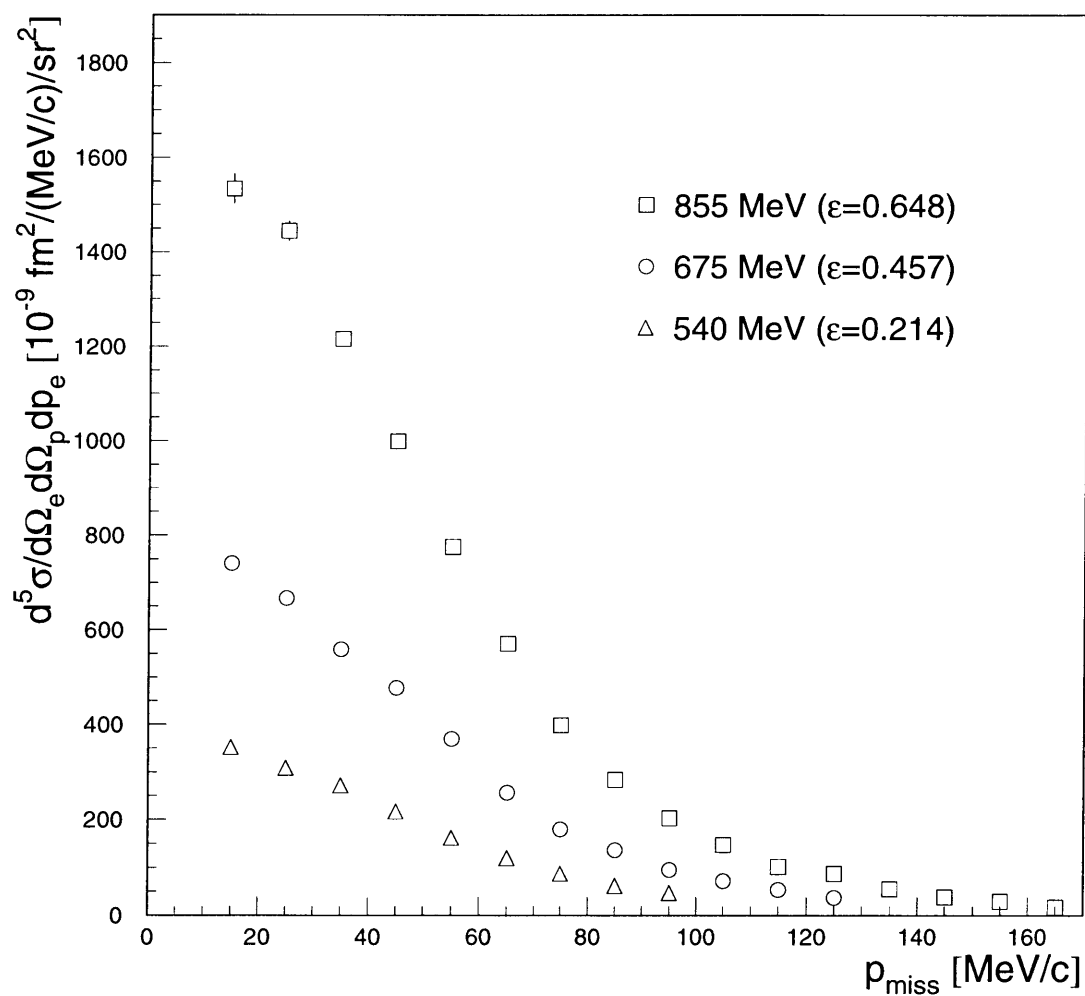
Figure 6-5: Measured ^{3}He(e,e$'$p)^{2}H cross sections as a function of missing momentum for the three beam energies.

of the kinematic dependence has been removed by dividing the cross sections by $p_p^2 \sigma_{ep}^{CC1}$, where σ_{ep}^{CC1} is one of de Forest's [18] prescriptions for the off-shell electron-proton cross section. To compare the momentum distributions measured at our three kinematics, the ratio of each data set to the average result is plotted in Figure 6-7. A systematic dependence on the virtual photon polarization (ϵ) is observed, with the magnitude of the measured momentum distribution increasing with ϵ.

To compare the overall magnitude of the data sets to each other and to theory, we have evaluated the following dimensionless integral:

$$N = 4\pi \int_{10}^{100} \rho_2(p_m) \cdot p_m^2 dp_m \tag{6.1}$$

where the limits ($10 < p_m < 100$ MeV/c) of the integral correspond to the region of overlap of the three data sets. The results are superimposed on Figure 6-6 with their corresponding statistical uncertainties.

Compared to the value of N obtained from the 675 MeV data set, the values at 855 MeV and 540 MeV are 7.2% larger and 5.1% smaller, respectively. The magnitude of the measured momentum distribution is observed to increase with the virtual photon polarization, ϵ, indicating that the ratio (L/T) of the longitudinal (L) and transverse (T) response functions is larger than that given by σ_{CC1}^{ep}. However, we note that the systematic uncertainty in comparing our measurements to each other is 5–6%, which is comparable to the observed ϵ-dependence.

The data[†] of Jans *et al.* [48] from Saclay are also shown for comparison. The error bars shown for these data correspond to the total uncertainty (statistical plus systematic). Although the data were measured at a lower momentum transfer ($q \approx 430$ MeV/c) and in (nominally) perpendicular kinematics ($\vec{p}_m \perp \vec{q}$), they agree well with our measurements, particularly at higher p_m. We calculate the virtual photon polarization at the center of their kinematic setting to be 0.65, which is similar to the value at our 855 MeV kinematics ($\epsilon = 0.648$). From Jans' data, we determine a value of $N = 0.587$, which is 3.8% below the value at our 855 MeV

[†]The data shown are from Jans' "kinematics I".

kinematics ($N = 0.610$) and 2.4% larger than the average value ($N = 0.573$) from all three of our kinematics. The total uncertainty in N for Jans' data is difficult to calculate since the uncertainties given for his data are the sum of statistical and systematic uncertainties. However, their paper (Ref. [48]) quotes an uncertainty of 5% in the absolute normalization, so that we estimate the uncertainty in N calculated from their data to be 5% or greater. The values of N obtained in our experiment are therefore consistent with the value calculated from Jans' data within systematic uncertainty.

Figure 6-6 also shows three theoretical momentum distributions, shown as the solid and dashed lines. The solid line is a cubic-spline interpolation of the two-body part of the theoretical spectral function of Schulze and Sauer [49]. Their spectral function is derived from the Paris nucleon-nucleon potential [50], with the trinucleon bound state wavefunction of Ref. [51] and a continuum wavefunction computed from Fadeev equations. The momentum distribution of Salme [45] is shown as one of the dashed lines, and its values are very similar to Schulze and Sauer over our range of p_m. The Salme momentum distribution was the one used in our simulations of the radiative tail in Chapter 5. The second dashed line is the momentum distribution of Forest *et al.* [52], which was calculated from variational wave functions obtained in a Monte Carlo method using the Argonne v18 [53] nucleon-nucleon potential and the Urbana IX [54] three-nucleon interaction.

All of the calculations have a shape similar to the data. The average value of N for our three kinematics is 0.573, which is 21–23% below the value of N calculated from the theoretical curves. However, we note that a direct comparison of our "experimental momentum distributions" (which is the measured cross section divided by $p_p^2 \sigma_{CC1}^{ep}$) to these theoretical momentum distributions is only valid in the plane-wave impulse approximation (PWIA), which does not include final-state interactions (FSI) between the detected proton and the undetected (A-1) recoil system. An estimate of the final state interactions was obtained for the reaction $^4\text{He}(e,e'p)^3\text{Hp}$ using the HE4PT computer code of R. Schiavilla [55]. The results of the code indicated a 12% reduction in the cross section at our kinematics due to FSI. Although this calculation was for ^4He and not for ^3He, we expect the results to be similar for the two nuclei. Approximately

p_{miss} [MeV/c]	Momentum Distribution [(GeV/c)$^{-3}$]		
	540	675	855
15.0	421.76 ± 7.11	442.57 ± 7.91	464.61 ± 9.71
25.0	368.99 ± 4.36	395.20 ± 4.88	431.99 ± 6.32
35.0	324.73 ± 3.49	330.46 ± 3.64	361.24 ± 4.64
45.0	258.99 ± 2.99	283.08 ± 3.36	296.09 ± 3.62
55.0	197.39 ± 2.86	221.06 ± 2.92	229.50 ± 2.78
65.0	150.33 ± 2.86	157.42 ± 2.28	173.29 ± 2.20
75.0	112.70 ± 2.72	113.14 ± 1.82	125.86 ± 1.78
85.0	82.36 ± 2.61	89.11 ± 1.60	93.18 ± 1.54
95.0	65.16 ± 3.58	65.32 ± 1.39	70.07 ± 1.36
105.0		51.88 ± 1.48	53.12 ± 1.21
115.0		40.73 ± 1.68	38.24 ± 1.10
125.0		29.20 ± 1.98	33.35 ± 1.23
135.0			21.93 ± 1.10
145.0			16.24 ± 1.08
155.0			12.87 ± 1.16
165.0			7.75 ± 1.16

Table 6.2: Measured ^{3}He(e,e'p)^{2}H momentum distributions.

half of the discrepancy between our average value of N and that obtained from the theories is therefore attributed to FSI.

$$^3He(e,e'p)^2H$$

Measured Momentum Distributions
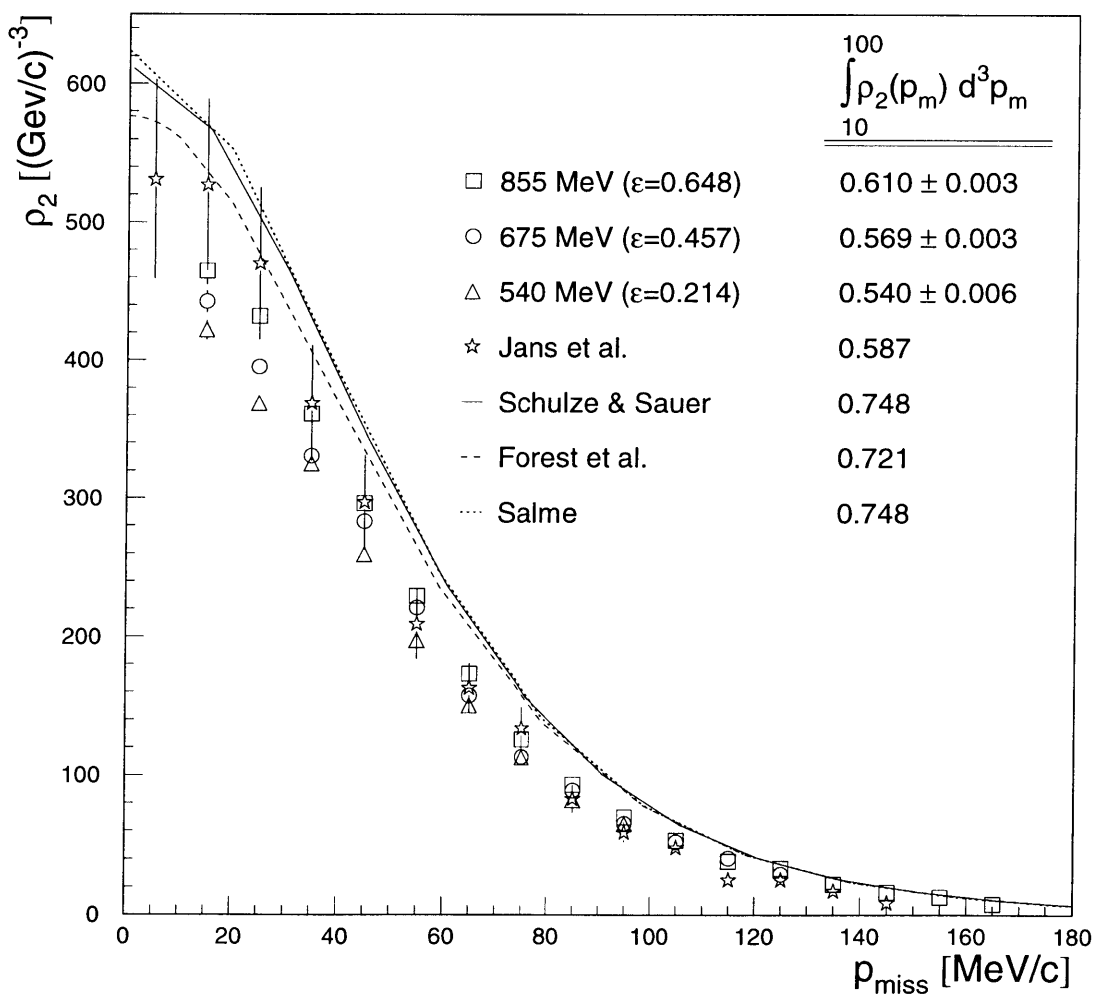
Figure 6-6: Measured $^3He(e,e'p)^2H$ momentum distributions, ρ_2, as a function of missing momentum for the three beam energies.
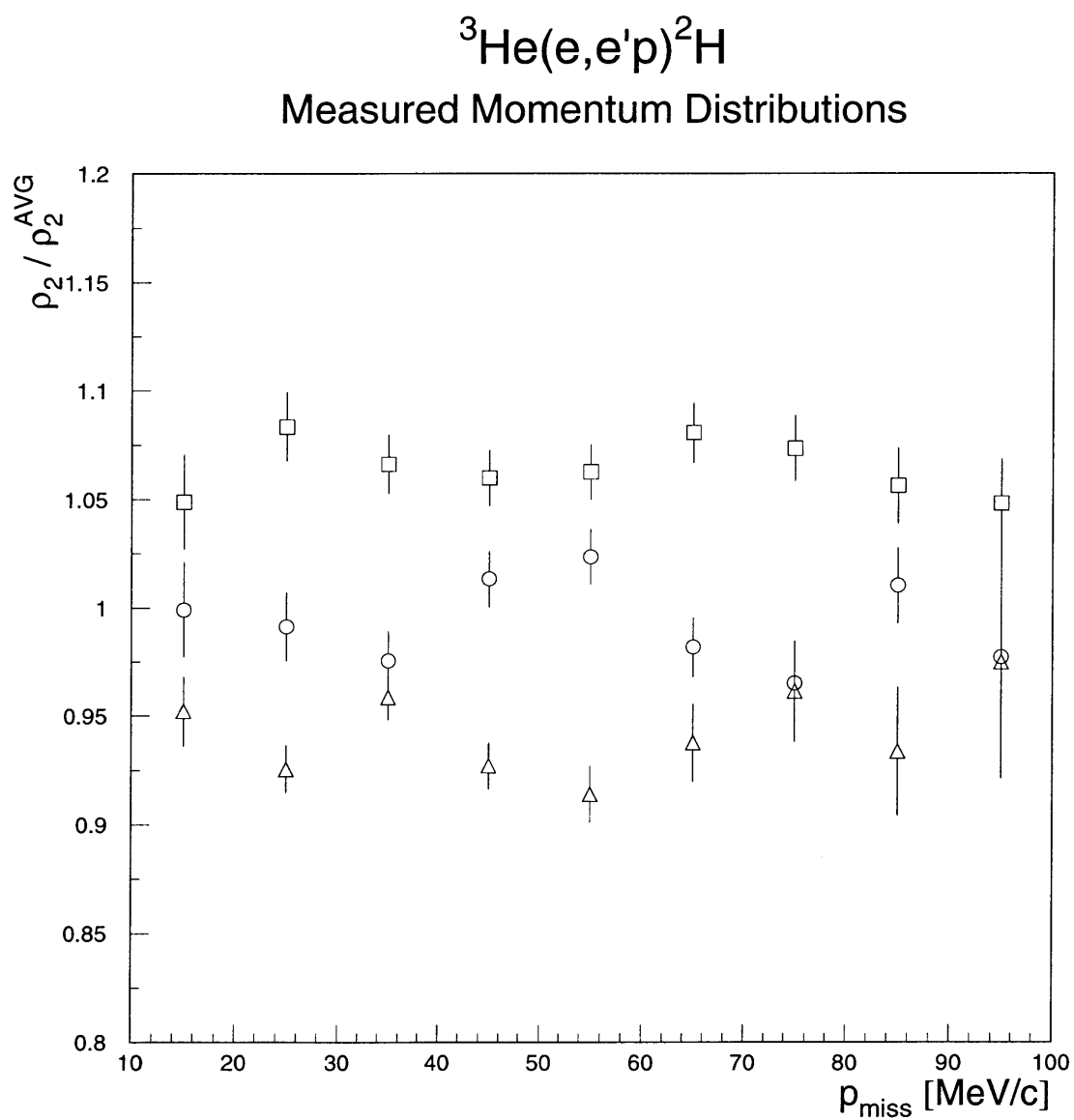
Figure 6-7: Measured ^{3}He(e,e'p)^{2}H momentum distributions compared to average value.

p_{miss} [MeV/c]	Momentum Distribution $[(GeV/c)^{-3}]$		
	540	675	855
15.0	122.70 ± 2.43	238.34 ± 5.25	494.63 ± 12.81
25.0	118.03 ± 1.70	239.40 ± 3.79	490.92 ± 8.35
35.0	115.95 ± 1.56	224.15 ± 3.23	467.33 ± 6.89
45.0	106.07 ± 1.61	216.59 ± 3.32	435.59 ± 6.23
55.0	93.21 ± 1.81	199.13 ± 3.52	391.40 ± 5.51
65.0	74.06 ± 1.76	162.41 ± 3.25	348.21 ± 5.29
75.0	66.17 ± 1.94	129.14 ± 2.67	282.49 ± 4.76
85.0	52.92 ± 2.52	112.19 ± 2.46	229.52 ± 4.23
95.0		98.23 ± 2.56	192.95 ± 3.91
105.0		74.69 ± 2.61	151.13 ± 3.44
115.0		63.82 ± 3.61	130.92 ± 3.57
125.0			116.83 ± 4.04
135.0			82.77 ± 3.50
145.0			65.17 ± 3.70
155.0			54.44 ± 4.10
165.0			43.93 ± 5.02

Table 6.3: Measured $^4He(e,e'p)^3H$ cross sections.

6.2.2 $^4He(e,e'p)^3H$

The measured cross sections for the $^4He(e,e'p)^3H$ reaction channel as a function of missing momentum are presented in Table 6.3 and Figure 6-8. The errors given in the table and shown in the figure are statistical only, and the absolute systematic uncertainties are 5–6% as discussed at the end of this chapter. The statistical error bars are too small to be visible in the figure, except for the first few points at 855 MeV. As with the $^3He(e,e'p)^2H$ results, the shape of the measured cross section vs. missing momentum is similar in all three kinematics, and the magnitude varies by a factor of approximately four from the lowest to the highest beam energy.

The measured momentum distributions for the same data are presented in Figure 6-9 and Table 6.4. As with the cross section data, the errors given are statistical only, and the systematic uncertainty is 5–6%. If PWIA is valid, the measured momentum distributions should be a function of p_m only and should therefore be independent of the kinematics. The measured momentum distributions at the three kinematics are indeed very similar, indicating that most
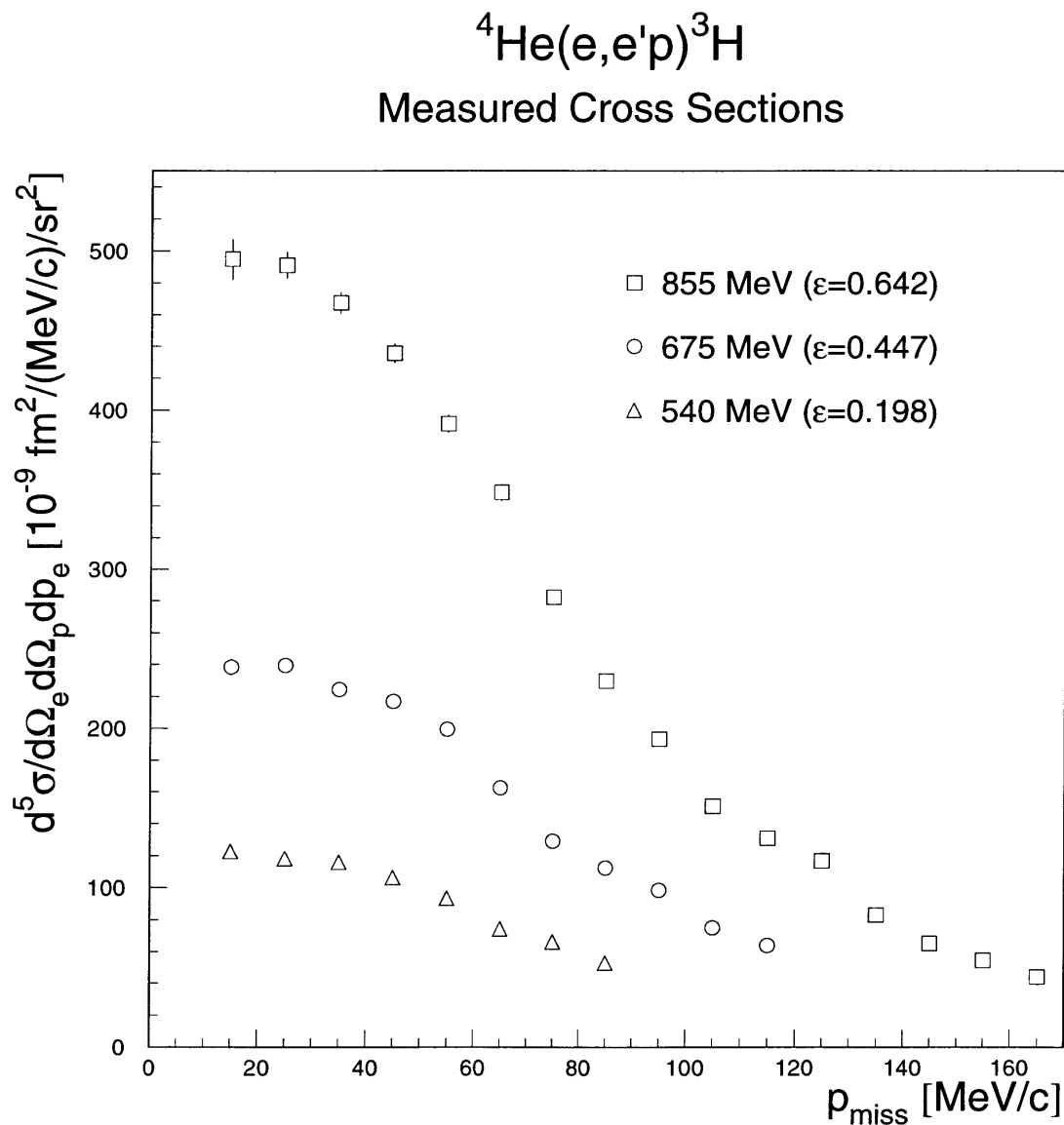
Figure 6-8: Measured ^{4}He(e,e$'$p)^{3}H cross sections as a function of missing momentum for the three beam energies.

p_{miss}	Momentum Distribution [(GeV/c)$^{-3}$]		
[MeV/c]	540	675	855
15.0	153.79 ± 3.04	145.78 ± 3.21	153.01 ± 3.96
25.0	147.89 ± 2.13	145.66 ± 2.30	148.52 ± 2.53
35.0	145.00 ± 1.95	136.73 ± 1.97	141.06 ± 2.08
45.0	133.62 ± 2.03	132.16 ± 2.03	130.87 ± 1.87
55.0	121.37 ± 2.36	123.77 ± 2.19	118.44 ± 1.67
65.0	100.69 ± 2.40	104.24 ± 2.09	108.30 ± 1.65
75.0	93.13 ± 2.73	85.90 ± 1.77	93.15 ± 1.57
85.0	77.56 ± 3.69	78.17 ± 1.71	79.79 ± 1.47
95.0		72.93 ± 1.90	70.18 ± 1.42
105.0		58.97 ± 2.06	58.00 ± 1.32
115.0		52.76 ± 2.98	52.18 ± 1.42
125.0			48.62 ± 1.68
135.0			36.33 ± 1.53
145.0			30.10 ± 1.71
155.0			26.41 ± 1.99
165.0			22.35 ± 2.56

Table 6.4: Measured ^{4}He(e,e′p)^{3}H momentum distributions.

of the kinematic dependence has been removed by dividing the cross sections by $p_p^2 \sigma_{ep}^{CC1}$, where σ_{ep}^{CC1} is one of de Forest's [18] prescriptions for the off-shell electron-proton cross section. To compare the momentum distributions measured at our three kinematics, the ratio of each data set to the average result is plotted in Figure 6-10. In contrast with the ^{3}He(e,e′p)^2H results, no systematic dependence on the virtual photon polarization (ϵ) is observed. Across the measured p_m range in Figure 6-10 the measured momentum distributions are observed to fluctuate about the average value by less than ±5%.

As with the ^{3}He(e,e′p)^{2}H results, to compare the overall magnitude of the data sets to each other and to theory we have evaluated the following dimensionless integral:

$$N = 4\pi \int_{10}^{90} \rho_2(p_m) \cdot p_m^2 dp_m \tag{6.2}$$

where the limits ($10 < p_m < 90$ MeV/c) of the integral correspond to the region of overlap
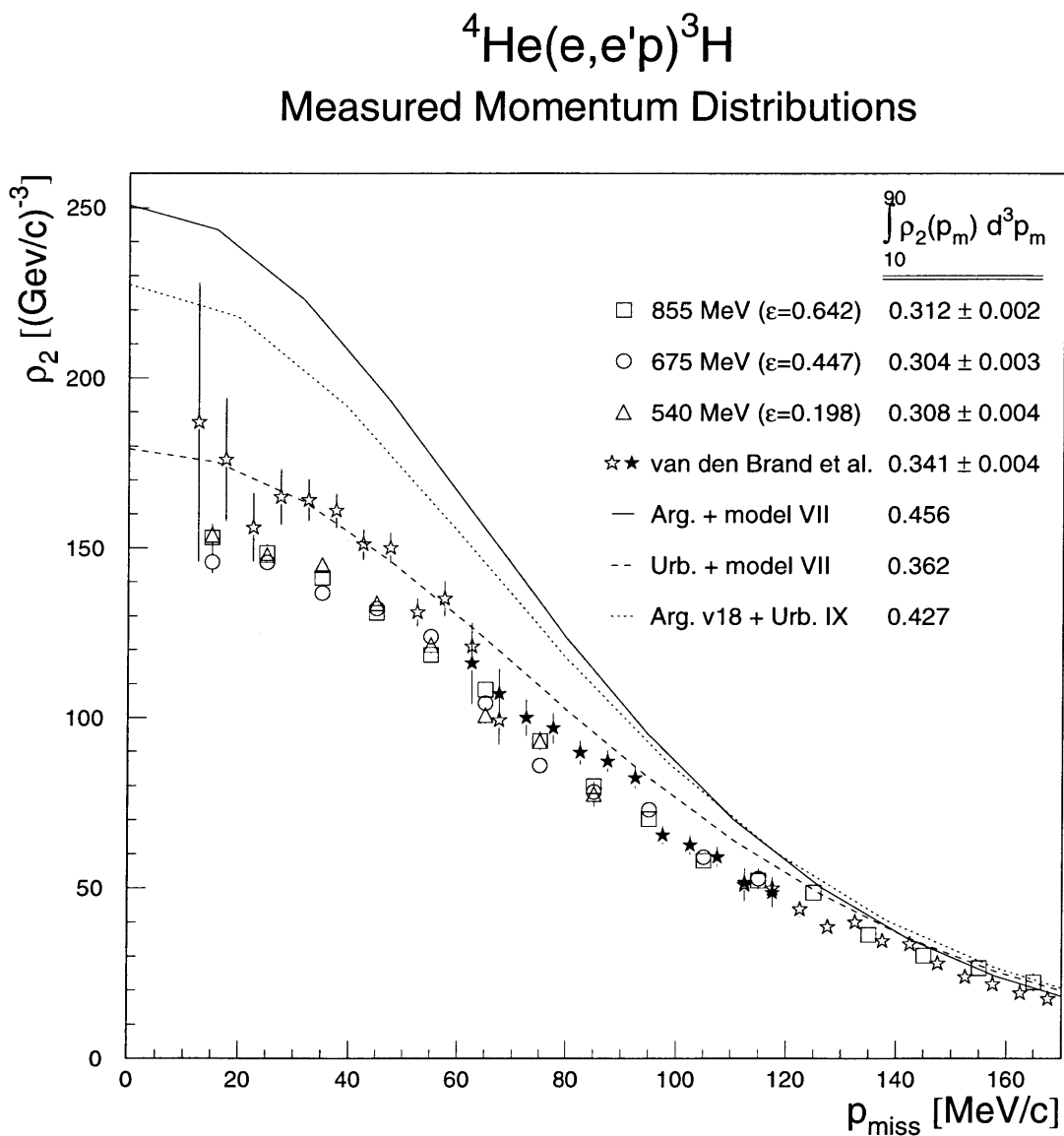
Figure 6-9: Measured ^{4}He(e,e'p)^{3}H momentum distributions, ρ_2, as a function of missing momentum.
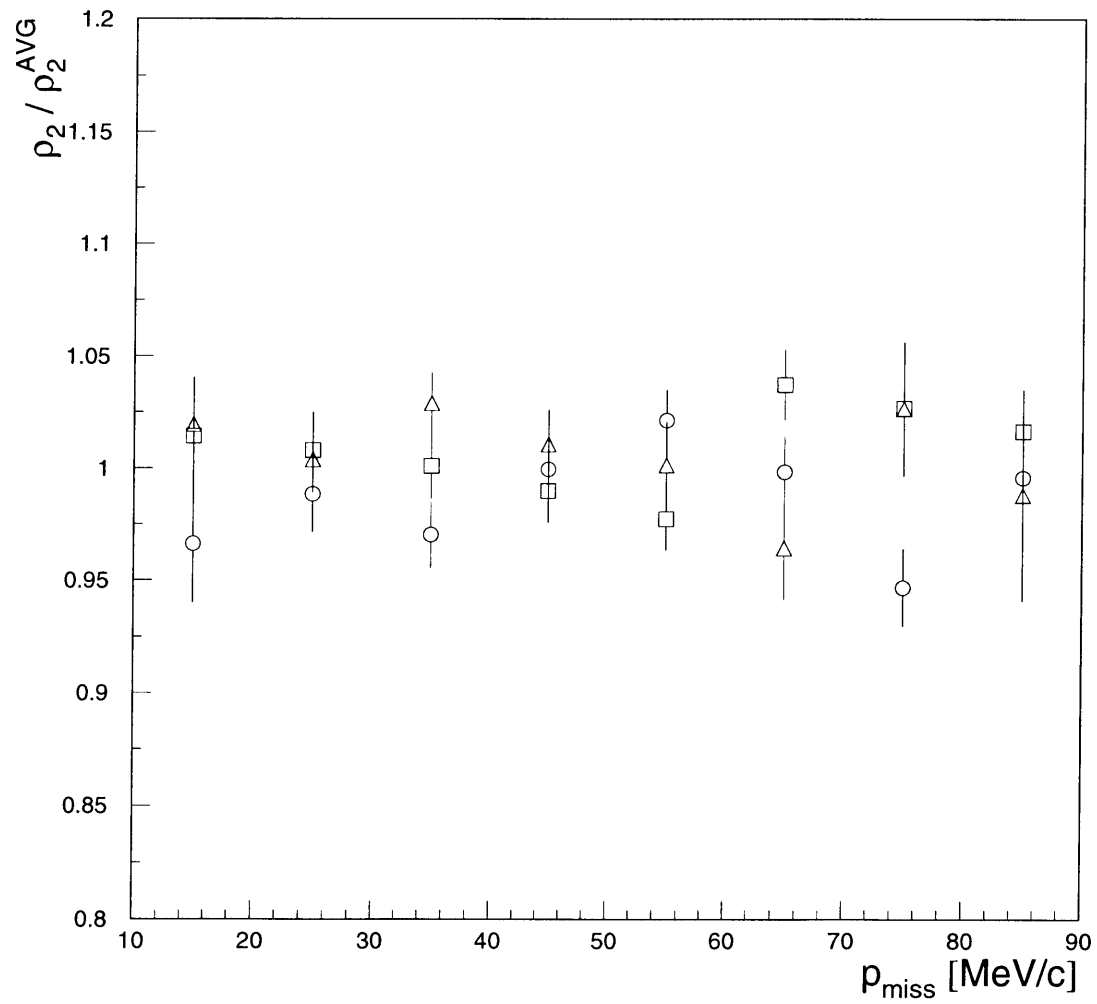
Figure 6-10: Measured ^{4}He(e,e$'$p)^{3}H momentum distributions compared to average value.

of the three data sets. The results are superimposed on Figure 6-9 with their corresponding statistical uncertainties. The value of N obtained is similar at all three of our kinematics, with N varying at most by $\pm 1.3\%$ about the average value (0.308). We also note that the value of N is not directly correlated to the virtual photon polarization (ϵ), with the smallest N obtained at the middle ϵ. Within our estimated systematic uncertainty (5–6%) we conclude that the experimental momentum distribution is independent of ϵ, indicating that the ratio (L/T) of the longitudinal (L) and transverse (T) response functions is the same as σ_{ep}^{CC1}.

In Figure 6-9 the experimental momentum distributions are also compared to previous measurements[‡] made at NIKHEF by van den Brand *et al.* [56, 57]. As with our data, the error bars shown reflect only the statistical uncertainty. Compared to our measurements, these data were measured at a lower momentum transfer ($q \approx 430$ MeV/c) and in (nominally) perpendicular kinematics ($\vec{p}_m \perp \vec{q}$). We calculate the virtual photon polarization at the center of their kinematic setting to be 0.48, which is similar to the value at our 675 MeV ($\epsilon = 0.457$) kinematics. To determine the value of N for these data, the value of ρ_2 at $p_m = 62.5$ and 67.5 MeV/c was computed as the error-weighted average of the data from kinematics A and kinematics B (which overlap at these two values of p_m). We obtain a value of $N = 0.341 \pm 0.004$ (statistical uncertainty only) from their data, which is 12% higher than the corresponding value at our 675 MeV kinematics. For comparison, the absolute systematic uncertainty given for the NIKHEF data is 5.7% (Ref. [57]) and our absolute systematic uncertainty at the 675 MeV kinematics is also 5.7%, as discussed at the end of this chapter. The discrepancy between the NIKHEF measurements and ours is therefore larger than, but comparable to, the total systematic uncertainty. As a function of p_m our data are systematically smoother than the NIKHEF results, but the overall shape is quite similar. We emphasize that a direct comparison of our measurements to the NIKHEF data is only valid in PWIA, since the kinematics of the two experiments differ substantially.

Theoretical calculations of the ^{4}He(e,e$'$p)^{3}H momentum distribution have been performed by Schiavilla *et al.* [58] and, more recently, Forest *et al.* [52] using a Monte Carlo technique.

[‡]The data shown in Figure 6-9 are for kinematics denoted A, B, and C in reference [57].

Two different momentum distributions from Ref. [58] are shown as the solid and coarse dashed lines in Figure 6-9. They were calculated from variational wave functions using either the Argonne or the Urbana model of the nucleon-nucleon potential, and "model VII" of the three nucleon interaction (TNI). The two potentials give quite different results at low p_m, and the calculation using the Urbana potential comes closest to the measured data. Schiavilla [58] notes that the differences in the momentum distribution calculated from the two potentials

> "...appear to be primarily due to the differences in the radii that we calculate with these models."

The third theoretical momentum distribution, shown as the fine dashed line in Figure 6-9, is a more recent calculation from Forest *et al.* [52]. This calculation uses the Argonne v18 [53] nucleon-nucleon potential and Urbana IX [54] three-nucleon interaction, and results in a momentum distribution that, at low p_m, falls between the two other calculations.

A value of N was obtained by integrating each of the calculations, with the results superimposed on Figure 6-9. Our measured values fall significantly below all of the calculations. The average value of N for our three kinematics is 0.308, which is 15–32% below the values obtained from the various calculations. However, as was noted in the discussion of the $^3\mathrm{He}(e,e'p)^2\mathrm{H}$ results, final-state interactions (FSI) were estimated to result in a 12% reduction in the cross section at our kinematics (using the HE4PT computer code of Ref. [55]). Accounting for the effects of FSI, our measured data are therefore 3–20% below the predictions.

6.3 Continuum Breakup Reaction Channels

For missing energies above the two-nucleon knockout threshold (7.72 MeV in ^{3}He and 26.1 MeV in ^{4}He) the final states of the (e,e$'$p) reaction form a continuum in missing energy. Higher missing energy above the the two-nucleon knockout threshold corresponds to higher relative kinetic energies of the undetected reaction products. We have extracted six-fold differential cross sections and spectral functions in this region, corresponding to the reaction channel ^{3}He(e,e$'$p)np, and to the sum of the reaction channels ^{4}He(e,e$'$p)^{2}Hn and ^{4}He(e,e$'$p)nnp.

The cross sections and spectral functions extracted in the continuum region are 2-dimensional quantities, histogrammed as a function of both missing energy and missing momentum. The cross section and spectral function results are presented and compared to theory as a function of missing energy for a fixed missing momentum. Momentum distributions for the continuum channels are also determined and compared to theory by integrating the experimental and theoretical spectral functions over selected regions of missing energy.

6.3.1 ^{3}He(e,e$'$p)np

At our kinematics, the radiative-unfolded ^{3}He(e,e$'$p)np cross section showed significant strength only for $E_m < 20$ MeV. The higher missing energy region ($E_m > 20$ MeV) was dominated by radiative tail as shown, for example, in Figure 6-1. The final results presented here are therefore for the $E_m < 20$ MeV region determined from the $p_p = 660$ and 585 MeV/c settings. The range of p_m covered is determined by the limits of the acceptance as shown in Figure 3-8.

In Figure 6-11, the experimental radiative-corrected cross section (upper plot) and spectral function (lower plot) results are shown for $p_m = 45 \pm 5$ MeV/c. These results were obtained with the 2D radiative-unfolding technique, and the 2DFPM unfolding technique yields similar results. The integrated results with both unfolding techniques will be presented later in this section. In the figure, the two-body ^{3}He(e,e$'$p)^{2}H peak appears at 5.5 MeV and exceeds the y-scale of the plot, and the continuum ^{3}He(e,e$'$p)np strength starts around 7 MeV. The size of the continuum cross section varies considerably among the three kinematic settings (each of which corresponds to a different value of the virtual photon polarization, ϵ), but the shape is

independent of the kinematics. In comparison, the experimental spectral function is relatively insensitive to the kinematic setting. This is analogous to the results observed for the two-body breakup channels ^{3}He(e,e'p)^{2}H and ^{4}He(e,e'p)^{3}H, where the measured momentum distributions had little (or no) dependence on the virtual photon polarization (ϵ).

For comparison, the theoretical spectral function of Schulze and Sauer [49] for $p_m = 45$ MeV/c is superimposed on the experimental spectral function in Figure 6-11. The calculation is not averaged over the finite p_m range (± 5 MeV/c), but is sufficiently linear over that range that any error introduced is negligible. The theoretical curve predicts the shape of the data very well, and its magnitude is approximately 20% greater than the data on average.

To more easily compare the data sets to each other and to theory, and to generalize the results to other values of p_m, we have integrated both the experimental and theoretical spectral functions over missing energy from the ^{3}He(e,e'p)np threshold to 20 MeV. The result is a momentum distribution for the three-body breakup channel which we have denoted $\rho_{3,20}$ following the notation of Jans *et al.* [48]:

$$\rho_{3,20}(p_m) = \int_{E_{m1}}^{20.00} S(E_m, p_m) dE_m \tag{6.3}$$

When integrating the theory, the lower limit, E_{m1}, of the integration was the ^{3}He(e,e'p)np threshold ($E_m = 7.72$ MeV). For the data, a lower limit of $E_{m1} = 7.0$ MeV was chosen to include data that, because of resolution effects, appear just below the 3-body breakup threshold.

The experimental values of $\rho_{3,20}$ were evaluated with both the 2D and 2DFPM radiative-unfolding techniques. The 2D results are are given in Table 6.5 and Figure 6-12. The analogous 2DFPM results are given in Table 6.6 and Figure 6-13. To put these results into context with the data shown in Figure 6-11, we note that the continuum spectral function results of Figure 6-11 are embodied by the three points at $p_m = 45$ MeV/c in Figure 6-12. The results obtained with the two radiative-unfolding techniques are very similar in all respects, except that the results with the 2DFPM technique are approximately 4% larger than the corresponding 2D results. The sign of this difference is consistent with the studies of the 2D and 2DFPM techniques in Chapter 5 which, in the 2D case, showed a greater contribution to the continuum from the

Figure 6-11: ^{3}He(e,e′p) radiative-corrected cross sections (upper plot) and spectral functions (lower plot) extracted from the data at each of the three kinematic settings. These data were radiatively-corrected using the 2D unfolding technique.

p_{miss}	$\rho_{3,20}$ $[(\text{GeV}/c)^{-3}]$		
[MeV/c]	540	675	855
15.0	103.79 ± 3.52	106.14 ± 3.17	117.73 ± 3.33
25.0	99.20 ± 2.32	99.77 ± 2.12	105.76 ± 2.17
35.0	90.35 ± 1.88	87.22 ± 1.72	96.13 ± 1.72
45.0	76.84 ± 1.72	77.87 ± 1.56	79.99 ± 1.43
55.0	63.23 ± 1.72	62.48 ± 1.43	66.11 ± 1.25
65.0	52.67 ± 1.87	50.88 ± 1.31	56.36 ± 1.16
75.0	35.63 ± 1.63	42.84 ± 1.22	46.06 ± 1.09
85.0	32.14 ± 1.53	30.38 ± 1.07	36.96 ± 1.07
95.0	25.94 ± 1.75	27.44 ± 1.04	29.98 ± 1.03
105.0		21.05 ± 1.05	22.16 ± 0.94
115.0		17.36 ± 1.18	17.19 ± 0.90
125.0		13.41 ± 1.37	14.55 ± 0.92
135.0			11.86 ± 0.93
145.0			9.92 ± 0.98
155.0			8.87 ± 1.09
165.0			5.77 ± 1.20

Table 6.5: Measured ^{3}He(e,e$'$p)np momentum distributions, determined with the 2D radiative unfolding technique.

two-body radiative tail.

For both unfolding techniques, the measured values of $\rho_{3,20}(p_m)$ exhibit some dependence on the virtual photon polarization, ϵ. To compare the values obtained at the three kinematics, the ratio of each data set to the average result is shown in Figure 6-14. As with the measured ^{3}He(e,e$'$p)^{2}H momentum distributions, the experimental value of $\rho_{3,20}(p_m)$ at each p_m generally increases with ϵ. In contrast to the ^{3}He(e,e$'$p)^{2}H results, this ϵ-dependence appears to vary with p_m.

To compare the overall magnitude of the measurements to each other and to theory, we have further integrated the results to obtain the following dimensionless integral:

$$N = 4\pi \int_{10}^{100} \rho_{3,20}(p_m) \cdot p_m^2 dp_m \qquad (6.4)$$

where the limits ($10 < p_m < 100$ MeV/c) of the integral correspond to the region of overlap

p_{miss} [MeV/c]	$\rho_{3,20}$ [(GeV/c)$^{-3}$]		
	540	675	855
15.0	105.71 ± 3.51	110.04 ± 3.17	123.04 ± 3.32
25.0	103.07 ± 2.32	104.31 ± 2.11	111.24 ± 2.17
35.0	91.69 ± 1.88	94.36 ± 1.72	99.59 ± 1.72
45.0	79.52 ± 1.72	80.34 ± 1.56	83.68 ± 1.43
55.0	65.77 ± 1.72	64.86 ± 1.43	69.24 ± 1.25
65.0	54.02 ± 1.87	53.89 ± 1.31	58.89 ± 1.16
75.0	37.38 ± 1.63	44.40 ± 1.22	48.28 ± 1.09
85.0	33.06 ± 1.53	31.39 ± 1.07	38.79 ± 1.07
95.0	25.31 ± 1.75	28.27 ± 1.04	31.22 ± 1.03
105.0		21.57 ± 1.05	23.00 ± 0.94
115.0		17.65 ± 1.18	17.81 ± 0.90
125.0		14.08 ± 1.37	14.83 ± 0.92
135.0			12.37 ± 0.93
145.0			10.17 ± 0.98
155.0			9.04 ± 1.09
165.0			5.99 ± 1.20

Table 6.6: Measured ^{3}He(e,e'p)np momentum distributions, determined with the 2DFPM radiative unfolding technique.
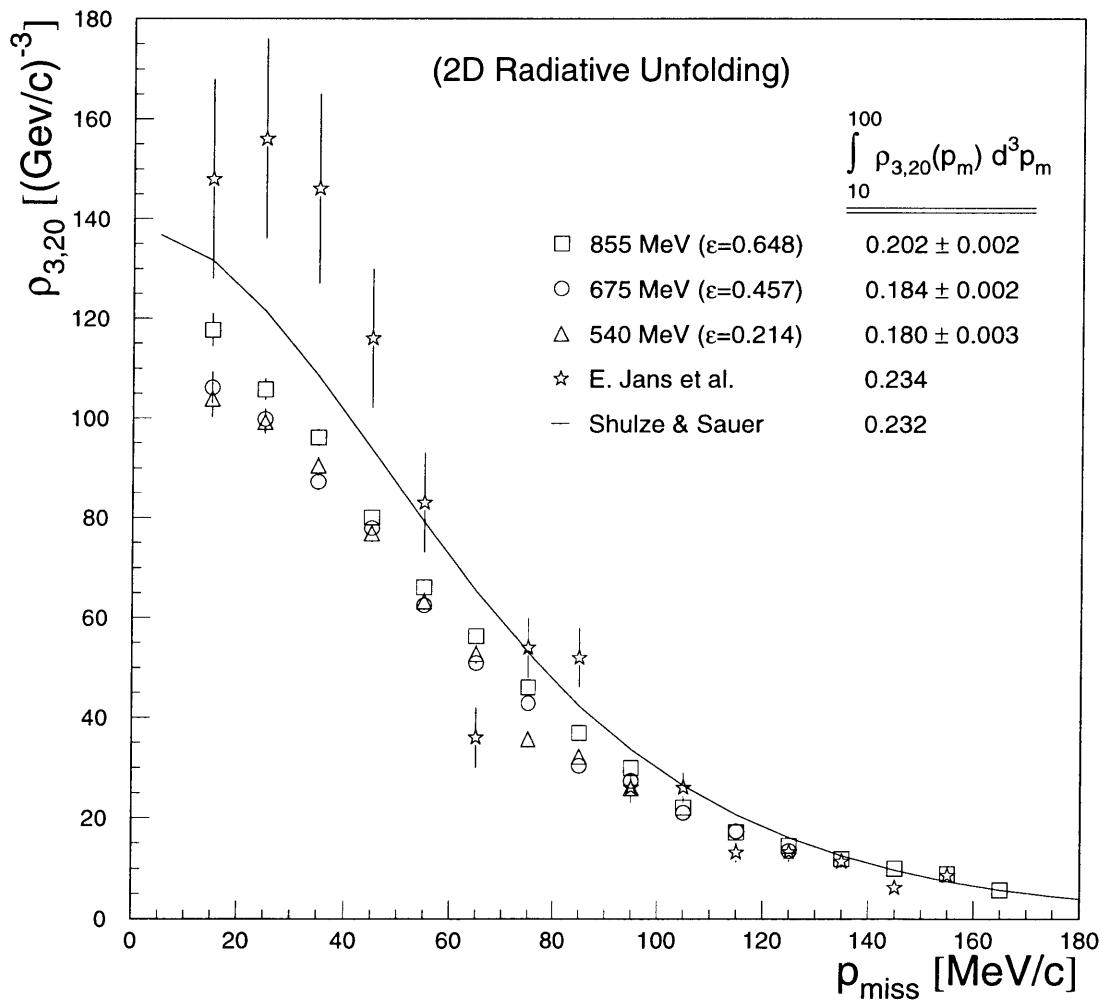
Figure 6-12: Measured ^{3}He(e,e'p)np momentum distributions, $\rho_{3,20}$, with 2D radiative unfolding.
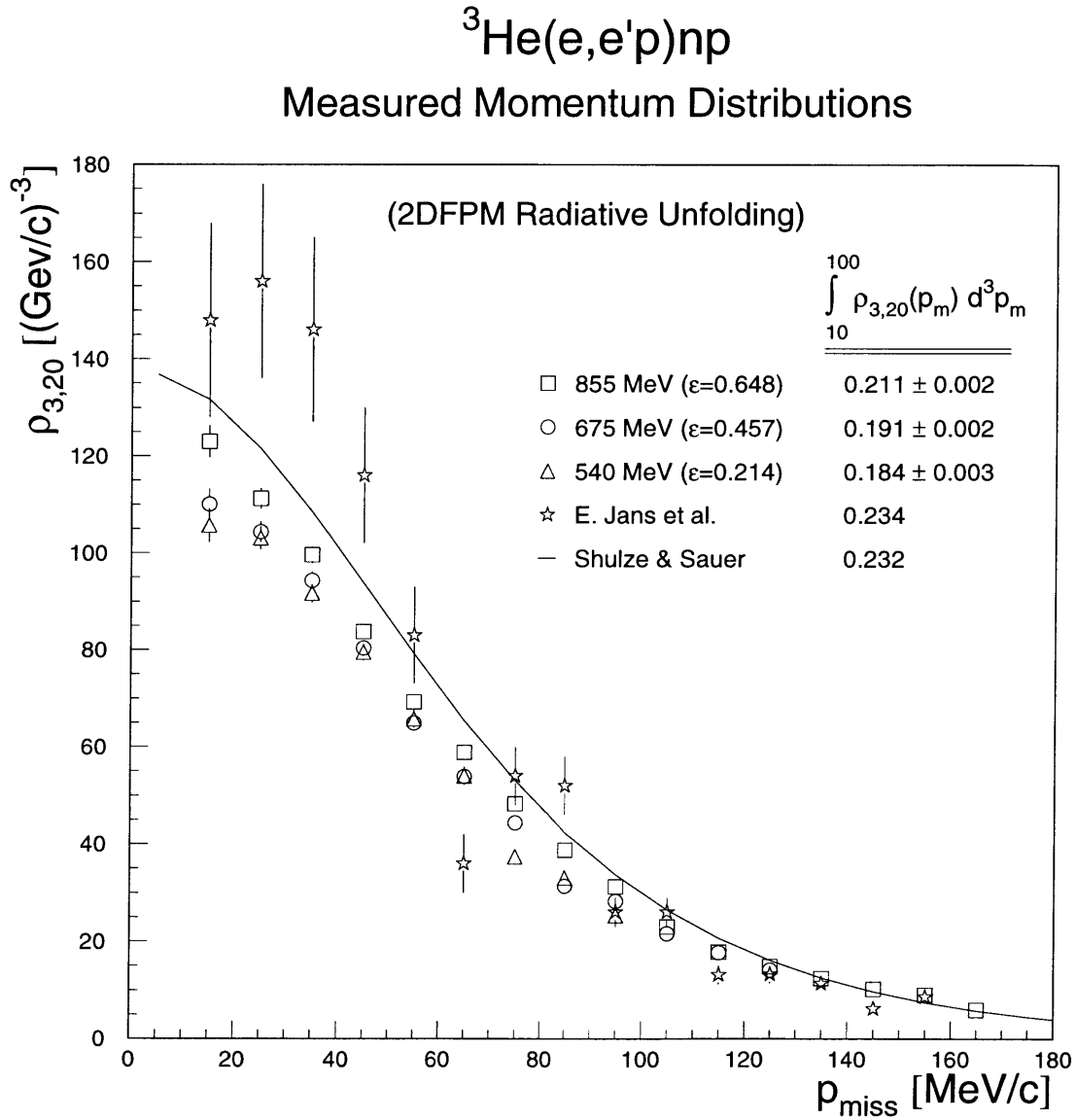
Figure 6-13: Measured ^{3}He(e,e'p)np momentum distributions, $\rho_{3,20}$, with 2DFPM radiative unfolding.
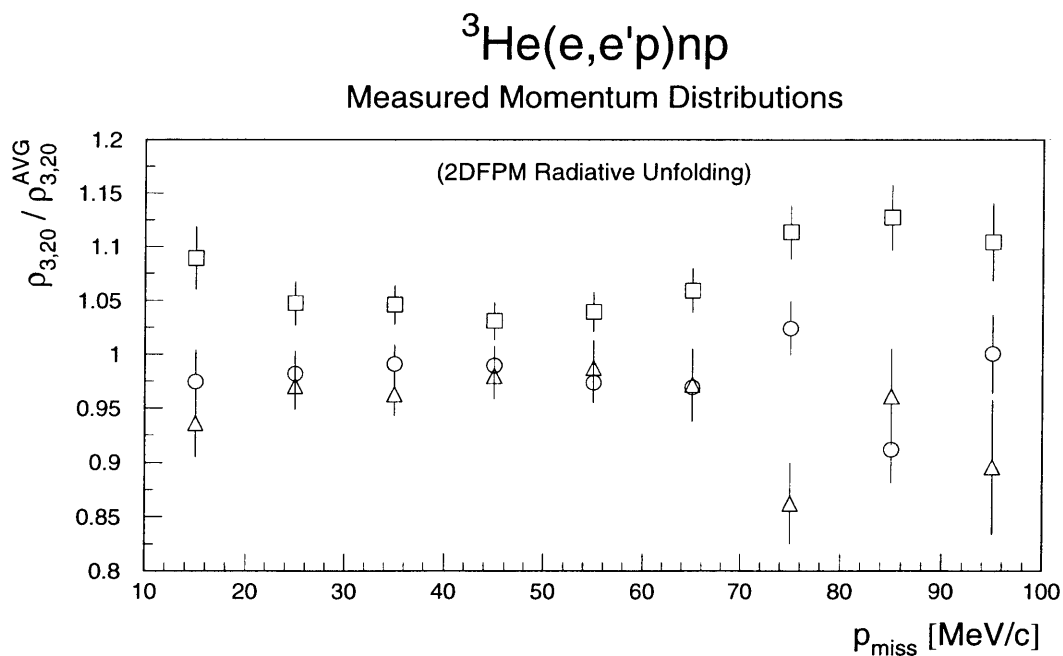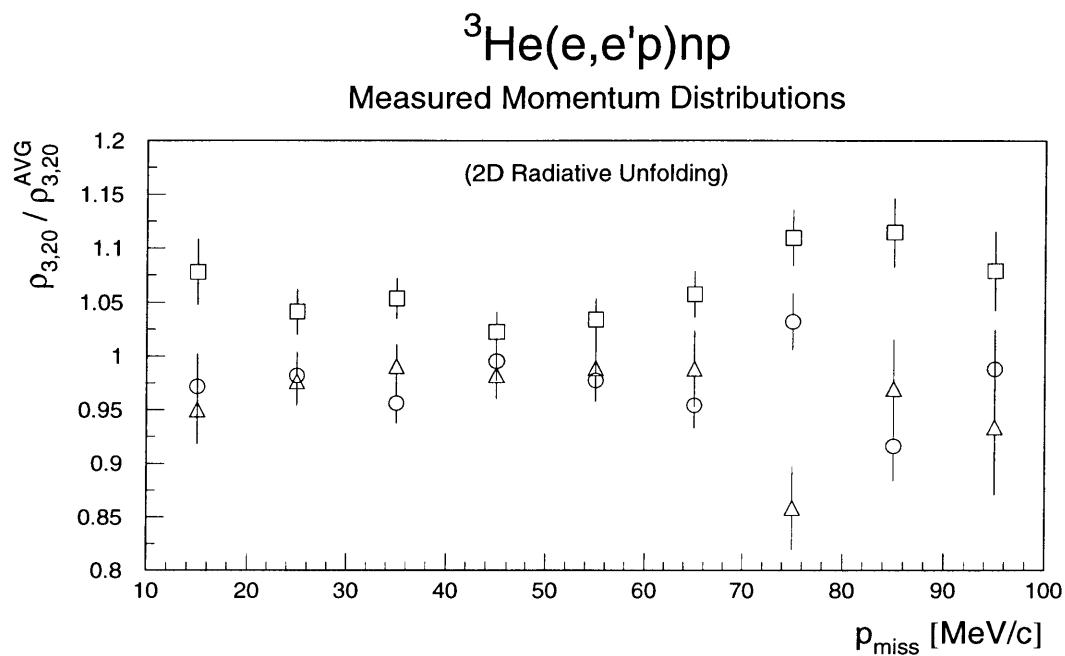
Figure 6-14: Measured ^{3}He(e,e'p)np momentum distributions compared to average value. The upper and lower plots are for the results obtained with 2D and 2DFPM radiative unfolding, respectively.

of the three data sets. The results are superimposed on Figures 6-12 and 6-13 with their corresponding statistical uncertainties.

Compared to the value obtained at 675 MeV, the values of N at 855 MeV and 540 MeV are +9.8% larger and -2.2% smaller, respectively, for the 2D unfolding technique. In the 2DFPM technique, the corresponding differences are +10% and -4%, respectively. The magnitude of N is observed to increase with the virtual photon polarization, ϵ, indicating that the ratio (L/T) of the longitudinal (L) and transverse (T) response functions is larger than that given by σ^{ep}_{CC1}. However, we note that the estimated systematic uncertainty in comparing our measurements to each other is 5–6%, which is comparable to this observed ϵ-dependence. These observations are similar to those seen in the $^3\text{He}(e,e'p)^2\text{H}$ results.

In Figures 6-12 and 6-12 we also show the measured data[§] of Jans *et al.* [48] from Saclay. The error bars shown for these data correspond to the total uncertainty (statistical plus systematic). Compared to our kinematics, the data were measured at a lower momentum transfer ($q \approx 430$ MeV/c) and in (nominally) perpendicular kinematics ($\vec{p}_m \perp \vec{q}$). We calculate the virtual photon polarization at the center of their kinematic setting to be 0.65, which is similar to the value at our 855 MeV kinematics ($\epsilon = 0.648$). From Jans' data, we determine a value of $N = 0.234$, which is 11-15% greater than the corresponding value at our 855 MeV kinematics ($N = 0.202$ for the 2D unfolding and $N = 0.211$ for the 2DFPM unfolding). As was noted in the discussion of the $^3\text{He}(e,e'p)^2\text{H}$ results, the total uncertainty in N for Jans' data is difficult to calculate since the uncertainties given for his data are the sum of statistical and systematic uncertainties. Their paper (Ref. [48]) quotes an uncertainty of 5% in the absolute normalization, so that the uncertainty in N calculated from their data is at least 5%. The systematic uncertainty in our absolute normalization is also 5–6% as discussed at the end of this chapter.

Theoretical predictions of $\rho_{3,20}$ were determined by integrating (using a cubic spline interpolation) the spectral function of Schulze and Sauer [49]. This spectral function was described in the discussion of the $^3\text{He}(e,e'p)^2\text{H}$ results. The values of $\rho_{3,20}$ obtained are shown as the solid curve in Figures 6-12 and 6-13. The shape of the data as a function of p_m is reproduced well by

---

[§]The data shown are from Jans' "kinematics I".

the theory. The average value of N obtained at our three kinematics (0.189 in the 2D unfolding and 0.195 in the 2DFPM unfolding) is -18.5% and -16.7% smaller than the corresponding value obtained from the theory ($N = 0.232$). As discussed earlier in this chapter, an estimate of the final-state interactions (FSI) for the ^{4}He(e,e′p)^{3}H reaction indicated a 12% reduction in the theoretical cross section. This accounts for approximately two-thirds of the difference between our measurements and the spectral function of Schulze and Sauer. This result is very similar to that observed for the ^{3}He(e,e′p)^{2}H momentum distribution.

6.3.2 ^{4}He(e,e$'$p)^{2}Hn and ^{4}He(e,e$'$p)nnp

As with ^{3}He, the radiative corrections are a very important part of the ^{4}He continuum cross section. A critical difference between the two nuclei is that the continuum strength relative to the two-body strength is much smaller in ^{4}He than in ^{3}He. The contribution of the two-body radiative tail (i.e. the tail that propagates strength out of the two-body peak) to the continuum is therefore a much larger correction. The systematic uncertainty due to the radiative unfolding is therefore much larger in ^{4}He than in ^{3}He.

After radiative unfolding, the continuum ^{4}He(e,e$'$p) cross section shows significant strength only for missing energies below 45 MeV. Above this missing energy the measured strength is 100% radiative tail as was shown in Figure 6-3. The experimental results presented here are therefore restricted to $E_m < 45$ MeV.

In Figure 6-15, the experimental cross section and spectral function as a function of missing energy is shown for a fixed missing momentum of $p_m = 50 \pm 20$ MeV/c. These results were obtained with the 2D radiative-unfolding method. The onset of the continuum strength is clearly observed at $E_m = 26.1$ MeV, which is the threshold for the three-body breakup of ^{4}He. As with the other results presented earlier in this chapter, the cross section is highly dependent on the kinematic setting and the spectral function is not.

Superimposed on the data is the theoretical spectral function of Efros *et al.* [59]. Theirs is the first full calculation of the ^{4}He spectral function and employs the Lorentz integral transform method to completely take into account final state interactions among the residual undetected particles (note that FSI with the detected proton is not included). The model used for the nucleon-nucleon potential is the semirealistic Trento potential. Considering the large size of our radiative corrections (a sample of the uncorrected results is shown in the lower plot of Figure 6-15), the agreement between the experiment and theory is excellent. The data have the same shape as the theory, and the magnitude is somewhat reduced as might be expected from FSI effects.

To more easily compare the data sets to each other and to theory, and to generalize the results to other values of p_m, we have integrated both the experimental and theoretical spectral

^{4}He(e,e'p) Measured Cross Sections and Spectral Functions

$(30 \leq p_{miss} \leq 70 \text{ MeV/c})$
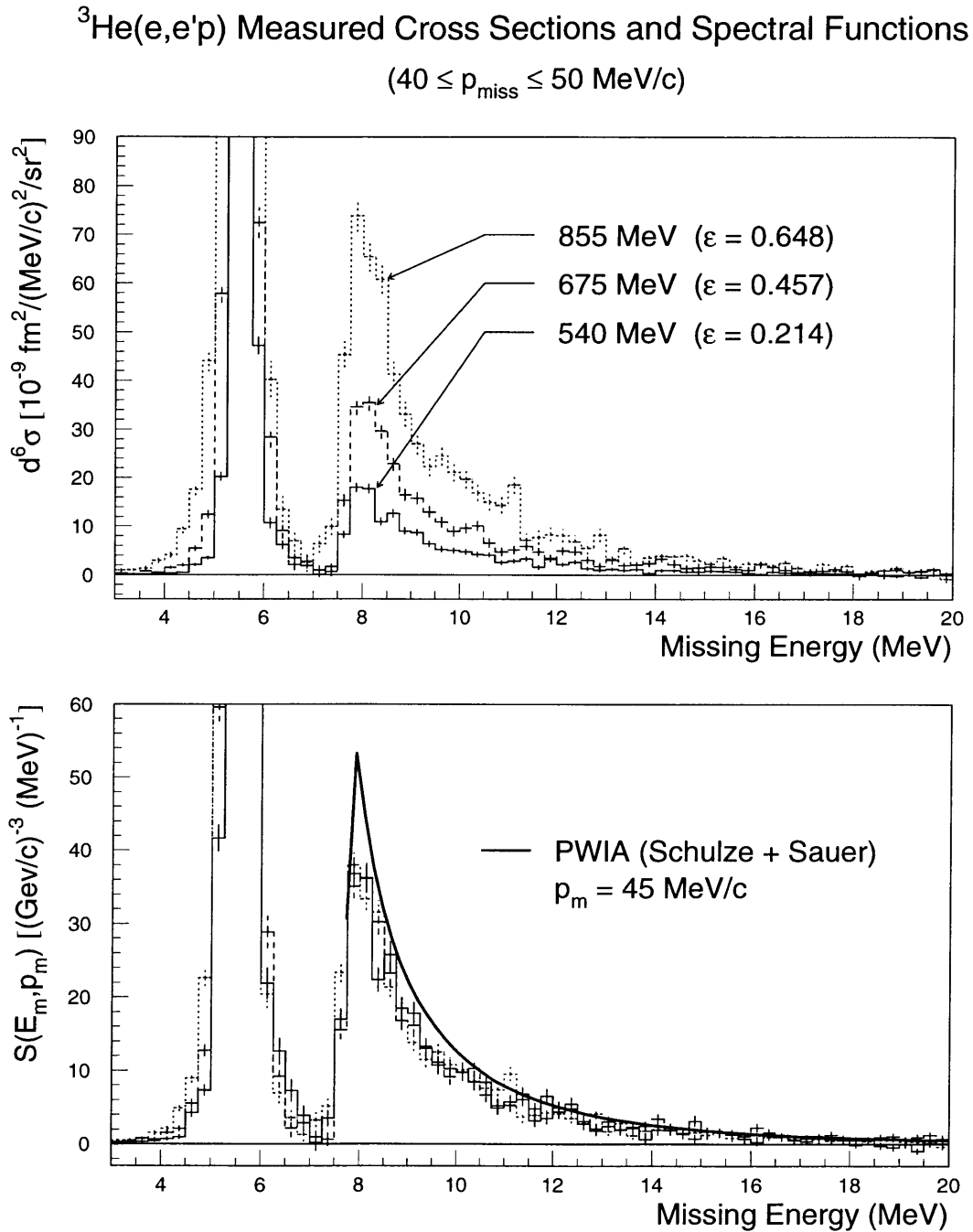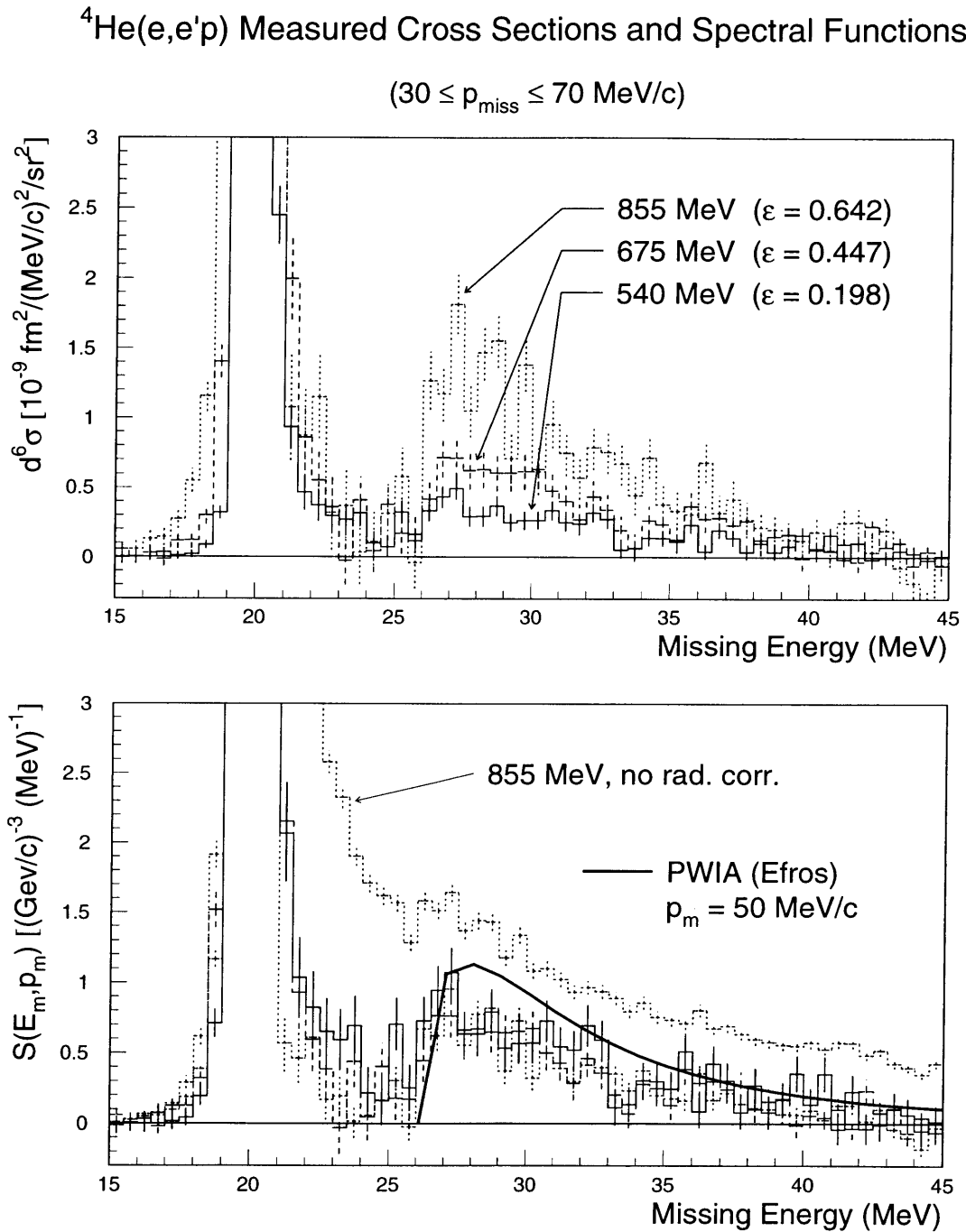
Figure 6-15: ^{4}He(e,e'p) radiative-corrected cross sections (upper plot) and spectral functions (lower plot) extracted from the data at each of the three kinematic settings. These data were radiatively-corrected using the 2D unfolding technique.

functions over missing energy from the ^{4}He(e,e'p)^{2}Hn threshold to 45 MeV. The result is a momentum distribution for the sum of the three- and four-body breakup channels, which we have denoted $\rho_{3-4,45}$:

$$\rho_{3-4,45}(p_m) = \int_{E_{m1}}^{45.00} S(E_m, p_m) dE_m \tag{6.5}$$

When integrating the theory, the lower limit, E_{m1}, of the integration was the ^{3}He(e,e'p)np threshold ($E_m = 26.07$ MeV). For the data, a lower limit of $E_{m1} = 25.0$ MeV was chosen to include data that, because of resolution effects, appear just below the 3-body breakup threshold.

The experimental values of $\rho_{3-4,45}$ were evaluated with both the 2D and 2DFPM radiative-unfolding techniques. The 2D results are givn in Table 6.7 and Figure 6-16, and the corresponding 2DFPM results are given in Table 6.8 and Figure 6-17. The results obtained with the two techniques differ substantially more than in the ^{3}He(e,e'p) continuum results, reflecting the larger systematic uncertainty associated with the very large radiative correction. The results obtained with the 2DFPM technique are a smoother function of p_m, and are generally larger than those obtained with the 2D technique.

To evaluate the kinematic dependence of the measured value of $\rho_{3-4,45}$, the ratio of to the results to the average result at the three kinematics is shown in Figure 6-18. The upper plot is the result with 2D radiative unfolding, and the lower plot for 2DFPM radiative unfolding. The 2DFPM results are smoother and show no systematic dependence on the kinematic setting. In the 2D results, the kinematics corresponding to the smallest value of ϵ yield the largest value of $\rho_{3-4,45}$.

To compare the overall magnitude of the measurements to each other and to theory, we have further integrated the results to obtain the following dimensionless integral:

$$N = 4\pi \int_{10}^{90} \rho_{3-4,45}(p_m) \cdot p_m^2 dp_m \tag{6.6}$$

where the limits ($10 < p_m < 90$ MeV/c) of the integral correspond to the region of overlap of the three data sets. The results are superimposed on Figures 6-16 and 6-17 with their corresponding

| p_{miss} | $\rho_{3,4-45}$ $[(\text{GeV}/c)^{-3}]$ | | |
[MeV/c]	540	675	855
15.0	9.18 ± 1.21	12.07 ± 1.28	12.20 ± 1.04
25.0	7.27 ± 0.82	5.80 ± 0.83	5.38 ± 0.67
35.0	8.03 ± 0.73	4.18 ± 0.71	4.90 ± 0.55
45.0	6.94 ± 0.76	6.56 ± 0.69	5.60 ± 0.50
55.0	8.28 ± 0.98	5.96 ± 0.71	5.68 ± 0.48
65.0	5.86 ± 1.10	6.64 ± 0.77	5.81 ± 0.50
75.0	4.63 ± 0.97	4.77 ± 0.79	4.20 ± 0.53
85.0	6.71 ± 0.99	4.40 ± 0.79	4.37 ± 0.57
95.0	7.76 ± 1.37	4.66 ± 0.85	3.36 ± 0.58
105.0		3.30 ± 0.91	3.49 ± 0.60
115.0		2.86 ± 1.02	3.19 ± 0.59
125.0		3.60 ± 1.32	2.70 ± 0.59
135.0			1.80 ± 0.63
145.0			3.43 ± 0.76

Table 6.7: Measured momentum distributions, $\rho_{3-4,45}$, for the sum of the reaction channels ^{4}He(e,e′p)nd and ^{4}He(e,e′p)nnp, with 2D radiative unfolding.

| p_{miss} | $\rho_{3,4-45}$ $[(\text{GeV}/c)^{-3}]$ | | |
[MeV/c]	540	675	855
15.0	8.64 ± 1.21	9.65 ± 1.28	8.98 ± 1.04
25.0	8.13 ± 0.82	7.59 ± 0.83	8.15 ± 0.67
35.0	8.30 ± 0.73	8.22 ± 0.71	7.25 ± 0.55
45.0	7.52 ± 0.76	7.61 ± 0.69	7.11 ± 0.49
55.0	8.82 ± 0.98	6.43 ± 0.71	6.80 ± 0.48
65.0	7.46 ± 1.10	7.89 ± 0.77	7.01 ± 0.50
75.0	5.10 ± 0.97	6.46 ± 0.79	5.81 ± 0.53
85.0	5.36 ± 0.99	5.35 ± 0.79	5.70 ± 0.57
95.0	10.96 ± 1.37	4.99 ± 0.85	4.39 ± 0.58
105.0		4.22 ± 0.91	5.06 ± 0.60
115.0		3.65 ± 1.02	3.88 ± 0.59
125.0		2.64 ± 1.32	3.02 ± 0.59
135.0			2.56 ± 0.63
145.0			3.85 ± 0.76

Table 6.8: Measured momentum distributions, $\rho_{3-4,45}$, for the sum of the reaction channels ^{4}He(e,e′p)nd and ^{4}He(e,e′p)nnp, with 2DFPM radiative unfolding.

Figure 6-16: Measured momentum distributions, $\rho_{3-4,45}$, for the sum of the reaction channels ^{4}He(e,e$'$p)nd and ^{4}He(e,e$'$p)nnp, with 2D radiative unfolding.

^{4}He(e,e'p)nd + ^{4}He(e,e'p)nnp
Measured Momentum Distributions
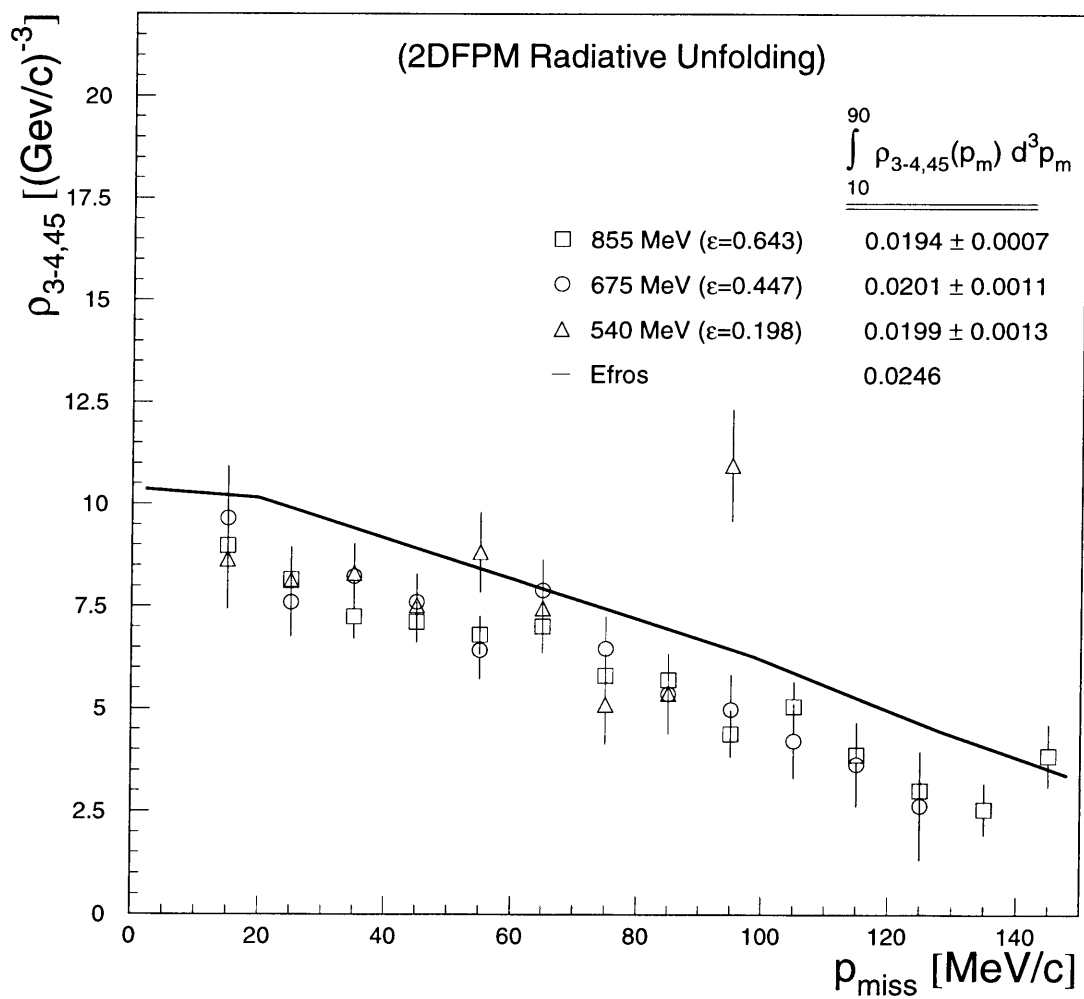
Figure 6-17: Measured momentum distributions, $\rho_{3-4,45}$, for the sum of the reaction channels ^{4}He(e,e'p)nd and ^{4}He(e,e'p)nnp, with 2DFPM radiative unfolding.
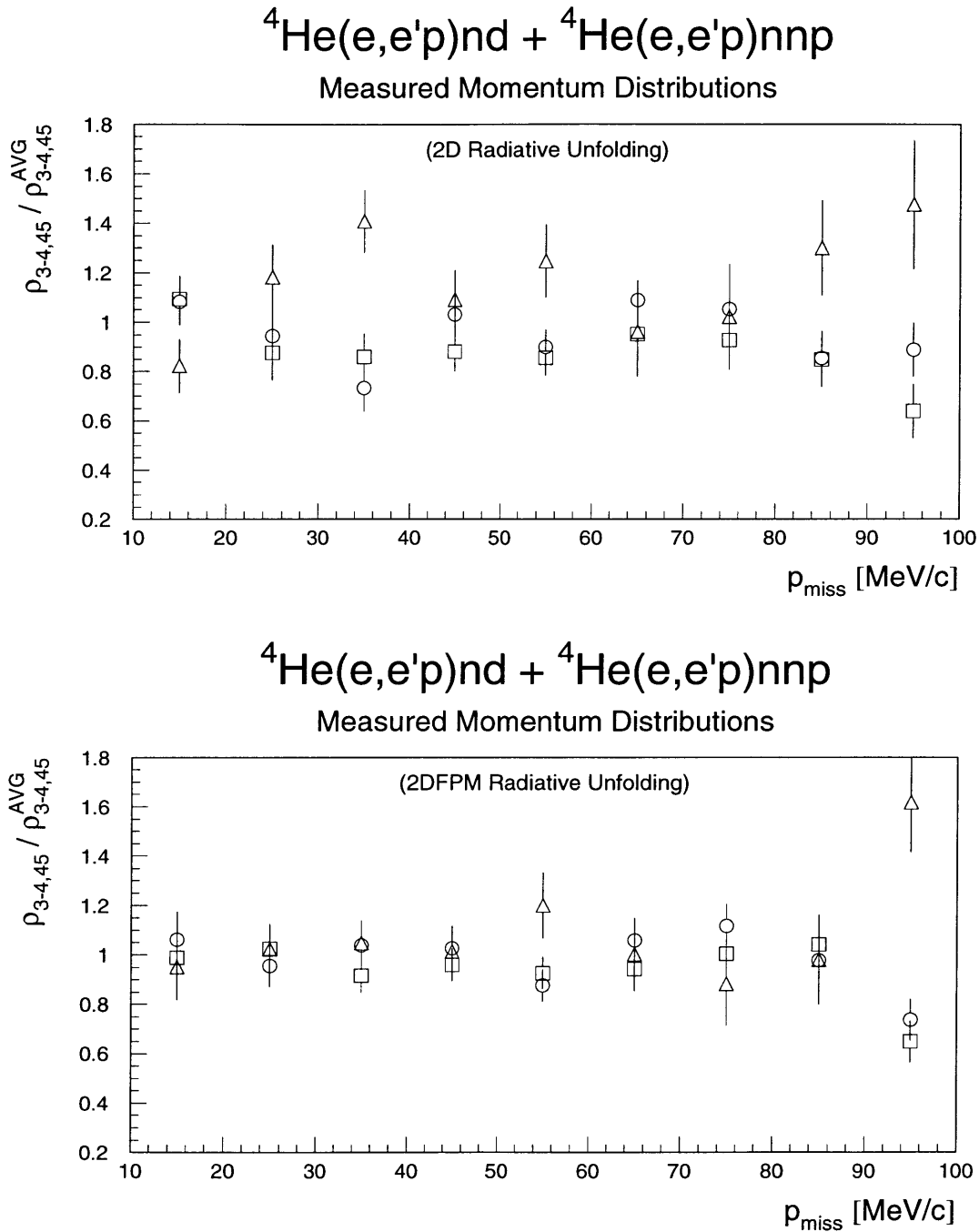
Figure 6-18: Measured momentum distributions, $\rho_{3-4,45}$, for the sum of the reaction channels ^{4}He(e,e'p)nd and ^{4}He(e,e'p)nnp compared to the average value. The upper and lower plots are for the results obtained with 2D and 2DFPM radiative unfolding, respectively.

statistical uncertainties. To further emphasize the small magnitude of these continuum cross sections, we note that the values of N obtained are approximately ten times smaller than the values of N obtained (although with a slightly different definition) from the ^{3}He results.

For the 2DFPM unfolding technique, the value of N at the three kinematics are equal within our systematic uncertainty. In contrast, the 2D results give a large ϵ-dependence: compared to the value obtained at 675 MeV, the values of N at 855 MeV and 540 MeV are -7.4% smaller and +19.6% larger, respectively. The magnitude of N is thus observed to decrease with increasing ϵ, which is a trend opposite of that observed in the ^{3}He results. In comparison to the 2DFPM unfolding technique, the 2D technique is more physically realistic, since it attempts to account for a change in p_m in the radiative tails. However, the 2D technique results in negative cross sections at high missing energy, which is an unphysical result. The results obtained with the 2DFPM unfolding technique appear to be more reasonable, since they yield smoother values of $\rho_{3-4,45}$, and a positive cross section at high missing energy as seen in Figure 6-3. If we choose to believe the 2DFPM results, than the value of N is independent of the virtual photon polarization (ϵ), and we conclude that the ratio (L/T) of the longitudinal (L) and transverse (T) response functions is the same as σep^{CC1}. This conclusion is consistent with the result reported for the two-body breakup channel ^{4}He(e,e$'$p)^{3}H. If we choose instead to believe the results obtained with the 2D unfolding technique, than we conclude that the L/T ratio is smaller than that given be σep^{CC1}. We emphasize here that the uncertainty in choosing between the two techniques is compounded by the large size of the radiative corrections. In ^{3}He, where the relative contribution of the two-body tail to the low- missing-energy continuum is much smaller, the two unfolding techniques yielded much more similar results.

The corresponding values of $\rho_{3-4,45}$ computed (using a cubic-spline interpolation) from the theoretical spectral function of Efros *et al.* [59] are also shown in Figures 6-16 and 6-17 for comparison. The shape of the data as a function of p_m is reproduced well by the theory. The average value of N obtained at our three kinematics (0.0187 in the 2D unfolding and 0.0198 in the 2DFPM unfolding) is -24.0% and -19.5% smaller than the corresponding value obtained from the theory ($N = 0.0246$). As discussed earlier in this chapter, an estimate of the final-state

interactions (FSI) for the ^{4}He(e,e$'$p)^{3}H reaction indicated a 12% reduction in the theoretical cross section. This accounts for approximately half of the difference between our measurements and the theoretical spectral function.

6.4   Systematic Uncertainty

Sources of systematic uncertainty in the measured (e,e'p) cross sections are give in Table 6.9 and are described in detail in this section. The first seven rows of the table consider uncertainties in the overall normalization of the cross sections, including knowledge of the target density, dead time, and absolute detection volume. The next five rows of the table consider uncertainties due to possible offsets in the central value of kinematic quantities such as the beam energy, spectrometer angles, and beam and target location. Systematic offsets in these quantities alter the kinematic region that is probed by the measurement, and hence introduce an uncertainty in the measured cross section.

The total systematic uncertainty in the (e,e'p) measurements is the sum of all the individual uncertainties added in quadrature, and is given in the final row of the table. Since these values are absolute uncertainties for each kinematic setting, it is useful to also define the "relative uncertainty", which is the uncertainty in comparing two measurements at different kinematics. In general one might expect that some uncertainties cancel out when doing such a comparison, so that the relative uncertainty is less than the absolute uncertainty. However, in considering each of the individual uncertainties it was determined that there were no substantial cancellations in our case. Our estimate of the relative uncertainty is therefore the same as the total absolute uncertainty. The remainder of this section discusses the individual uncertainties in detail.

The largest uncertainty is in the target density measured in the elastic scattering runs. A detailed error analysis of this uncertainty was presented in Chapter 4, and the uncertainty given in Table 6.9 is the total uncertainty from Table 4.10.

The product of the charge and target density in the (e,e'p) runs was determined from the number of counts measured in Spectrometer C in the elastic and (e,e'p) runs. This contributes a statistical ($\sqrt{N}$ associated with the number of counts measured) and a systematic (associated with the dead time correction) uncertainty to the measured cross sections. The uncertainties are a sum of the contributions from both the elastic and the (e,e'p) runs. The dead-time correction for an individual run or consecutive series of runs is assigned an uncertainty of 1%.

The detection volume for the (e,e'p) cross sections was defined in part by software cuts

Beam Energy	[MeV]	^{3}He			^{4}He		
		540	675	855	540	675	855
density in elastic run	[%]	4.4	4.8	3.4	4.0	4.9	3.7
Spect. C statistical (elastic + (e,e′p) runs)	[%]	1.2	1.0	1.7	2.5	1.7	2.6
Spect. C dead time (elastic + (e,e′p) runs)	[%]	1.4	1.4	1.4	1.4	1.4	1.4
coincidence dead time	[%]	1	1	1	1	1	1
detection volume $\Delta\theta_{tgt}, \Delta\phi_{tgt}$	[%]	1.0	1.0	1.0	1.0	1.0	1.0
detection volume Δz_{react}	[%]	1.5	1.1	0.9	1.6	1.1	1.0
absolute y_{tgt} (± 0.5 mm)	[%]	1.1	0.8	0.7	1.1	0.8	0.7
beam energy (± 160 keV)	[%]	0.34	0.25	0.16	0.34	0.25	0.16
central e$^-$ spect. angle (± 0.1 mrad)	[%]	0.02	0.05	0.07	0.02	0.05	0.07
central proton spect. angle (± 0.1 mrad)	[%]	0.02	0.03	0.04	0.02	0.03	0.04
horizontal beam position (± 1 mm)	[%]	0.06	0.39	0.72	0.06	0.39	0.72
total	[%]	5.3	5.5	4.5	5.5	5.7	5.1

Table 6.9: Estimated systematic uncertainty in the measured (e,e′p) cross sections.

on ϕ_{tgt} in Spectrometer A (the electron spectrometer) and θ_{tgt} in Spectrometer B (the proton spectrometer). An estimate of the uncertainty in the detection volume resulting from these cuts is provided by the analysis of the elastic scattering data presented in Chapter 4. With various values of the cuts, the extracted target density changed by a maximum of 0.6% (for the ϕ_{tgt} cut in Spectrometer A) and 0.4% (for the θ_{tgt} cut in Spectrometer B). The linear sum of these values gives a 1.0% uncertainty in the detection volume due to the angular cuts. Another check on the systematic uncertainty associated with the ϕ_{tgt} cut in Spectrometer A is shown in Figure 6-19. The figure shows the measured ^{4}He(e,e′p)^{3}H momentum distribution for three different cuts on ϕ_{tgt}: ± 75, ± 60 and ± 45 mrad. The measured momentum distributions are shown in the upper plot of the figure, and the distributions compared to the average value is shown in the lower plot. Integrated over the indicated range of p_m, the results differ by less than one percent for the various cuts. This indicates that the detection volume is correctly calculated and that the systematic uncertainty associated with the ϕ_{tgt} cut is < 1%.

The target extent in this experiment was defined by a cut on the variable z_{react}, which is the position of the reaction vertex along the beam line. The value of z_{react} was determined from the
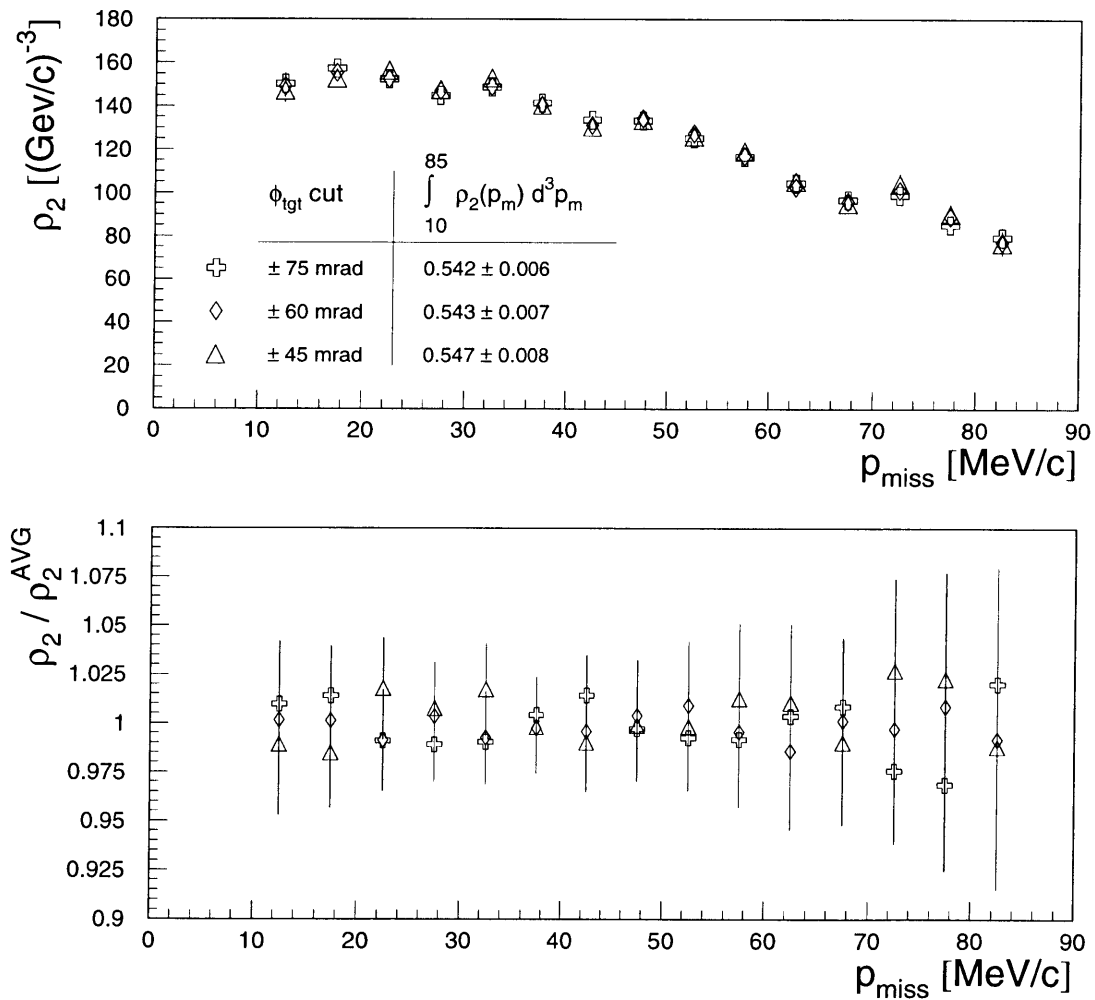
Figure 6-19: ^{4}He(e,e'p)^{3}H momentum distribution determined from the 540/660 data, for different cuts on ϕ_{tgt} in Spectrometer A.

value of y_{tgt} reconstructed in Spectrometer B and the position of the incident beam. Uncertainty in the y_{tgt} reconstruction in Spectrometer B therefore generates an uncertainty in z_{react} and and hence in the overall cross section. The effect of uncertainty in the y_{tgt} reconstruction was broken down into two effects: first, we consider the relative y_{tgt} reconstruction, which determines how well we can define a target segment of length Δz_{react}. Secondly, we consider the absolute y_{tgt} reconstruction, which determines how well we know the position of that target segment along the beam line. These are each discussed in detail below.

To determine the relative accuracy of the y_{tgt} reconstruction we have used elastic scattering data from ^{12}C, which was measured with a flat target at a number of positions along the beam line (this is the same data that was discussed in Chapter 4). The position of the target along the beam line was changed by remotely moving the table on which it is mounted. The position of this table was determined during the experiment from the measured voltage across a variable resistor (as described in Chapter 3). The absolute position of the table along the beam line was calibrated to ± 0.5 mm using data taken with sieve slits in both spectrometers. Its relative position was calibrated in a table-top measurement of position vs. voltage, and its uncertainty was determined to be approx 4×10^{-3} mm, which is much smaller than the absolute position uncertainty. The table readout therefore provides a very accurate measure of the relative distance between two or more target positions, and can be used as a check on the corresponding values reconstructed by the spectrometer.

The y_{tgt} spectra reconstructed in Spectrometer B at each of the target locations is shown in Figure 6-20. The width of the peaks is consistent with a y_{tgt} resolution of approximately 1.8 mm FWHM. A gaussian peak shape was fit to each of the spectra to determine its mean value, which is tabulated as y_{tgt}^B in Table 6.10. The difference between the value of y_{tgt} reconstructed in Spectrometer B (y_{tgt}^B) and the value from the target table (y_{tgt}^{table}) differ by values ranging from $+0.028$ cm to $+0.055$ cm at each position. This absolute discrepancy is consistent with the uncertainty in in the horizontal beam position (± 1 mm) (equivalent to a shift of $y_{tgt}^B = \pm 1 \times \cos 45°$ at this spectrometer angle) and the absolute uncertainty in y_{tgt}^{table} (± 0.5 mm). From the data in Table 6.10, we determine that the maximum error in the relative y_{tgt} reconstruction

position	table voltage [Volts]	y_{tgt}^{table} [cm]	y_{tgt}^{B} [cm]	$(y_{tgt}^{B} - y_{tgt}^{table})$ [cm]
1	0.596	-2.742	-2.687	+0.055
2	1.794	-1.888	-1.847	+0.041
3	4.283	-0.114	-0.086	+0.028
4	6.785	+1.670	+1.703	+0.033
5	7.971	+2.515	+2.565	+0.050

Table 6.10: A comparison of the value of y_{tgt} determined from the target table calibration and the value reconstructed in Spectrometer B (see text).

of of Spectrometer B is $0.055 - 0.028 = 0.027$ cm. The maximum error in the relative z_{react} reconstruction is therefore $0.027/\sin\theta_B$ cm, where θ_B is the central spectrometer angle of Spectrometer B. For example, in the 540 MeV ^{3}He kinematics ($\theta_B = 26.23°$) this yields an uncertainty of 0.061 cm; since the cut on z_{react} used throughout this experiment is ± 2.0 cm, the resulting uncertainty in Δz_{react} is $0.061/4.0 = 1.5\%$. The corresponding uncertainties at other kinematics were evaluated in the same manner, and are given in the sixth row of Table 6.9.

To estimate the error due to uncertainty in the absolute value of y_{tgt}, the data were analyzed using several z_{react} cuts that were shifted upstream or downstream from the central location. The cuts were kept constant in the detection volume calculations and only changed in analysis of the raw data. The variation in the extracted two-body breakup momentum distribution with the different cuts then provided an estimate of the uncertainty due to the absolute y_{tgt} reconstruction. A sample result from the analysis is shown in Figure 6-21, which gives the two-body breakup momentum distribution (ρ) for the ^{3}He(e,e'p)^{2}H reaction measured in the 855/660 kinematics. In the upper plot, the momentum distribution ρ_0 is the result extracted with the standard cut -2.0 cm $< z_{react}$ $+2.0$ cm. Overlayed are the corresponding distributions obtained with shifted z_{react} cuts; for example "+1 mm shift" indicates a software cut -1.9 cm $< z_{react}$ $+2.1$ cm. The lower plot gives the ratio of ρ/ρ_0 to illustrate the variation of ρ with the cuts. For a shift in z_{react} of ± 1 mm (which corresponds to a shift of ± 0.72 mm in y_{tgt} in
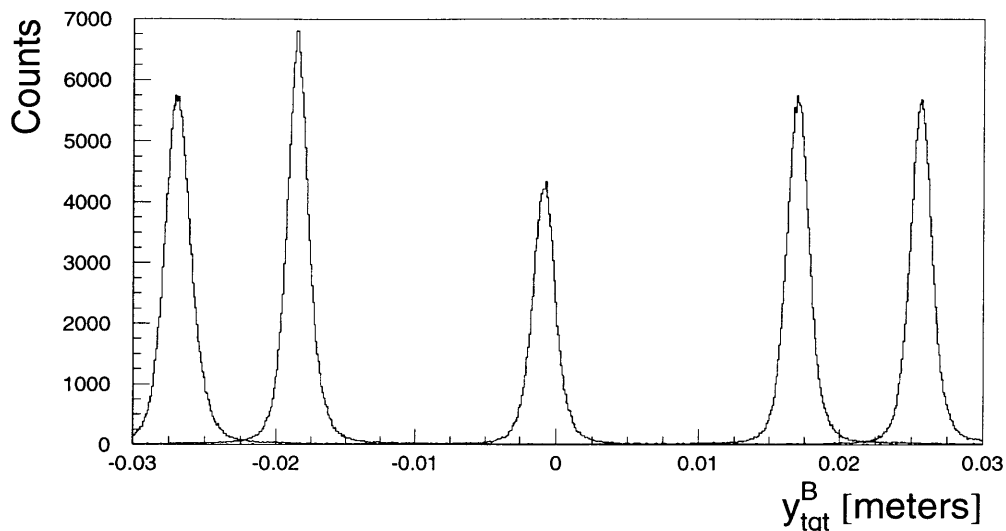
Figure 6-20: Reconstruction of y_{tgt} in Spectrometer B for a thin ^{12}C target at various locations along the beam line.

Spectrometer B at this angle) or less, the momentum distribution changes by less than 1%. Based on this result, we estimate that an uncertainty of ± 0.5 mm in the absolute value of y_{tgt} gives a $\pm 0.7\%$ uncertainty in the absolute cross section at these kinematics. Similar analyses were done for the ^{3}He 675/660 and 540/660 kinematics, with the results given in Table 6.9. The uncertainties for ^{4}He were assumed to be the same and were set to the same values as ^{3}He.

The remaining rows in Table 6.9 are associated with uncertainty in the absolute value of the beam energy, central spectrometer angle, and horizontal beam position (which is equivalent to uncertainty in the scattering angles). These uncertainties were evaluated for the ^{3}He(e,e'p) ^{2}H reaction at the 540/660 and 855/660 kinematics using the Monte Carlo code MCEEP [60]. These simulations were performed by J. Zhao [61] and the results are given in Table 6.11. The count rate was evaluated for both a positive and negative shift in the kinematic quantities, and the maximum of the two values was taken to be the resulting uncertainty, which was then entered into Table 6.9. The uncertainties for the E_{beam} = 675 MeV kinematics were not specifically evaluated, and were taken to be the average of the corresponding values at 540 and
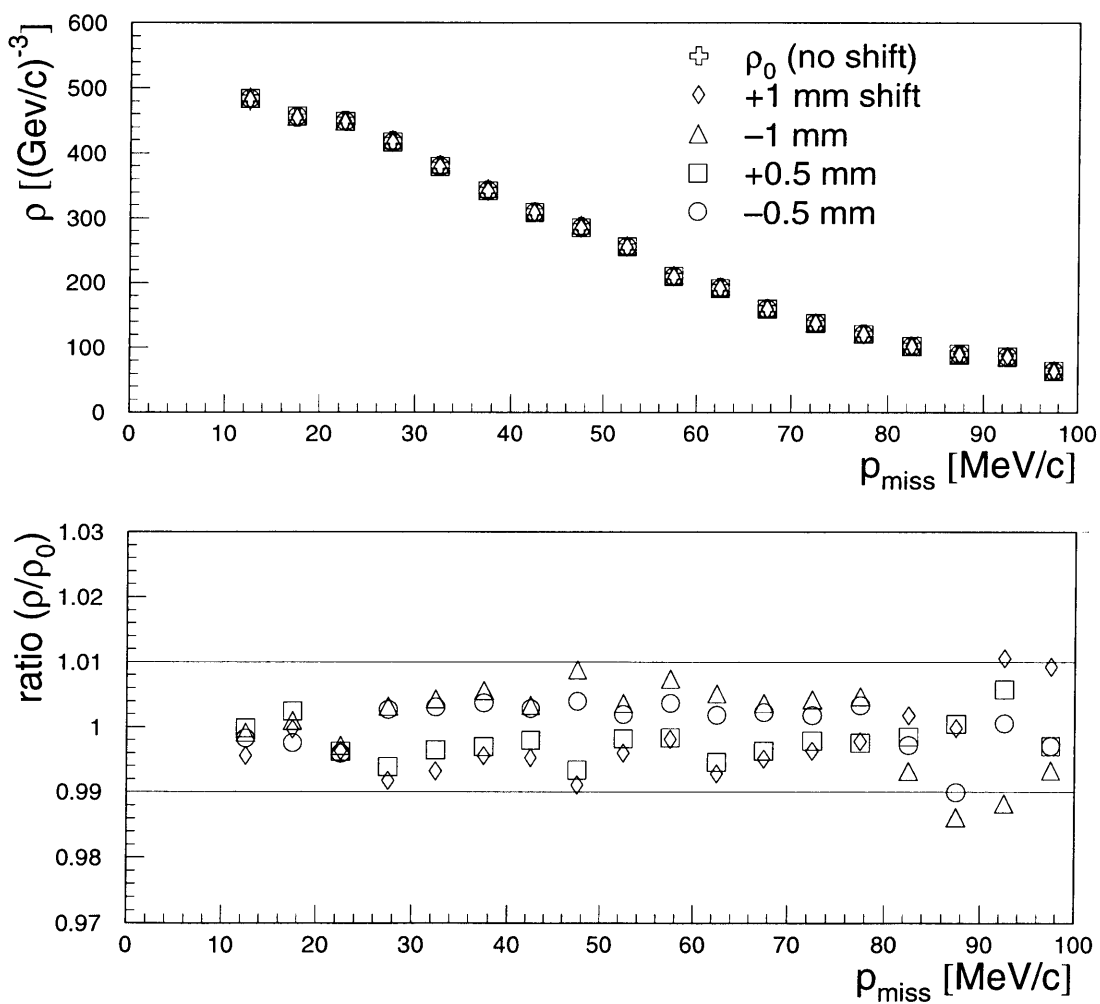
Figure 6-21: ^{3}He(e,e'p)^{2}H momentum distribution determined from the 855/660 data with various shifts in the z_{react} cut.

855 MeV. All of these uncertainties due to offsets in energy and angle are generally quite small compared to the other uncertainties.

description	E_0 [MeV]	θ_e [deg]	θ_p [deg]	counts (a.u.)	change (%)
central values	540.11	103.8525	26.2274	34121×10^2	-
$+\Delta E_0$	540.27	103.8525	26.2274	34009×10^2	-0.33
$-\Delta E_0$	539.95	103.8525	26.2274	34236×10^2	$+0.34$
$+\Delta\theta_e$	540.11	103.8582	26.2274	34113×10^2	-0.02
$-\Delta\theta_e$	540.11	103.8468	26.2274	34128×10^2	$+0.02$
$+\Delta\theta_p$	540.11	103.8525	26.2331	34127×10^2	$+0.02$
$-\Delta\theta_p$	540.11	103.8525	26.2217	34114×10^2	-0.02
+1 mm horiz. beam pos	540.11	103.8739	26.2425	34102×10^2	-0.06
-1 mm horiz. beam pos	540.11	103.8311	26.2123	34131×10^2	$+0.03$
central values	855.11	52.3586	46.4131	13413×10^3	-
$+\Delta E_0$	855.27	52.3586	46.4131	13392×10^3	-0.16
$-\Delta E_0$	854.95	52.3586	46.4131	13428×10^3	$+0.11$
$+\Delta\theta_e$	855.11	52.3643	46.4131	13404×10^3	-0.07
$-\Delta\theta_e$	855.11	52.3529	46.4131	13422×10^3	$+0.07$
$+\Delta\theta_p$	855.11	52.3586	46.4188	13418×10^3	$+0.04$
$-\Delta\theta_p$	855.11	52.3586	46.4074	13408×10^3	-0.04
+1 mm horiz. beam pos	855.11	52.3039	46.4248	13508×10^3	$+0.71$
+1 mm horiz. beam pos	855.11	52.4133	46.4015	13317×10^3	-0.72

Table 6.11: Effects of offsets in beam energy, spectrometer angle and horizontal beam position on the ^{3}He(e,e'p)^{2}H count rate for the 540 and 855 MeV kinematics. Beam energy uncertainties of ± 160 keV and angular uncertainties of 0.5 mrad are considered.

Chapter 7

Summary and Conclusions

We have measured the quasielastic (e,e'p) cross section in ^{3}He and ^{4}He over a broad range of missing energy (0–150 MeV) and missing momentum (0–300 MeV/c), in nominally parallel kinematics ($\vec{p}_m$ parallel to $\vec{q}$) and at a central momentum transfer $|\vec{q}| = 685$ MeV/c. The general results of these measurements are summarized in Table 7.1, where the results for each nucleus have been categorized according to the specific regions of missing energy and missing momentum probed by the experiment. The boundaries between the various regions are approximate values, chosen to illustrate the general behavior of the results.

At high missing energy ($E_m > 20$ MeV in ^{3}He, $E_m > 45$ MeV in ^{4}He) and low missing momentum ($p_m < 100$–150 MeV/c), the measured continuum cross section was found to be completely dominated by radiative tail. This was evidenced by a radiative-unfolded cross section that fluctuated between positive and negative (depending on the unfolding technique employed) and confirmed by a Monte Carlo simulation of the radiative effects for one of the ^{3}He kinematics. The radiative-corrected measured cross sections in this region were consistent with zero within our precision.

At high missing energy and high missing momentum ($p_m >100$–150 MeV/c), the spectrum appeared to be dominated by protons rescattered from the edges of the collimator in Spectrometer B. In this effect, coincident protons from (e,e'p) reactions at low missing energy and missing momentum (for example, from the large two-body breakup channel) apparently lost a significant amount of energy in the collimator material, thereby appearing at higher measured values of missing energy and missing momentum. These results illustrate the difficulty

^{3}He(e,e$'$p):

	$p_m < 100\text{--}150$ MeV/c	$100\text{--}150 < p_m < 300$
$E_m < 20$ MeV	• S^{exp} nearly independent of ϵ → L/T slightly larger than σ_{ep}^{CC1} • $S^{exp}/S^{th} = 0.77\text{-}0.84$	• inaccessible in QE parallel kinematics.
$E_m > 20$ MeV	• measured strength is 100% radiative tail.	• measured strength dominated by collimator scattering and radiative tail.

^{4}He(e,e$'$p):

$E_m < 45$ MeV	• S^{exp} independent of ϵ → L/T described by σ_{ep}^{CC1} • BIG rad. corr. in continuum • $S^{exp}/S^{th} = 0.68\text{-}0.85$ • good agreement with first-ever calculation of Sth	• inaccessible in QE parallel kinematics.
$E_m > 45$ MeV	• measured strength is 100% radiative tail.	• measured strength dominated by collimator scattering and radiative tail.

Table 7.1: A summary of the experimental results.

of (e,e'p) measurements in the continuum, where one is sensitive to these types of background and, in contrast to the two-body breakup channel, there is no distinct missing energy peak to distinguish the real signal from the background. In this experiment, the high resolution of the Mainz spectrometers was an important asset in understanding these phenomena, allowing the identification of background processes through accurate angular and position reconstruction of the detected particle.

Since all other regions were dominated by either radiative corrections or background, final cross sections were extracted only for the region of low missing energy and low missing momentum. Absolute cross sections were determined with a systematic uncertainty of 5-6%. The Plane Wave Impulse Approximation (PWIA) was applied to the data to extract experimental spectral functions and momentum distributions. This analysis employed de Forest's CC1* prescription of the e-p cross section [18] and the free nucleon form factors of Ref. [46]. The e-p cross section was averaged (with the appropriate kinematic factor) over the experimental acceptance at each kinematic setting using a Monte Carlo technique. The experimental spectral functions (in contrast to the measured cross sections) are therefore relatively insensitive to the details of the acceptance.

Detailed results for this region were presented in Chapter 6. In general, the shape of all of the results agreed well with PWIA predictions. In ^{3}He the experimental momentum distributions and spectral functions were seen to have some dependence on the virtual photon polarization (ϵ), indicating that the ratio (L/T) of the longitudinal (L) and transverse (T) response functions is larger than that given by σ_{CC1}^{ep}. This behavior was observed in both the two-body and continuum reaction channels. However, we note that the magnitude of the observed ϵ-dependence is comparable to our systematic uncertainty. In ^{4}He, the experimental momentum distributions and spectral functions[†] were found to be independent of ϵ within our

---

*The analysis discussed in Appendix G showed that, at our kinematics, de Forest's CC2 prescription gave approximately the same results as CC1.

†As shown in Chapter 6, the continuum spectral function obtained with 2DFPM unfolding was independent of ϵ. The corresponding result with 2D unfolding exhibited an ϵ-dependence, but the results with this technique are physically unrealistic since they give a systematically negative cross section at higher missing energy. See Chapter 6 for further discussion.

systematic uncertainty, indicating that the ratio L/T for the two-body and continuum breakup channels is consistent with that given by σ_{CC1}^{ep}.

Since the L/T ratio for the measured cross sections was found to be similar to σ_{ep}^{CC1}, an explicit separation of the longitudinal and transverse response functions was not performed on the measured cross sections. An L/T separation of the data is possible, but would be complicated because of our large experimental acceptance. From the experimental spectral functions we learn that the L/T behaviour of the measured cross sections is the same or comparable to σ_{ep}^{CC1} within our systematic uncertainty, so that there is little further information to be gained by doing a complicated L/T separation.

Although detailed calculations do not exist to establish a connection between the (e,e′p) and (e,e′) phenomenology in ^{3}He and ^{4}He, it is interesting to compare our results to the L/T ratios obtained in inclusive ^{3}He(e,e′) and ^{4}He(e,e′) reactions. In ^{3}He(e,e′), Zghiche *et al.* [5] report a 10% reduction in L/T based on a y-scaling analysis of measured data. In our ^{3}He(e,e′p) measurements, we find that L/T is slightly larger than that given by σ_{CC1}^{ep}, although the enhancement is comparable to our systematic uncertainty. In the inclusive ^{4}He(e,e′) reaction, Carlson and Schiavilla [7] have shown that PWIA is insufficient for reproducing the ratio L/T for the inclusive data, and pion degrees of freedom are required. This contrasts with our ^{4}He(e,e′p) results, where L/T is well-described by PWIA using σ_{CC1}^{ep}. Our data also contrast with previous (e,e′p) measurements on other nuclei at quasielastic kinematics, such as ^{12}C(e,e′p) where an enhancement of T/L was seen at higher missing energies, starting at about the 2-nucleon emission threshold [12]. These ^{12}C data also showed a significant difference between the transverse and longitudinal missing energy spectra; in our results the shape of the ^{3}He and ^{4}He missing energy spectra were found to be independent of ϵ for the region of missing energy ($E_m < 20$ MeV in ^{3}He and $E_m < 45$ MeV in ^{4}He) where significant strength was observed.

To compare the overall magnitude of the measurements and the theory, the experimental and theoretical spectral functions have been integrated over selected regions of missing energy and missing momentum. The value of the integral is denoted N^{exp} for the experimental result and N^{theory} for the corresponding theoretical result. The missing energy and missing momentum

Reaction	S^{theory}			N^{exp}/N^{theory}
^{3}He(e,e'p)^{2}H	Salme *et al.*		(Ref. [45])	0.77
	Schulze *et al.*		(Ref. [49])	0.77
	Forest *et al.*		(Ref. [52])	0.79
^{3}He(e,e'p)np	Schulze *et al.*		(Ref. [49])	0.81 (0.84)
^{4}He(e,e'p)^{3}H	Schiavilla *et al.*	(Arg.)	(Ref. [58])	0.68
	Schiavilla *et al.*	(Urb.)	(Ref. [58])	0.85
	Forest *et al.*		(Ref. [52])	0.72
^{4}He(e,e'p)nd + ^{4}He(e,e'p)nnp	Efros *et al.*		(Ref. [59])	0.69 (0.80)

Table 7.2: A comparison of the experimental and theoretical spectral functions for the various reaction channels. The quantity N^{exp} is the integral of the experimental spectral function over a selected region of missing energy and missing momentum, as defined in Chapter 6, and N^{theory} is the integral of the theoretical spectral function over the same limits. The value of N^{exp} is the average value obtained at each of three kinematic settings. For the continuum channels, the results are given for both the 2D (no brackets) and 2DFPM (in brackets) radiative-unfolding techniques.

limits of the integration were different for each reaction channel and were presented in Chapter 6. The ratio N^{exp}/N^{theory} for each of the measured reaction channels is given in Table 7.2. In each case, the value of N^{exp} is the average value obtained at each of the three kinematic settings. For the continuum breakup channels, the result is given for both the 2D and 2DFPM unfolding techniques. For the ^{4}He continuum channel, the ratio N^{exp}/N^{theory} varied from 0.69 to 0.80 depending on the radiative-unfolding technique used. The difference between the two results reflects the large systematic uncertainty in the radiative unfolding, which is due to the relatively large radiative correction to the ^{4}He continuum.

If PWIA and the theoretical spectral functions are correct, one expects $N^{exp}/N^{theory} = 1$. (For our analysis, this result also assumes that σ_{ep}^{CC1} is the correct off-shell electron-proton cross section and that the free nucleon form factors of Ref. [46] are correct, since these two factors are

used in determining an experimental spectral function.) However, PWIA does not account for final-state interactions (FSI) between the detected proton and the recoiling (A-1) system. As discussed in Chapter 6, an estimate of FSI was obtained for the ^{4}He(e,e'p)^{3}Hp reaction using the HE4PT computer code of R. Schiavilla [55], which indicated a 12% reduction in the cross section at our kinematics. Although this calculation was for ^{4}He and not for ^{3}He, we expect the results to be similar for the two nuclei. For our results, we therefore expect $N^{exp}/N^{theory} = 0.88$ when accounting for FSI (with unknown theoretical uncertainty).

The experimental values of N^{exp}/N^{theory} tabulated in 7.2 fall between 3% and 22% below this value. These discrepancies could be due to several factors including the off-shell cross section, the free nucleon form factors, the final-state interactions, the theoretical descriptions of the spectral functions, or our systematic uncertainty. Additionally, there could be contributions from effects that go beyond PWIA+FSI, such as meson exchange currents. We emphasize that in general the shape of the experimental spectral functions versus missing energy and missing momentum are well-reproduced by the PWIA predictions. Therefore any physical process that can explain the observed shift in magnitude must not introduce dramatic changes in the shape of the theoretical cross section. More complete calculations that include effects beyond PWIA are required to further interpret the data.

Appendix A

Kinematic Correction

In elastic scattering measurements, the observed peaks in the measured energy and momentum spectra are broadened due to the finite angular acceptance. What is usually called a *kinematic correction* to the momentum is not really a correction (since it is not correcting any error) but refers to the introduction of a new variable which corresponds to the momentum that the event would have if it had scattered at the central spectrometer angle. The new variable then has no kinematic broadening.

For a given scattering angle (θ), the final energy (E_f) of an elastically scattered electron is

$$E_f = \frac{E_i}{1 + \frac{2E_i}{M_A}\sin^2\theta/2}. \tag{A.1}$$

where E_i is the incident electron energy and M_A is the mass of the target nucleus. Expanding the expression about the central scattering angle (θ_0) gives

$$E_f(\theta) \approx E_f(\theta_0) + (\theta - \theta_0) \cdot \left(\frac{dE_f}{d\theta}\right)_{\theta=\theta_0} \tag{A.2}$$

where

$$\frac{dE_f}{d\theta} = -\frac{E_f^2}{M_A}\sin\theta. \tag{A.3}$$

For small out-of-plane angles we have $(\theta - \theta_0) \approx \phi$, i.e. the difference between the scattering

angle and the central spectrometer angle is approximately the horizontal transport angle ϕ, so

$$E_f(\theta) \approx E_f(\theta_0) - \phi \frac{E_f^2}{M_A} \sin \theta_0. \tag{A.4}$$

We define the kinematically-corrected momentum:

$$p_{kin} = p \left(1 + \phi \frac{p}{M_A} \sin \theta_o \right) \tag{A.5}$$

where p is the detected particle momentum. For highly relativistic electrons, $p \approx E$, and by comparing to (A.4) we identify $p_{kin} \approx E_f(\theta_0)$.

Appendix B

Radiative Unfolding

B.1   Introduction

The radiative unfolding of the (e,e'p) data was done with the program RADCOR, which was written in FORTRAN by A. Rokavec [39]. This code was based on an earlier work by E. Quint [62] at NIKHEF. For our analysis a minor modification was made to RADCOR's calculation of the external bremsstrahlung correction. This was done to correctly account for the contribution of the stainless steel walls of the Helium target cell, as described in section B.2.2 below.

In the following sections we give the correction factors used by RADCOR for each of the three types of radiative processes considered. A complete discussion of radiative unfolding for (e,e'p) is given in Ref. [39, 62, 63], and the reader is directed there for further details.

B.2   Correction Factors used by RADCOR

Three distinct types of radiative processes are considered:

1. *Internal bremsstrahlung* (also known as *Schwinger radiation* [64]), where the radiation of real or virtual photons occurs in an interaction with the same nucleus as the (e,e'p) reaction,

2. *External bremsstrahlung*, where the radiation of real photons occurs in an interaction with another nucleus, and

3. *Ionization loss*, where a particle loses energy because of excitation or ionization of atoms.

B.2.1   Internal Bremsstrahlung

The correction factor for internal bremsstrahlung used by RADCOR is that proposed by Penner [65]:

$$C_{schw} = \frac{e^{\delta_{real}}}{1 + \delta_{virt}}$$ (B.1)

where "real" and "virt" denote the contributions from real and virtual photons respectively. The real-photon part is given by

$$\delta_{real} = \frac{\alpha}{\pi} \ln\left(\frac{E_i E_f b}{\eta^2 (\Delta E)^2}\right) \left[\ln\left(\frac{-q_\mu{}^2}{m_e^2}\right) - 1\right] \; ;$$ (B.2)

with*

$$b = 1 + \frac{2\omega}{M} \sin^2\left(\frac{\theta_e}{2}\right),$$

$$\eta = 1 + \frac{2E_i}{M} \sin^2\left(\frac{\theta_e}{2}\right),$$

$$q_\mu{}^2 = \omega^2 - |\vec{q}|^2 < 0$$

The virtual-photon part is given by

$$\delta_{virt} = \frac{\alpha}{\pi}\left\{\frac{13}{6}\left[\ln\left(\frac{-q_\mu{}^2}{m_e^2}\right) - 1\right] - \frac{17}{18} - \frac{\pi^2}{6} - \frac{1}{2}\ln^2\left(\frac{E_i}{E_f}\right) + L_2\left(\cos^2\left(\frac{\theta_e}{2}\right)\right)\right\}$$ (B.3)

The cutoff energy, ΔE, is defined in RADCOR to be equal to one-half the size of the missing energy bin. L_2 is the Spence function, which is defined by

$$L_2(x) = -\int_0^x \frac{\ln(1-y)}{y} dy$$ (B.4)

---

*Quint [62] and Holtrop [63] indicate a misprint in Penner [65], who defines $b = 1 + (\omega/2M)\sin^2(\theta_e/2)$.

and has a series solution (see Ref. [66]):

$$L_2(x) = \sum_{i=1}^{\infty} \frac{x^i}{i^2} \tag{B.5}$$

In RADCOR, the above sum is evaluated for only a finite number of terms. The final term in the sum is defined to be the first term where either $i > 100$ or $x^i < 0.0001$.

B.2.2 External Bremsstrahlung

The correction factor used for external bremsstrahlung was:

$$C_{ext} = \exp\left\{ t_{\text{rad}} \left[-\left(\zeta - \frac{1}{2} \right) + \zeta \ln\frac{E}{\Delta E} + \zeta\frac{\Delta E}{E} - \frac{1}{2}\left(\frac{\Delta E}{E} \right)^2 \right] \right\} \tag{B.6}$$

which is the same as that suggested by Friedrich [67] when the substitution $\zeta \to 2 - \eta$ is applied. The factor t_{rad} is the target thickness in radiation lengths, $t_{\text{rad}} = t/X_0$, with t and X_0 the target thickness and unit radiation length, respectively, in [gm/cm^2]. The unit radiation length, X_0, was calculated from (see Ref. [68]):

$$X_0 = 716.405(A/Z)/[Z(l_1 - f(Z)) + l_2][\text{gm/cm}^2] \tag{B.7}$$

where l_1 and l_2 have the values given in Table B.1, and $f(Z)$ is given by

$$f(Z) = (Z\alpha)^2\{1.202 + (Z\alpha)^2[-1.0369 + 1.008(Z\alpha)^2/((Z\alpha)^2 + 1)]\} \tag{B.8}$$

The function ζ is equivalent to the parameter b of Ref. [68], and is given by

$$\zeta(Z) = \frac{1}{9}[12 + (Z + 1)/(l_1 Z + l_2)] \tag{B.9}$$

The cutoff energy, ΔE, is defined in RADCOR to be equal to one-half the size of the missing energy bin. This is the same definition of ΔE that was used in the internal bremsstrahlung correction.

Z	l_1	l_2
1	5.31	6.114
2	4.79	5.621
3	4.74	5.805
4	4.71	5.924
≥ 5	$5.216 - \ln(Z)/3$	$7.085 - 2\ln(Z)/3$

Table B.1: Parameters for calculation of the radiation length [62, 68]

External Bremsstrahlung Correction for a Composite System

The gas target used in this experiment had thick stainless steel walls, which contribute to the external bremsstrahlung. The total correction due to the walls and helium gas is accounted for by using the value of t_{rad} for the composite wall-target system in equation (B.6). The value of t_{rad} for the composite system is calculated from $t_{\mathrm{rad}}^c = t^c/X_0^c$, where $t^c = t^{He} + t^{Fe}$ is the total thickness of the composite target, and X_0^c is the composite radiation length calculated from (see Ref. [70]):

$$\frac{1}{X_0^c} = \frac{t^{He}}{t^c}\left(\frac{1}{X_0^{He}}\right) + \frac{t^{Fe}}{t^c}\left(\frac{1}{X_0^{Fe}}\right) \tag{B.10}$$

The stainless steel material in the target walls is approximated by its largest component, iron (^{56}Fe). The other components of stainless steel tend to be close to iron in the periodic table so that the error introduced in the radiative correction (which is Z-dependent) by assuming 100% iron should be negligible.

To complete the calculation of C_{ext} for the composite target, the value of the function $\zeta(Z)$ is also needed. The function has a weak dependence on Z, as is illustrated in table B.2. The difference between the calculated values of $\zeta(Z)$ for Helium and Iron is 0.37%, which can be ignored. The value for Helium was therefore used throughout the analysis.

material	$\zeta(Z)$
^{3}He	1.3553
^{4}He	1.3553
^{56}Fe	1.3600

Table B.2: The calculated values of ζ for the target material used in this experiment

B.2.3 Ionization Loss

The factor used by RADCOR to correct for ionization loss (also referred to as *Landau straggling*) is based on the distributions of Findlay and Dusautoy [69] and is given by (see Ref. [62, 63]):

$$C_{Land} = \sum_{i=1}^{9} f_i \ / \ \sum_{i=1}^{9} f_i \ \mathrm{prob}(x) \tag{B.11}$$

where

$$\mathrm{prob}(x) \ = \ 1 - 1/\{2(1 + \sum_{i=1}^{4} \delta_i x^i)^4\}$$

$$x \ = \ \sqrt{2}(\Delta E/\xi - \Lambda - c_i)/d_i$$

$$\xi \ = \ 0.1536(Z/A)t/\beta^2 \ \mathrm{MeV}$$

$$\Lambda \ = \ \ln\{\xi\beta^2/(1 - \beta^2)\} - 1.8\ln(Z) - \beta^2 - 5.1004$$

$$d_i \ = \ \sqrt{g_i^2 + b^2}$$

$$b^2 \ = \ 2 \times 10^{-5} Z^{4/3} \lambda/\xi^2$$

The values of g_i, f_i, c_i and δ_i are given in Table B.3. The mean energy loss (λ) of a proton or an electron in an absorber is given by:

$$\lambda_{\mathrm{proton}} \ = \ 2\xi \ln\{\beta^2/(1 - \beta^2) - 0.9\ln(Z) - \beta^2 + 11.06469\}$$

$$\lambda_{\mathrm{electron}} \ = \ \xi\{19.26 + \ln(t/\rho)\}$$

where ρ is the target density in gm/cm^3 and t is the target thickness in gm/cm^2.

i	g_i	f_i	c_i	δ_i
1	0.737	0.0271	-1.48	0.196854
2	0.947	0.0798	-0.738	0.115194
3	1.23	0.1085	0.17	0.000344
4	1.68	0.1087	1.33	0.019527
5	2.40	0.0862	2.95	
6	3.68	0.0604	5.39	
7	6.18	0.0396	9.40	
8	12.3	0.0258	16.8	
9	39.7	0.0238	30.8	

Table B.3: Parameters used in the correction factor for Landau straggling (see Ref. [39, 62]).

RADCOR applied the ionization loss correction to the incident and final electrons and to the detected proton. The calculation considered only contributions from the Helium gas inside the cell, ignoring any contribution from the cell walls. The ionization loss correction was found to be negligible for our experiment: for $\Delta E = 0.875$ MeV, RADCOR calculated $C_{Land} = 1.000$ for the electrons and 0.9977 for the protons at our 855/660 ^{3}He kinematics. A separate calculation considering only the walls of the target cell showed that the contribution from the cell walls to C_{Land} was the same size as the contribution from the Helium gas. Since the size of the correction is negligible, the error in ignoring the wall contribution is insignificant.

There is some ambiguity in the definition of the cutoff energy, ΔE, for the ionization loss correction. This is discussed by Holtrop [63], who chooses the cutoff energy to be equal to the missing energy resolution. Since the ionization loss correction is small for our experiment we ignored this ambiguity and used the existing definition in RADCOR. For completeness, we note that RADCOR's definition of ΔE for the ionization loss correction is

$$\Delta E = \left\{ 0.5 + \text{nint}\left(\frac{\Delta E_m^{res}}{\Delta E_m} + 0.5 \right) \right\} \times \Delta E_m$$

where 'nint' indicates rounding to the nearest integer, ΔE_m^{res} is the missing energy resolution (FWHM) and ΔE_m is the width of the missing energy bin. For our analysis, $\Delta E_m^{res} = 0.5$ and $\Delta E_m = 0.25$, yielding $\Delta E = 0.875$.

Appendix C

Collimator Models for Spectrometers A and B

The nominal sizes of the collimators used in this experiment were 21 msr in Spectrometer A and 5.6 msr in Spectrometer B. The collimators each have complicated shapes, with multiple faces in the horizontal and vertical directions. These shapes were modelled as a series of horizontal and vertical slits located at the intersection of each of the faces. The slit models were then implemented in the Monte Carlo AEEXB [32], so that the acceptance-averaged cross sections and detection volumes calculated by AEEXB had the same angular constraints as the experimental data.

In Spectrometer A, the 21 msr collimator is approximately ±70 mrad in the vertical direction and ±75 mrad in the horizontal. The position and width of the slits used to model this collimator is given in Table C.1. In the table, 'drift distance' is the distance from the center of the target to the slit location, and corresponds to the dimension d in Figure 4-1 in Chapter 3. The slit dimensions h and v are the half-widths of the slits in the horizontal and vertical directions, respectively, as defined in Figure 4-1.

In Spectrometer B, the nominal collimator size was 5.6 msr (±70 mrad vertical, ±20 mrad horizontal). The dimensions of the slits used to model this collimator are given in Table C.2. The quantities in the table have the same definitions as described above for Spectrometer A.

Detailed drawings of the collimators are not currently available in digital format so are not presented here. The dimensions of the collimators were obtained from the blueprints in Mainz and were used to determine the slit dimensions.

horizontal slits		
slit #	drift (cm)	h (cm)
1	56.550	4.3598
2	58.146	4.4043
3	59.742	4.4825
4	61.358	4.5942
5	62.954	4.7392
6	64.550	4.9185

vertical slits		
slit #	drift (cm)	v (cm)
1	56.550	3.9550
2	59.143	4.1365
3	61.955	4.3325
4	64.550	4.5145

Table C.1: Dimensions of the horizontal and vertical slits used to model the 21 msr collimator in Spectrometer A.

horizontal slits		
slit #	drift (cm)	h (cm)
1	314.400	6.3176
2	317.700	6.3548
3	321.099	6.4228
4	324.398	6.5176

vertical slits		
slit #	drift (cm)	v (cm)
1	336.800	23.626
2	340.093	23.845
3	343.484	24.083
4	346.776	24.325

Table C.2: Dimensions of the horizontal and vertical slits used to model the 5.6 msr collimator in Spectrometer B.

Appendix D

Target Cell Dimensions

The target cell was a spheroidal shell with an 80 mm diameter. The cell was formed from a stainless steel cylindrical shell 100 μm thick and 66 mm in diameter. The spheroid was formed by expanding the cylinder with high pressure water, so that the final dimensions were as shown in Figure D-1. The thickness of the cell walls could not be directly measured, but was estimated as follows. The surface area of the spheroid is

$$
\begin{aligned}
A_s &= 2\pi r_s^2 \int_{\theta_1}^{\theta_2} \sin\theta d\theta = 2\pi r_s^2 (\cos\theta_1 - \cos\theta_2) \\
&= 2\pi r_s^2 \cdot 2\frac{\sqrt{r_s^2 - r_c^2}}{r_s}
\end{aligned}
$$

The cylindrical section from which it was formed has surface area

$$
A_c = 2\pi r_c l = 2\pi r_c \cdot 2\sqrt{r_s^2 - r_c^2}
$$

To calculate the thickness of the spheroid, it is assumed that the material stretches uniformly, and that the total volume of stainless steel remains constant ($V = A_s t_s = A_c t_c$). The estimated thickness of the spheroidal shell is then

$$
\begin{aligned}
t_s &= \frac{A_c}{A_s} \cdot t_c \\
&= \frac{r_c}{r_s} \cdot t_c = \frac{33}{40} \cdot 100\mu m = 82.5\mu m
\end{aligned}
$$
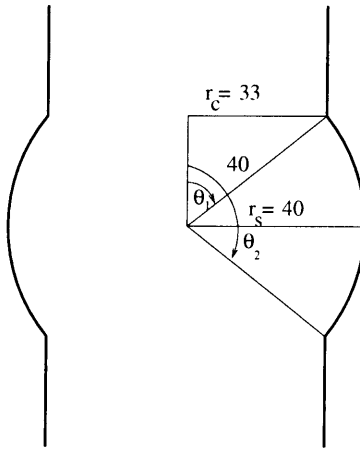
Figure D-1: Dimensions of the target cell in millimeters.

Appendix E

Beam Rastering Calibration Parameters

For all measurements using the Helium target, the incident beam was rastered by approximately ± 3.5 mm in the vertical and horizontal directions to distribute the deposited heat. The rastering was done by passing a sinusoidal current through coils placed in the beam line in the horizontal and vertical planes, as discussed in Chapter 3. The current in the coils was read out by an ADC and stored in the data stream for each event. In the data analysis, ESPACE reconstructed the beam position on the target for each event from these ADC values as follows:

$$x = (N_x \times \text{xslope}) + \text{xoffset} \tag{E.1}$$

$$y = (N_y \times \text{yslope}) + \text{yoffset} \tag{E.2}$$

where N_x and N_y are the ADC values corresponding to the current in the horizontal and vertical rastering coils, respectively. The coordinates x and y are specified in the beam coordinate system (shown in Figure 4-1 in Chapter 3), which is a right-handed coordinate system with y pointing upwards and z along the incident beam (pointing towards the beam dump).

The four calibration parameters (xslope, xoffset, yslope, yoffset) were determined from calibration runs that were regularly performed when the the beam was tuned or the beam energy was changed. The calibration technique is described briefly in Chapter 3 and in detail in Ref. [22].

Table E.1 lists the raster calibration runs performed during our experiment and the calibration parameters obtained from each of them.

horizontal cal. run	xoffset (mm)	xslope (mm/channel)	vertical cal. run	yoffset (mm)	yslope (mm/channel)
950622141437	-1.669E+01	1.312E-01	950622145633	-1.180E+01	9.207E-02
950622142803	-1.720E+01	1.346E-01	950622150655	-1.176E+01	9.163E-02
950623164910	-1.213E+01	9.423E-02	950623170114	-7.194E+00	5.621E-02
950625000608	-1.389E+01	1.085E-01	950625002854	-9.271E+00	7.102E-02
950625174512	-1.394E+01	1.085E-01	950625175154	-8.937E+00	7.077E-02
950625235037	-1.444E+01	1.126E-01	950625235621	-7.075E+00	5.505E-02
950626040142	-1.241E+01	9.553E-02	950626040754	-7.200E+00	5.625E-02
950629071350	-2.306E+01	1.818E-01	950629071830	-1.341E+01	1.046E-01
950629124159	-2.306E+01	1.818E-01	mystery[a]	-1. 310E+01	1.046E-01
950629225642	-1.798E+01	1.410E-01	950629230101	-1.224E+01	9.631E-02
950630030845	-1.784E+01	1.410E-01	950630031413	-1.169E+01	9.250E-02
950701055722	-1.007E+01	7.941E-02	950701060027	-1.233E+01	9.956E-02
950701234350	-1.009E+01	8.033E-02	950701234718	-1.243E+01	9.956E-02
950707135457	-1.272E+01	1.037E-01	950707135833	-1.079E+01	8.322E-02
950707184417	-1.283E+01	1.031E-01	950707184806	-1.063E+01	8.322E-02
950707215203	-1.227E+01	9.823E-02	950707215828	-1.164E+01	9.456E-02
950709014812	-1.228E+01	9.639E-02	950709015135	-1.200E+01	9.633E-02
950709134107	-1.215E+01	9.726E-02	950709134831	-1.126E+01	9.373E-02
950710033826	-1.068E+01	8.127E-02	950710034206	-1.229E+01	9.633E-02
950710160402	-1.050E+01	8.223E-02	950710160835	-1.243E+01	9.631E-02
950711044920	-9.971E+00	8.033E-02	950711045706	-1.225E+01	9.584E-02
950711170618	-9.930E+00	8.033E-02	950711171018	-1.210E+01	9.633E-02
950712064246	-1.664E+01	1.320E-01	950712064544	-1.191E+01	9.501E-02
950712071116[b]	-1.643E+01	1.312E-01	950712071539[c]	-1.210E+01	9.501E-0 2
950712133749	-1.630E+01	1.312E-01	950712134103	-1.225E+01	9.454E-02

Table E.1: Beam Rastering Calibration Parameters.

[a]No run number for this data file.

[b]Run number is 2 hours earlier than actual run time.

[c]Run number is 2 hours earlier than actual run time.

Appendix F

List of (e,e′p) Runs Analyzed

kinematics	run number	length (min.)	kinematics	run number	length (min.)
540/660	950622210020	37	675/425	950625190455	31
	950622214007	25		950625193624	31
	950622222125	25		950625200935	35
540/585	950623014620	29		950625210339	27
	950623022732	30	855/660	950624062925	30
	950623025856	33		950624070549	29
540/500	950623053809	39		950624073928	29
	950623061826	32		950624081755	28
	950623065601	32	855/585	950624033122	36
540/425	950623080633	31		950624040908	27
	950623084025	32	855/500	950624093411	31
	950623091354	31		950624100658	30
675/660	950625032420	30		950624111552	31
	950625035844	32		950624114824	30
	950625043709	33	855/425	950624150830	31
675/585	950625061519	31		950624154116	9
	950625064819	31		950624163137	15
	950625072045	31		950624173100	34
	950625075318	21			
675/500	950625085937	30			
	950625093040	31			
	950625100324	30			

Table F.1: ^{3}He(e,e′p) runs analyzed.

kinematics	run number (min.)	length	kinematics	run number	length (min.)
540/660	950630033034	32	540/425	950712192134	37
	950630040359	32		950712200057	18
	950630043649	31		950712202032	37
	950630050854	33		950712213522	33
	950630054332	31	675/660	950707164431	30
	950630061609	30		950707191704	40
540/585	950630073558	32	675/585	950707204034	34
	950630085029	33		950707221416	30
	950630092436	31		950707225951	30
	950630095615	32		950707233211	29
540/500	950630130243	51	675/500	950708011254	31
	950630140924	37		950708015422	31
	950630151327	31		950708022826	32
	950712100342	30		950708030335	30
	950712103511	19		950708033445	33
	950712113105	12		950708040901	31
	950712114426	31		950708044140	31
	950712121607	32		950708051409	42
540/425	950712140354	31		950708055855	31
	950712143623	38	675/425	950708084609	31
	950712151632	31		950708091817	31
	950712154938	29		950708135129	30
	950712162003	34		950708142310	39
	950712165459	32		950708150321	32
	950712172823	31		950708153607	29
	950712180156	32		950708160929	33
	950712183538	45		950708164428	31

Table F.2: ^{4}He(e,e'p) runs analyzed.

kinematics	run number	length (min.)	kinematics	run number	length (min.)
855/660	950702031033	31	855/425	950702184421	6
	950702034459	30		950702190504	34
	950702042009	30		950702200310	22
	950702045427	31		950702202731	7
855/585	950702075712	15		950702210847	32
	950702092137	34		950702203544	32
	950702105248	30		950702214130	30
	950702112546	33		950711215252	31
	950702122624	27		950711222516	31
855/500	950702134439	5		950711233531	32
	950702135129	31		950711225718	33
	950702145529	35		950712001349	31
	950702153253	46			
	950702162113	41			

Table F.3: ^{4}He(e,e'p) runs analyzed (continued).

Appendix G

Off-Shell Electron-Nucleon Cross Section

As presented in Chapter 2, the (e,e'p) cross section in PWIA factorizes into the product of a kinematic factor, the off-shell electron-nucleon cross section, and the spectral function:

$$\frac{d^6\sigma}{d\Omega_e d\Omega_p dp_e dp_p} = p_p^2 \times \sigma_{eN} \times S(p_m, E_m) \tag{G.1}$$

The extraction of an experimental spectral function from the measured cross section requires the choice of a prescription for σ_{eN}, of which there are several [71]. We chose the CC1 prescription of de Forest [18], σ_{CC1}, which is commonly used by others (see Ref. [10], for example). The determination of σ_{CC1} also required a choice of free-nucleon form factors. We chose the parameterization of Simon *et al.* [46] as discussed below.

The cross section σ_{CC1} is calculated from [18]:

$$\sigma_{eN} = \sigma_M \left[\frac{q_\mu^4}{q^4} W_c + \left(\frac{q_\mu^2}{2q^2} + tan^2\frac{1}{2}\theta \right) W_T + \frac{q_\mu^2}{q^2} \left(\frac{q_\mu^2}{q^2} + tan^2\frac{1}{2}\theta \right)^{1/2} W_I cos\phi \right.$$
$$\left. + \left(\frac{q_\mu^2}{q^2} cos^2\phi + tan^2\frac{1}{2}\theta \right) W_S \right] \tag{G.2}$$

where $\sigma_M = 4\alpha^2 E_1^2 cos^2(\theta/2)/q_\mu^4$ is the Mott cross section, E_1 is the incident beam energy, θ is the electron scattering angle, ϕ is the angle between the scattering and ejectile as shown in Figure 2-1 (Chapter 2), and q and q_μ are the three- and four-momentum transfer, respectively.

The W's are given by

$$
W_C = \frac{1}{4\bar{E}E'} \left\{ (\bar{E} + E')^2 \left(F_1^2 + \frac{\bar{q}_\mu^2}{4m^2}\kappa^2 F_2^2 \right) - q^2(F_1 + \kappa F_2)^2 \right\}
$$

$$
W_T = \frac{\bar{q}_\mu^2}{2\bar{E}E'}(F_1 + \kappa F_2)^2
$$

$$
W_S = \frac{p'^2 sin^2\gamma}{\bar{E}E'} \left(F_1^2 + \frac{\bar{q}_\mu^2}{4m^2}\kappa^2 F_2^2 \right) \tag{G.3}
$$

$$
W_I = -\frac{p' sin\gamma}{\bar{E}E'}(\bar{E} + E') \left(F_1^2 + \frac{\bar{q}_\mu^2}{4m^2}\kappa^2 F_2^2 \right)
$$

where $\bar{E} = (p^2 + m^2)^{1/2}$, with p the initial momentum of the struck proton and m the mass of the proton, and κ is the anomalous magnetic moment of the proton ($= \mu_p - 1 = 1.793$).

F_1 and F_2 are the Dirac and Pauli form factors, respectively, of the proton. In terms of the Sachs form factors, G_E and G_M, they are given by

$$
F_1(q_\mu^2) = \frac{G_E(q_\mu^2) + \tau G_M(q_\mu^2)}{1 + \tau} \tag{G.4}
$$

$$
F_2(q_\mu^2) = \frac{G_M(q_\mu^2) - G_E(q_\mu^2)}{\kappa(1 + \tau)} \tag{G.5}
$$

Simon et al. [46] have extracted the Sachs form factors from measurements of electron-proton scattering at Mainz over a range of q^2 from 0.14 to 1.4 fm^{-2}. They have combined these data with data measured at higher q^2 (up to 130 fm^{-2}) at other laboratories to obtain the following parametrization of the form factors:

$$
G(q_\mu^2) = \sum_{n=1}^{4} \frac{a_n}{1 + q_\mu^2/m_n^2} \tag{G.6}
$$

where $G = G_E$ or G_M/μ, and the coefficients m_n, a_n are those given in Table G.1.

The CC1 prescription was compared to de Forest's CC2 prescription [18] at various points inside our experimental acceptance [61]. At each point, the ratio $\sigma_{CC1}/\sigma_{CC2}$ was found to be constant within 0.5% for the three values of the beam energy (corresponding to three values

	a_1	a_2	a_3	a_4	m_1^2 [fm^{-2}]	m_2^2 [fm^{-2}]	m_3^2 [fm^{-2}]	m_4^2 [fm^{-2}]
G_E	0.312	1.312	-0.709	0.085	6.0	15.02	44.08	154.2
G_M/μ	0.694	0.719	-0.418	0.005	8.5	15.02	44.08	355.4

Table G.1: Parameters for the form factors $G_E(q^2)$ and $G_M(q^2)$ from Ref. [46].

of the virtual photon polarization, ϵ). The ϵ-dependence of the extracted spectral functions is therefore independent (within 0.5%) of the choice of σ_{CC1} versus σ_{CC2}. In addition, the ratio $\sigma_{CC1}/\sigma_{CC2}$ was found to vary from 0.97 to 1.03 at different points across the acceptance. The magnitude of the experimental spectral functions (which are an average over the experimental acceptance) should therefore be relatively insensitive to the choice of σ_{CC1} versus σ_{CC2}. A more exact comparison of the spectral functions extracted with σ_{CC1} versus σ_{CC2} would require averaging over the acceptance with a Monte Carlo.

Appendix H

Computer Dead-Time Corrections

H.1 Introduction and Notation

The computer dead time was measured by a series of scalers as discussed in Chapter 3. Corrections were applied to the measured data to account for the computer dead time, as discussed below. The corrections are different for coincident and singles events, and each case is discussed separately.

For our experiment, the data can be divided into four types of events, each corresponding to specific combinations of the three spectrometers: $AB\bar{C}, A\bar{B}\bar{C}, \bar{A}B\bar{C}$ and $\bar{A}\bar{B}C$. For example, $AB\bar{C}$ denotes events where Spectrometers A and B fired and Spectrometer C did not. All other possible combinations beyond these four were removed from the hardware trigger by using large prescale factors as discussed in Chapter 3. Since Spectrometer C only appears by itself, we will use the shorthand notation $AB, A\bar{B}, \bar{A}B$ and $\bar{A}\bar{B}C$ to label the four combinations.

The data recorded for each event included a bit pattern indicating which spectrometers fired in that event. Histograms $H_{AB}, H_{A\bar{B}}, H_{\bar{A}B}$ and $H_{\bar{A}\bar{B}C}$ (corresponding to each of the four combinations) were acquired from the measured data by cutting on this bit pattern. From these histograms we calculated the dead-time corrected histograms of coincidences (H^c_{AB}) and singles (H^c_A, H^c_B, H^c_C) as discussed below.

235

H.2   Computer Dead-Time Correction for AB Coincidence Events

The dead-time corrected coincidence histogram H_{AB}^c was determined from H_{AB} by

$$H_{AB}^c = \eta_{dt}^{AB} \times H_{AB} \tag{H.1}$$

where η_{dt}^{AB} is the computer dead-time correction for coincidences between Spectrometers A and B. For AB coincidences, the relevant dead time is the time that either Spectrometer A or Spectrometer B was dead. This is given by the sum of the individual dead times of the two spectrometers (dead_A + dead_B), minus the time that they were both dead (dead_AB). The computer dead-time correction used for AB coincidences was therefore

$$\eta_{dt}^{AB} = \frac{\text{total time}}{\text{total time} - (\text{dead\_A} + \text{dead\_B} - \text{dead\_AB})} \tag{H.2}$$

which is the same factor used by other Mainz experiments (see Ref. [25] for example). The times dead_A, dead_B and dead_AB are the times measured from the dead-time module as shown in Figure 3-6 in Chapter 3.

H.3   Computer Dead-Time Correction for Singles

H.3.1   Time Method

For the purposes of this discussion a singles event for a given spectrometer is defined as any event where that spectrometer fired. In the following discussion, singles determined from Spectrometer A are used as an example. The same conclusions hold for Spectrometer B, and the corresponding formulae can be obtained by swapping the indices $A \leftrightarrow B$. The correction for Spectrometer C is simplified since there is only one type of event $(\bar{A}\bar{B}C)$ containing Spectrometer C. The correction for Spectrometer C is presented in the next section.

To calculate the dead-time corrected singles histogram for Spectrometer A, H_A^c, we must

generally consider contributions from both $A\bar{B}$ events and AB events:

$$H_A^c = H_{A\bar{B}}^c + H_{AB}^c \tag{H.3}$$

$$= (\eta_{dt-pre}^{A\bar{B}} \times H_{A\bar{B}}) + (\eta_{dt}^{AB} \times H_{AB}) \tag{H.4}$$

where $H_{A\bar{B}}$ is the measured histogram of events where only Spectrometer A fired (and not B) and H_{AB} is the measured histogram of events where both Spectrometers A and B fired. The AB coincidence dead-time correction, η_{dt}^{AB}, is as defined in Eqn. (H.2). The correction factor for $A\bar{B}$ events, $\eta_{dt-pre}^{A\bar{B}}$, is very different from η_{dt}^{AB} for our experimental configuration. It includes both dead-time and prescaling corrections and requires further discussion.

If the trigger electronics in Mainz are in their design configuration, the correction factor for $A\bar{B}$ events is

$$\eta_{dt-pre}^{A\bar{B}} = m_A \times \frac{\text{total time}}{\text{total time} - \text{dead\_A}} \tag{H.5}$$

where m_A is the prescaling factor for Spectrometer A. For example, for a prescaling factor $m_A = 2$ and a fractional dead time $\alpha \equiv \frac{\text{dead\_A}}{\text{total time}} = 0.20$, the correction factor for the design configuration is $\eta_{dt-pre}^{A\bar{B}} = 2.5$.

However, in our experiment the trigger electronics differed from the design configuration. The difference was that the prescaling module on each spectrometer (which prescales the singles triggers for that spectrometer) was not inhibited. The module therefore continued to count triggers while the computer was dead. In this case equation (H.5) is incorrect, and takes on a complicated solution as shown by Friedrich [72]. He showed that for the above example ($m_A = 2$ and $\frac{\text{dead\_A}}{\text{total time}} = 0.20$) the overall correction factor was 2.14048 instead of 2.5. The correction factor for an arbitrary prescale value and fractional dead time has been derived by Merkel [73], and his computer program has been used to calculate the correction factor for a few sample cases give in Table H.1

As can be seen in the table, for $m = 1$ (i.e. no prescaling) the correction factor is equal to that obtained from Equation (H.5). As the prescaling value is increased, the contribution of

	m=1	m=2	m=5	m=20
$\alpha = 0.1$	1.11111	2.03637	5.00086	20.00000
$\alpha = 0.2$	1.25000	2.14049	5.01859	20.00000
$\alpha = 0.3$	1.42857	2.32037	5.10015	20.00010

Table H.1: Prescaling and dead-time correction factor $\eta^{A\bar{B}}_{dt-pre}$ as a function of prescale factor (m) and fractional dead time (α) as calculated with the computer code of Merkel [73].

the dead time is reduced and the overall correction factor approaches the prescaling factor. For $m = 20$, the effect of the dead time is negligible, even for a fractional dead time of $\alpha = 0.30$, so that the overall correction factor $\eta^{A\bar{B}}_{dt-pre} = m = 20$. The qualitative explanation is that as the prescale value is increased, the average distance between pulses coming out of the prescaler is very long, so that the probability of a pulse arriving during the dead time is small. A general discussion of dead time in scaling circuits can be found in Ref. [74].

For most of the singles data analyzed in this experiment, the prescaling factor (m) was sufficiently large and the fractional dead time (α) sufficiently small that

$$\eta^{A\bar{B}}_{dt-pre} \rightarrow m_A \tag{H.6}$$

based on the results of Merkel's program. However, this analysis ignores the case where there is a significant number of AB coincidences in the data stream, as there was in many of our runs. These AB coincidence events arrive randomly with respect to the prescaled $A\bar{B}$ events, so that computer dead time caused by an AB event can contribute to the dead time for $A\bar{B}$ events. We therefore propose that that complete correction factor is

$$\eta^{A\bar{B}}_{dt-pre} \rightarrow m_A \times \frac{\text{total time}}{\text{total time} - \text{dead\_AB}} \tag{H.7}$$

where dead_AB accounts for the dead time due to AB events.

We refer to equation (H.4), with η^{AB}_{dt} given by (H.2) and $\eta^{A\bar{B}}_{dt-pre}$ given by (H.7), as the *Time Method* for dead-time correction of singles events. The method is quite complicated and

requires several assumptions. Fortunately, there are a number of scalers which allow the check of these calculations. The scalers also allow the formulation of a simpler dead-time calculation. The check of the method and an explanation of the second method are discussed in the next two sections.

H.3.2 Scaler Check of Time Method

The hardware trigger condition for each spectrometer in this experiment was a coincidence between the ΔE and TOF scintillators. For each spectrometer a scaler records the number of these ΔE-TOF coincidences. The number recorded by one of these scalers is not affected by the computer dead time and so defines the number of **raw triggers** for a given spectrometer.

We define the number of **measured triggers** for a particular spectrometer as the number of recorded events in which that spectrometer fired. The number of measured triggers times the prescaling and dead-time corrections should equal the number of raw triggers. Checking this statement for one of the data sets provides a check of the prescaling and dead-time corrections.

As an example, we consider one of the elastic scattering runs from ^{4}He, run number 950707143036. The number of raw triggers recorded by the scalers is $N_A^{raw} = 1.362 \times 10^7$ for Spectrometer A, $N_B^{raw} = 9.67 \times 10^5$ for Spectrometer B, and $N_C^{raw} = 8.72 \times 10^5$ for Spectrometer C.

The data set was analyzed to determine which spectrometers fired in each event, and the total number of measured triggers corresponding to each spectrometer combination obtained. This gave $N_{A\bar{B}} = 93159, N_{\bar{A}B} = 31954, N_{AB} = 2507$ and $N_{\bar{A}\bar{B}C} = 84885^*$. The measured computer dead times were dead_A $= 110.3$ sec, dead_B=31.4 sec, and dead_AB=7.1 sec and the total run time was 647 seconds. The prescaling values were 140 for Spectrometer A, 30 for Spectrometer B and 10 for Spectrometer C. Substituting into (H.4), the dead-time corrected

---

*This data set (run 950707143036) was also found to contain two $\bar{A}BC$ events, which were ignored.

number of measured triggers in Spectrometer A is then given by:

$$
\begin{aligned}
N_A^c &= (\eta_{dt-pre}^{A\bar{B}} \times N_{A\bar{B}}) + (\eta_{dt}^{AB} \times N_{AB}) \\
&= \frac{m_A \times \text{total time} \times N_{A\bar{B}}}{\text{total time} - \text{dead\_AB}} \\
&+ \frac{\text{total time} \times N_{AB}}{\text{total time} + (\text{dead\_A} + \text{dead\_B} - \text{dead\_AB})} \\
&= \frac{140 \times 647 \times 93159}{647 - 7.1} + \frac{647 \times 2507}{647 - (110.3 + 31.4 - 7.1)} \\
&= 1.319 \times 10^7 + 3.166 \times 10^3 \\
&= 1.319 \times 10^7
\end{aligned}
$$

and in Spectrometer B,

$$
\begin{aligned}
N_B^c &= (\eta_{dt-pre}^{\bar{A}B} \times N_{\bar{A}B}) + (\eta_{dt}^{AB} \times N_{AB}) \\
&= \frac{m_B \times \text{total time} \times N_{\bar{A}B}}{\text{total time} - \text{dead\_AB}} \\
&+ \frac{\text{total time} \times N_{AB}}{\text{total time} + (\text{dead\_A} + \text{dead\_B} - \text{dead\_AB})} \\
&= \frac{30 \times 647 \times 31954}{647 - 7.1} + \frac{647 \times 2507}{647 - (110.3 + 31.4 - 7.1)} \\
&= 9.693 \times 10^5 + 3.166 \times 10^3 \\
&= 9.724 \times 10^5
\end{aligned}
$$

We note that the term containing N_{AB} makes either a negligible or a small contribution to N_A^c and N_B^c.

The only type of event containing Spectrometer C is $\bar{A}\bar{B}C$. Therefore the dead-time corrected number of triggers in Spectrometer C, N_C^c, only has contributions from $\bar{A}\bar{B}C$ events and the Time Method gives:

$$
N_C^c = (\eta_{dt-pre}^{\bar{A}\bar{B}C} \times N_{\bar{A}\bar{B}C})
$$

The fractional dead time (α) for Spectrometer C was 0.134; putting this into Merkel's program

(as discussed in the last section) with the prescaling factor $m_C = 10$ yielded

$$\eta_{dt-pre}^{\bar{A}\bar{B}C} \quad \rightarrow \quad m_C = 10$$

so that

$$
\begin{aligned}
N_C^c &= m_C \times N_{\bar{A}\bar{B}C} \\
&= 10 \times 84885 = 8.489 \times 10^5
\end{aligned}
$$

Comparing these results to the number of raw triggers measured by the scalers gives

$$
\begin{aligned}
\frac{N_A^c - N_A^{raw}}{N_A^{raw}} &= -3.2\% \\
\frac{N_B^c - N_B^{raw}}{N_B^{raw}} &= +0.6\% \\
\frac{N_C^c - N_C^{raw}}{N_C^{raw}} &= -2.7\%
\end{aligned}
$$

The significant disagreement between N^c and N^{raw} for Spectrometers A and C indicates that there is a 2-7–3.2% error due to the dead-time correction, which is unacceptably large. This result indicates that the Time Method for determining the prescaling and computer dead-time corrections for singles events is incorrect. We therefore turn to another method, which uses the number of raw triggers instead of the measured dead time to calculate the prescaling and dead-time corrections.

H.3.3 Scaler Method

Consider again the analysis of events from Spectrometer A. We analyze the data and acquire two histograms $H_{A\bar{B}}$ and H_{AB} as a function of some variable x. To obtain the corrected singles histogram, $H_A^c(x)$, we must combine $H_{A\bar{B}}$ and H_{AB} with the appropriate factors as shown in Equation H.4:

$$H_A^c(x) = \eta_{dt-pre}^{A\bar{B}} \times H_{A\bar{B}}(x) + \eta_{dt}^{AB} \times H_{AB}(x) \tag{H.8}$$

where $\eta_{dt-pre}^{A\bar{B}}$ and η_{dt}^{AB} are the correction factors we need to determine.

In general, the singles and coincident events sample from different distributions, so that $H_{A\bar{B}}(x)$ is not proportional to $H_{AB}(x)$. However, if all the coincidences between Spectrometer A and B are random, then the coincident events sample the same distribution as the singles events and $H_{A\bar{B}}(x) \propto H_{AB}(x)$. In that case we can write Equation H.8 as

$$H_A^c(x) = \eta_{dt-pre}^A \times (H_{A\bar{B}}(x) + H_{AB}(x)) \tag{H.9}$$

$$= \eta_{dt-pre}^A \times H_A(x) \tag{H.10}$$

where $H_A(x) = H_{A\bar{B}}(x) + H_{AB}(x)$ and η_{dt-pre}^A is a new correction factor, which we obtain from the ratio of raw and measured triggers:

$$\eta_{dt-pre}^A = \frac{N_A^{raw}}{N_{A\bar{B}} + N_{AB}} \tag{H.11}$$

$$= \frac{N_A^{raw}}{N_A} \tag{H.12}$$

with $N_A = N_{A\bar{B}} + N_{AB}$.

A qualitative way of viewing this correction method is that it treats the whole data acquisition system as a "black box" with N_A^{raw} triggers at the input and N_A measured triggers at the ouput. The effect of prescaling and dead time inside the box is described by the ratio of the input to the output, $\eta_{dt-pre} = N_A^{raw}/N_A$. We refer to this correction method as the Scaler Method since the correction is now based on the scalers that count the raw triggers, instead of the times recorded by the dead-time module.

In our experiment, an analysis of the singles data was required in only two cases:

1. Elastically-scattered electrons detected in Spectrometer A or B. In this case the AB coincidence events had a flat coincidence timing spectrum, indicating that they were completely random. Therefore $H_{A\bar{B}}(x) \propto H_{AB}(x)$ as required above.

2. Quasielastic electrons detected in Spectrometer C. In this case there are no coincidences with the other spectrometers, as described in Chapter 3, so that $N_C = N_{\bar{A}\bar{B}C}$ and $H_C =$

$H_{\bar{A}\bar{B}C}$. Since there are no coincidences with other spectrometers, the Scaler Method is also valid for Spectrometer C.

Summarizing the Scaler Method, the dead-time corrected singles histograms for all three spectrometers are given by

$$H_A^c = \eta_{dt-pre}^A \times H_A$$

$$H_B^c = \eta_{dt-pre}^B \times H_B$$

$$H_C^c = \eta_{dt-pre}^C \times H_C$$

where

$$H_A = H_{A\bar{B}} + H_{AB}, \qquad \eta_{dt-pre}^A = \frac{N_A^{raw}}{N_A}, \qquad N_A = N_{A\bar{B}} + N_{AB}$$

$$H_B = H_{\bar{A}B} + H_{AB}, \qquad \eta_{dt-pre}^B = \frac{N_B^{raw}}{N_B}, \qquad N_B = N_{\bar{A}B} + N_{AB}$$

$$H_C = H_{\bar{A}\bar{B}C}, \qquad \eta_{dt-pre}^C = \frac{N_C^{raw}}{N_C}, \qquad N_C = N_{\bar{A}\bar{B}C}$$

H.3.4 Comparison of Time and Scaler Methods

We now apply the Time and Scaler correction methods independently to a sample run and compare the results. For the sample run, we use run number 950707143036, which is the same ^{4}He elastic-scattering run used in the scaler check of the Time Method in Section H.3.2. For $H(x)$, we use a histogram of the kinematically-corrected momentum, p_{kin}, with the cuts described in Table 4.9 in Chapter 4.

For the Time Method we acquire two histograms, $H_{A\bar{B}}(x)$ and $H_{AB}(x)$ as shown in the top two plots of Figure H-1 Each of the histograms are then multiplied by the appropriate correction factors $\eta_{dt-pre}^{A\bar{B}} = 141.55$ and $\eta_{dt}^{AB} = 1.263$ as calculated in Section H.3.2, resulting in the two histograms shown in the second row of Figure H-1. Those two histogram are then summed to obtain the corrected histogram $H_A^c = \eta_{dt-pre}^{A\bar{B}}H_{A\bar{B}} + \eta_{dt}^{AB}H_{AB}$.

The analogous results for the Scaler Method are shown in Figure H-2. First the sum of the singles and coincidence histograms is taken, $H_A = H_{A\bar{B}} + H_{AB}$, which is shown in the top plot. This is then multiplied by the correction factor $\eta_{dt-pre} = N_A^{raw}/N_A = 142.344$ to obtain the corrected histogram H_A^c in the lower plot.

In the region of the ^{4}He elastic peak (640 MeV/c $< p_{kin} < $ 660 MeV/c), the corrected histograms have 2.691×10^6 counts with the Time Method and 2.777×10^6 counts with the Scaler Method. The value obtained from the Time Method is 3.1% less than the Scaler Method. Recall that in the scaler check in section H.3.2, the Time Method underestimated the number of raw triggers by approximately the same amount (3.2%).

In the data analysis presented in this thesis we have chosen to use the Scaler Method to correct the singles data for prescaling and dead time, since this method reproduces the number of raw triggers by definition. In contrast, the Time Method employs some complicated assumptions about the data acquisition system, and fails to reproduce the number of raw triggers.
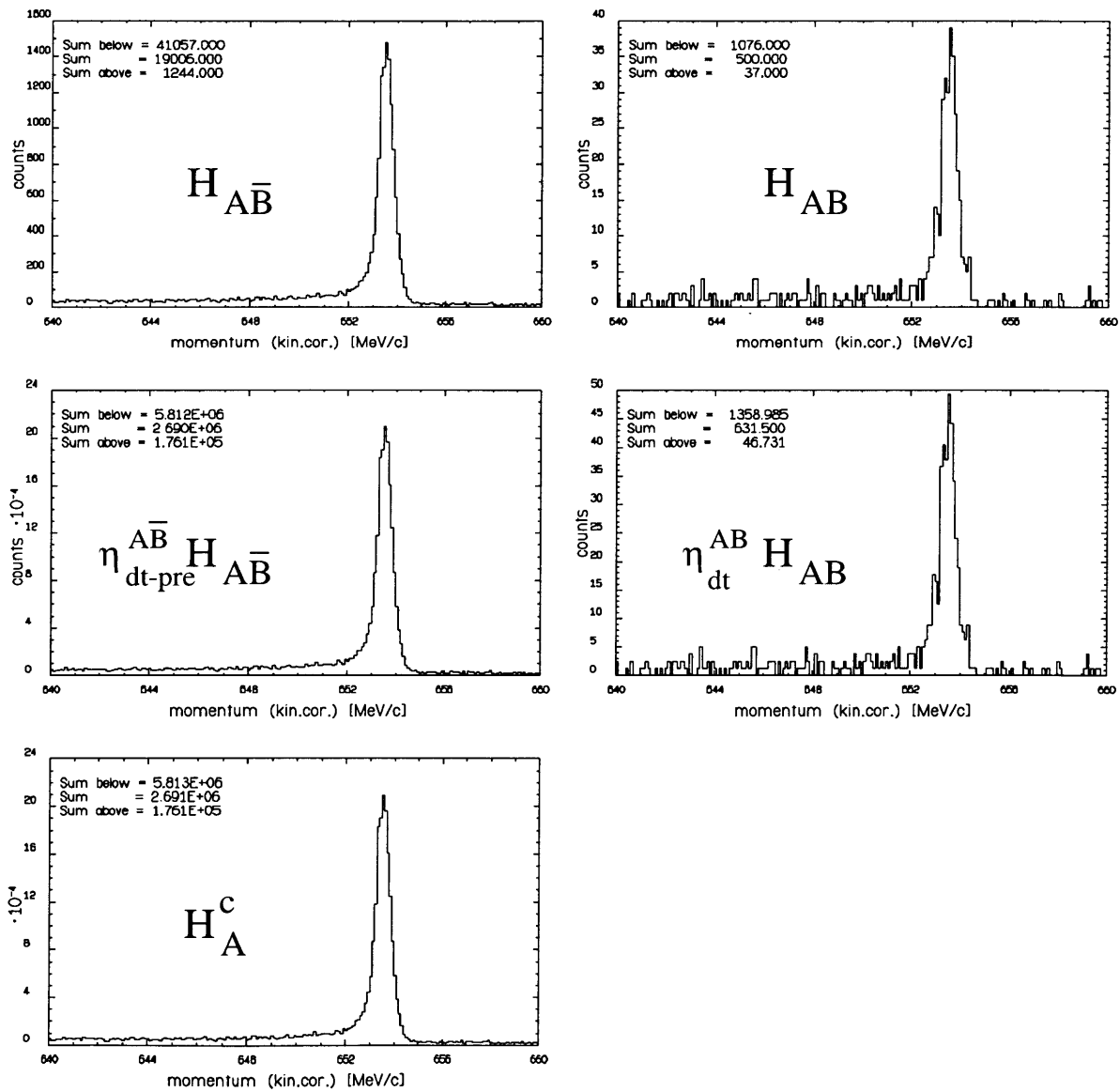
Figure H-1: Example of prescaling and computer dead-time corrections by the Time Method. See text for details.
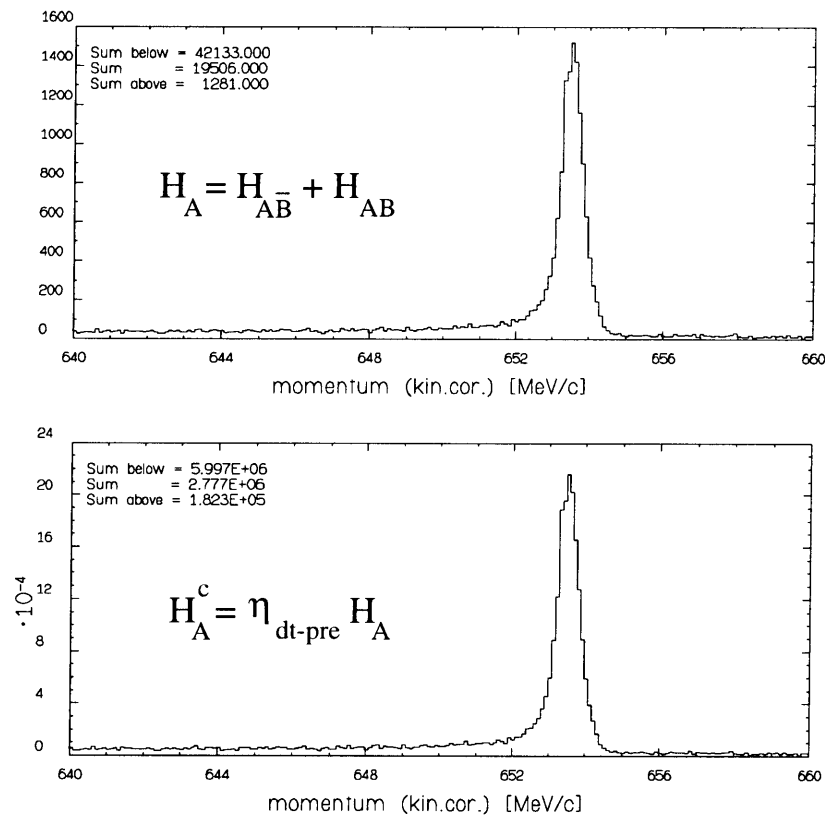
Figure H-2: Example of prescaling and computer dead-time corrections by the Scaler Method. See text for details.

Bibliography

[1] Amos deShalit and Herman Feshbach, *Theoretical Nuclear Physics Volume I: Nuclear Structure* (John Wiley & Sons, New York, 1974).

[2] D.B. Day *et al.*, Phys. Rev. Lett. **59** (1987) 427.

[3] D. Day, J.S. McCarthy, T.W. Donnelly and I. Sick, Ann. Rev. Nucl. Part. Sci **40** (1990) 357.

[4] T.W. Donnelly and I. Sick, *Superscaling in inclusive electron-nucleus scattering*, submitted to Phys. Rev. Lett. (1998).

[5] A. Zghiche *et al.*, Nuclear Physics **A572** (1994) 513-539; *ibid.* **A584** (1995) 757.

[6] J.M. Finn R.W. Lourie and B.H Cottman, Phys. Rev. C **29** (1984) 2230.

[7] J. Carlson and R. Schiavilla, Phys. Rev. C **49** (1994) 2880.

[8] C. Marchand *et al.*, Physics Letters **153B** (1985) 29.

[9] L. Lakehal-Ayat *et al.*, Nuclear Physics **A553** (1993) 693.

[10] J.E. Ducret *et al.*, Nuclear Physics **A553** (1993) 697.

[11] J.M. Le Goff *et al.*, Phys. Rev. C **55** (1997) 1600.

[12] P.E. Ulmer *et al.*, Phys. Rev. Lett. **59** (1987) 2259.

[13] J.J. Kelly, *Nucleon Knockout by Intermediate Energy Electrons*, Advances in Nuclear Physics, Vol. 23, pp. 75-294 (ed. J.W. Negele and E. Vogt, Plenum Press, 1996).

[14] T. de Forest, Jr., *Ann. of Phys.* **45** (1967) 365.

[15] S. Boffi *et al.*, Physics Reports **226** (1993) 1.

[16] S. Boffi *et al.*, Nuclear Physics **A435** (1985) 697.

[17] M.N. Rosenbluth, Physical Review **79** (1950) 615.

[18] T. de Forest Jr., Nuclear Physics **A392** (1983) 232.

[19] K.I. Blomqvist *et al.*, Nucl. Instr. and Meth. **A403** (1998) 263.

[20] W. Boeglin, Czech. J. Phys. **45** (1995) 295.

[21] G. Rosner, University of Mainz, private communication.

[22] W. Wilhelm, Diploma thesis, University of Mainz, unpublished, 1993.

[23] S. Schardt, Ph.D. thesis, University of Mainz, unpublished, 1994.

[24] M.O. Distler, Diploma thesis, University of Mainz, unpublished, 1990.

[25] A. Richter, Ph.D. thesis, University of Mainz, unpublished, 1994.

[26] M. Korn, Ph.D. thesis, University of Mainz, unpublished, 1995.

[27] T.W. Donnelly, *Perspectives in the Structure of Hadronic Systems*, pp. 37-68 (ed. M.N. Harakeh *et al.*, Plenum Press, New York, 1994).

[28] K. Merle, Ph.D. thesis, University of Mainz, unpublished, 1976.

[29] E.A.J.M. Offermann *et al.*, Phys. Rev. C **44** (1991) 1096.

[30] E.A.J.M. Offermann, Ph. D. thesis, University of Amsterdam, unpublished, 1988.

[31] J. Kelly, Ph.D. thesis, MIT, unpublished, 1981.

[32] E.A.J.M Offermann and J. Mandeville, *AEEXB: A program to model the $A(e,e'X)B$ reaction*, modified version available upon request.

[33] C.R. Ottermann *et al.*, Nuclear Physics **A436** (1985) 688.

[34] A. Amroun *et al.*, Nuclear Physics **A579** (1994) 596.

[35] J. Heisenberg and H.P. Blok, Ann. Rev. Nucl. Part. Sci. **33** (1983) 569.

[36] C.S. Tripp, Ph.D. thesis, Rensselaer Polytechnic Institute, unpublished, 1995.

[37] S. Wolf, University of Mainz, private communication.

[38] E.A.J.M. Offermann, *ESPACE: Event Scanning Program for A1 Collaboration Experiments*, unpublished.

[39] A. Rokavec, Ph.D. thesis, University of Ljubljana, unpublished, 1994.

[40] A. Liesenfeld, University of Mainz, private communication.

[41] W.H. Press *et al.*, *Numerical Recipes* (Cambridge University Press, 1986).

[42] P.R. Bevington and D.K. Robinson, *Data Reduction and Error Analysis for the Physical Sciences* (McGraw-Hill, Inc., 1992).

[43] J. Templon, *Radiative-Tail Simulations for Mainz Expt. A1/1-93*, University of Georgia Experimental Subatomic Physics Report 98–001 (1998).

[44] C.E. Vellidis, *AEEXB: A program for Monte Carlo simulations of coincidence electron scattering experiments*, Bates internal report, unpublished, 1998.

[45] A. Kievsky *et al.*, Phys. Rev. C **56** (1997) 64.

[46] G.G. Simon *et al.*, Nuclear Physics **A333** (1980) 381.

[47] A. Kozlov, Institut für Kernphysik, University of Mainz, private communication.

[48] E. Jans *et al.*, Nuclear Physics **A475** (1987) 687.

[49] R.W. Schulze and P.W. Sauer, Phys. Rev. C **48** (1993) 38.

[50] M. Lacombe *et al.*, Phys. Rev. C **21** (1980) 861.

[51] A. Stadler *et al.*, Phys. Rev. C **44** (1991) 2319.

[52] J.L. Forest *et al.*, Phys. Rev. C **54** (1996) 646.

[53] R.B. Wiringa *et al.*, Phys. Rev. C **51** (1995) 38.

[54] B.S. Pudliner *et al.*, Phys. Rev. Lett. **74** (1995) 4396.

[55] R. Schiavilla, Phys. Rev. Lett. **65** (1990) 835.

[56] J.F.J. van den Brand *et al.*, Phys. Rev. Lett. **60** (1988) 2006.

[57] J.F.J. van den Brand, Ph.D. thesis, University of Amsterdam, unpublished, 1988.

[58] R. Schiavilla *et al.*, Nuclear Physics **A449** (1986) 219.

[59] V.D. Efros *et al.*, Phys. Rev. C **58** (1998) 582.

[60] P.E. Ulmer, *MCEEP: Monte Carlo for Electro-Nuclear Coincidence Experiments*, CEBAF Tech. Note 91-101 (1991).

[61] J. Zhao, private communication.

[62] E. Quint, Ph. D. thesis, University of Amsterdam, unpublished, 1988.

[63] M. Holtrop, Ph. D. thesis, MIT, unpublished, 1995.

[64] J. Schwinger, Phys. Rev. **75** (1949) 898.

[65] S. Penner, *Nuclear Structure Physics*, Proceeding of the 18th Scottish University Summer School in Physics, page 69 (1977).

[66] M. Abramowitz and I.A. Stegun, *Handbook of Mathematical Functions*, National Bureau of Standards Applied Mathematics Series 55, (June 1964), page 1004.

[67] J. Friedrich, Nucl. Instr. and Meth. **129** (1975) 505.

[68] Y.S. Tsai, Rev. Mod. Phys. **46** (1974) 815.

[69] D.J.S. Findlay and A.R. Dusautoy, Nucl. Instr. and Meth. **174** (1980) 531.

[70] W. R. Leo, *Techniques for Nuclear and Particle Physics Experiments* (Springer-Verlag, Berlin, 1987), page 40.

[71] J.A. Caballero *et al.*, Nuclear Physics **A555** (1993) 709.

[72] J.M. Friedrich, diploma thesis, University of Mainz, unpublished, 1995.

[73] H. Merkel, University of Mainz, private communication.

[74] R. D. Evans, *The Atomic Nucleus* (New York, McGraw-Hill, 1955).

Acknowledgements

Like all large endeavors, this work is the result of the contributions of many individuals. The list of acknowledgements is long, but very important, so I have therefore attempted it. I apologize for any possible omissions, which are unintentional.

First and foremost I would like to thank my adviser, Bill Bertozzi. It was a privilege to work with him, and to have the benefit of his remarkable physics insight and expertise. Bill gave generously of his time and attention over the years, and we shared many long and interesting discusssions that helped me through the general exams, shaped my physics knowledge and guided this thesis.

I would also like to thank especially Shalev Gilad, who provided so much day-to-day advice and encouragement throughout the long years of data analysis. Shalev always took the time to listen both to my problems and my successes.

I would like to thank Prof. Thomas Walcher and Prof. Rainer Neuhausen, who invited me to spend a year as a guest student in Mainz. They arranged for my financial support and took an interest in my progress and well-being during my stay.

I owe a great deal to Werner Boeglin and Eddy Offermann, who offered their expertise to this project and their friendship to me. My time in Mainz was greatly enriched by them, and they continued to take an active interest in this work long after they had moved on to other endeavors. Most of the software I used to analyze the data was a product of their effort.

I would also like to acknowledge all of the students and other scientists in Mainz who are part of the A1 Collaboration. The three-spectrometer system is a result of their hard work and dedication, and this experiment was made possible by their efforts. In Mainz I had the good fortune of sharing an office with Alfred Richter, Arnd Liesenfeld, Axel Wagner and Ralph Böhm. They accepted their unilingual guest readily and warmly, and encouraged my tortured efforts to speak a few words of German. I enjoyed their company on many occasions, and thank them for making my stay an enjoyable one.

I would also like to thank the postdocs (past and present) in the Nuclear Interactions Group at MIT who together contributed to all phases of this experiment: Jian-Ping Chen, Dan

Dale, Adam Sarty, Jeff Templon and Jianguo Zhao. Similarly, I thank our collaborators from California State University who participated in the experiment: Konrad Aniol, Martin Epstein, and Dimitri Margaziotis. I would also like to acknowledge the Darmstadt group (Michael Kuss, Toshimi Suda, Gerhard Schrieder) for their contributions to the experiment, particularly for their efforts in installing and operating the Helium target.

The simulations of the radiative tail (shown in Chapter 5) were done by Jeff Templon, who worked closely with Costas Vellidis to develop and debug the techniques employed. I am very grateful for the tremendous effort that this entailed.

I am also indebted to Peggy Berkovitz in the Physics Education Office at MIT who kept all the administrivia in order. More importantly, she was always ready with kind words of encouragement. Similarly, I'd like to thank Joanne Gregory in LNS for her help, thoughts and laughter. I'm also grateful to Monika Baumbusch, who organized money, travel and housing while I was in Mainz and also insured that I had a great social life. I enjoyed the hospitality of her and her husband Conny on many occasions.

Bill Donnelly was always forthcoming with his time to discuss my results and to give advice. I am appreciative of his generosity and interest, and for his presence on my thesis committee. Thanks also to another member of the committee, George Clark, for his patience in reading a thesis with such an arcane topic. I'd like to thank Dennis Skopik, who was my adviser during my M.Sc. at the University of Saskatchewan, for his encouragement and also for providing me with office space in his lab during several holiday visits to Saskatoon.

Since arriving at MIT in the fall of 1992 I have had the good fortune to enjoy the friendship of a lot of great people. Mark Wang was one of the first, and I am grateful that we continue to keep in touch. Vincanzo Lia and I endured much of the early class work and exams together, and I am thankful for that camaraderie. A fantastic piece of luck was meeting someone who became a good friend, Dennis Hall, through a random housing assignment. I am also grateful for the friendship of Christian Kunz, who saved my sanity on more than one occasion with his excellent sense of humor, fun, and adventure. I have also had the pleasure of the company of Marcello Pavan, Roman Fleck and Michael Distler. Together with Christian, we have enjoyed countless

lunches, several martinis, and some great parties. Todd Brennan is another good friend, and I owe him a special debt of gratitude for his generous hospitality. Another remarkable person that this project introduced me to is Simon Sirca from Ljubljana, an excellent travel companion and friend who in many ways introduced me to European culture.

There are many others whose company I have enjoyed while at MIT, including Pam Campos, Jiang Chen, Dirk DeSchepper, Steve Dolfini, Kevin Fissum, Juncai Gao, Nik Gregory, Maurik Holtrop, Dave Jordan, Nikos Kaloskamis, Nilanga Liyanage, Joe Mandeville, Jeff Martin, Art Mateos, Indranath Neogy, jae Roh, David Rowntree, Bill Schmitt, Taeksu Shin, Mark Sutter, Bryan Tipton, Costas Vellidis, Glen Warren, and Zilu Zhou. They have all helped to make graduate school a much more enjoyable experience.

I thank all my family and especially my parents, Lionel and Aline Florizone, for their love and support in all my endeavors. My Mom has always been very pro-education, but I think she is still a bit surprised how strongly I took that message to heart. I am also very grateful to Blaine and Pat Holmlund and family for the kindness, caring and generosity they have shown me.

Finally, I would like to thank Mona Holmlund for her incredible patience and encouragement during this long project. I am ever grateful for her love and for her presence in my life.

Biographical Note

Richard Florizone was born on December 26, 1967 in Prince Albert, Saskatchewan, Canada. He graduated from St. Mary High School in Prince Albert in 1985, and spent the following year as a Rotary International Exchange Student in Mornington, Victoria, Australia where he attended Mornington High School and Frankston TAFE. In October, 1990 he received the B. Sc. in Engineering Physics with Great Distinction and was awarded the President's Medal from the University of Saskatchewan. He received an M. Sc. from the University of Saskatchewan in October, 1992 with his thesis work completed at the Saskatchewan Accelerator Laboratory. His graduate studies at MIT began in September 1992 and included one year living in Mainz, Germany, where his thesis experiment was conducted.